

# SHARING

## SELF-ORGANIZED HETEROGENEOUS ADVANCED RADIO NETWORKS GENERATION

### Deliverable D3.6

#### Performance assessments of the most promising Multi-point transmission and reception techniques

<b>Date of delivery</b>	16/02/2016
<b>Contractual date of delivery</b>	31/12/2015
<b>Project number</b>	C2012/1-8
<b>Editor</b>	Sylvie Mayrargue (CEA)
<b>Authors</b>	Benoît Denis (CEA), Nicolas Cassiau (CEA), Christophe Delaveaud (CEA), Cyril Jouanlanne (CEA), Fatima Kaddour (CEA), Dimitri Ktenas (CEA), Sylvie Mayrargue (CEA), Jun Ting Chen (EUR), David Gesbert (EUR), Sandeep Kottath (EUR), Nivine Abbas (Orange), Thierry Clessienne (Orange), Berna Sayrac (Orange), Raphaël Visoz (Orange), Serdar Sezginer (SEQ), Grégory Gougeon (SIR), Yoann Corre (SIR), Yves Lostanlen (SIR), Antoine Berthet (SUP), Chien Chun Cheng (SUP), Mohamad Assaad (SUP), Anne Ferréol (TCS), Yolanda Fernandez (TTI), Adrian Sanchez (TTI).
<b>Dissemination level</b>	PU
<b>Workpackage</b>	3
<b>Version</b>	0.5
<b>Total number of pages</b>	136

#### Abstract:

SHARING project WP3 was dedicated to advanced techniques that are needed to cope with traffic increase, and to fulfil the objective of "services for everyone everywhere". This latter objective implies the offer of a homogeneous quality of service all over the network, whatever the user location (cell center or cell edge). Several new features have been introduced in 3GPP LTE to address these issues, such as CoMP (Coordinated Multi-Points), Carrier Aggregation (CA), and advanced receivers. Previously introduced features, such as MIMO and Multi-User-MIMO also contribute to these objectives. The project, though, did not limit itself to investigate existing solutions in 3GPP, but also considered new schemes, potential candidates for 5G, such as interference alignment, Linear Dispersion codes and Interference Maps.

**Keywords:** Small cells, Interference management, Interference cancellation, Interference mitigation, MIMO, MU-MIMO, CoMP, Carrier aggregation, Reconfigurable power amplifier, Miniature antenna, Frequency agility,

#### Document Revision History

Version	Date	Author	Summary of main changes
0.1	13/07/2015	CEA, TTI	Creation of the Table of Contents (ToC)
0.2	27/10/2015	CEA	Part A ready
0.3	26/01/2016	CEA	Part B ready
0.4	2/02/2016	CEA	Part A and B integrated. Introduction, Executive Summary ready.
0.5	15/02/2016	CEA	Reviews taken into account

# TABLE OF CONTENTS

<b>EXECUTIVE SUMMARY</b> .....	<b>8</b>
<b>1 INTRODUCTION</b> .....	<b>12</b>
<b>2 PART A: MULTI-POINT TRANSMISSION AND RECEPTION TECHNIQUES</b> .....	<b>13</b>
2.1 MULTI-POINT COOPERATION AT THE TRANSMITTER.....	13
2.1.1 <i>Asymptotic Performance analysis of Coordinated Multi-cell MIMO schemes</i> .....	14
2.1.2 <i>Distributed CoMP schemes with limited Feedback and time average QoS</i> .....	14
2.1.3 <i>Design and Analysis of CSIT Allocation for JP-CoMP</i> .....	15
2.1.4 <i>Precoder and Scheduler Design Strategies for CoMP based on Distributed CSI</i> .....	17
2.2 INTERFERENCE CANCELLATION AT THE RECEIVER AND ADVANCED TRANSCEIVERS.....	20
2.2.1 <i>Fundamental limits of advanced MIMO schemes with various CSI</i> .....	20
2.2.2 <i>Widely Linear receiver solutions to suppress or avoid interference with advanced MIMO schemes</i> .....	21
2.2.3 <i>Downlink multi-user CoMP with interference aware receivers</i> .....	23
2.2.4 <i>Advanced interference mitigation in the uplink</i> .....	25
2.2.5 <i>Interference cancellation within imperfect channel information in LTE DL transmission</i> .....	28
2.2.6 <i>Interference alignment with incomplete CSIT</i> .....	29
2.2.7 <i>Enhanced spatial modulation schemes</i> .....	31
2.3 FLEXIBLE INTERFERENCE MANAGEMENT CONCEPT.....	33
2.3.1 <i>Joint location and interference prediction for ICIC</i> .....	34
2.3.2 <i>Calibration framework for physical layer abstraction of codewords IC receivers</i> .....	35
2.3.3 <i>Advanced scheduling for intra and inter-site CoMP</i> .....	36
2.3.4 <i>Cross-layer performance evaluation of CoMP</i> .....	37
2.3.5 <i>Deterministic channel modelling enhancements for MIMO</i> .....	38
2.3.6 <i>Impact of beamforming in a large scale real environment</i> .....	40
2.4 RF AND ANTENNA DESIGN .....	42
2.4.1 <i>Reconfigurable RF front-end to support carrier aggregation</i> .....	42
2.4.2 <i>Design of miniature multi-band frequency agile antenna system for carrier aggregation</i> .....	47
<b>3 PART B: NEW WORK, NOT YET REPORTED IN PREVIOUS DELIVERABLES</b> .....	<b>51</b>
3.1 MULTI-POINT COOPERATION AT THE TRANSMITTER.....	51
3.1.1 <i>The cost of distributed CSI feedback in JP CoMP</i> .....	51
3.1.2 <i>Asymptotic Performance analysis of advanced MIMO schemes</i> .....	55
3.1.3 <i>Distributed CoMP schemes with limited Feedback and time average QoS</i> .....	60
3.2 INTERFERENCE CANCELLATION AT THE RECEIVER AND ADVANCED TRANSCEIVERS.....	67
3.2.1 <i>Widely Linear receiver solutions to suppress or avoid interference with advanced MIMO schemes</i> .....	67
3.2.2 <i>Downlink multi-user CoMP with interference aware receivers</i> .....	80
3.2.3 <i>Advanced interference mitigation in the uplink</i> .....	85
3.2.4 <i>Interference Cancellation within Imperfect Channel Information in LTE DL Transmission</i> .....	93
3.2.5 <i>Enhanced Spatial Modulation Schemes</i> .....	97
3.3 FLEXIBLE INTERFERENCE MANAGEMENT CONCEPT.....	102
3.3.1 <i>Joint location and interference prediction for ICIC</i> .....	102
3.3.2 <i>Advanced scheduling for intra and inter-site CoMP</i> .....	109
3.3.3 <i>Cross-layer performance evaluation of CoMP</i> .....	113
3.3.4 <i>Impact of beamforming in a large-scale real environment</i> .....	118
3.4 RF DESIGN .....	120
3.4.1 <i>Reconfigurable RF front-end to support carrier aggregation</i> .....	120
<b>4 CONCLUSIONS</b> .....	<b>127</b>
<b>5 REFERENCES</b> .....	<b>128</b>
<b>6 GLOSSARY</b> .....	<b>132</b>

## LIST OF FIGURES

Figure 1 Configuration of a multi-cell MIMO network under JP CoMP	17
Figure 2 A toy example illustrating the network of interest, with 4 Base Stations ( $M=4$ ) each with two antennas ( $J=2$ ) serving 4 UEs ( $K=4$ ).	18
Figure 3: Variation of Sum Rate with Number of Feedback Bits $B$ .	19
Figure 4 - The MIMO (or MISO) scheme of LTE-A in downlink	22
Figure 5 - LD MIMO Code scheme of symbols $\{a_{ij}\}$ with $N_e$ transmitted antennas and $K$ temporal length	22
Figure 6 - Alamouti LD MIMO Code scheme with $N_e=K=2$	22
Figure 7. Scenario of the study	24
Figure 8. Scenario for D3.6.B	25
Figure 9 - SC-FDMA transmission for users to eNodeB	27
Figure 10 - The second MIMO scheme of LTE-A with multiple users	27
Figure 11 - The time-frequency Resource Block into LTE-A	28
Figure 12 BER vs SNR in the strong interference region, $SIR = 0$ dB	29
Figure 13: A topology of the 6-cell network.	31
Figure 14: Illustration for a network with 5 transmit-receive pairs, where each transmitter has three links.	31
Figure 15 PEP curves for 10 bpcu-4-Tx	32
Figure 16 Two scheduling approach for CoMP	37
Figure 17 Weakness of the studied scheduler	37
Figure 18. Macro-cell layer deployment in a real dense urban environment	39
Figure 19. Channel impulse response at test UE location with basic (left) and full (right) complexity models	40
Figure 20. Condition Number prediction	40
Figure 21. CDF of the SINR (left) and of the mean user peak throughput (right) with two and four antennas beamforming, compared to single transmit antenna	41
Figure 22 Block diagram of the reconfigurable PA supporting CA.	42
Figure 23 Band 20 instantaneous bandwidth reduction illustration	48
Figure 24: Measured and simulated reflection coefficients at band 20 antenna in three different states.	48
Figure 25 : Picture of the antenna system	49
Figure 26 Pictures of the prototype during the measurement campaign	50
Figure 27: Average rate per user as a function of the number of users $K$ with $\sigma_j^2 = \sigma^2 = 0.154$	
Figure -28: Fluctuations of the downlink SINR (ROBF algorithm) around the target value. $K = 25$ UTs per cell and target SINR = 3 dB per UT.	60
Figure -29: Comparison of downlink power per UT as a function of the number of antennas per BS. $K = 25$ UTs per cell and target rate = 3 bits/s/Hz ( $\log(1 + \gamma_{i,j})$ ) per UT.	60
Figure -30: Average power Vs target QoS for a two cell scenario, each cell consisting of two UTs, $N_t = 5$ , $P_{\text{peak}} = 10$ dB.	65

Figure -31: Time average power vs time average queue-length for a two cell scenario, each cell consisting of two UTs, $N_t = 5$ , peak power per BS = 10 dB Target QoS value= 10 dB.	66
Figure-32: Average power vs number of transmit antennas, peak power = 10 dB, target QoS = 10 dB, $V = 100$ .	66
Figure 33 – Double Alamouti LD MIMO Code scheme with $N_e=K=4$ according to Figure 6	73
Figure 34 – Offset of the imaginary part of a symbol constellation such as O-QAM	74
Figure 35 – BPSK without interference $N_r=2$	76
Figure 36 – QPSK without interference $N_r=2$	76
Figure 37 – O-QPSK without interference $N_r=2$	76
Figure 38 – O-QPSK without interference $N_r=2$	77
Figure 39 – BPSK with BPSK interference of same power to UE	77
Figure 40 – QPSK with BPSK interference of same power to UE	78
Figure 41 – O-QPSK with BPSK interference of same power to UE	78
Figure 42 – BPSK with O-QPSK interference of same power to UE	78
Figure 43 – O-QPSK with O-QPSK interference of same power to UE	79
Figure 44 – UE with QPSK interference of same power and $N_r=2$	79
Figure 45. Considered QPSK modulation	81
Figure 46. Serial interference cancellation receiver	82
Figure 47. Scenario for D3.6.B	82
Figure 48. Diagrams of the precoders used in the scenario for $NT = 2$	83
Figure 49. Performance of the receivers in the presence of one interferer.	83
Figure 50. Performance of the receivers in the presence of two interferers. $NT = 2$ .	84
Figure 51. Diagrams of the precoders used in the scenario for $NT = 4$	84
Figure 52. Performance of the receivers in the presence of two interferers. $NT = 4$ .	85
Figure 53 - General scheme for FDE MMSE Equalization in the context of SC-FDMA users transmission	86
Figure 54 – BER without interference $N_r=3$ , $L_0=1$ and $M=96$	90
Figure 55 – BER without interference $N_r=3$ , $L_0=1$ and $M=192$	91
Figure 56 – Direct Approach without interference $N_r=3$ , $L_0=1$	91
Figure 57 – BER with interference ( $dJ=5$ dB) $N_r=3$ , $L_0 = 1$ and $M=96$	92
Figure 58 – BER with interference ( $dJ=5$ dB) $N_r=3$ , $L_0=1$ and $M=192$	92
Figure 59 – Direct Approach with interference ( $dJ=5$ dB) $N_r=3$ , $L_0=1$	92
Figure 60 One-dimensional model arranging pilot and data symbols	94
Figure 61 An example of an asynchronous interference	95
Figure 62 BER vs. SIR under SNR= 30 dB with triply selective channels	96
Figure 63 BER vs. different propagation delay, $\tau$	96
Figure 64 An illustration of ESM-2TX9b: crosses are 64QAM, the heavy/empty circles are the 8APK0/8APK1, the heavy/empty squares are the 8APK2/8APK3, and the heavy/empty triangles are 8APK4/8APK5 signal constellations	98
Figure 65 The SVER performance of 2TX9b.	100
<b>Figure 66 The SVER performance of 4TX11b</b>	101

Figure 67 Impact of the number of Rx antennas	101
Figure 68: Location-dependent ICI estimation model	103
Figure 69: Deterministic interference map (Siradel)	104
Figure 70 CDF of ICI error in regular sensing positions	106
Figure 71 CDF of ICI error: low resolution fingerprinting and updated IM	107
Figure 72: CDF of ICI error: updated IM and low resolution IM vs active UE rates	108
Figure 73: Semi-deterministic IM based on exponential variogram: irregular sensing positions with active UE rate of 15%	108
Figure 74 Impact of system load on JP CoMP Categories performance	111
Figure 75 Deployment scenarios for DPS performance assessment	112
Figure 76 Impact of cluster size on DPS performance	113
Figure 77: A tri sector site with coordination areas	114
Figure 78: Throughput performance with mobility (solid lines) and without mobility (dashed line)	115
Figure 79: Throughput performance with two classes of mobility.	117
Figure 80: Performance obtained by system level simulation.	118
Figure 81. Small-cell network deployed in a dense urban environment (dots are small cell locations)	119
Figure 82 ACLR results vs PA OBO requirement modifying TOI parameter for a) 1CC, b) 2CCs, c) 3CCs, d) 4CCs and e) 5CCs in intra-band contiguous CA configuration.	122
Figure 83 ACLR simulated results from 2CCs to 3CCs supporting intra-band non-contiguous CA.	123
Figure 84 ACLR simulated results for 4CCs supporting intra-band non-contiguous CA.	124
Figure 85 ACLR simulated results for 5CCs supporting intra-band non-contiguous CA.	125
Figure 86 Picture of the hardware prototype developed in WP7.	125
Figure 87 a) Power gain and b) PAE results for different operating points in AFT20S015N prototype.	126

## LIST OF TABLES

Table 1 PA OBO requirements for intra-band contiguous CA.	43
Table 2 PA OBO requirements for intra-band contiguous CA and intra-band non-contiguous CA.	44
Table 3 Energy efficient enhancement provided by the reconfigurable PA for different CA configurations up to 3CCs.	45
Table 4 Energy efficient enhancement provided by the reconfigurable PA for different CA configurations up to 5CCs.	46
Table 5. Enhanced SM, 2 TX, 9 BPCU	98
Table 6 Receiver Complexity ( $NR = 1$ )	99
Table 7 Percentage of throughput gain (or loss) brought by CoMP vs.the case where CoMP feature is disactivated, respectively for a Conventional Scheme [67] (Reference) and for the proposed algorithm (Proposed) in terms of Cell-Edge ( $\Delta_{05}$ ) and Cell Average ( $\Delta_{50}$ ) Throughput.	110
Table 8 Simulation Setting	117
Table 9. Simulation parameters	119
Table 10. Results from the small-cell network simulation	120
Table 11 PA OBO requirements considering ACLR specification for different TOI values in intra-band contiguous CA configuration.	123
Table 12 PA OBO requirements up to 3CCs in different CA configurations.	124
Table 13 PA OBO requirements for 4CCs in different CA configurations.	124
Table 14 PA OBO requirements for 5CCs in different CA configurations.	125

## EXECUTIVE SUMMARY

This document reports all work that has been performed in the context of SHARING WP3. **Part A** contains the summary of all work done, including that which was already reported, so as to give an overview of the whole project. **Part B** contains the details of the new contributions (since last reported results). SHARING project

WP3 was dedicated to advanced techniques that are needed to cope with traffic increase, and to fulfil the objective of “services for everyone everywhere”. This latter objective implies the offer of an homogeneous quality of service all over the network, whatever the user location (cell center or cell edge). Several new features have been introduced in 3GPP LTE to address these issues, such as CoMP (Coordinated Multi-Points), Carrier Aggregation (CA), and advanced receivers. Previously introduced features, such as MIMO and Multi-User-MIMO contribute to the same objectives. The project, though, did not limit itself to investigate existing solutions in 3GPP, but also considered new schemes, potential candidates for 5G, such as interference alignment, Linear Dispersion codes and Interference Maps.

Thus, in WP3, research work on the above mentioned domains was structured in several Tasks. For sake of clarity, contributions have been grouped in a slightly different way. Titles of the original Tasks have been kept, but the content of each section is now as follows:

- **“Multi-point cooperation at the transmitter”** encompasses work related to computations of beamforming weights in the context of CoMP. Computation can be performed either in a centralized or distributed fashion.
  - Computation of the multi-cell beamforming precoders by a *distributed* scheme based on Random Matrix Theory is proposed in the context of massive MIMO in Part A section 2.1.1 and Part B Section 3.1.2, (Task 3.1 = T3.1)
  - The problem of *distributed* coordinated beamforming in a multi-cell system is considered in Part A section 2.1.2 and Part B section 3.1.3. The goal is to minimize the time average energy expenditure such that a time average quality of service (QoS) is satisfied for each user. (T3.1)
  - In Section 2.1.3.1, *centralized and distributed* schemes under non-perfect Channel State Information (CSIs) cases are compared in terms of asymptotic number of feedback bits needed to maintain a constant gap to the sum rate achieved by the perfect CSI scheme when increasing the Signal to Noise Ratio (SNR ).(T3.1)
  - In Section 2.1.3.2, in order to reduce the performance loss between *distributed and centralized* precoding schemes, a smart allocation of CSI feedback bits is proposed, so that a UE located near the base station gets more feedback bits. (T3.1)
  - In Sections 2.1.3.3, and Part B 3.1.1, the previous method is extended to multiple antennas at the base station and a large number of users. Through analysis using random matrix theory, this work shows that the degradation of the sum rate performance of *distributed* precoding does not vanish in large system limit. (T3.1)
  - Section 2.1.4 addresses the problem of joint precoding across base stations for interference mitigation. Section 2.1.4 aims at creating dynamic cooperation clusters, which can help cancel in a dynamic manner the strongest sources of interference. Dynamic cluster formation is based on the concept of broadcast feedback set by users in the uplink. (T3.1)
- **“Interference cancellation at the receiver and advanced transceivers”** includes all contributions related to interference mitigation, not necessarily in a CoMP context, where advanced transceivers are used for this purpose.
  - Section 2.2.1 deals with the ultimate performance limit of the K-user multi-antenna broadcast channel with confidential messages and outdated CSI knowledge. The objective is to find the DoF (Degrees of Freedom), which capture the behavior of the capacity in high SNR regime. Similarly to the case without secrecy constraint, it was found in this



- work that outdated CSI is useful to increase the secrecy capacity in the high SNR regime (T3.1)
- Sections 2.2.2 and 3.2.1 present an interference mitigation scheme at the Downlink (DL) receiver when the transmitted signal is built with a linear dispersion (LD) code. The scheme is based on the concept of widely linear (WL) receivers. Indeed, provided that a user or its interferer uses a non-circular modulation, a widely linear minimum mean square (MMS) receiver supersedes a simple MMSE receiver since it may reject an interferer using a single antenna (T3.1)
  - In Sections 2.2.3 and 3.2.2, interference aware receivers are introduced at the Downlink (DL) receiver at the UEs, in order to mitigate interference generated by non perfectly orthogonal precoders in DL MU-MIMO in one or several CoMP cells (T3.1).
  - Sections 2.2.4 and 3.2.3 focus on Uplink (UL) LTE receivers in presence of interference caused by a Multi-user MIMO scheme. Taking into account that LTE UL uses SC-FDMA modulation, two receivers respectively using a direct and an indirect approach are compared, based on the DMRS pilot symbols, either receiver filter coefficients are directly computed from the pilot symbols (direct approach), or the channel coefficients are first computed, and then the receiver filter coefficients are derived from them (indirect approach) (T3.2).
  - Section 2.2.5 provides a signal-to-interference-plus-noise ratio (SINR) analysis focusing on the comparison between the conventional interference rejection combination (IRC) and the proposed interference rejection techniques taking into account the difference between the interfering pilots and the interfering data signal in terms of their covariance matrices. In Part B Section 3.2.4, the performance of the proposed schemes is evaluated under more practical considerations such as non-synchronized cases and triply selective channels due to time, frequency and spatial variations. (T3.2).
  - Section 2.2.6, deals with interference alignment schemes. Such schemes have been proposed in the literature as a mean to cancel intercell interference by combining transmit beamformers at the source (eg. base station), and receive beamformers at the destination (eg. UEs). However, complete CSIT should be known on the transmit side in order to compute the Beamforming (BF) weights, which might not scale well when the number of transmitters increases. In this work, it is shown that (Section 2.2.6.1) not all CSI need to be known, and that, 2.2.6.2, in the case the network is not fully connected (not all transmitters interfere with all receivers), a graph-based algorithm can be used to determine how the transmitters share the time-frequency resources for interference avoidance.(T3.3)
  - Sections 2.2.7 and 3.2.5 deal with the Spatial Modulation (SM) concept. SM is a Multiple Antenna transmit scheme where the active antenna index carries some information bits. The Enhanced SM (ESM) presented here targets higher spectral efficiency by using multiple signal constellations: additional information bits are transmitted by both antenna and constellation combinations indices. The impact of the number of receive antennas is also investigated showing that the performance gains increases with the number of receive antennas (T3.2)
  - **“Flexible interference management concept”** presents various cross-layer algorithms (Physical (PHY) and MAC) that deal with interference issues. It also contains a contribution on realistic ray-tracing channel models, which was used by another contribution of this section.
    - Sections 2.3.1 and 3.3.1 deal with the construction of an interference map that can be used to predict interference which can be useful e.g in a handover procedure. This map is built in two steps: a first map is obtained via a statistical model, based on PPP (Poisson Point Process) that needs as inputs the network’s nodes density, the path loss parameters and the distance between the considered UE and its first interfering node. Then, this map is refined by using the interference measurements reported by active UEs to the central base station. The final map is thus obtained by a Kriging interpolation on the errors between measurements and the initial map. (T3.3)

- Section 2.3.2: It is usual to build metrics that characterize a block fading channel, w.r.t. a given type of receivers. These metrics are called ESM (Effective SNR Metrics). They summarize SINRs on several blocks in a single figure, making it equivalent to an AWGN SNR. Section 2.3.2 proposes an improvement of the calibration of such a metric in the context of a turbo linear codeword interference canceller (L-CWIC in 3GPP). The goal is to use this metric to predict the Packet Error Rate (PER), and then operate link adaptivity in terms of Modulation and Coding Schemes. (T3.3)
- Section 2.3.3 considers the performance of JT CoMP for intra and inter-site scenarios. The aim is twofold: on the one hand, to evaluate the JT CoMP scheme in order to better understand its benefits and on the other hand to show if a better gain is achieved with intra site cooperation or with an inter site cooperation. Considering two types of schedulers (distributed and centralized scheduling) it was shown that the performance improvement of the CoMP UEs is obtained to the detriment of the legacy UEs. To address the weakness of conventional schedulers, a centralized opportunistic approach was proposed, thus introducing more fairness between the non-Comp UEs and Comp UEs. The objective of Section 3.3.2 is to evaluate the effectiveness of this algorithm for other categories of CoMP. It is shown that network load is a key factor in choosing the best CoMP category (JT, DPS). Indeed when the load is low, a lot of spectral resources are available and coherent JT outperforms the other categories. In contrast, at high loads, available resources are scarce, only CoMP categories that do not need additional spectral resource are efficient. The contribution suggests that the combined use of both Coherent JT and Dynamic Point Selection (DPS) Without Muting (W/o) allows obtaining a very wide operational range from low to high network load with just one scheme. (T3.3)
- In Sections 2.3.4 and 3.3.3, the impact of mobility on JP-CoMP scheduling schemes is studied. First, a mobility model was proposed and validated by system level simulations. Then in Section 3.3.3, this model is used to study the impact of mobility on scheduling schemes in the presence of inter-cell coordination. Several CoMP scheduling strategies are compared, both in the static and the mobility case. It is shown that a scheduler prioritizing non-CoMP users in the static case brings performance degradation, while in the mobility case the same scheduler outperforms other strategies. Taking this fact into account, a mobility-aware scheduler is proposed, which deprioritizes mobile CoMP users. This scheduler improves the performance by giving the chance to mobile cell-edge users to be served in better radio conditions whenever cell coordination is not adapted (T3.1).
- Section 2.3.5 is an input to all others, since it provides channel impulse responses in realistic scenarios, obtained by a ray based model. These MIMO channel models are spatially and temporally richer than those of 3GPP. **It is to be noted that examples of channel impulse responses provided by Section 2.3.5 were exploited by contributions in Sections 2.3.1 and 3.3.1 on interference maps.**(T3.1)
- Sections 2.3.6 and 3.3.4 provide a system level evaluation of the beamforming gain w.r.t. the SINR distribution. Channel impulse responses are derived from the same ray based model as Section 2.3.5. (T3.3)
- **“RF and antenna design”** was dedicated to a Front-end RF (RF power amplifier (PA) and antenna), capable of accommodating Carrier Aggregation (CA), even at the lowest frequencies currently allocated to LTE (band 20), thanks to a wideband PA and a frequency agile antenna. These two contributions (PA and antenna) from two different partners have resulted in an integrated demonstration, reported in WP7.
  - 2.4.1 and 3.4.1. The power amplifier (PA) is one of the most power consuming components at RF front-end. Depending on the CA configuration (intra-band contiguous or intra-band non-contiguous) and the number of component carriers (CCs), different output back-off (OBO) levels are required at the PA. Therefore a reconfigurable RF front-end was proposed capable to adapt its performance using different operating points at the PA thereby improving energy efficiency (Figure 22). The solution was compared to a conventional PA with single operating point to evaluate energy efficiency enhancements.

- 2.4.2 An LTE dual band frequency agile antenna whose size is suited to small cell base station has been designed. It supports several CA modes and has been optimized in terms of size and volume thanks to a bandwidth reduction and the use of frequency agility technique.

## 1 INTRODUCTION

SHARING project WP3 was dedicated to advanced techniques that are needed to cope with traffic increase, and to fulfil the objective of “services for everyone everywhere”. This latter objective implies the offer of an homogeneous quality of service all over the network, whatever the user location (cell center or cell edge). Several new features have been introduced in 3GPP LTE to address these issues, such as CoMP (Coordinated Multi-Points), Carrier Aggregation (CA), and advanced receivers. Previously introduced features, such as MIMO and Multi-User-MIMO contribute to the same objectives. The project, though, did not limit itself to investigate existing solutions in 3GPP, but also considered new schemes, potential candidates for 5G, such as interference alignment, Linear Dispersion codes and Interference Maps.

Thus, in WP3, research work on the above mentioned domains was structured in several Tasks. For sake of clarity, contributions have been grouped in a slightly different way. Titles of the original Tasks have been kept, but the content of each section is now as follows:

- **“Multi-point cooperation at the transmitter”** encompasses work related to computations of beamforming weights in the context of CoMP.
- **“Interference cancellation at the receiver and advanced transceivers”** includes all contributions related to interference mitigation, not necessarily in a CoMP context, where advanced transceivers are used for this purpose.
- **“Flexible interference management concept”** presents various cross-layer algorithms (PHY and MAC) that deal with interference issues. It also contains a contribution on realistic ray-tracing channel model, which was used by another contribution of this section.
- **“RF and antenna design”** is dedicated to a Front-end RF (RF power amplifier (PA) and antenna), capable of accommodating CA, even at the lowest frequencies currently allocated to LTE (band 20), thanks to a reconfigurable and energy efficient wideband PA and a frequency agile antenna. These two contributions (PA and antenna) from two different partners have resulted in an integrated demonstration, reported in WP7.

This document reports all work that has been performed in the context of SHARING WP3. **Part A** contains the summary of all work done, including that which was already reported, so as to give an overview of the whole project. **Part B** contains the details of the new contributions (since last reported results).

## 2 PART A: MULTI-POINT TRANSMISSION AND RECEPTION TECHNIQUES

As indicated in the Introduction, this Part of the document contains the summary of **all** work performed in the context of SHARING WP3. Contributions already reported in D3.2, D3.3, D3.4 and D3.5, as well as the current ones. These latter are presented in detail in Part B.

The subsections of Part A correspond respectively to the descriptions of the 4 tasks within W3. However, for sake of readability, contributions were grouped in a slightly different way from that in the Technical Annex. Indeed, Section 2.1 encompasses all work related to computations of beamforming weights in the context of CoMP (Coordinated Multi-Points). Section 2.2 includes all contributions related to interference mitigation, not necessarily in a CoMP context, where advanced transceivers are used for this purpose. These two latter sections are mainly concerned with PHY layer algorithms, while Section 2.3 presents cross-layer algorithms (PHY and MAC) in order to deal with interference issues. Section 2.3 also contains a contribution on realistic ray-tracing channel models, to be used by other contributions. Last, Section 2.4 is dedicated to a Front-end RF (RF power amplifier and antenna), capable of accommodating Carrier Aggregation (CA), even at the lowest frequencies currently allocated to LTE (band 20), thanks to a wideband PA and a frequency agile antenna.

### 2.1 Multi-point cooperation at the transmitter

CoMP was introduced in the context of 3GPP Release 9 as a Technical Report [1], and further specified in Release 11 [2]. In CoMP a number of TX (transmit) points provide coordinated transmission in the Downlink (DL), and a number of RX (receive) points provide coordinated reception in the Uplink (UL). The main reason to introduce CoMP is to improve network performance at cell edges. Indeed, users located at cell-edge experience both lower received signal power and increased inter-cell interference compared to those at cell center.

Note that most of the time, cells are equipped with multiple antennas, so that CoMP algorithms in fact compute weights at each transmit antenna point.

CoMP can be done in a number of ways:

- when data is available for transmission at each Tx point involved in CoMP, the scheme is coined JP-CoMP (Joint Processing CoMP). Two variants are defined
  - o Joint Transmission (JT), when data to a single UE is simultaneously transmitted from *multiple* transmission points
  - o Dynamic Point Selection (DPS), transmission from one TX-point at a time in each subframe
- when data to a single UE is available at a single Tx point, one can talk of CS/CB (coordinated scheduling/ coordinated beamforming), providing Tx points exchange control signals, The scheduling decisions as well as any beams are coordinated to control the interference that may be generated.

JP CoMP is the most efficient, though most complex type of CoMP schemes. Indeed, on the one hand data is to be available at various cooperating points, and on the other hand broadcasting the same data from different points exploits wireless resources that otherwise would be used for other User Equipments (UEs). Therefore, benefits of JP CoMP schemes have to outweigh this loss. At minimum, JP CoMP should be only used for cell edge users.

In addition, in the CoMP case, precoders weight calculations can be either centralized or distributed

In T3.1, the Multi-cell CoMP was addressed under the form of

- Coordinated Beamforming
  - o In Sections 2.1.1 and Part B 3.1.2, a *distributed* scheme based on Random Matrix Theory is proposed in the context of massive MIMO for computation of the multi-cell beamforming precoders

- In Sections 2.1.2 and Part B 3.1.3 the problem of *distributed* coordinated beamforming in a multi-cell system is considered. The goal is to minimize the time average energy expenditure such that a time average quality of service (QoS) is satisfied for each user. .
- Joint Processing
  - In Section 2.1.3.1, perfect and non-perfect Channel State Information (CSIs) cases are compared in terms of asymptotic number of feedback bits needed to maintain a constant gap when increasing the SNR, both in *centralized and distributed* schemes.
  - In Section 2.1.3.2, in order to reduce the performance loss between *distributed and centralized* precoding schemes, a smart allocation of CSI feedback bits is proposed, so that a UE located near the base station gets more feedback bits.
  - In Sections 2.1.3.3, and Part B 3.1.1, the previous method is extended to multiple antennas at the base station and a large number of users, so that random matrix theory applies. Nonetheless, this work shows that the cost of *distributed* precoding does not vanish in large system limit.
  - In Section 2.1.4 the problem of joint precoding across base stations for interference mitigation is addressed. The approach taken in Section 2.1.4 consists in creating dynamic cooperation clusters, which can help cancel in a dynamic manner the strongest sources of interference. Dynamic cluster formation is based on the concept of broadcast feedback set by users in the uplink and exploits the reciprocity of propagation path loss in uplink and downlink. In addition the precoder method allows to opportunistically exploit any additional CSI feedback decoder by base station relative to user located outside the cluster, permitting the opportunistic mitigation of inter-cluster interference, which classical CoMP approaches are unable to do.

### 2.1.1 Asymptotic Performance analysis of Coordinated Multi-cell MIMO schemes

In Part B, section 3.1.2, the problem of Coordinated Beamforming (CB) in massive multiple input multiple output (MIMO) systems is considered. Massive MIMO is one of the unavoidable techniques in future wireless networks. It refers to the idea of scaling up the number of antennas on the BS to a few hundreds and to exploit the large number of antennas to achieve greater spectral efficiency and serve many tens of users. In this work, we propose an optimal decentralized multi-cell beamforming algorithm for massive MIMO systems that requires limited amount of information exchange between the BSs. In order to overcome the heavy backhaul requirement, a decentralized approach is proposed to compute the multi-cell beamforming vectors. In this algorithm, BSs must exchange parameters at the slow fading time scale rather than the instantaneous channel realizations (fast fading coefficients). Tools from random matrix theory (RMT) are used to formulate the proposed algorithm.

Using a large system analysis, closed form expression for the lower bound on the set of feasible target SINR are provided. Furthermore, it is proven that when the dimensions of the system become large, the achieved SINR in the uplink and downlink by the proposed algorithm matches the target SINR. Moreover, it is also proven that when the dimensions of the system become large, the allocated power by the proposed algorithm is asymptotically optimal.

A heuristic extension of the latter decentralized beamforming algorithm is then provided, to incorporate the individual BS transmit power constraints. Finally, the impact of pilot contamination on the performance of this algorithm is investigated and a heuristic adaptation that improves the system performance is proposed.

### 2.1.2 Distributed CoMP schemes with limited Feedback and time average QoS

In Part B, section 3.1.3,, the problem of distributed coordinated beamforming in a multi-cell system is considered. The goal is to minimize the time average energy expenditure such that a time average Quality of Service (QoS) is satisfied for each user. . The motivation to consider the time average QoS constraint comes from the fact that it provides the flexibility to dynamically allocate resources

over the fading channel states as compared to instantaneous QoS constraints. In terms of energy savings, time average QoS constraint can lead to better performance, due to the fact that the transmissions can be delayed until favorable channel conditions are seen, thus minimizing the energy expenditure. The problem is formulated as a stochastic optimization problem and the proposed solution is based on the technique of Lyapunov optimization, which provides simple online solutions based only on the current knowledge of the system state (as opposed to other approaches such as dynamic programming which suffer from very high complexity).

Contributions in this work are as follows. First the *feasible QoS region* is formulated, i.e. the set of target QoS constraints that are achievable by some control policy. The time average constraint is modelled as a *virtual queue* and the problem is transformed into a queue stabilization problem while minimizing the average energy expenditure. Then the technique of Lyapunov optimization is used to formulate a dynamic control strategy that satisfies the time average QoS targets. The resulting algorithm leads to a decentralized design in which the base stations (BSs) can formulate the beamforming vectors using only the local Channel State Information (CSI). The BSs would only have to exchange virtual queue-length information among each other. Then provide a performance analysis of this algorithm is provided in the case when the BSs exchange the virtual queue-length information with delays. Finally, the impact of limited feedback is studied, when the BS can obtain the CSI of a limited number of users at a time and an algorithm to select the optimal set of users which must feedback their CSIs is provided.

### 2.1.3 Design and Analysis of CSIT Allocation for JP-CoMP

The precoding of JP-CoMP requires CSIT from all the transmitters to all the receivers. In the JP-CoMP scheme, the user data is shared among the transmitters via backhaul links, and the transmitters deliver the data to the users in a cooperative way. Specifically, for instance, the transmitters jointly compute the precoders for each user using cooperative MIMO techniques. However, the precoding requires the global CSIT, i.e., the channels from all the transmitters to all the receivers. While it is quite straightforward to implement such a scheme in a centralized way, it is more desired to search for a distributed solution for JP-CoMP, due to various considerations such as robustness. However, it is challenging to implement the precoding algorithm in a distributed way, due to the issues of global CSIT acquisition. While the user data can be streamed from a data center such that all the transmitters have the same copy of the data, the global CSIT acquisition requires over-the-air signalling, which is prone to errors due to uncorrelated estimation noise and is outdated due to signalling latency. This situation is identified as JP-CoMP precoding via distributed CSIT.

Specifically, under the precoding scheme via distributed CSIT, the transmitters may have different versions of the global CSIT due to signalling delay over the backhaul and the quantization errors. For example, the CSIT between a user and a BS needs to be quantized and broadcast to all the BSs via the backhaul. Yet, due to backhaul latency, the CSIT may arrive at different BSs at different delay, and hence the BSs may observe at a specific time instant different CSIT of the same channel.. We consider the case that each transmitter computes the precoder based on its own version of the global CSIT. Note that when all the transmitters have perfect global CSIT, such precoding scheme is equivalent to the centralized precoding for JP-CoMP. However, when the transmitters have only imperfect CSIT, which is different across transmitters due to the distributive nature, a performance loss is expected. Therefore, it is important to understand how the system performance is affected by the structure of the distributed CSIT and, in addition, how to distribute the CSIT over limited signalling.

We have done a series of works to address the above issue. They are summarized as follows

#### 2.1.3.1 JP-CoMP with limited backhaul

Consider a  $K$ -cell JP-CoMP network that serves  $K$  users, where each BS (transmitter) and each user (receiver) is equipped with a single antenna. The user data is available at all the transmitters, which perform cooperative MIMO to serve all the  $K$  users simultaneously. The CSIT is obtained via the feedback from the receivers to the transmitters over capacity limited channels with  $B$  bits per feedback link. We study two precoding and CSIT configurations. In the first

configuration, a centralized precoding is considered, where a central controller collects all the quantized CSIT and computes the precoders for all the transmitters using the zero-forcing (ZF) scheme. In the second configuration, each transmitter has its own global quantized CSIT (modelled by the true CSIT corrupted by independent noise), and based on such distributed CSIT, each transmitter computes its own precoder individually using ZF scheme. We analyse how many bits are required in order to maintain roughly a constant gap from the case with perfect global CSIT, when increasing the SNR.

Results, presented in [3], show that, in the centralized CSIT scheme, the total number of feedback bits required scales as  $K \log_2(K-1)P$ , where  $P$  is the transmission power. By contrast, in the distributed CSIT scheme, the number of feedback bits scales roughly as  $K \log_2((2K-1)K-1)P$ , which is roughly  $K \log_2(K)$  bits more than the centralized scheme, in order to maintain similar sum rate gap from the perfect global CSIT scheme. This suggests that we do pay a price for distributed implementation.

### 2.1.3.2 Spatial CSIT allocation for JP-CoMP schemes

While distributed precoding via local CSIT suffers from performance loss compared to centralized precoding, one may want to know whether it is possible to minimize the performance loss through a smart CSIT allocation. Specifically, it is of high interest to investigate how to allocate the number of bits for the feedback of the quantized CSIT from the receiver to transmitter as well as from one transmitter to another transmitter.

A CSIT allocation strategy was developed and presented in [3]. It is based on the distance defined on the *interference level matrix*, which measures the signalling noise level of each feedback link, i.e., the variance of the noise that corrupts the CSIT being fed back. The basic idea is that more bits should be allocated to acquire the CSIT from the user nearby (in terms of the distance measured by the interference level), and fewer bits should be allocated to the remote users. We demonstrate that such dynamic CSIT allocation scheme achieves much better sum rate performance than the uniform CSIT allocation under high SNR regimes.

### 2.1.3.3 The cost of distributed CSI feedback in JP CoMP

In Part B, section 3.1.1, these results were extended to the case where each transmitter is equipped with multiple antennas. An example topology where  $n$  transmitters serve  $K$  users is illustrated in the figure below, where each transmitter is equipped with  $M$  antennas. In particular, we are interested in the limiting case of large system, where both number of antennas  $M$  and number of users  $K$  scale to infinity, with the ratio  $M/K$  being constant.



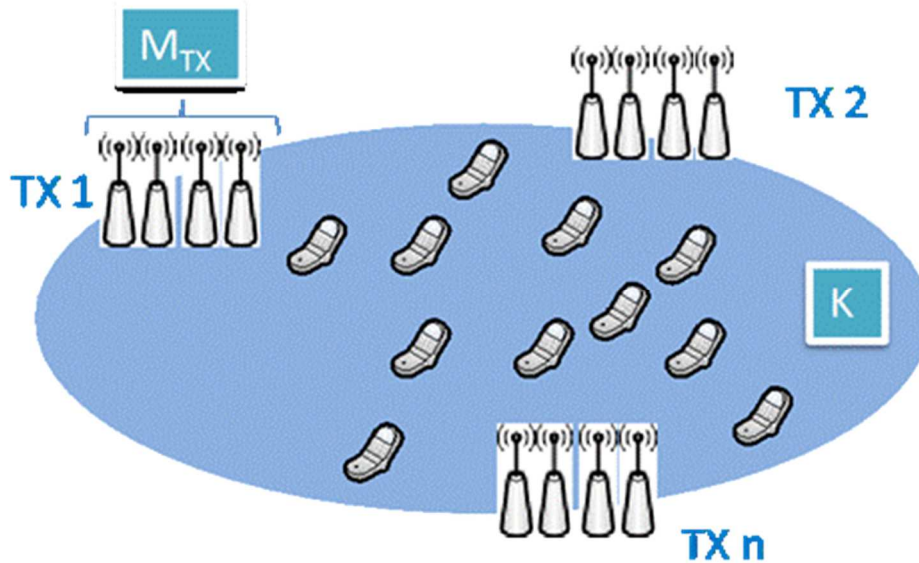


**Figure 1 Configuration of a multi-cell MIMO network under JP CoMP**

Our results found that the price of distributed precoding does not vanish in large system limit. Specifically, consider a centralized precoding scheme where a central controller collects the global CSIT corrupted by noise (due to estimation or latency) and design the precoder jointly for all the transmitters using the regularized-ZF (RZF) scheme. Consider a distributed scheme where each transmitter has its own version of global CSIT estimate (corrupted by noise with same covariance as the centralized scheme, while the noise is uncorrelated across transmitters). The theoretical results via random matrix theory show that the distributed scheme suffers from sum rate loss with a constant gap from the centralized scheme even when the number of transmitter antennas  $M$  grows to infinity. These results suggest that we cannot benefit from the large antenna system to mitigate performance loss due to distributed precoding with distributed CSIT.

#### **2.1.4 Precoder and Scheduler Design Strategies for CoMP based on Distributed CSI**

Since we are heading to an 'all connected' world, where there are more and more devices being part of wireless network, there is a need to develop new strategies for coordinated transmission from nearby transmitters to any device in order to avoid or manipulate interference [47]. In [3], a distance based user centric clustering of base stations and a subsequent broadcast feedback of the CSI was proposed. A distributed scheduler design approach was proposed in [3], and is summarized below.

Base stations in the network are assumed to access the data from a cloud but they need instantaneous CSI for the precoder design.

##### **2.1.4.1 : Opportunistic Feedback Mechanisms for Decentralized Network MIMO systems**

In such a dense network, a distance based user centric clustering of base stations and a subsequent broadcast feedback of the CSI was proposed. In the first phase, each Base Station (BS) will find the neighboring UEs. Hence each UE will have different set of neighboring BSs. This can be accomplished by BSs measuring the path loss of different UEs in the neighborhood using the location information. Then these BSs will send pilot signals for UEs to estimate the channels. Each UE will estimate channels from a neighborhood of BSs. In the case of dense heterogeneous networks, channel estimation has to be performed on the basis of orthogonal pilots in order to avoid pilot contamination. In such a case, it was shown in the context of the SHARING project [12] that using broadcast feedback does not require any additional resources but gives a scalable feedback allocation.

The main highlight of broadcast feedback is that it leads to a distributed CSI knowledge depending on UE location, each BS can have CSI from a different set of UEs in the neighborhood. Here JP-CoMP is used, and hence it is assumed that the data of UEs are shared among the BSs. When the system is of low mobility, there are many ways to have data sharing, for instance using distributed caching. But needless to say, the principle of broadcast feedback can be exploited in contexts of transmitter coordination schemes other than JP-COMP, such as interference alignment strategies or coordinated scheduling along with broadcast feedback.

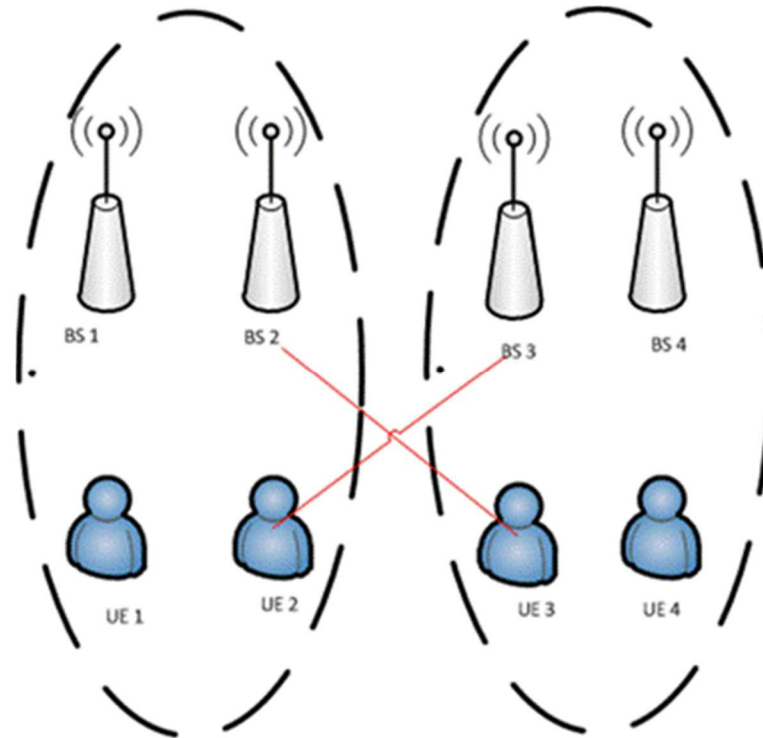


**Figure 2** A toy example illustrating the network of interest, with 4 Base Stations ( $M=4$ ) each with two antennas ( $J=2$ ) serving 4 UEs ( $K=4$ ).

Further work within SHARING [11] focussed on the precoder optimization in such a system where the CSI is distributed [47]. A classical limitation of CoMP clustering is the degradation created by inter-cluster interference which is left unaddressed by cooperation mechanisms within the cluster. This degradation is particularly severe in smaller cluster sizes (2 or 3 cells), while it is desirable to maintain clusters small in order to reduce feedback requirements. A feedback and cooperation architecture which addresses this problem was proposed. It was pointed out that the broadcast feedback scheme often leads to BS decoding the CSI feedback of additional users that do not end up being admitted in the cluster of users served by this BS, for instance because the CSI of the same user is also received by other BS that are closer to the user. Note that the ability for one base station to receive short CSI packets from out of cluster user is currently not in line with LTE standardization. The idea is hereby presented as an exploratory topic for future standard evolutions. In previous cluster-based cooperation techniques, this extra CSI information available at the BS is not suitably exploited. A scheme allowing to capitalize on this possible extra feedback in an opportunistic manner was proposed.

This leads to a challenging decentralized MIMO precoding problem whose general solution is still open. Subsequently a heuristic method built on the known notion of interference leakage was proposed. The new algorithm hence strikes a compromise between minimizing within-cluster and out-of-cluster interference that provides substantial gain over classical precoders ignoring inter-cluster interference. The preminent feature and advantage of this method is that the computation of precoders at each base station is completely decentralized.

All the mathematical equations and its derivation including the main distributed precoding algorithm can be found in the paper [11]. Nonetheless, more details are now given:

The opportunistic CoMP precoder works as follows: the base stations which manage to decode the channel information broadcast by a user on the uplink will join a cooperation cluster to perform JT- CoMP towards that user. The precoder is based on the classical notion of regularized zero-forcing, allowing to null out the intra-cluster interference at the user side. When the BS does not decode the uplink feedback of a user, it then acts as a source of interference towards that user. However the probability that the BS represents a strong interferer to a user without having been able to decode the CSI of the user on the uplink, is limited, thanks to the reciprocity principle for path loss coefficients. In other words, a key principle of the algorithm is that there is a natural duality between decodability of the broadcast CSI in the uplink (related to distance between the user and the BS), the strength of the downlink interference, and the need to cooperate.

### Performance Analysis of Opportunistic Precoder:

The performance of the new opportunistic precoding algorithm is compared with conventional precoding approach (ZF in each cluster of network MIMO) in Figure 3 for various amounts of feedback quantization bits  $B$ . As can be seen, when the number of bits gets large, BSs receive a more accurate feedback but fewer BSs are able to actually decode it, which leads to performance decrease. Conversely, when the number of quantization bits  $B$  becomes too small, most BSs can decode the feedback, leading to wider cooperation clusters, albeit with poor CSI quality. This is the same behaviour for the ZF beamformer (conventional) and opportunistic beamformer.

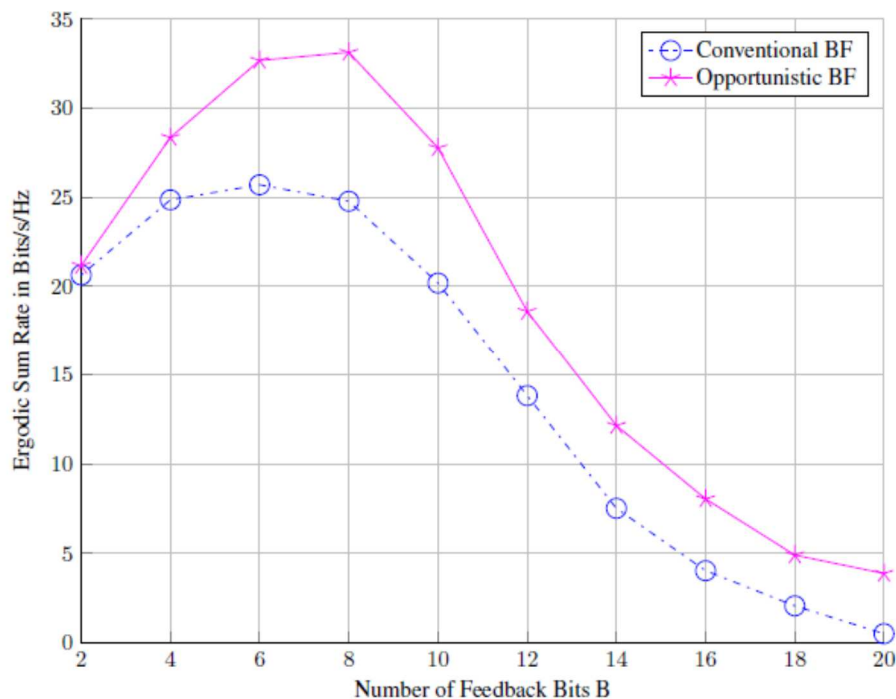


Figure 3: Variation of Sum Rate with Number of Feedback Bits  $B$ .

#### 2.1.4.2 Distributed Scheduler Design Strategies for Network MIMO

In 2.1.4.1 and [3], the idea of broadcast feedback [12] and the distributed precoder design arising out of distributed CSI [11] were explored. In this part, the focus is on the distributed scheduler design for CoMP.

A CoMP setting where a set of  $M$  base stations are jointly serving  $K$  UEs is considered. Due to the distributed nature of the wireless media, it is assumed that the CSI of the UEs are not completely present at all base stations. This situation may arise due to the different quality of CSI at different base stations or due to the fact that some base stations have higher delays for updating a UE's CSI. In such a case of distributed CSI, different possible scheduler design approaches are explored.

### **Conclusions:**

A decentralized precoding method was proposed, that is capable of exploiting additional opportunistic out-of-cluster broadcast feedback in Network MIMO. The method shows clear gain over a conventional network MIMO setup which exploits CSI limited to its own cluster. This decentralized precoding can also be applied for any case of distributed CSI, not just for the case of broadcast feedback.

## **2.2 Interference cancellation at the receiver and advanced transceivers**

This section contains summary of work performed in T3.1, T3.2, and T3.3 concerning transmitter and receiver schemes able to mitigate interference at the receiver, either uplink or downlink or both.

- Section 2.2.1 deals with the ultimate performance limit of the K-user multi-antenna broadcast channel with confidential messages and outdated CSI knowledge. The objective is to find the DoF (Degrees of Freedom), which captures the behavior of the capacity in high SNR regime. Similarly to the case without secrecy constraint, it was found in this work that outdated CSI is useful to increase the secrecy capacity in the high SNR (T3.1)
- Section 2.2.2 presents an interference mitigation scheme at the DL receiver when the transmitted signal is built with a linear dispersion code. The scheme is based on the concept of widely linear receivers. Indeed, provided that a user or its interferer uses a non-circular modulation, a widely linear minimum mean square receiver supersedes a simple MMSE receiver since it is able to reject an interferer using a single antenna (T3.1). Additional results are provided in Part B Section 3.2.1
- Section 2.2.3 Interference aware receivers are introduced at the DL receiver at the UEs, in order to mitigate interference generated by non perfectly orthogonal precoders in DL MU-MIMO in one or several CoMP cells (T3.1). Additional results are provided in Part B Section 3.2.2
- Section 2.2.4 focuses on UL LTE receivers in presence of interference caused by a Multi-user MIMO scheme. Taking into account that LTE UL uses SC-FDMA modulation, two receivers are compared, respectively the direct and indirect approach: based on the DMRS pilot symbols, either receiver filter coefficients are directly computed from the pilot symbols (direct), or the channel coefficients are first computed, and then the receiver coefficients are derived from them (indirect) (T3.2) Additional results are provided in Part B Section 3.2.3.
- Section 2.2.5 provides an SINR analysis focusing on the comparison between the conventional interference rejection combination (IRC) and the proposed interference rejection techniques taking into account the difference between the interfering pilots and the interfering data signal in terms of their covariance matrices. (T3.2). Additional results are provided in Part B 3.2.4.
- Section 2.2.6. Interference alignment has been proposed in the literature as a means to cancel intercell interference by combining transmit beamformers at the source (eg. base station), and receive beamformers at the destination (eg. UEs). However, complete CSIT should be known on the transmit side in order to compute the BF weights, which might not scale well when the number of transmitters increases. In this work, it is shown that (2.2.6.1) not all CSI need to be known, and that, 2.2.6.2, in the case the network is not fully connected (not all transmitters interfere with all receivers), a graph-based algorithm can be used to determine how the transmitters share time-frequency resources for interference avoidance.(T3.3)
- Section 2.2.7 The Spatial Modulation concept is a Multiple Antenna transmit scheme where the active antenna index carries some information bits. It is extended here to the case of multiple signal constellation where these additional information bits are transmitted by both antenna *and* constellation combinations indices. (T3.2). Additional results are provided in Section 3.2.5.

### **2.2.1 Fundamental limits of advanced MIMO schemes with various CSI**

In D3.2, the performance of a multi-antenna broadcast channel with secrecy constraint such that each message must be conveyed to its intended receiver reliably while keeping it secret to

unintended receivers was investigated. A practical scenario was addressed, where the CSIT is completely outdated or delayed, i.e., independent of the current channel state. This setup, particularly relevant to fast fading channels where the channel training/feedback process causes a delay larger than the coherence time, has attracted significant attention recently [9]. The main finding is that completely outdated CSIT enables to increase the Degree of Freedom (DoF) performance of multi-user networks by space and time interference alignment, characterizing the *behaviour* of the capacity in the high Signal to Noise Ratio (SNR) regime [9]. Similarly, our work [10] in the two-user multi-antenna broadcast channel showed that completely outdated CSIT is also useful to increase the secrecy capacity in the high SNR regime.

In [3], the work of [10] was generalized to the case of  $K$ -user multi-antenna broadcast channel with confidential messages. As a performance measure, we have considered the secrecy degrees of freedom (SDoF), the pre-log factor of the secrecy capacity that captures the behavior of the secrecy capacity in high SNR regime. Notice that the capacity of the multi-antenna broadcast channel remains an open problem even without secrecy constraints. The objective was to quantify the loss of DoF due to the additional secrecy constraints.

### **2.2.2 Widely Linear receiver solutions to suppress or avoid interference with advanced MIMO schemes**

This section focusses on the advanced MIMO schemes for the LTE-A downlink (see Figure 4) in presence of interferences. The purpose is to give new alternatives to improve a BER gain for users (UE) thanks to the antenna diversity at eNodeB transmissions in the context of high density cellular-network.

In D3.2 [3], the contribution focussed on Alamouti Linear Dispersion (LD) Code and Widely Linear (WL) receiver in presence of real signals either for user or for interference. In part B of this deliverable, section 3.2.1 extends the previous results to WL receivers for any LD Code or symbol constellation (real or not). More precisely the double Alamouti scheme with four transmit antennas is compared to the optimal Alamouti with two transmit antenna. The analyses of the O-QAM constellation behaviour is given in order to show some advantages of the WL receiver.

This study focusses on linear dispersive (LD) MIMO codes (see Figure 5), in order to jointly exploit the spatial and temporal diversity of the transmitted signal. Indeed, the purpose is to take into account the space-time fading dispersion of the propagation channel between the eNodeB antennas and UE receivers. The LD codes provide a good tradeoff between the spatial multiplexing gain and the joint spatial and temporal multiplexing gain. The linearity of the coding allows to use medium complexity processing at the receiver (Successive Interference Cancellation (SIC), or Maximum Likelihood (ML) implemented with sphere decoder). Such codes are designed for any number of transmit and/or receive antennas. The temporal diversity allows the use of as few as a single receive antenna for users (UE) in a MISO scheme. This is a useful feature, since generally, it is easier to design more antennas in eNodeB than in UE receivers. The most famous LD Code is Alamouti [18] where the number of transmitted antennas is equal to  $N_t=2$  and the temporal coding length is also  $K=2$  (see Figure 6).

A high density of users in the LTE-A radio communication network necessitates designing small cellular deployment with the drawback of mutual interference. Thus, interference is coming from the others eNodeB in LTE-A downlink and contributes to the additive noise. In this context, the covariance matrix of the additive noise is unknown and cannot be assumed to be spatially white.

The purpose is to define on the one hand the best MIMO scheme with LD codes for the downlink and on the other hand designing a UE receiver that suppresses or avoids interference. In [20] an MMSE receiver is proposed for the reception of the Alamouti useful signal in presence of synchronous Alamouti intra network interferers. The purpose here is to analyse and define LD codes with more than  $N_t=2$  transmitted signals in order to improve the UE BER. The receiver is an MMSE Equalizer that exploits the LD transmitted Code in the context of flat fading propagation channel and interferences.

As the number  $N_r$  of UE antennas is small, the receiver needs to exploit additional diversity such as the potentially non circularity of the interferences and/or users transmitted signals. Indeed, the

signals complex properties such as second order non circularity offers new receiver possibilities to avoid interference with the Widely Linear (WL) approaches of [21] where one interference can be cancelled with a single receive antenna : single antenna interference cancellation (SAIC). The complex properties of the signals depend on the constellation used such as BPSK, QPSK or QAM. A new MMSE receiver based on a widely linear processing has been proposed in [19] for Alamouti Code in the context of frequency selective channel. In [17] a general analysis of WL receivers with LD code is given.

The aim of this work is to propose LD Codes with  $N_e > 2$  transmitted antennas for the MIMO scheme adapted to a WL receiver able to suppress interference. According to Figure 5 the temporal length is  $K$ . The number of coding symbols  $\{a_{ij}\}$  is  $L$  for  $N_e$  antennas and  $K$  symbol duration. In this study, the performance analysis is given in full rate context ( $K = L$ ), and the scheme is open loop without any prior information on the downlink propagation channel.

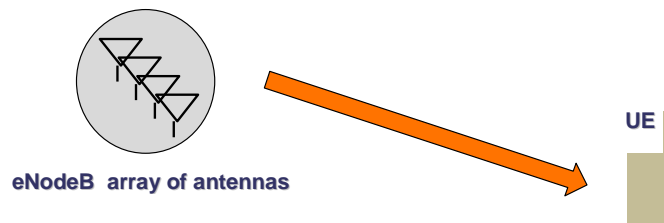


Figure 4 - The MIMO (or MISO) scheme of LTE-A in downlink

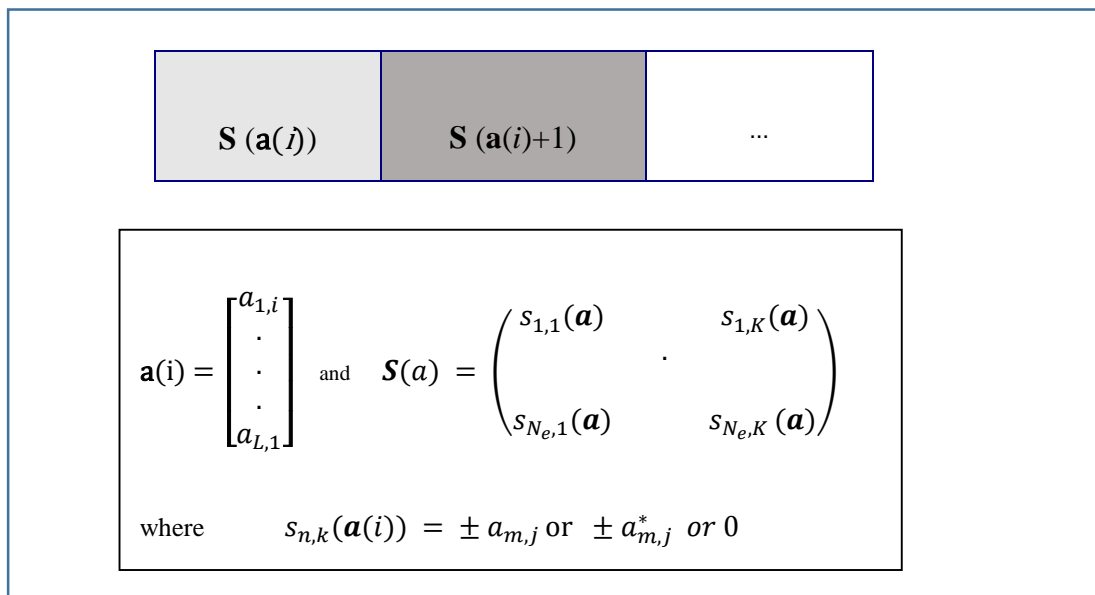


Figure 5 - LD MIMO Code scheme of symbols  $\{a_{ij}\}$  with  $N_e$  transmitted antennas and  $K$  temporal length

$$\mathbf{S}_{Al}(\mathbf{a}) = \begin{pmatrix} a_1 & -a_2^* \\ a_2 & a_1^* \end{pmatrix} \text{ with } \mathbf{a} = \begin{bmatrix} a_1 \\ a_2 \end{bmatrix}$$

Figure 6 - Alamouti LD MIMO Code scheme with  $N_e=K=2$

Without interference, an LD MIMO Code scheme is optimal when it is equivalent to a SIMO scheme where the gain of the SIMO channel vector is equal to the average of the  $N_e$  MIMO transmitted channel vectors gains. An optimal MIMO scheme with an infinite number of transmit antennas is equivalent to an AWGN SIMO transmission where the performance (BER) depends on the noise

power. In addition, an optimal LD MIMO Code for the MMSE receiver is also optimal for the WL MMSE receiver. Also a non-optimal MIMO Code for MMSE receiver can be optimal for WL MMSE receiver.

In this context, the Alamouti MIMO code with  $N_e=2$  transmission antenna is optimal for MMSE receiver and WL MMSE receiver. The Alamouti-MMSE receiver is then equivalent to the WL Alamouti-MMSE one either without interference or with circular interference (QAM, ...). The WL Alamouti-MMSE improves the BER only in presence of non-circular symbols (BSPK, O-QAM (see Figure 34)) either for user or interference.

When the number of transmission antennas  $N_e$  is larger than 2, the performance of LD Code (MMSE and WL MMSE) receivers improves. Without interference, the Alamouti-MMSE receiver is a little bit more performant than the MMSE receiver in presence of real or circular constellations such as QAM. Indeed, the optimal LD Code MMSE receiver does not exist in full rate and open loop context. In presence of non-circular constellation such as O-QAM, the WL MMSE receiver is more performant than the (WL or not) Alamouti MMSE receivers. In presence of interference, the (WL or not) MMSE receiver is better than the (WL or not) Alamouti-MMSE.

Whatever the interference context, the WL MMSE receiver gives better performance than the MMSE when the user or interference constellations are non-circular (BPSK, O-QAM) with a non-null second moment. In presence of one interferer, the MMSE receiver needs at least  $N_r=2$  antennas. With a single antenna either the user or the interference must be non-circular, so that WL-MMSE applies..

Thus, the downlink LTE interface can be improved by on the one hand modifying the standard by replacing QAM by O-QAM modulation, and on the other hand using a WL receiver, with an LD Code MIMO scheme such as the double-Alamouti of Figure 33 with  $N_e=4$ .

Detailed calculations and additional results can be found in Part B 3.2.1

### 2.2.3 Downlink multi-user CoMP with interference aware receivers

#### Context

The DL of LTE was investigated. More specifically, cooperation between cells (CoMP) was examined. CoMP was introduced in LTE release 9 [1], and refined in Release 11 [2]. It aims at improving the quality of service of users at cell edge. Joint Processing - Joint Transmission mode was implemented. In this mode, data for a user is available at more than one point. Data is therefore simultaneously transmitted from multiple points.

Serving a single UE from several eNBs nevertheless causes a resource loss. This issue can be solved by combining CoMP with MU-MIMO mode 5. MU-MIMO mode 5 allows transmitting data to several users from a single point on the same time and frequency resources, thanks to precoders [7].

If, on paper, the idea of using the potential of MIMO systems to realize MU cooperative transmissions is seducing, it turns out that many practical obstacles arise when it comes to practice. One of the most critical aspects is the quantity of information to feedback to the eNBs and the frequency of this feedback for precoder computation. In order to minimize this feedback, the LTE standard provides a much reduced set of precoders [7]. Unfortunately the very poor resolution of these precoders gives rise to interference at the co-scheduled receivers.

In this context, and in the aim of increasing the role of the receiver in the mitigation of interference in the network, advanced receivers for interference management have been introduced in release 12 studies [8]. Performance and complexity of such receivers have been investigated in [3].

The scenario is illustrated on Figure 7, where UE0 and UE1 share the same time and frequency resources. UE0 aims to reject interference from data intended to UE1. The black oval shapes represent the radiation direction of the antennas obtained with precoders.

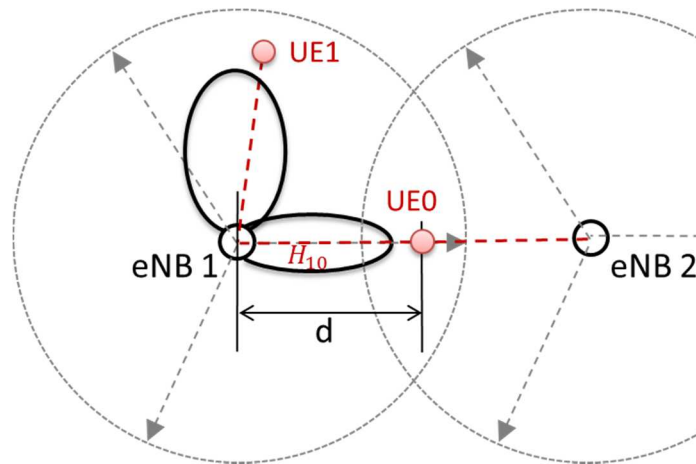


Figure 7. Scenario of the study

### **Interference aware receivers**

Firstly, Interference Aware (IA) receivers from literature were studied. The three categories of receivers envisioned in release 12 were considered:

- Interference Suppression (IS) receivers. These receivers apply linear filtering to the received signal to suppress the interference. They do not explicitly cancel the interference.
- Maximum Likelihood (ML) receivers. These are non-linear receivers.
- Interference Cancellation (IC) receivers. IC receivers are also non-linear receivers. Linear Code word level Successive Interference Cancellation (SIC) (L-CWIC) was considered among the four types of IC receivers considered in [15] (the three other types are Maximum Likelihood CWIC, Symbol Level IC and Parallel IC)

A DL MU-MIMO CoMP link level simulation chain was developed. Receivers from each of the three categories above were adapted to the scenario and implemented in the chain, respectively:

- Single Layer (SL) Minimum Mean Square Error (MMSE) equalizer [13].
- Interference Aware Max Log MAP (IA-ML) receiver [14].
- SIC-SL MMSE receiver [15]. This receiver reconstructs and cancels the interference, using the SL-MMSE structure. In the 3GPP taxonomy it is a Linear Code word level SIC.

### **Performance assessment**

BER of UE0 (Figure 7) was chosen as the performance indicator for the algorithms studied. A geometrical channel model (Spatial Channel Model [16]) was implemented in order to model the scenario of Figure 7. Inter Site Distance is 500m. UE0 is equipped with 2 receive antennas and each eNB is equipped with 2 transmit antennas. For the scheme of Figure 7, the precoder that maximizes the antenna gain in the direction of UE0, together with its orthogonal precoder given by the standard [7] were selected. QPSK modulation is used for both UEs.

It was shown that without any knowledge of the interference (from precoder of UE1), UE0 experiences a BER floor, whatever its location ( $d$  on Figure 7) and the precoders used. Simulations nevertheless proved that the three IA receivers studied are able to reject all interference from UE1 (i.e. no error floor is observed)

### **Part.B further studies**

This work is described in Section 3.2.2. A second interferer has been introduced, as shown in Figure 8. The three IA receivers studied in the first part of the project have been improved and adapted to this new scenario:

- IA-ML has been implemented in the interference cancellation process of the SIC receiver (instead of SL-MMSE, implemented in the first part of the study). The new receiver is named SIC IA-ML.



- For the SL-MMSE receiver, the filtering operation at the receiver implies to compute suitable Log Likelihood Ratios (LLRs). Theoretical LLRs were therefore computed and implemented in the receiver.
- The IA-ML receiver was modified in order to take the second interferer into account.

The scenario for assessing the performance of these receivers is shown on Figure 8. The distance  $d$  is fixed at  $ISD/2$  (500m). By letting  $\theta$  vary, the robustness of the IA receivers with respect to a non perfect location of UE0 is assessed. BER of UE0 (Figure 8) is still chosen as the performance indicator for the algorithms studied. UE0 is equipped with 2 receive antennas. A precoder that maximizes the antenna gain in the direction of UE0 with  $\theta = 0^\circ$ , together with its orthogonal precoder were selected from the standard for the scheme of Figure 8.

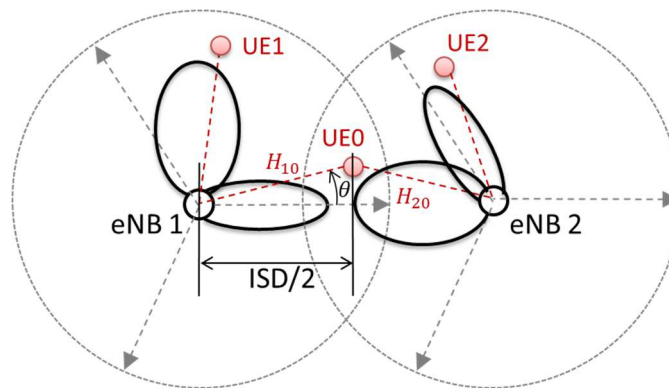


Figure 8. Scenario for D3.6.B

### Hardware implementation issues

The computational complexity of SL-MMSE, including the complexity of the LLRs, and IA-ML algorithms was assessed in WP7. Both algorithms were shown to be implementable

### 2.2.4 Advanced interference mitigation in the uplink

This section focused on the receiver optimization of user (UE) signals in presence of interferences in LTE-A uplink. The purpose is to give new alternatives solutions for high density user context and frequency selective propagation channel.

In D3.3 [4], the frequency adaptive MMSE equalization in presence of interference and multiple users was evaluated with the true channel matrix and the true covariance matrices. The results showed the need of an adaptive approach to mitigate external interference. Part B section 3.2.3 addresses the channel and frequency adaptive spatial equalizer estimation with the LTE DMRS sequence. For that, the channel matrix and the spatial equalizer are estimated in the time domain in order to deduce their estimation into the frequency domain. As a by-product, the channel and spatial equalizer order are estimated. Their order depends on the delay spread of the frequency selective propagation channel.

The Single carrier frequency division multiple accesses (SC-FDMA) represented into Figure 9 is considered in this work for the user transmitted signal. According to Figure 10, the second MIMO scheme of LTE-A uplink is considered, where multiple users can transmit simultaneously on the same time-frequency slots, i.e. Resource Blocks (RB) (Figure 11). Indeed, in the first MIMO scheme, the Base Station or eNodeB schedules a single user in one time-frequency RB. Thus, the choice of the second MIMO scheme has the advantage to increase the user density.

A high density in the LTE-A radio communication network makes it necessary to design a small cells deployment with the drawback of mutual interference. Thus, interference comes from the other users in LTE-A uplink and contribute to additive noise. In this context, the additive noise covariance matrix is unknown and cannot be assumed to be temporally and spatially white.

The issue of high density users takes place mainly in urban and/or indoor contexts where propagation between UE and base stations (eNodeB) is composed of multi-paths. Thus, the

frequency selectivity of propagation channel must be considered in this study. Frequency selectivity occurs when the multi-paths delay spread is larger than the inverse of the transmitted bandwidth. It means that the paths delay spread  $\Delta\tau = \Delta D/c$  verifies  $\Delta\tau > 1/B$  where  $B$  is the user bandwidth,  $c$  is the light speed and  $\Delta D$  is the Distance difference of arrival between the first and last path.

Both frequency selective propagation channel and SC-FDMA require Frequency Domain Equalization (FDE) for the reception of users signal. In addition the second MIMO scheme needs multiple antennas at Base Station or eNodeB in order to be able to separate with a spatial criteria multiple users that transmit on the same time-frequency Resource Block (RB). In addition signal Equalization must be adapted to the context of unknown coloured noise due to interference. On each frequency bin the channel is assumed to be flat.

In [36], the authors propose a scheme based on a joint MMSE-FDE and Sequential Interference Cancellation (SIC) approach to perform the equalisation in a multi user context. Each user is allocated a specific set of frequency sub carriers, but transmits several spatially multiplexed streams thanks to the use of several antennas. The use of the SIC method, and the exploitation of  $N_r = N_t$  antennas at the eNodeB, allows to detect each data stream of each user.

The authors in [37] analyse 2 types of non-linear receivers in the case of single antenna users scheduled on the same time/frequency slots. The Maximum Likelihood Detection (MLD) approach is based on a first FDE-MMSE filtering and then consists in a joint demodulation of the users, at symbol rate, i.e. the detection of previous symbols is not taken into account for the detection of the current ones. Potential timing offsets between the users are compensated. An FDE-MMSE-SIC approach is also analysed. Non-linear methods have better performance than linear MMSE, but the latter is good enough provided there is enough diversity on the propagation channel.

In [38], the authors propose an FDE turbo equalizer of the LTE-A uplink. The method also allows to improve the estimation of the feedback parameters needed at the transmit side for closed loop spatial multiplexing schemes. Turbo receivers for single user MIMO in LTE-A uplink are presented in [39]. A SIC and a Parallel Interference Cancellation (PIC) approaches are considered. At each iteration, the soft detection of each stream is cancelled from the received signal, either sequentially (SIC) or in parallel (PIC). The iterative processes improve the BER performance by several dBs. When the number of receive antennas increases compared to the number of multiplexed streams, the gain provided by the iterations gets smaller.

An SVD-based closed loop scheme is analysed for LTE-A uplink in [40]. The results show that the existing down-link codebooks when used for the uplink need to be improved.

In a multi users context, [41] proposes a SIC like MMSE FDE equalizer which allows for a reduction of the level of inter symbol and inter antennas interferences.

[42] analyses a receiver method in the case where multiple users access the same time/frequency slots. They focus on the transmission of improper constellations, and hence propose an evolved MMSE-FDE with widely linear processing that need rectilinear properties of interference.

The above state of the art for the LTE-A uplink shows that interference cancellation is most of the time performed by using SIC with iterative algorithms and Zero-Forcing (ZF) solutions. In addition, additive noise is generally assumed to be spatially white and frequency channel matrices are assumed to be known. The main purpose of this work is to focus on the frequency channel estimation with the determination of its order  $L$  that depends on the delay spread and is defined by rounding up to the nearest integer the solution of  $\Delta\tau = \Delta D/c = (2L+1)/B_{\text{LTE}}$ . The bandwidth  $B_{\text{LTE}}$  is one of LTE bandwidth (1.4MHz , 3MHz , 5MHz , 10MHz, 15MHz or 20MHz). Secondly, an alternative solution for interference cancellation and/or coloured noise with non-iterative frequency adaptive filters is proposed.

This is the reason why the purpose of this work is to design FDE spatial filters in order to cancel interference and equalize the frequency selective channel. These filters are estimated from the Demodulation Reference Signal (DMRS) represented in Figure 11. In presence of multiple users using the same RB, these DMRS sequence are orthogonal in the frequency domain. The adaptive filters need the estimation of a weighting matrix that depends on the frequency. Thus the work focusses also on the estimation of this matrix and the determination of its order. Two Mean Square Error approaches are considered to design adaptive filter

- **The indirect approach** is built on the use of a channel matrix estimate and of the covariance matrix of the signals at the output of antennas
- **The direct approach** is based on a direct estimation of the filter using the Demodulation Reference Signal (DMRS) and the signals at the output of antennas

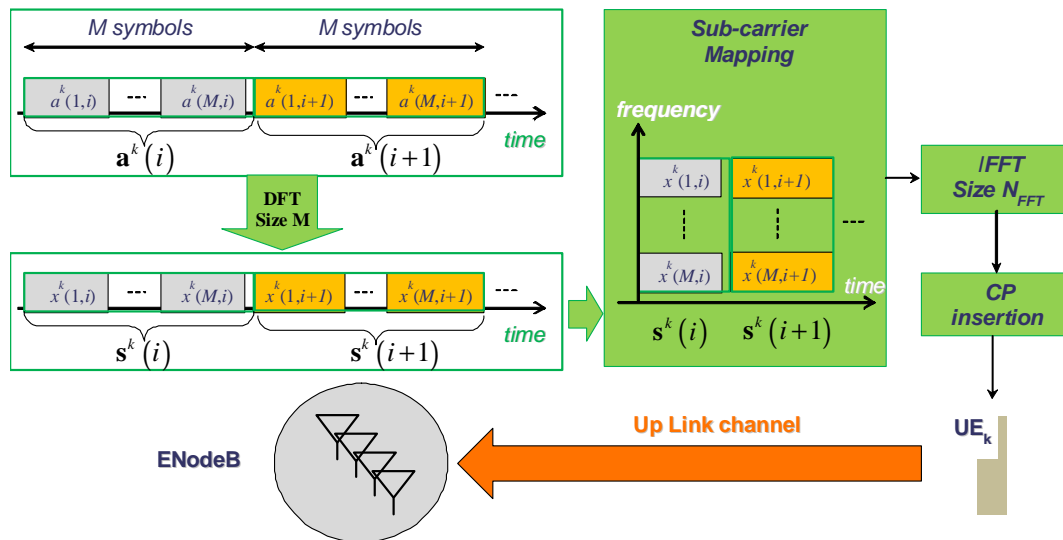


Figure 9 - SC-FDMA transmission for users to eNodeB

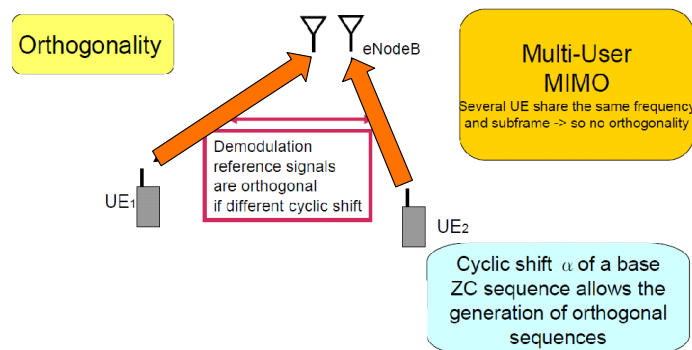
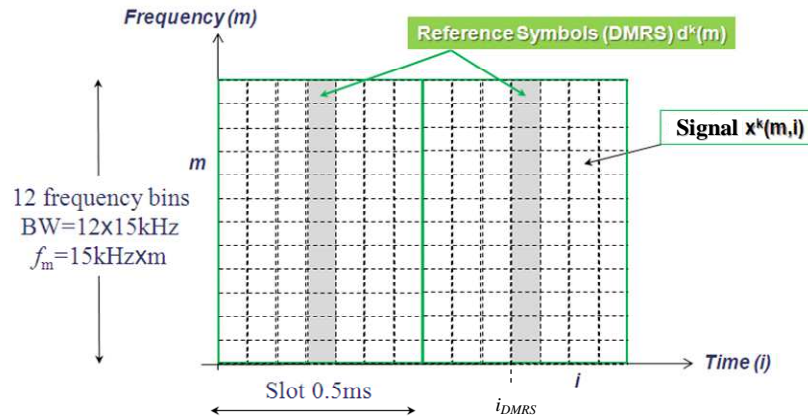


Figure 10 - The second MIMO scheme of LTE-A with multiple users



**Figure 11 - The time-frequency Resource Block into LTE-A**

This study shows that it is necessary to design adaptive filters in presence of unknown interferences. Both direct and indirect approaches need the estimation of the channel order ( $L$  and  $L_w$  respectively), in order to optimize the BER of the users symbols. These channels order depend on the multi-paths delay spread  $\Delta\tau$  such that  $\Delta\tau B_{LTE} = 2L + 1$  and  $L_w \geq L$ . Simulations show the necessity to estimate these orders. These results can be found in Part B Section 3.2.3.

In presence of frequency selective propagation channels, the more robust algorithm is the direct approach. This result is particularly true in presence of interference.

### 2.2.5 Interference cancellation within imperfect channel information in LTE DL transmission

In this contribution, reported in [4], we investigated interference rejection combining (IRC)-like receivers in interference limited scenarios, where a two-user interference channel is considered for MIMO-OFDM systems. Specifically, the system model assumes that a neighboring base station and the serving base station interfere each other by sending simultaneously the signal that includes the pilot symbols and the data symbols, under the same frequency channel. For this particular model, we derived three novel schemes that outperform the conventional IRC receiver for interference suppression. The main contribution here was to take into account the difference between the interfering pilots and the interfering data signal in terms of their covariance matrices. These schemes separate and regroup different kinds of interference, such as the pilots and the data signals, and then suppress them with the different strategies. Furthermore, in each strategy, the impact of imperfect CSI, i.e., the channel estimation errors and the errors in covariance estimation, is also taken into account in the proposed receivers.

The schemes were derived based on the linear MMSE (LMMSE) and the SIC criterions, namely, IRC Diagonal Loading (IRC-DL), least squares estimation with compensation (LS-C), and LMMSE with compensation (LMMSE-C), respectively. The main difference between these schemes is how much information they need about the interfering signal, for example, the SIR value and the modulation types. In general, more information brings more benefits for a receiver to perform interference suppression. We start with the conventional IRC and show the differences between all the schemes. The conventional IRC treats interference as a Gaussian noise. Therefore, it only needs a single covariance matrix from interference. Then, IRC-DL separates the interfering symbols into the pilot and the data symbols, which needs some extra information, i.e., the pilot-data structure of interference, in order to do that efficiently. Next, LS-C further decodes the interfering pilot symbols and suppresses them from the received signal. This needs to estimate the interfering channel, which requires the pilot information in order to use them. Finally, LMMSE-C improves the estimation results of LS-C for the interfering channel. It is mainly based on the accurate information of the SIR value. These results provide different options for a receiver design based on how much information of interference can be obtained at the receiver side. We also presented the optimal approach in the

sense of the maximum likelihood detection and treated as a performance benchmark for the proposed schemes.

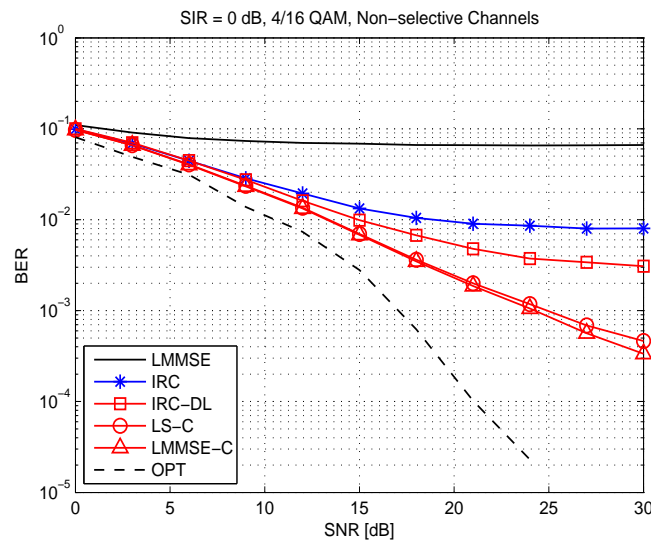


**Figure 12 BER vs SNR in the strong interference region, SIR = 0 dB**

In this contribution, the most promising gains we have found are shown in Figure 12. In this figure, we compare the uncoded BER performance at SIR = 0 dB. These curves show the substantial improvements of the proposed schemes over the conventional solutions. The first gain can be found between two conventional schemes LMMSE and IRC, which comes from detecting the presence of interference. Then, our first scheme IRC-DL provides extra gains from IRC, due to exploiting the pilot-data structure about interference. Next, the LS-C and LMMSE-C show the benefits to decode the interfering pilot symbols, which improve the BER value from  $10^{-2}$  to  $10^{-3}$ , which is compared to the conventional IRC at SNR = 30 dB. Finally, the optimal receiver (OPT) shows the possible improvement when the interfering data symbols are fully decoded in the way to improve the channel estimation on both serving and interfering channels.

In Part B, Section 3.2.4, we provide a signal-to-interference-plus-noise ratio (SINR) analysis focusing on the comparison between the conventional IRC and the proposed schemes given in [4]. Moreover, the performance of our proposed schemes is evaluated under more practical considerations. These scenarios include non-synchronized cases and triply selective channels where both serving and interfering channels are time variant, frequency selective and spatially correlated.

### 2.2.6 Interference alignment with incomplete CSIT

Interference management is one of the important issues for the next generation wireless communication networks. As the network gets more and more dense, interference becomes one of the major factors to combat for high system throughput. Many techniques have been proposed to manage the interference over different scenarios. For instance, interference alignment focuses on the scenario where there are a number of transmit and receive pairs that strongly interfere with each other, and without an interference-aware design, the interference energy would be much larger than the noise energy. The basic idea of interference alignment is to leverage the multiple antennas through proper beamformer designs at the transmitters and receivers for interference mitigation. At the transmitter side, the beamformers are optimized to steer the signal towards the directions not interfering the undesired users. Meanwhile, at the receiver side, the decorrelators are computed to suppressed residual interference that is not eliminated by the transmit beamformers. It was shown in the literature that, provided that there are sufficient number of transmit and receive antennas, the interference can be completely eliminated by the joint design of all the transmit beamformers and receive decorrelators of all the user pairs.

In general, interference management algorithms require the complete global CSIT from all the users. The amount of complete global CSIT scales with the number of total transmit antennas times the number of total receive antennas over all the users. This implies that without a compromise to a sub-optimal solution that requires only partial global CSIT, various interference management techniques will not be scalable to large networks with many antennas. The problem of reduced CSIT for interference management is addressed and the research progress can be summarized into two folds:

- i. Interference alignment with incomplete CSIT: Under the case that the network is fully connected, i.e., all the transmitters can interfere to all the receivers, theoretical results have been established in this project to show that under some scenarios there is no need to acquire the complete CSIT in order to find a feasible interference alignment solution, i.e., there exist transmit beamformers and receive decorrelators that can completely eliminate the interference and computed based on only a few entries of the channel matrix of the network. With these results, algorithms have been developed for CSIT allocation, which determine which entries of the entire channel matrix should be acquired for interference alignment.
- ii. Interference management with topological CSIT: Under the case that the network is partially connected, i.e., some transmitters will never interfere with some receivers, algorithms have been developed for interference management using graph theoretical approach.

Specifically, the contributions, reported in [5], are summarized as follows.

#### 2.2.6.1 Interference management with incomplete CSIT

With the goal of reducing the amount of CSIT while preserving the interference alignment feasibility, the key results developed in this project are summarized as follows.

- To study the CSIT reduction for interference alignment, the problem of finding the minimum CSIT allocation that preserves interference alignment feasibility has been formulated and interference alignment feasibility condition has been derived for strictly incomplete CSIT.
- The notion of tightly-feasible interference channel (IC) was proposed to describe the antenna configuration of the transmitters and receivers where interference alignment becomes infeasible if any one of the antennas is removed. Under tightly-feasible ICs, a CSIT allocation policy that preserves the interference alignment feasibility has been presented to significantly reduce the amount of CSIT acquisition.
- The notion of super-feasible IC was proposed to describe the antenna configuration where interference alignment is still feasible if some of the transmit and receive antennas are removed. Under this situation, it is shown that there is a tradeoff between the number of antennas and the CSIT requirements. A heuristic algorithm that exploits any additional antenna to reduce the amount of CSIT acquisition has been proposed.
- In addition, a new simple and intuitive algorithm for testing and feasibility of single-stream interference alignment was developed.

#### 2.2.6.2 Interference alignment with topological CSIT

The scenario of partially connected interference network is considered, which captures the practical situation where some interference links become negligible when the receiver is sufficiently far away from the interfering transmitter. The key results on algorithm development under this scenario are summarized as follows.

- An interference avoidance approach built upon distance-2 fractional graph coloring over the clustered line graph corresponding to the original network topology has been proposed. Specifically, for a partially connect network, the interference avoidance approach manages the interference by activating only a subset of transmitter-receiver pairs at each timeslot. The problem is then transferred to how to partition the communication links (from a transmitter to a receiver) into disjoint groups, such that the links within the same group do not interfere

with each other. It turns out that such link partition problem can be transferred into the fractional coloring problem (in graph theory) by transforming the IC into the line graph.

As for an illustrate example, Figure 13 illustrates the topology of a 6-cell network. The left subfigure illustrate the partially interference channel, where the black nodes denote the transmitters, white nodes denote the receivers and the solid lines denote the wireless links. The subfigure on the right illustrate the corresponding line graph of the wireless links, where each node represents a wireless link in the left figure, and each edge connecting two nodes represents the case that the corresponding two wireless links on the left figure interfere with each other.

As a result, the wireless link partition problem on the left figure is equivalent to a distance-2 fractional coloring problem on the line graph illustrated in the right hand side figure. Specifically, with the coloring problem, the goal is to assign  $m$  out of  $n$  colors to each node such that any two adjacent nodes has no color in common. Correspondingly, it can be shown that each receiver in the left figure can be delivered  $m$  independent messages during  $n$  timeslots, considering all the transmitters and receivers equipped with single antenna.

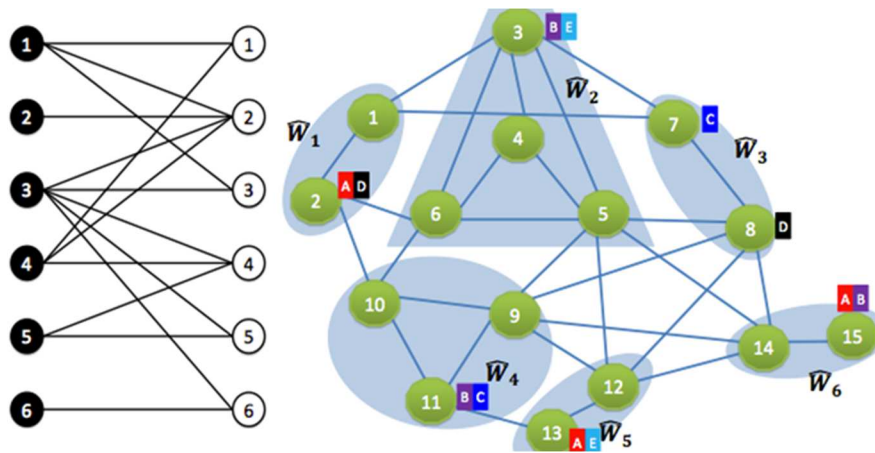


Figure 13: A topology of the 6-cell network.

- An interference alignment approach is proposed to partially connected interference network, which can be shown to improve the throughput over the interference avoidance method. Figure 14 illustrates an example on how to transform the partially connected network topology into a model in a vector space.

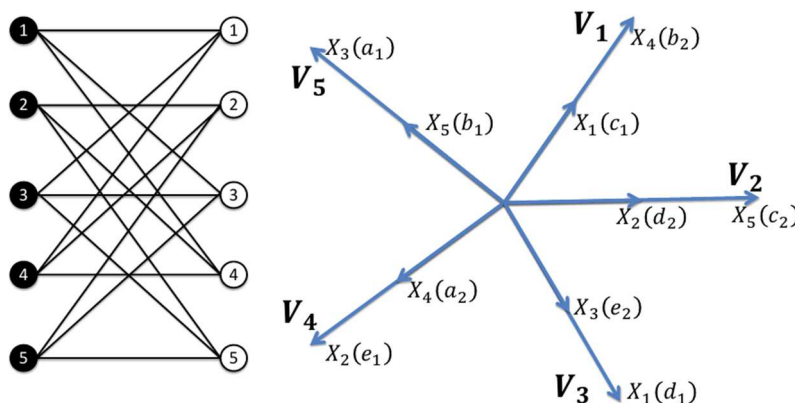


Figure 14: Illustration for a network with 5 transmit-receive pairs, where each transmitter has three links.

### 2.2.7 Enhanced spatial modulation schemes

Spatial modulation (SM) is a recently introduced transmission concept which is suited to MIMO systems with a smaller number of RF chains than transmit antennas. This scheme requires low

energy consumption and low computational complexity at both TX and RX sides. However, a main problem of SM is that the spectral efficiency remains low compared to conventional MIMO systems based on spatial multiplexing.

In this contribution, reported in [4], a new concept of SM introduced using multiple signal constellations to improve spectral efficiency. This scheme, referred to as Enhanced SM (ESM), conveys information using one or two active transmit antennas and one or two secondary modulations in addition to the primary modulation. Here, instead of the active antenna index, information bits are transmitted by antenna and constellation combinations. The number of those combinations is the double or the quadruple of the number of active antenna indices in conventional SM systems, and this increases the number of bits transmitted per channel use.

ESM was devised by combining several ideas. The first one is to transmit symbols from a primary constellation when a single TX antenna is activated and to transmit symbols from a secondary constellation when two TX antennas are activated. The second idea is to define a set of secondary constellations whose size is half of the primary constellation size in order to transmit the same number of bits during the single active antenna periods and the two active antenna periods. The third idea is to design the secondary constellations through geometric interpolation in the signal space in such a way as to maximize the minimum Euclidean distance between transmitted signal vectors.

The concept of using multiple signal constellations is the basic deviation of ESM from conventional MIMO schemes. Here, instead of the active antenna index, information bits are transmitted by antenna and constellation combinations. The number of those combinations is the double or the quadruple of the number of active antenna indices (or index combinations) in conventional SM systems, and this increases the number of bits transmitted per channel use by 1 or 2, when the signal constellation of conventional SM is used as a primary constellation in ESM. Alternatively, when the signal constellations are selected in such a way that ESM operates at the same spectral efficiency as conventional SM, ESM achieves higher performance.

In this study, we give design examples using two and four TX antennas and QPSK, 16QAM and 64QAM as primary modulations. The proposed technique is compared to conventional SM as well as to spatial multiplexing (SMX), and the results indicate that in most cases, ESM provides a substantial performance gain over conventional SM and SMX. Specifically, it was found that with two TX antennas ESM potentially gains up to 6 dB over conventional SM. With four TX antennas, ESM leads to higher gains: it gains up to 9 dB over SM. Meanwhile it reduces the maximum-likelihood (ML) decoder complexity.

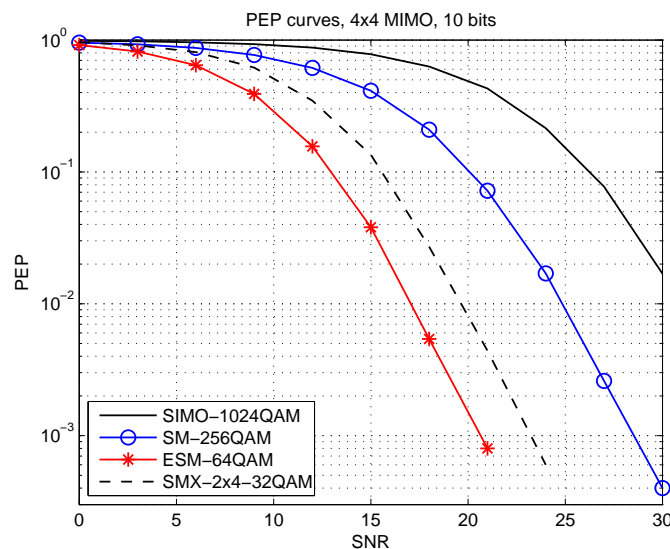


Figure 15 PEP curves for 10 bpcu-4-Tx



In this contribution, the most promising gains are shown in Figure 15. In this figure, numerical results of the Pairwise Error Probability (PEP) performance were carried out in the case of a 10 bpcu transmission with 4 Tx antennas, where ESM uses 64QAM as primary modulation and the conventional SM uses 1024 QAM to achieve the same throughput. Here, ESM gains around 2 dB over SMX and more than 7 dB over conventional SM at  $PEP = 10^{-2}$ . Note that this gain is higher than the other cases, e.g., 8-bpcu or 6-bpcu. It reveals that ESM achieves better SNR gains with respect to conventional SM when higher-order constellations are used for increased spectral efficiency.

In Part B Section 3.2.5, we extend the contribution of enhanced spatial modulation (ESM) in [4] that allows multiple signal constellations to be used by different active antenna combinations. In order to achieve high spatial efficiency, the technique referred to as ESM-64QAM extended to transmit one more bit compared to the previous work in [4]. Moreover, the impact on the number of receive antennas is also investigated, which shows that the performance gains increase as the number of receive antennas increases.

## 2.3 Flexible interference management concept

Summary of work done in T3.3 and T3.1, dealing mainly with cross-layer issues on how to mitigate interference

- Section 2.3.1 deals with the construction of an interference map that can be used to predict interference, which can be useful eg. in a handover procedure. This map is built in two steps: a first map is obtained via a statistical model, based on PPP (Poisson Point Process) that needs as inputs the network's nodes density, the path loss parameters and the distance between the considered UE and its first interfering node. Then, this map is refined by using the interference measurements reported by active UEs to the central base station. The final map is thus obtained by a Kriging interpolation on the errors between measurements and initial map. Additional results are provided in Section 3.3.1 (T3.3)
- It is usual to build metrics that characterize a block fading channel, w.r.t. a given type of receivers. These metrics are called ESM (Effective SNR Metrics). They summarize SINRs on several blocks in a single figure, making it equivalent to an AWGN SNR. Section 2.3.2 proposes an improvement of the calibration of such a metric in the context of a turbo linear codeword interference canceller (L-CWIC in 3GPP). The goal is to use this metric to predict the PER, and then operate link adaptivity in terms of Modulation and Coding Schemes. (T3.3)
- 2.3.3 considers the performance of JT CoMP for intra and inter-site scenarios. The aim is twofold: on the one hand, to evaluate the JT CoMP scheme in order to better understand its benefits and on the other hand to show if a better gain is achieved with intra site cooperation or with inter site cooperation. Considering two types of schedulers (distributed and centralized scheduling), it was shown that the performance improvement of the CoMP UEs is obtained to the detriment of the legacy UEs. To address the weakness of the conventional scheduler, a centralized opportunistic approach was proposed, thus introducing more fairness between the non-CoMP UEs and CoMP UEs. Additional results are provided in 3.3.2 (T3.1)
- In Section 2.3.4, the impact of mobility on JP-CoMP scheduling schemes is studied. First, a mobility model was proposed and validated by system level simulations. Then, this model is used to study the impact of mobility on scheduling schemes in the presence of inter-cell coordination. Several CoMP scheduling strategies are compared, both in the static and the mobility case. It is shown that a scheduler prioritizing non-CoMP users in the static case brings performance degradation, while in the mobility case the same scheduler outperforms other strategies. Taking this fact into account, a mobility-aware scheduler is proposed, which deprioritizes mobile CoMP users. This scheduler improves the performance by giving the chance to mobile cell-edge users to be served in better radio conditions whenever cell coordination is not adapted. Additional results are provided in Section 3.3.3 (T3.1).
- Section 2.3.5 is an input to all others, since it provides channel impulse responses in realistic scenarios, obtained by a ray based model. These MIMO channel models are spatially and temporally richer than than eg those of 3GPP. It is to be noted that examples of channel impulse

responses provided by Section 2.3.5 were exploited by contributions in Sections 2.3.1 and 3.3.1 on interference maps. (T3.1)

- Section 2.3.6 provides a system level evaluation of the beamforming gain wrt. SINR distribution. Channel impulse responses are derived from the same ray based model as Section 2.3.5. Additional results are provided in Part B Section 3.3.4 (T3.3)

### 2.3.1 Joint location and interference prediction for ICIC

The emerging wireless communication standard Long Term Evolution Advanced (LTE-A) introduces significant technological enhancements to meet the ambitious requirements set by the Third Generation Partnership Project (3GPP) in terms of high data rate and high spectral efficiency. In addition to allow smaller cells and to keep the network closer to the users, the enhancements are also obtained by several improved algorithms of radio resource management, handover decision, traffic offloading, Inter-Cell Interference Coordination/Cancellation (ICIC), etc. Most of these algorithms are based on the knowledge of the channel state and interference level experienced by UEs. In the downlink, the Inter-Cell Interference (ICI) is caused by the neighboring evolved Node B (eNBs) transmitting in the same frequency bandwidth. The ICI level randomness is due to the radio channel variations (i.e., shadowing and fast fading effects) and to the locations of the interfering eNBs, which impact the path loss caused by the distance between the interfering eNBs and the interfered UE. Several works assume the ICI follows a Gaussian distribution (by invoking the central limit theorem [23]) and derive the ICI statistics parameters accordingly, as given in [22]. However, higher layer algorithms need a more accurate channel estimation/prediction. Recent research focusses on the construction of Interference Maps (IMs) that represent the ICI level as a function of the 2D UE locations, especially in Heterogeneous Networks (HetNets), which are constructed with different tiers (i.e., macro and micro cells). IMs can be designed using: (i) fingerprinting techniques (deterministic approach), or (ii) location-dependent ICI estimation models (stochastic approach). The high resolution fingerprinting involves a drive test step where measurements of the Received Signal Strength (RSS) at each location of the considered area are collected [24]. This method thus needs a pre-training step, greedy in terms of time, or alternatively, blind crowd sourcing (i.e., performing calibration "on the fly" as UEs physically sense and report their ICI conditions). The latter method may take too much time to collect the minimum amount of field measurements to converge properly and thus, it may introduce significant latency in the system after initialization. To overcome this drawback, low resolution fingerprinting (where the ICI levels may also be collected from UEs that send their locations and RSS measurements to the eNB) is obtained by estimating the ICI level of the non-visited locations using spatial interpolation techniques as shown in [25] and [26]. Unlike the latest fingerprinting methods, location-dependent ICI estimation models (eg. [27], [28]) derive an analytical expression of the expected average ICI level as a function of UEs locations, based on a priori stochastic assumptions (typically, about the eNBs spatial distribution). These methods are expected to be more flexible and to cope with HetNets complexity, at the price of less accurate mapping (though hopefully still sufficient to trigger ICIC or handover actions). Such methods are able to take into account different network configurations, especially that of small cells (e.g., small cells' sleep mode) which is essential in such scenario.

In this study, a semi-deterministic method was followed to build the interference map, i.e., the IM is first constructed by a stochastic-based location-dependent ICI estimation model, and then updated according to the deterministic UE measurements. As a first step, we developed an analytical model that predicts the interference level as a function of the UE position. This work was presented in [5]. The developed location-dependent ICI estimation model is based on stochastic geometry. More specifically, the developed model relies on the Poisson Point Process (PPP) formalism (and its large arsenal of mathematical tools) in order to derive a closed form of ICI estimation under realistic propagation channel assumptions, including both fast fading and shadowing. Since the ICI level depends on the deployment type, both cross-tier and co-tier interference location-dependent ICI estimation models are derived. The analytical model needs as inputs the network's nodes density, the path loss parameters and the distance between the considered UE and its first interfering node. In fact, the statistical interference map is obviously biased in comparison with the ICI level that would be physically experienced by the UEs, for various reasons (e.g., strong a priori spatial distribution assumptions). Besides, it may be also practically challenging to get reliable a priori

information in real systems, due to the possible inaccuracy and/or low representativeness of the assumed statistical model parameters in practical operating environments. On the other hand, the location-dependent ICI estimation model allows an interference map initialization when starting from scratch. To construct a more reliable interference map, an update on the IM is performed with a self-learning procedure. As defined in the standard, the active UEs report their measurements to the eNB. Accordingly, based on this information, the observed "gap" between the measured ICI level and the estimated level can be evaluated at all the sensing points. Since the active UEs can be sparsely (i.e., under low deployment density) and/or non-uniformly distributed in the geographic area of interest, the whole IM has to be updated with regards to the finite number of observed gaps, using spatial interpolation of the perceived prediction errors. Two spatial interpolation techniques are thus investigated: (i) the Inverse Distance Weighting (IDW), and (ii) the Kriging.

The performance analysis given in Part B. Sec 3.3.1 compares the proposed algorithm with traditional approaches, where the interference map is directly constructed by spatial interpolation, according to the ICI measured by the active UEs. This comparison between the two approaches shows the benefit of using the location-dependent ICI estimation model for IM initialization. In our simulations, the active UEs' ICI measurements are taken from a realistic interference map obtained by ray-tracing techniques over 1 km<sup>2</sup> area, provided by Siradel (see section 2.3.5). The numerical results are given for different rates of active UEs, drawn either regularly or irregularly (i.e., regular and irregular active UE positioning). For the Kriging technique two variograms models are studied: (i) exponential model and (ii) Von Kármán model.

### **2.3.2 Calibration framework for physical layer abstraction of codewords IC receivers**

#### **Background**

Within the evolution of wireless systems, the cross layer optimization between PHYSical layer (PHY) and Medium-Access Control layer (MAC) has drawn a lot of attention, due to the improved data rate and Quality of Services (QoS) it offers.

In Multiple Input Multiple Output (MIMO) transmissions, the PHY-MAC cross layer design is based on mechanisms such as fast link adaptation (FLA), which exploits the instantaneous feedback from the receiver to inform the transmitter about the radio link quality (see, e.g., [29]). The key idea of the FLA mechanisms are to predict the packet error rate (PER) for different modulation and coding schemes (MCSs) in order to select the MCSs together with the MIMO precoding that maximize the throughput under a certain QoS constraint (10% PER in LTE).

Therefore, accurate and fast prediction of the link-level performance at the receiver side is of paramount importance for advanced mobile communications. Due to the constraints of limited feedback and finite size precoding codebooks, the residual interference at the receiver output remains a major impediment to reach the high MIMO spectral efficiencies promised by information theory. This is why advanced receivers regain a lot of attention in 3GPP. Among them, the class of iterative Linear Minimum Mean Square Error based soft Interference Cancellation (LMMSE-IC) and decoding receivers, or turbo Linear CodeWord Interference Cancellation (turbo L-CWIC) receivers in 3GPP, offer a particularly interesting trade-off between complexity and performance. As a result, performance prediction methods, or PHY abstractions that are able to capture their behaviour in order to derive precisely the limited feedback metrics is of great interest in practice.

The conventional PHY abstractions consist in compressing the Signal to Interference and Noise Ratios (SINRs) at the receiver output into a single Effective SINR Metric (ESM) that is used to read AWGN Packet Error Rate (PER) Look-Up Tables (LUT) simulated offline. Several ESM are possible, among which the Mutual Information ESM (MIESM) is known for its robustness and stability. The conventional PHY abstractions rely on the assumption that an analytical SINR formula exist. Nonetheless, in the case of reduced complexity Maximum-Likelihood (ML) receiver, some references propose to use approximate SINRs that results from the calibrated combination of the LMMSE SINR and the Genie Aided SNR (the Genie Aided SNR models a receiver that can remove perfectly the interference)

**SHARING contribution:**

This contribution addresses the design of PHY abstractions for the class of turbo L-CWIC receivers. This work builds on previous research studies carried out in this field in the framework of the ARTIST 4G collaborative project [30],[31]. The proposed PHY abstraction is inspired from the EXtrinsic Information Transfer (EXIT) chart framework which underlines the MIESM compression technique. The key idea is to estimate at a given iteration the ESM at the output of the LMMSE filters, then to calculate the interference estimation reliability (IER) variance for the next iteration. The IER variance along with the Channel State Information at the Receiver (CSIR), are able to reproduce the ESM for the next iteration and so on.

In [31], a one-dimensional (1D) calibration was proposed to minimize the prediction error caused by invalid assumptions that cannot be avoided in order to derive a simple SINR analytical formula. These assumptions yield too optimistic PER predictions. In SHARING, we revisited the calibration method by proposing a more rigorous framework to minimize the predicted throughput error that dramatically influences the FLA mechanisms. We also suggested a novel multi-dimensional calibration approach that corrects the ESM by both increasing the IER variance and applying two correction factors to the MIESM compression. We confirmed that 1D calibration factor are relatively robust to the channel frequency selectivity or number of fading blocks. However, if the receiver has an estimation of the number of fading blocks (which is roughly the bandwidth divided by the coherence bandwidth) then more accurate PER prediction methods were suggested. These methods rely on multi-dimensional calibration and, thus, need pre-stored calibration factor tables with respect to the number of fading blocks. Monte Carlo simulations showed that the 3D and 8D calibrations yielded substantial better throughput prediction than 1D for MIMO turbo-coded transmission. The work detailed in [5] was published in [32].

**2.3.3 Advanced scheduling for intra and inter-site CoMP**

In D3.2, the performance of the Joint transmission (JT) DL CoMP scheme has been considered for intra and inter-site scenarios. The aim is twofold: on the one hand, to evaluate the JT CoMP scheme in order to better understand its benefits and on the other hand to show if a better gain is achieved with intra site cooperation or with inter site cooperation. This last point is key for the future deployments choice since black fiber and time/phase synchronization are needed to enable the inter-site JT DL CoMP. The deployment cost for inter-site collaboration can only be warranted if significant gains can be achieved. Note that in this study a perfect backhaul assumption has been used. CoMP for inter-site scenario requires close coordination between geographically separated eNBs. Two types of schedulers are considered in D3.2, as shown in Figure 16:

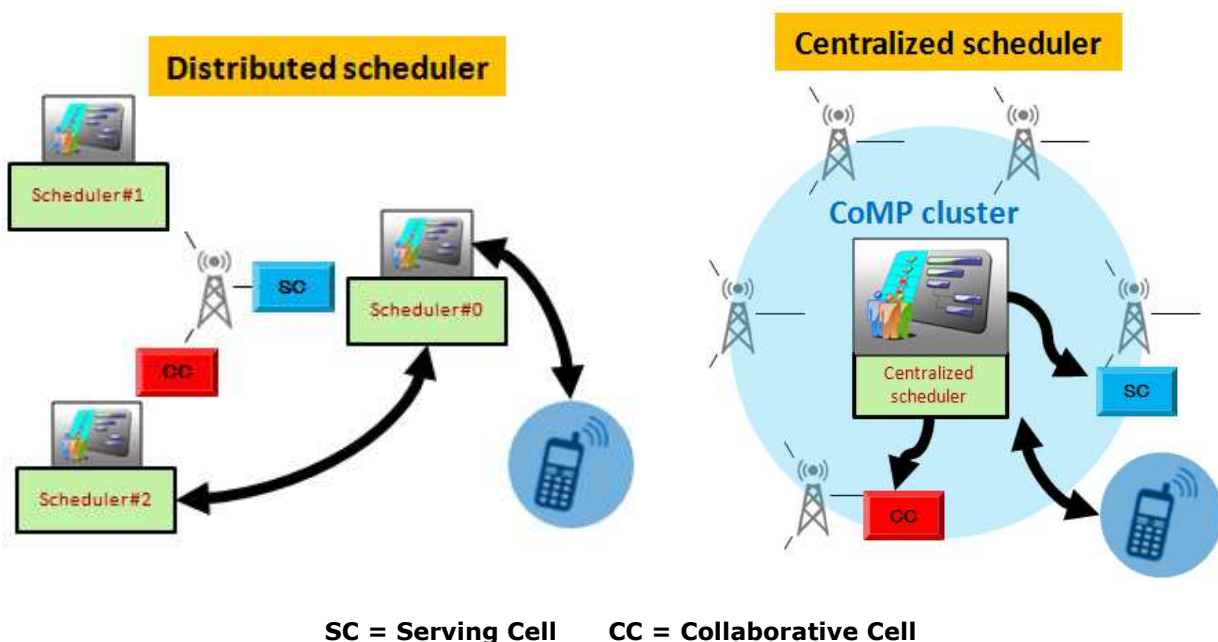


**Figure 16 Two scheduling approach for CoMP**

In the distributed case the resource allocation is performed per cell in parallel while the centralized scheduler allocates the resource per CoMP cluster. The CoMP transfer function (Figure 17) shows for a given UE the throughput when activating the CoMP function as a function of the throughput when disabling the CoMP feature. Each point represents an UE. The motivation here is to evaluate separately the impact of CoMP on the CoMP candidate UEs on the one hand and legacy UEs on the other hand.

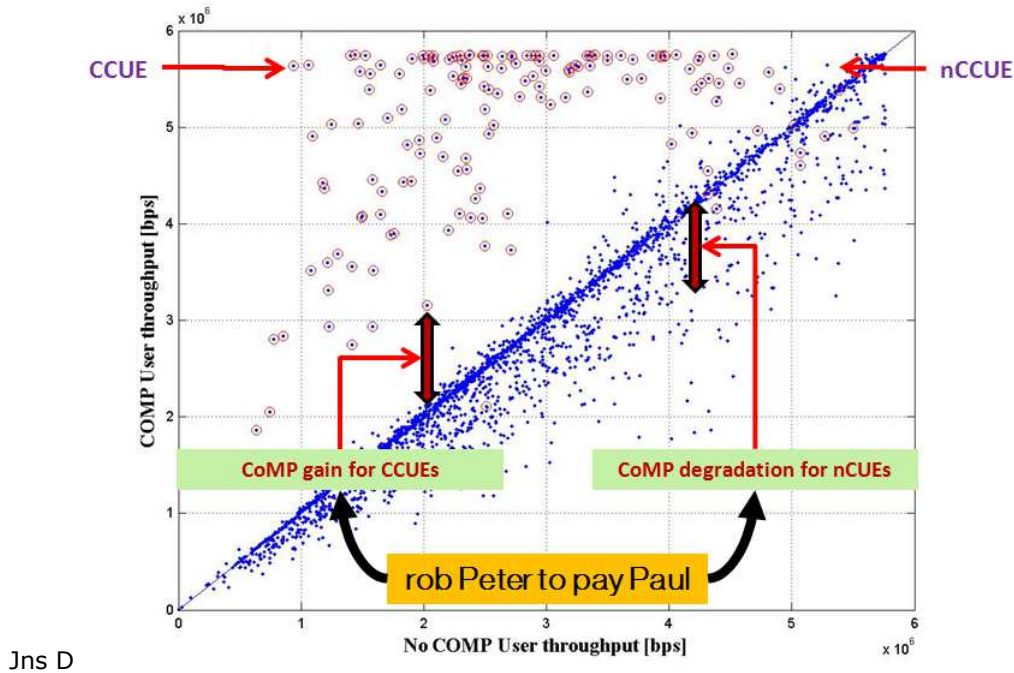


**Figure 17 Weakness of the studied scheduler**

D3.1 addressed the Coherent JT category and proposed the assessment of a scheduler based on a prioritization of the CoMP UEs on the one hand and non CoMP UEs on the other hand. D3.1 proposed the introduction of a centralized scheduling. The improvement of the CoMP performances is obtained to the detriment of the legacy UEs. The goal of D3.2 was to address the weakness of this scheduler (highlighted by Figure 17) through a centralized opportunistic approach (to introduce more fairness between the non-CoMP UEs and CoMP UEs). The system-level simulation results indicate clearly that compared to JP with the Conventional Scheme [67] JT with the proposed scheme can maintain performance gains for legacy UEs (see D3.2). In Part B section 3.3.2, the objective is to evaluate the effectiveness of this algorithm for other categories of CoMP.

### 2.3.4 Cross-layer performance evaluation of CoMP

Inter-cell interference is one of the key challenges faced in mobile communication systems. It restricts the re-usability of the radio resource and limits spectral efficiency. Since the days of GSM, various techniques have been used to cope with interference.

Coordinated MultiPoint, a main feature on the LTE-A roadmap, is mentioned as a promising approach to mitigate its effects through the coordination of multiple cells. We focus in this work on joint processing (JP) schemes, where all cells of the coordination cluster are involved in the transmission and thus cooperating cells resources are no longer available for other users. JP schemes have been demonstrated as an efficient approach to improve cell-edge user's throughput but this is at the cost of higher resource consumption. Thus there is a trade-off between the performance of cell-edge users and the ability of the network to process all traffic.

However, it was common in the previous studies to assume *static* or *semi static* users in the performance evaluation of CoMP schemes. We first proposed a mobility model and we validated it by system level simulations. Then we used this model to study the impact of mobility in the presence of inter-cell coordination. We show that although mobility is generally thought as improving throughput performance, it has a critical impact on the performance of CoMP schemes. Indeed, in the presence of coordination mechanisms mobility can lead to bad performance if the scheduling strategy is not well chosen. By prioritizing CoMP users, mobility surprisingly causes a throughput degradation. However, prioritizing non-CoMP users in the presence of mobility outperforms many other strategies in sharp contrast to the scenario without mobility. This is due to the fact that prioritizing non-CoMP users in a scenario with mobility gives the chance to CoMP users to move and to be served in good radio conditions without performing coordination.

Motivated by the above observation, in this work, described in Part B, Section 3.3.3, a mobility-aware scheduler is proposed, that exploits mobility as additional information in order to schedule users on the downlink of cellular data networks. Indeed, coordination will be performed primarily for users staying at the cell edge, without mobility. Other cell-edge users are likely to move and to be served in better radio conditions where cell coordination is not required. Thus, the extra resource consumption incurred by the joint transmission from several base stations can be avoided for these users. We compare the performance of the proposed scheduler to other usual scheduling policies through the analysis of flow-level traffic models. We show that this scheduler improves the global performance and we validate the results by system level simulations

### **2.3.5 Deterministic channel modelling enhancements for MIMO**

In [3], a realistic simulation scenario was built, that was the basis of different studies within the SHARING project, with the aim of reducing the gap between real network performance and simulations with simplified models. To date, before being standardized, all new features are exhaustively debated between companies using theoretical analysis and large simulation campaigns to support their technological candidates. For this purpose, simplified models are used to bound the run-time of the simulations, but also to offer an objective basis for comparison between features in competition. However, when being deployed in the field, technology performance may differ from the simulated ones. Additional simulations in a realistic scenario can thus help assessing the performance of a technology in realistic conditions.

The scenario addressed here is based on a digital map data of a dense urban environment as illustrated in Figure 18. Macro-cells and small-cells may be deployed in realistic locations, on top of high building rooftops and inside streets respectively. The wideband radio channel from a base station to a user can be predicted thanks to SIRADEL highly efficient ray-based model Volcano [48], providing the multi-path characteristics typical from an urban environment.

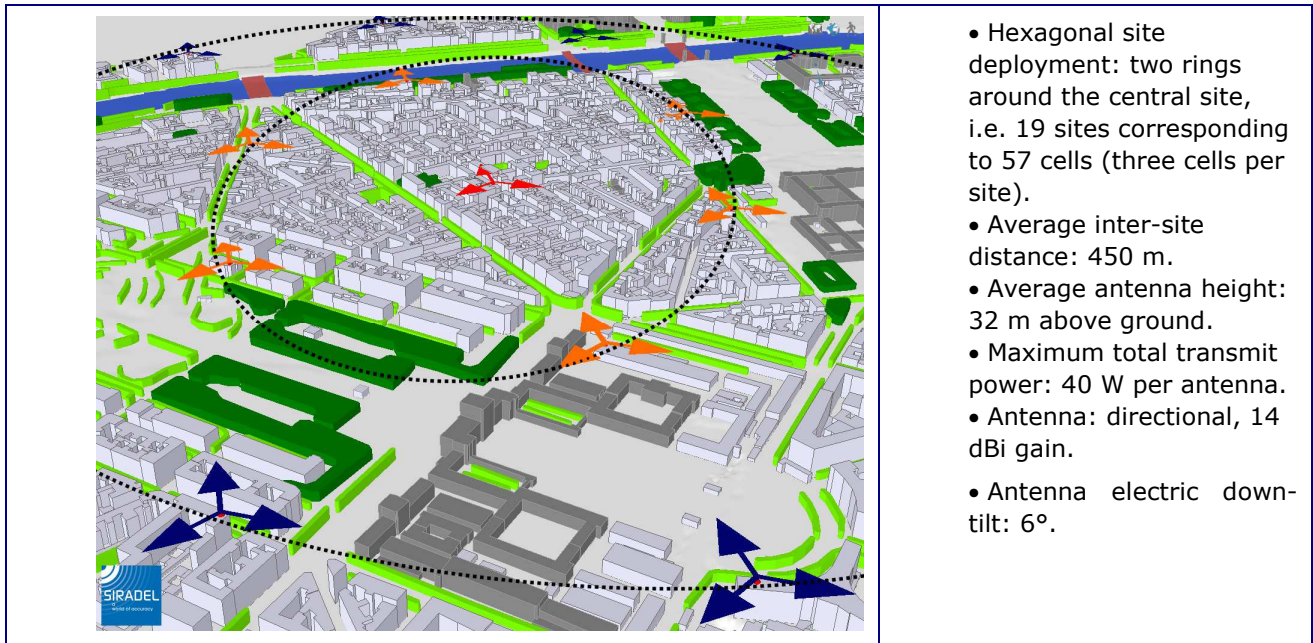


Figure 18. Macro-cell layer deployment in a real dense urban environment

Assessment of the RRM or MIMO algorithms requires the multi-path channel prediction to be highly realistic (e.g. in terms of delay spread, coherency bandwidth or angular spread). The implementation choices or parameterization adapted to the narrowband power simulation are obviously not sufficient. Extensions of the Volcano ray-tracing algorithm were thus developed and different settings were evaluated to refine the channel model. Two different levels of modelling complexity were compared, named 'Basic' and 'Full'. The basic-complexity model generates the strongest specular contributions that may be considered as appropriate for precise and time-optimized assessment of the narrowband received power. The full-complexity model is the outcome of the enhancements in the model implementation, allowing for a richer multi-path prediction with additional allowed combinations between reflections and diffractions, the construction of long-delay contributions and the introduction of the diffuse scattering contribution to capture a more realistic angular diversity around terminals.

The channel characteristics computed from the two levels of modelling complexity were compared on a dense urban scenario, where a single sectored macro base station transmits a vertically-polarized signal to a UE having an isotropic antenna. Several outdoor UE locations were computed, distributed over a 500 m x 500 m grid with a 5 m resolution. Figure 19 shows the channel impulse response at one of these locations. The 'Full' model leads to a far richer one thanks to diffuse scattering. In addition, distant dominant buildings contribute to non-negligible propagation paths with large excess delay, increasing the delay spread and, consequently, reducing the coherence bandwidth. The angular diversity is also increased at the base station side and at the UE side as well, which is of great importance for an accurate MIMO channel prediction.

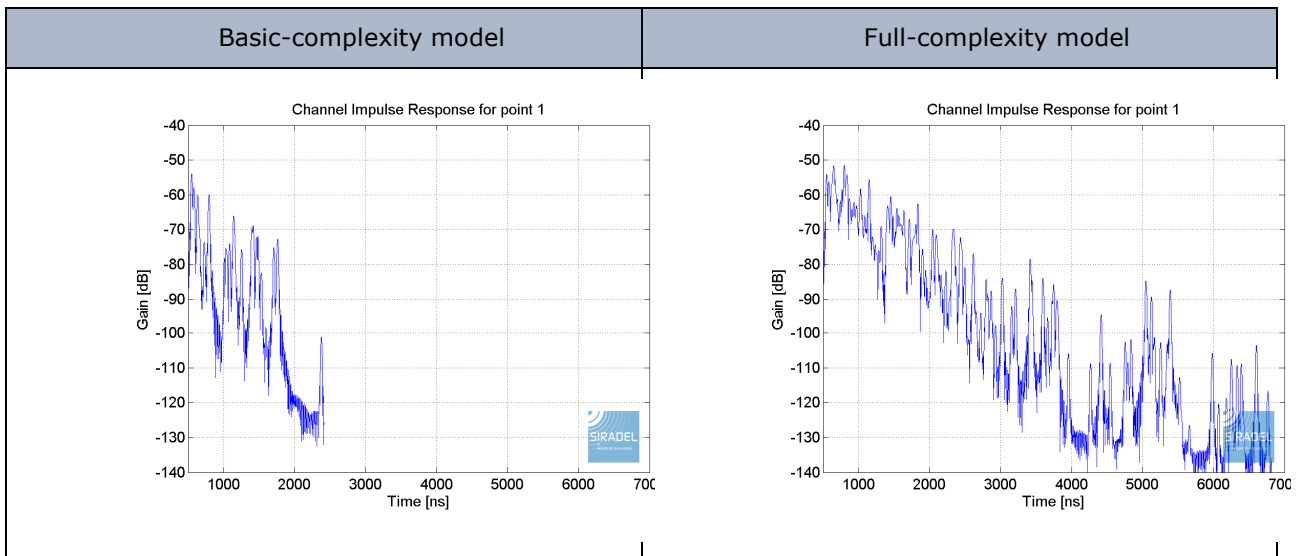


Figure 19. Channel impulse response at test UE location with basic (left) and full (right) complexity models

A typical consequence of the channel enrichment can be observed on the prediction of the channel rank. The rank is an indicator of how many data streams can be spatially multiplexed on the MIMO channel. In a 2x2 MIMO system, another key indicator is the Condition Number (CN) of the MIMO matrix. A well-conditioned matrix with CN close to 0 dB allows for reliable multi-layer reception.

Figure 20 shows the mean CN from the MIMO channel computed between the base station and the UE moving along a street perpendicular to the direct path. The base station antenna system is composed of 2 elements separated by  $2\lambda$ , while 2 antenna elements are separated by  $\lambda$  at the UE. The mean CN is averaged over several locations in order to smooth out the fluctuations. The basic-complexity model shows the highest mean CN, indicating high correlation in the spatial modes due to poor channel predictions. This is especially true when the UE is in Non-Line of Sight where the additional contributions from the full-complexity model impact largely the angular diversity.

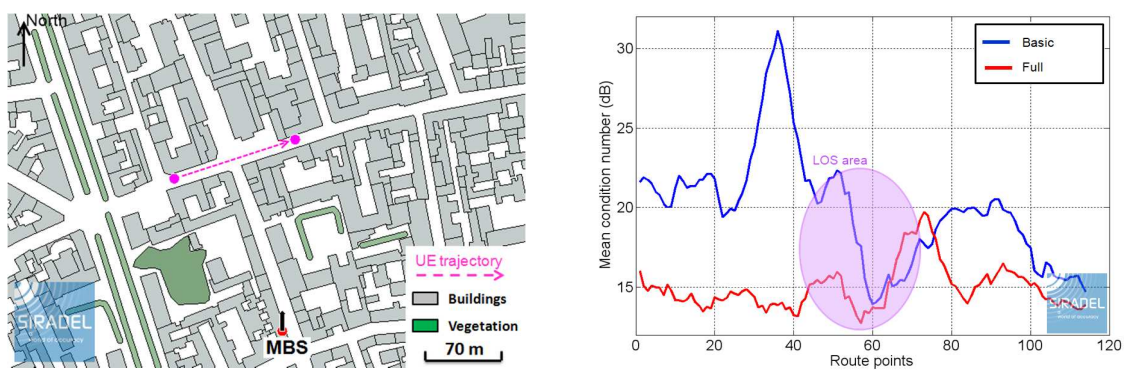


Figure 20. Condition Number prediction

The enrichment of the deterministic channel predictions in the temporal and angular domain impacts very significantly the predicted wideband and MIMO channel parameters. This is expected to be a key improvement for the creation of realistic scenarios dedicated to the evaluation of 3D beamforming, MIMO precoding, interference cancellation and RRM.

### 2.3.6 Impact of beamforming in a large scale real environment

A first study of the impact of beamforming was performed in [3], showing the decrease of the interference level in a dense urban environment, but assuming a constant traffic load of the cells. A new simulation approach has been developed, so-called Monte-Carlo, where discrete users are



randomly dropped in the prediction area, and KPI statistics are built from a succession of runs. At each run, the simulator determines the user throughput from a mapping with its estimated SINR, making it possible to evaluate the traffic load of the cells to which are attached the users. The simulation process is then able to estimate both the interference decrease and the traffic load decrease achievable thanks to the beamforming. The simulation approach is evaluated with a dense outdoor small-cell deployment and the impact on the cell-center and cell-edge user throughputs are assessed into a scenario with medium traffic load (i.e. the average small-cell traffic load is estimated around 15%).

As an example, we assessed the performance of an LTE network when applying the Transmission Mode 6, so called 'Closed loop spatial multiplexing using a single transmission layer' [7]. It consists in precoding the signal so that the phase shift on the different antenna ports results in a beamforming effect. The precoding matrices are specified for 2 and 4 antenna ports, leading to 4 and 16 equivalent radiation patterns respectively. The signal towards a served UE is then increased, but the interference to other cells in the same direction is increased as well. However, the interference to other cells out of the beam is decreased.

The evaluation consisted thus in determining how the SINR was impacted by the beamforming, considering the realistic scenario presented in section 2.3.5, and deterministic propagation predictions between the macro-cells and the UEs. Figure 18 presents the macro network together with its main deployment parameters. This figure shows the macro-cells deployed on two rings (in orange and blue) around a central three-sector site (in red) with an average Inter-Site Distance (ISD) of 450 m. These are not located on real sites, but dominant locations have been selected that are representative of an operational network. A 50% traffic load was assumed for all cells.

A square calculation zone of 1250 m side length and 5 m resolution is centered on the central macro site, representing UE locations at 1.5 m above ground. The path-loss from each eNodeB (eNB) to each UE location was computed with the Volcano ray-based propagation model at a frequency of 2.6 GHz. The cell selection was assumed to be based on the best received power from each cell.

The simulation was performed in the following three cases: one single antenna at the eNB (no beamforming), two and four antennas at the eNB (with beamforming). Note that precoding matrices are normalized, so that the total transmit power remains the same whatever the number of antennas of the eNB. This allows a fair comparison of the three cases.

The impact of beamforming on the SINR is illustrated by the CDF of Figure 21 (left). We observe a positive impact, with a 2.4 dB gain in average for the two antennas case, and 5 dB for the four antennas case.

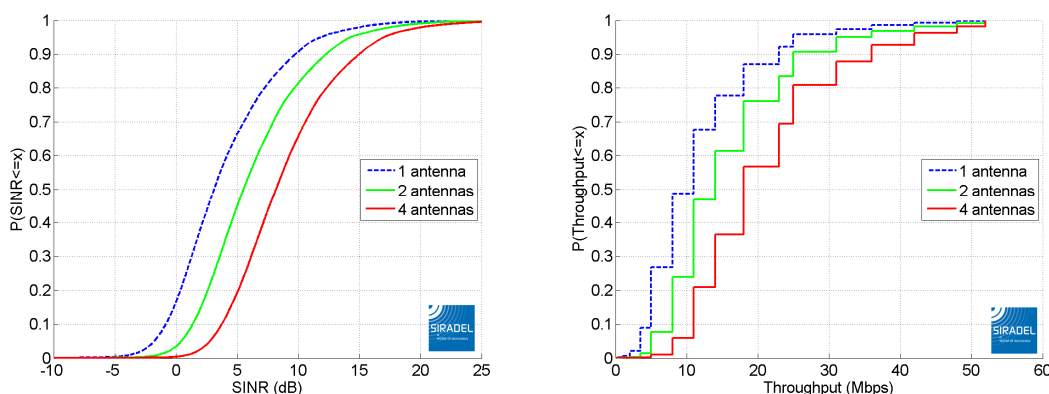


**Figure 21. CDF of the SINR (left) and of the mean user peak throughput (right) with two and four antennas beamforming, compared to single transmit antenna**

Finally, the LTE channel capacity was determined from a link-to-system mapping table. Figure 21 (right) shows the CDF of the mean user peak throughput, considering a typical 10 MHz bandwidth. It is increased by 4.1 Mbps and 9.2 Mbps in average for the two and four antennas cases

respectively. The mean user peak throughput of cell-edge users (5%-ile) is 3.5, 5 and 8 Mbps for the one, two and four antennas cases respectively.

In Section 3.3.4, a new simulation approach is proposed, making it possible to estimate the cell traffic loads depending on user traffic demand. The simulation process is then able to estimate both the interference decrease and the traffic load decrease achievable thanks to the beamforming.

## 2.4 RF and antenna design

This section presents a summary of the work done in Task T3.4

The scope of this study is to evaluate the requirements of an RF front-end to support different Carrier Aggregation (CA) configurations and provide energy savings.

- 2.4.1 The power amplifier (PA) is one of the most power consuming components at RF front-end. Depending on the CA configuration (intra-band contiguous or intra-band non-contiguous) and the number of component carriers (CCs), different output back-off (OBO) levels are required at PA. Therefore a reconfigurable RF front-end was proposed capable to adapt its performance using different operating points at PA and improve energy efficiency (Figure 22). The solution was compared to a conventional PA with single operating point to evaluate energy efficiency enhancements. Additional results are provided in Part B Section 3.4.1.
- 2.4.2 An LTE dual band frequency agile antenna whose size is adapted to a small cell base station has been designed. It supports several CA modes and has been optimized in terms of size and volume thanks to a bandwidth reduction and the use of frequency agility technique.

In the context of WP7, a demonstrator combining RF front end and antenna system has been tested. It shows the compatibility between both subsystems and demonstrates the possibility of increasing the energy efficiency as well as the level of integration of a small cell base station despite the use of a new technology enabler such as carrier aggregation.

### 2.4.1 Reconfigurable RF front-end to support carrier aggregation

#### 2.4.1.1 Introduction

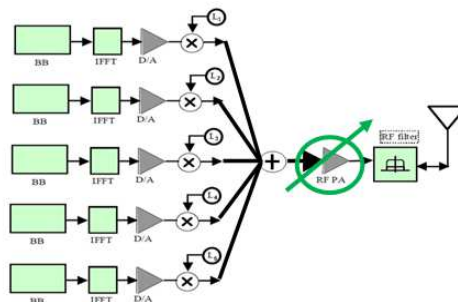


Figure 22 Block diagram of the reconfigurable PA supporting CA.

The analysis focuses on intra-band contiguous CA and intra-band non-contiguous CA, evaluating up to 5 CCs. The details about the intra-band contiguous CA analysis were included in D3.5 [6] and this document presents the intra-band non-contiguous CA results.

The solution was also tested in a hardware prototype developed in WP7 defining different operating points depending on the PA requirements due to CA configuration. The evaluated scenario is a small cell scenario where the maximum transmitted power is not so challenging and a dedicated PA per CC is costly. Therefore the proposed innovation presents as a promising solution to improve energy efficiency.

To define the OBO level at PA associated to each CA configuration, two evaluations were combined appropriately. Firstly, LTE-A waveform was characterized by Complementary Cumulative Distribution Function (CCDF). It is normally sufficient to apply 0.01% CCDF of the

waveform to define PA OBO requirement in case of single CC. Nevertheless aggregating CCs, unwanted emissions and particularly Adjacent Channel Leakage power Ratio (ACLR) specification closely related to linearity performance of the device were also studied. ACLR specification measures the nonlinear characteristics of a device, which indicates the amount of spectral regrowth occurring in adjacent channels. It defines the required OBO level to achieve at least -45 dBc ACLR [44]. From both evaluations, the OBO level can be defined as the most restrictive value between the 0.01% CCDF of the waveform and the value to achieve -45 dBc ACLR for each CA configuration.

The study was done using different E-UTRA test models defined by 3GPP to evaluate the technical specifications. Among them, E-UTRA test model 1.1 (E-TM1.1) verifies most specifications related to PA. The analysis was divided in three phases: intra-band contiguous CA evaluation reported in [6], intra-band non-contiguous CA evaluation and energy efficiency improvement evaluation reported here.

#### 2.4.1.2 Intra-band contiguous CA evaluation

In [6], the simulations performed for intra-band contiguous CA were described. Table 1 summarizes the PA OBO requirements for intra-band contiguous CA with different number of CCs, presenting the results from the CCDF evaluation and the ACLR evaluation.

**Table 1 PA OBO requirements for intra-band contiguous CA.**

Number of CCs	0.01% CCDF (PAPR)	PA OBO (ACLR = 45 dB)	Total PA OBO
1	9.6 dB	8.7 dB	9.6 dB
2	11.8 dB	13.4 dB	13.4 dB
3	13.3 dB	15.9 dB	15.9 dB
4	14.3 dB	17.7 dB	17.7 dB
5	15.2 dB	18.9 dB	18.9 dB

The higher the number of CCs, the higher the required OBO level at PA as expected. Linearity requirements at PA increase with the number of CCs. The target of this study is to define the minimum OBO level at PA to fulfil specifications and provide energy savings at the same time.

The simulations reported in [6] were performed using a PA model where only the 1dB compression point output power was modified to analyze PA performance at different OBO levels. In further simulations, the third-order intercept point (TOI) was also introduced as a simulation parameter and in section 3.4.1 the simulated results are presented. This parameter influences clearly in the PA OBO requirements. The higher the number of CCs, the higher the TOI impact over PA OBO requirements. Usually amplifiers present the 1dB compression point output power 10dB below TOI. If the amplifier has TOI value 8dB above the 1dB compression point output power, the PA OBO requirement for 5CCs can increase up to 2dB. With TOI value 12dB above the 1dB compression point output power, the PA OBO requirement for 5CCs can decrease up to 1dB. Therefore the defined PA OBO requirements should be considered as reference values and slight variations for each specific PA should be understood.

#### 2.4.1.3 Intra-band non-contiguous CA evaluation

PA OBO requirements analysis was extended to intra-band non-contiguous CA configuration. LTE-A waveform analysis for intra-band contiguous CA from 1CC to 5CCs presented in [6] is also applicable to intra-band non-contiguous CA. However ACLR analysis which reflects the amount of spectral regrowth occurring in adjacent channel due to the nonlinear characteristics should be calculated because CCs are positioned differently. The simulated results are presented in section 3.4.1 and Table 2 summarizes the PA OBO requirements for intra-band contiguous CA and intra-band non-contiguous CA up to 5CCs.

**Table 2 PA OBO requirements for intra-band contiguous CA and intra-band non-contiguous CA.**

Number of CCs	Intra-band contiguous	Intra-band non-contiguous	
		GAP = BW	GAP = 2*BW
1	9.6 dB	-	-
2	13.4 dB	12.6 dB	10.5 dB
3	15.9 dB	14.5 dB	14.3 dB
		<b>1CC + GAP = BW + 3CCs</b>	<b>2CCs + GAP = BW + 2CCs</b>
4	17.7 dB	17 dB	16.2 dB
		<b>1CC + GAP = BW + 4CCs</b>	<b>2CCs + GAP = BW + 3CCs</b>
5	18.9 dB	18.5 dB	18 dB

The PA OBO requirements for intra-band contiguous CA are the most restrictive ones. The requirements relax for intra-band non-contiguous CA, specially increasing the gap among CCs.

#### 2.4.1.4 Energy efficiency improvement evaluation

To evaluate the proposed solution a hardware prototype was developed in WP7. AFT20S015N from Freescale (see [http://cache.nxp.com/files/rf\\_if/doc/data\\_sheet/AFT20S015N.pdf?pspll=1](http://cache.nxp.com/files/rf_if/doc/data_sheet/AFT20S015N.pdf?pspll=1)) was the selected PA. It was tested at different operating points from 28V to 14V. Details about its development are shown in D7.3 [43]. In this document, Part B section 3.4.1 presents the measured results. The maximum output power in AFT20S015N prototype is around 38.6 dBm.

Two different energy efficiency evaluations have been done considering that the reconfigurable PA should be capable to support up to 3CCs or 5CCs in intra-band contiguous CA configuration. For 3CCs, the most restrictive PA OBO requirement is 15.9 dB and 18.9 dB for 5CCs.

In the first evaluation with up to 3CCs, the reconfigurable PA should adapt its output power level considering PA OBO requirements from 15.9 dB to 9.6 dB. Considering 38.6 dBm as the peak output power level, the maximum average output power level is so 22.7 dBm for 3CCs contiguous (the most restrictive configuration). In this configuration 3CCs are aggregated, thus the maximum average output power per CC is 18 dBm. This average output power per CC, 18 dBm, is considered as the reference for other CA configurations. Accordingly, the average output power for 2CCs is 21 dBm because 2CCs with 18 dBm each are aggregated.

Depending on CA configuration different PA OBO levels are required, so as the output power level. Therefore different operating points can fulfil the requirements and improve energy efficiency. Table 3 presents power-added-efficiency (PAE) improvements in AFT20S015N for different CA configurations using different operating points.

**Table 3 Energy efficient enhancement provided by the reconfigurable PA for different CA configurations up to 3CCs.**

CA mode	Average power (dBm)	PA OBO (dB)	Peak power (dBm)	PAE (%) at peak power		PAE (%) enhancement
				Single operating point	Different operating point	
1CC	18 dBm	9.6 dB	27.6 dBm	9.5 % (28V)	17.4 % (14V)	45.4 %
2CCs (GAP=2*BW)	21 dBm	10.5 dB	31.5 dBm	17.3 % (28V)	25.7 % (16V)	32.7 %
2CCs (GAP=BW)	21 dBm	12.6 dB	33.6 dBm	22.5 % (28V)	31.2 % (18V)	27.9 %
2CCs	21 dBm	13.4 dB	34.4 dBm	26.1 % (28V)	33.1 % (20V)	21.1 %
3CCs (GAP=BW)	22.7 dBm	14.5 dB	37.2 dBm	37.6 % (28V)	38.8 % (26V)	3.1 %
3CCs	22.7 dBm	15.9 dB	38.6 dBm	40.2 % (28V)	40.2 % (28V)	0 %

For 1CC, the required peak power is 27.6 dBm and 14V operating point is sufficient to fulfil this requirement. Another example is 2CCs contiguous with 34.4 dBm peak power which can be achieved with 20V instead of 28V providing energy savings. Using the proposed solution, PAE enhancement can reach up to 45% switching from 3CCs in intra-band contiguous CA configuration to only 1CC.

In the second evaluation with up to 5CCs, the most restrictive configuration is 5CCs contiguous with 18.9 dB OBO requirement. Considering 38.6 dBm as the maximum peak output power level, the maximum average output power is so 19.7 dBm, which refers to 12.7 dBm output power per CC because 5CCs are aggregated. Assuming 12.7 dBm as the reference average output power per CC, the evaluation was done for different CA configurations defining optimized operating points for each one. Table 4 shows PAE enhancements in AFT20S015N for different CA configurations using different operating points.

**Table 4 Energy efficient enhancement provided by the reconfigurable PA for different CA configurations up to 5CCs.**

CA mode	PA OBO (dB)	Peak power (dBm)	Average power (dBm)	PAE (%) at peak power		PAE (%) enhancement
				Single operating point	Different operating point	
1CC	9.6 dB	22.3 dBm	12.7 dBm	3.5 % (28V)	6.8 % (14V)	48.5 %
2CCs (GAP=2*BW)	10.5 dB	26.2 dBm	15.7 dBm	7.4 % (28V)	14 % (14V)	47.1 %
2CCs (GAP=BW)	12.6 dB	28.3 dBm	15.7 dBm	10.3 % (28V)	17.5 % (14V)	41.1 %
2CCs	13.4 dB	29.1 dBm	15.7 dBm	11.9 % (28V)	19.8 % (16V)	39.9 %
3CCs (GAP=BW)	14.5 dB	31.9 dBm	17.4 dBm	18 % (28V)	26.7 % (18V)	32.6 %
3CCs	15.9 dB	33.3 dBm	17.4 dBm	21.3 % (28V)	29.8 % (18V)	28.5 %
4CCs (GAP=BW)	16.2 dB	34.9 dBm	18.7 dBm	26.6 % (28V)	33.5 % (20V)	20.6 %
4CCs (GAP=BW)*	17 dB	35.7 dBm	18.7 dBm	29.6 % (28V)	36 % (22V)	17.7 %
4CCs	17.7 dB	36.4 dBm	18.7 dBm	33 % (28V)	36.8 % (24V)	10.3 %
5CCs (GAP=BW)	18 dB	37.7 dBm	19.7 dBm	37.6 % (28V)	38.9 % (26V)	3.3 %
5CC (GAP=BW)*	18.5 dB	38.2 dBm	19.7 dBm	39.5 % (28V)	39.5 % (28V)	0 %
5CCs	18.9 dB	38.6 dBm	19.7 dBm	40.2 % (28V)	40.2 % (28V)	0 %

In this case the required peak power for 1CC is 22.3 dBm and 14V operating point is sufficient to fulfil this requirement, reaching up to 48.5% PAE improvement. For 2CCs contiguous, the required peak power is 29.1 dBm and using 16V operating point, PAE improvement is 39.9%. For 3CCs contiguous, PAE enhancement can reach 28.5% and 10.3% for 4CCs contiguous.

#### 2.4.1.5 Conclusions

A complete evaluation about PA OBO requirements for different intra-band CA configurations (intra-band contiguous and intra-band non-contiguous) was done. The evaluation has analyzed LTE-A waveform and ACLR specification using E-UTRA test models. The impact of TOI value at PA was also analyzed performing different simulations. It concluded that some variations in PA OBO requirements are expected depending on each particular PA, because not all PA parameters are included in the simulations. The defined PA OBO requirements should be used as reference values for typical PAs.

Using the commercial PA, AFT20S015N, the proposed solution was analyzed in terms of PAE enhancement, showing PAE improvement up to 45% between the most restrictive CA configuration and the least restrictive one. Therefore the proposed solution using the reconfigurable RF front-end to support CA provides clearly energy savings compared to conventional PA with single operating point.

### 2.4.2 Design of miniature multi-band frequency agile antenna system for carrier aggregation

An LTE dual band frequency agile antenna has been designed whose size is adapted to a small cell base station. It supports several carrier aggregation modes and has been optimized in terms of size and volume thanks to a bandwidth reduction and the use of frequency agility technique.

Also, the antenna system is made of two distinct antennas with two separate access points. Both antennas are collocated on the same PCB. A work has been carried out in order to limit the coupling between both antennas despite their close proximity. Thus, they can be operated at the same time without generating uncontrolled interferences.

The radiation pattern of both antennas has been optimized so that the base station can operate when placed against a wall with the main radiation direction normal to wall.

#### 2.4.2.1 Design presentation

The antenna system is based on two patch antennas. This antenna topology has been selected mainly because of its radiation pattern. In fact, if the antenna ground plane is large enough (compared to the operating wavelength), a microstrip patch antenna will have a relatively high gain and the main beam will be oriented towards the top hemisphere while the back radiation level will remain very low.

In the SHARING case, the antenna system should operate LTE band 7 (2500-2690 MHz) and band 20 (871-957 MHz). The miniaturization effort has been mainly put on band 20 antenna due to its larger operating wavelength. In fact, the dimension of a patch antenna being half a wavelength, band 7 antenna is naturally 3 times smaller than band 20 antenna due to its smaller operating wavelength.

To miniaturize band 20 antenna without degrading its radiation performance, we have used the fact that at a given instant, the LTE system only uses one band 20 channel, and not the whole band, thus reducing the requested antenna instantaneous bandwidth. Indeed, as widely discussed in the literature [45]-[46], the size of an antenna limits its bandwidth and efficiency. The fractional bandwidth upper bound is generally estimated by (1) for a single-mode antenna where  $s$  is the voltage standing wave ratio,  $\eta_r$  the radiation efficiency,  $k=2\pi/\lambda$  and  $a$  the minimum radius of a sphere enclosing the antenna.

$$FBW_{ub} = \frac{1}{\eta_r} \frac{s-1}{\sqrt{s}} \left( \frac{1}{ka} + \frac{1}{(ka)^3} \right)^{-1} \quad (2.1)$$

Therefore, reducing the antenna instantaneous bandwidth has made its miniaturization possible without impacting its radiation efficiency. At the end, a miniaturization factor of 3 has been reached without performance reduction: Band 20 antenna maximum dimension has been reduced from half a wavelength to a sixth of a wavelength using classical folding and loading techniques.

In order to minimize the bandwidth as much as possible, band 20 antenna has been made dual resonant with two narrow band closely spaced resonances. As a result, the antenna only covers one band 20 channel (1<sup>st</sup> resonance Rx sub-channel – 2<sup>nd</sup> resonance Tx sub-channel) at a time. Band 20 antenna instantaneous bandwidth has then been reduced from 71 MHz to 20MHz (two times 10 MHz) as shown in Figure 23.

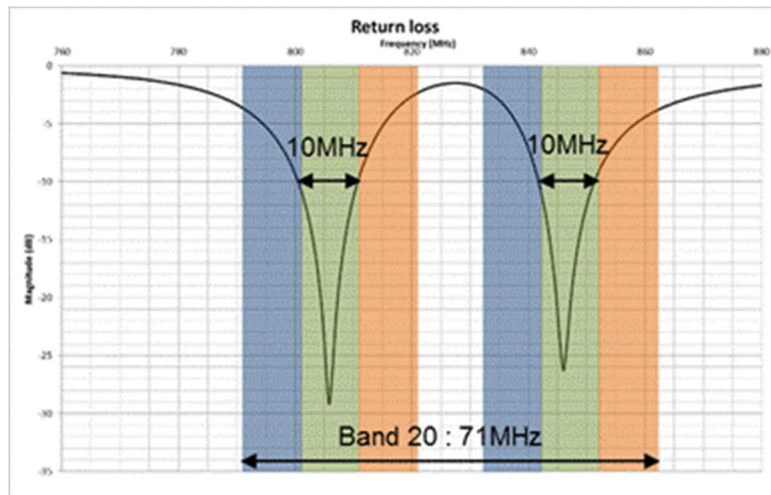


Figure 23 Band 20 instantaneous bandwidth reduction illustration

Frequency agility has then been introduced to the design to allow the antenna system to switch from one channel of band 20 to another and thus to cover the whole band 20. This principle is illustrated in Figure 24 and detailed in [6].

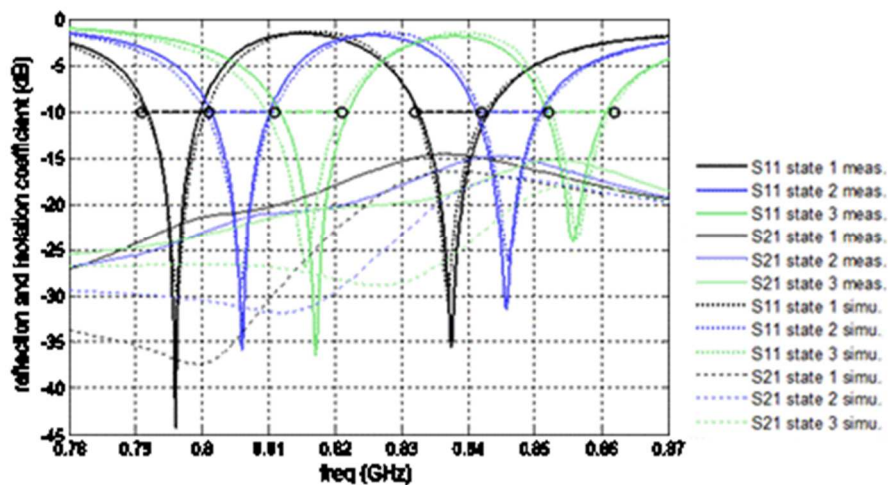
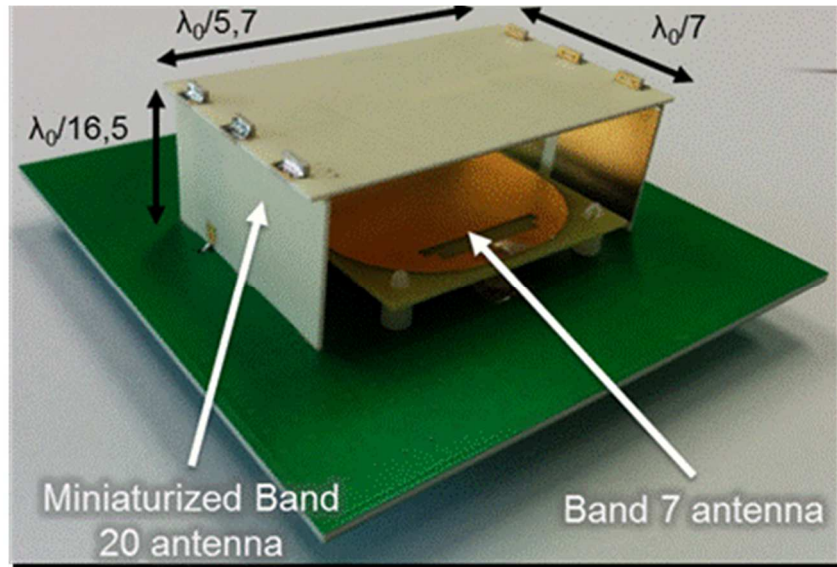


Figure 24: Measured and simulated reflection coefficients at band 20 antenna in three different states.

Figure 25 shows the complete realized antenna system prototype mounted on a 100x100 mm<sup>2</sup> ground plane.





**Figure 25 : Picture of the antenna system**

In order to optimize the volume occupied by the antenna system, band 20 antenna has been placed above band 7 antenna. This collocation has been possible thanks to their near field configuration. This point is explained in detail in [6].

#### 2.4.2.2 **Simulation and measurement campaign**

A simulation campaign has been carried out. During this campaign, every antenna parameters, including antennas dimensions, antennas location, materials, etc., has been selected and/or adjusted. The frequency agility principle has also been developed, demonstrated and optimized during this phase.

This simulation campaign is described in [6].

After the simulation phase, a prototype of the antenna system has been built and a complete measurement campaign has been carried out in CEA Grenoble anechoic chamber. Figure 26 shows the prototype in the anechoic chamber during the measurement campaign and the results are presented and compared to the simulation results in [43].

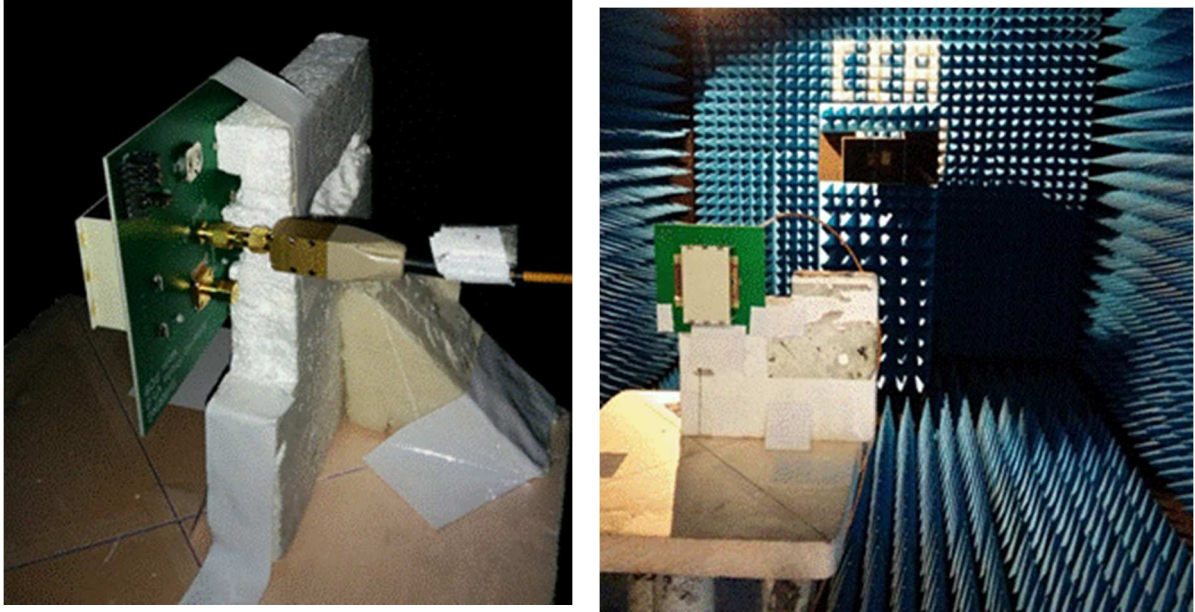


**Figure 26 Pictures of the prototype during the measurement campaign**

At the end, in spite of the miniaturization and the integration of both antenna within the same volume, the antenna system exhibits excellent results in terms of impedance matching, gain and radiation pattern control.

A demonstrator combining TTI RF front end and CEA antenna system has been tested. It shows the compatibility between both subsystems and demonstrates the possibility of increasing the energy efficiency as well as the level of integration of a small cell base station despite the use of new technology enablers such as carrier aggregation technique.

### 3 PART B: NEW WORK, NOT YET REPORTED IN PREVIOUS DELIVERABLES

Part B presents the work performed since delivery of D3.2, D3.3, D3.4 and D3.5. Similar to Part A, contributions were grouped in a slightly different way from that in the Technical Annex, even though the titles of subsections are those of WP3 Tasks.

#### 3.1 Multi-point cooperation at the transmitter

This section presents the work dedicated to computation of beamforming weights in a CoMP situation:

- In Section 3.1.1 the “price of distributedness” under distributive CSIT for JP-CoMP is investigated, where the BSs carry out distributed precoding strategies based on different noisy versions of the global CSIT. A finite SNR regime rate analysis under regularized ZF precoding for JP-CoMP is performed using the tools from random matrix theory. It is found that, the rate penalty of using distributed CSIT rather than centralized CSIT does not vanish even when the number of transmit antennas goes to infinity.
- In Section 3.1.2, the problem of coordinated beamforming in multicell MIMO and massive MIMO is considered. In this latter case, a *decentralized* beamforming allocation strategy using recent results from random matrix theory is presented. The developed strategy is suitable for real time traffic and requires very low signaling overhead between the base stations. The performance of this strategy has been analyzed analytically and its optimality is proven in the asymptotic regime.
- In Section 3.1.3, another sub-optimal *distributed* beamforming allocation was developed in the context of MIMO with small number of antennas and for non-real time traffic, in order to achieve time QoS constraints of the users. The optimality gap of the proposed solution is derived analytically as well.

##### 3.1.1 The cost of distributed CSI feedback in JP CoMP

###### 3.1.1.1 Introduction

Next generation wireless networks are foreseen to operate transmissions under massive cooperation and coordination among transmitters (TXs). This requires multiple TXs to exchange data and CSI related information with each other. With perfect message and CSI sharing, the different TXs can be seen as a unique virtual multiple-antenna array serving all RXs in a multiple-antenna Broadcast Channel (BC) fashion. Existing joint precoding however requires global multi-user CSI at each TX in order to achieve near optimal sum rate performance.

The problem of CSI imperfections has been a central one in the literature on the BC. The case of imperfect, noisy, or delayed CSI has been well investigated in the existing literature (e.g. [49] and [52]). However, almost all of the existing literature assumes *centralized* CSIT, i.e., the precoding is based on the basis of a *single* imperfect channel estimate, which is common to every TX. Although it is meaningful in the case of broadcasting using a single transmitting device, this assumption can be challenged when the joint precoding is carried out across distant TXs connected by heterogeneous and imperfect backhaul or having to communicate without backhaul (over the air) among each other. It is expected that the CSI exchange will introduce further delay and quantization noise, thus making the CSI intrinsically TX-dependent. This setting is referred to as distributed CSI (D-CSI) in this report.

From an information theoretic perspective, the study of TX cooperation in the D-CSI setting raises several intriguing and challenging open problems.

First, the capacity region of the broadcast channel under a general D-CSI setting is unknown. In [50], a rate characterization at high SNR is carried out using DoF analysis for the two TXs scenario. This study highlighted the penalty associated with the lack of a consistent CSI shared by the cooperating TXs from a DoF point of view, when using a conventional precoder.

Interestingly, it was also shown that classical robust precoders (i.e. made robust with respect to centralized forms of CSI imperfections) [53] do not restore the DoF. More importantly, the finite SNR performance analysis is uncharted territory. Although, the use of conventional linear precoders that are unaware of the D-CSI structure is expected to yield a loss with respect to a centralized (even imperfect) CSI setting, the quantifying of this loss in the finite SNR regime (dubbed here the “price of distributedness”) has not been addressed previously.

The main goal here is to study here comparatively the average rate achieved by popular precoders (namely regularized Zero Forcing (ZF)) in the centralized and distributed CSI settings. To render the problem amenable to closed form analysis, we consider the large number of antenna regime. Specifically we let the number of transmit antennas and the number of receive antennas jointly grow large with a fixed ratio, thus allowing to use efficient tools from the field of random matrix theory (RMT).

The main contribution in this section consists in providing a deterministic equivalent for the average rate per user in a D-CSI setting where each TX receives its *own* estimate of the global multi-user channel matrix with the quality (in a statistical sense) of this estimate varying from TX to TX. A key finding is that although all SINR levels undergo classical hardening effect, there is a non-vanishing price associated to distributed CSI feedback when compared with the centralized one.

### 3.1.1.2 System Model

#### Transmission Model

Consider a network MIMO system where there are  $n$  TXs jointly serving  $K$  receivers (RXs). Each TX is equipped with  $M_{\text{TX}}$  antennas and the total number of transmit antennas is denoted by  $M = nM_{\text{TX}}$  while every RX is equipped with a single-antenna. We assume that the ratio of transmit antennas to the number of users is fixed and given by  $\beta = M/K$ .

We further assume that the RXs have perfect CSI so as to focus on the imperfectness of CSI feedback and exchange among the TXs (due to limited feedback and exchange capability). We consider that the RXs treat interference as noise. The channel from the  $n$  TXs to the  $K$  RXs is represented by the multi-user channel matrix  $\mathbf{H} \in \mathbb{C}^{K \times M}$ , in which elements are distributed i.i.d.  $\mathcal{N}_{\mathbb{C}}(0,1)$ .

The transmission is described as:

$$\begin{bmatrix} y_1 \\ \vdots \\ y_K \end{bmatrix} = \mathbf{H}\mathbf{x} + \boldsymbol{\eta} = \begin{bmatrix} \mathbf{h}_1^H \mathbf{x} \\ \vdots \\ \mathbf{h}_K^H \mathbf{x} \end{bmatrix} + \begin{bmatrix} \eta_1 \\ \vdots \\ \eta_K \end{bmatrix} \quad (3.1)$$

where  $y_i$  is the signal received at the  $i$ -th RX,  $\mathbf{h}_i^H \in \mathbb{C}^{1 \times M}$  is the channel from all transmit antennas to RX  $i$ , and  $\boldsymbol{\eta} \triangleq [\eta_1, \dots, \eta_K]^T$  is the normalized Gaussian noise vector with i.i.d. elements in  $\mathcal{N}_{\mathbb{C}}(0,1)$  distributions.

The transmitted multi-user signal  $\mathbf{x}$  results from the precoding matrix  $\mathbf{T} \in \mathbb{C}^{M \times K}$ , applied to the  $K$ -dimensional vector  $\mathbf{s}$  composed of i.i.d. symbols i.e.,

$$\mathbf{x} = \mathbf{T}\mathbf{s} \quad (3.2)$$

where the  $i$ th column  $\mathbf{t}_i$  of  $\mathbf{T}$  represents the beamforming vector used to transmit to RX  $i$ .

Our main figure-of-merit is the average sum rate

$$R \triangleq \frac{1}{K} \sum_{k=1}^K \mathbb{E}[\log_2(1 + \text{SINR}_k)] \quad (3.3)$$

where

$$\text{SINR}_k = \frac{|\mathbf{h}_k^H \mathbf{t}_k|^2}{1 + \sum_{l \neq k} |\mathbf{h}_k^H \mathbf{t}_l|^2}. \quad (3.4)$$

### Distributed CSIT Model

General transmit cooperation scenarios rely on local CSI to be feedback to each TX, followed by an exchange mechanism over a wired/wireless backhaul. Backhaul links are subject to latency, which causes TX-specific CSI degradation. Hence, a suitable and general CSIT model is one whereby each TX must make a precoding decision based on a TX-dependent estimate of the global channel matrix, a problem known in control theory as Team Decision [55]. Note that in our model, no further communication (or message passing) is allowed among TX. Specifically, the  $j$ -th TX receives the multi-user channel estimate  $\hat{\mathbf{H}}^{(j)} \in \mathbb{C}^{K \times M}$  and computes the  $M_{\text{TX}} \times 1$  transmit coefficient  $\mathbf{x}_j$  solely as a function of  $\hat{\mathbf{H}}^{(j)}$ . Assume that the imperfect multi-user channel estimate is modeled by

$$\hat{\mathbf{H}}^{(j)} = \sqrt{1 - (\sigma^{(j)})^2} \mathbf{H} + \sigma^{(j)} \mathbf{\Delta}^{(j)} \quad (3.5)$$

where the first term captures the portion of the true channel and the second term captures the portion of the Gaussian noise from channel estimation, so that  $\mathbf{\Delta}^{(j)}$  has i.i.d. components. The coefficient  $\sigma^{(j)}$  captures the quality of the CSIT at the  $j$ -th TX.

### Regularized Zero Forcing with Distributed CSIT

We are interested in the impact of the D-CSIT model on the rate performance for a conventional precoding method. Hence we focus on the example of the popular *regularized ZF* MISO broadcast precoder (c.f. [54] and [53]). To compute the precoder, the  $j$ -th TX first computes a  $M \times K$  matrix

$$\mathbf{T}^{(j)} = \frac{\sqrt{P}}{\sqrt{\Psi^{(j)}}} (\hat{\mathbf{H}}^{(j)\text{H}} \hat{\mathbf{H}}^{(j)} + M\alpha \mathbf{I}_M)^{-1} \hat{\mathbf{H}}^{(j)\text{H}} \quad (3.6)$$

where  $\Psi^{(j)}$  is normalization factor for the transmission power at the  $j$ -th TX and  $\alpha$  is the regularizing coefficient for RZF precoder. The TX  $j$  then uses the  $j$ th  $M_{\text{TX}} \times K$  block of  $\mathbf{T}^{(j)}$  as the precoding matrix to steer the transmit signal.

#### 3.1.1.3 Main Results: Non-vanishing Price of Distributed CSIT

Using RMT, we derive the following results on asymptotic SINR in large networks.

**Theorem.** As  $K$  and  $M$  goes to infinity,  $\text{SINR}_k$  converges to  $\text{SINR}_k^0$  almost surely, where  $\text{SINR}_k^0$  is given as

$$\text{SINR}_k^0 = \frac{\left(\frac{1}{2} \sum_{j=1}^n \sqrt{1 - (\sigma^{(j)})^2}\right)^2 \frac{\delta^2}{(1+\delta)^2}}{I_k^0 + \Gamma^0/P} \quad (3.7)$$

in which  $\delta$  is a parameter depending on  $\alpha$  and  $\beta$ , and  $I_k^0$  and  $\Gamma^0$  are factors depending on  $\sigma^{(j)}$  and  $\delta$ .

The mathematical proof of the theorem is omitted here. Details can be found in [51].

From the above result, the case  $n=1$  corresponds to the centralized CSI configuration and the deterministic equivalent SINR is simplified as

$$\text{SINR}_k^0 = \frac{(1 - (\sigma^{(1)})^2) \delta^2}{\Gamma^0 ((1 - (\sigma^{(1)})^2) + (1 + \delta)^2 (\sigma^{(1)})^2) + \frac{(1+\delta)^2}{P}} \quad (3.8)$$

### Discussions

One can verify that  $\text{SINR}_k^0 (n > 1) < \text{SINR}_k^0 (n = 1)$ , which means the distributed CSIT configuration ( $n > 1$ ) always achieves smaller SINR than that of the centralized CSIT configuration under a large number of users  $K$  and a large number of transmit antennas  $M_{\text{TX}}$ .

This suggests that the performance degradation under distributed implementation using distributed CSIT does not vanish even though one employs arbitrarily many transmit antennas.

### 3.1.1.4 Simulations

We now verify using Monte-Carlo simulations the accuracy of the asymptotic expression derived in the main theorem. We consider a network consisting of  $n=3$  TXs with a sum power constraint given by  $P=10$  dB and we assume that  $(\sigma^{(j)})^2 = \sigma^2 = 0.1$  for all TXs. Note that the fact that error variances are equally distributed does not imply a centralized CSIT as CSI errors at the various TXs remain *independent* of each other

We use the optimal value for the parameter  $\alpha$  in the centralized case given as [56], eq. (53)

$$\alpha^{\text{CCSI}} = \frac{1 + \sigma^2 P}{1 - \sigma^2} \times \frac{1}{\beta P} \quad (3.9)$$

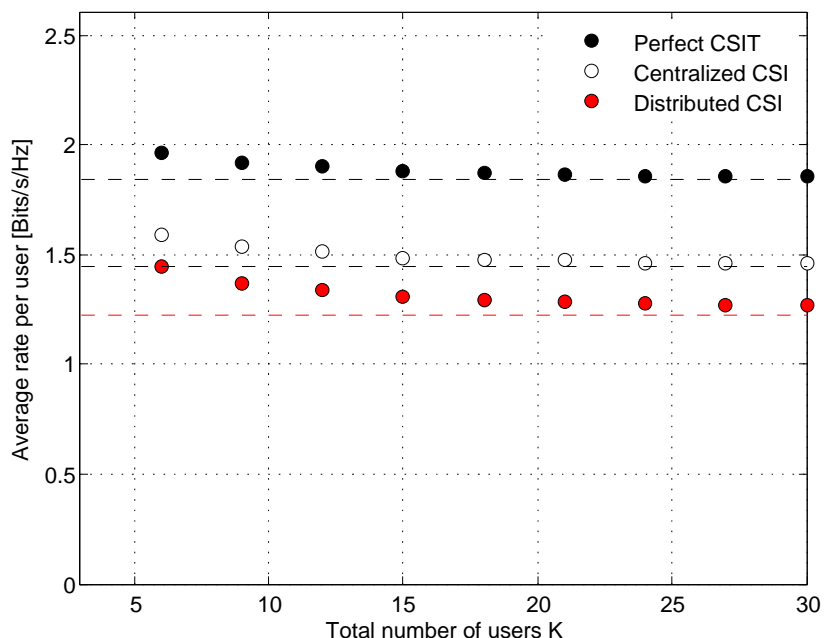


**Figure 27: Average rate per user as a function of the number of users  $K$  with  $(\sigma^{(j)})^2 = \sigma^2 = 0.1$ .**

In Figure 27, we show the rate per user as a function of the number of users for a square setting where  $M=nM_{\text{TX}}=K$  (i.e.,  $\beta = 1$ ). For comparison purpose, we also show the rate per user obtained in the case of centralized CSIT with  $(\sigma^{\text{CCSI}})^2 = 0.1$  and with perfect CSIT (obtained using  $n=1$ ). The large system deterministic equivalents are shown to be accurate with just 20 to 30 users and antennas. The cost of having distributed information is also highlighted by the losses compared to the centralized configuration for the same average feedback quality.

### 3.1.1.5 Conclusions

We have studied regularized ZF joint precoding in a distributed CSI configuration. Using RMT tools, an analytical expression has been derived to approximate the average rate per user in the large system limits. This new deterministic equivalent reveals the cost related not just to CSI feedback limitation, but also to backhaul sharing limitations, and can be helpful in terms of robust system design. The price of distributedness is evaluated here for a conventional

precoder, which further motivates the development of novel precoding schemes being more suitable to the distributed CSI setting.

### 3.1.2 Asymptotic Performance analysis of advanced MIMO schemes

We consider the problem of coordinated multi-cell downlink beamforming in massive multiple input multiple output (MIMO) systems consisting of  $N$  cells,  $N_t$  antennas per base station (BS) and  $K$  user terminals (UTs) per cell. Massive MIMO is one of the unavoidable techniques in future wireless networks. It refers to the idea of scaling up the number of antennas on the base station (BS) to a few hundreds and to exploit the large number of antennas to achieve greater spectral efficiency and serve many tens of users. In this work, we propose an optimal decentralized multi-cell beamforming algorithm for massive MIMO systems that requires limited amount of information exchange between the BSs. In order to overcome the heavy backhaul requirement, we propose in this work a decentralized approach to compute the multi-cell beamforming vectors. In our algorithm, the BSs must exchange parameters at the slow fading time scale rather than the instantaneous channel realizations (fast fading coefficients). We use tools from random matrix theory to formulate our algorithm

Using a large system analysis, we provide closed form expression for the lower bound on the set of feasible target SINR. Furthermore, we prove that when the dimensions of the system become large, the achieved SINR in the uplink and downlink by our algorithm match the target SINR. Moreover, we also prove that when the dimensions of the system become large, the allocated power by our algorithm is asymptotically optimal.

We then provide a heuristic extension of our decentralized beamforming algorithm to incorporate the individual BS transmit power constraints. Finally, we investigate the impact of pilot contamination on the performance of our algorithm and propose a heuristic adaptation that improves the system performance.

#### 3.1.2.1 System Model

We consider the multi-cell beamforming problem with  $N$  cells and  $K$  UTs per cell. Each BS is equipped with  $N_t$  antennas and each UT has a single antenna. Let  $h_{i,j,k} \in \mathbb{C}^{N_t}$  denote the channel from the BS  $i$  to the  $k$ -th UT in cell  $j$ . We consider the TDD mode where reciprocity between the uplink and downlink channels occurs. We assume that the elements of the channel vector are independent and identically distributed (i.i.d.) with Gaussian distribution, i.e.,  $h_{i,j,k} \propto \text{CN}(0, \sigma_{i,j,k} / N_t)$ . Let  $w_{i,j} \in \mathbb{C}^{N_t}$  denote the transmit downlink beamforming vector for the  $j$ -th UT in cell  $i$ . Likewise, let  $\Lambda_{i,j}^{\text{DL}}$  denote the received SINR for the  $j$ th UT in cell  $i$  and  $\gamma_{i,j}$  the corresponding target SINR.

The achieved SINR in downlink for the UT  $i,j$  is given by

$$\Lambda_{i,j}^{\text{DL}} = \frac{|w_{i,j}^H h_{i,i,j}|^2}{\sum_{(n,k) \neq (i,j)} |w_{n,k}^H h_{n,i,j}|^2 + N_0}. \quad (3.10)$$

In this work, we consider the downlink sum power minimization problem given by

$$\begin{aligned} \min_{w_{i,j} \forall i,j} \sum_{i,j} w_{i,j}^H w_{i,j} \\ \text{s.t. } \Lambda_{i,j}^{\text{DL}} \geq \gamma_{i,j} \quad \forall i,j. \end{aligned} \quad (3.11)$$

This problem has been widely studied in the literature [58][59][60] and it has been shown in [59] that it can be reformulated as a second order conic program where strong duality holds.

### 3.1.2.2 Algorithm Design

As shown in [59], the optimization problem (3.11) can be reformulated as a second order conic programming (SOCP) problem and, strong duality holds for this problem. This result has been exploited in [60] and the following iterative solution has been proposed.

Before introducing the algorithm, we define the following matrices.

$$H_{i,n} = [h_{i,n,1}, \dots, h_{i,n,K}] \in N_t \times K, \quad H_i = [H_{i,1}, \dots, H_{i,N}] \in N_t \times NK, \quad \lambda_i = [\lambda_{i,1}, \dots, \lambda_{i,K}] \in K \times 1, \\ \Lambda = \text{diag}(\lambda_1, \dots, \lambda_N) \in NK \times NK.$$

We also define the matrix  $\Sigma_i^\lambda = \frac{1}{N_t} H_i \Lambda H_i^H \in C^{N_t \times N_t}$ .

We recall here the Centralized BeamForming Algorithm **CBF** of [60]

Starting from any initial  $\lambda_{i,j}^0 > 0 \quad \forall i, j$ , the uplink power allocation is given by  $\lambda_{i,j} = \lim_{t \rightarrow \infty} \lambda_{i,j}^t$ , where

$$\lambda_{i,j}^{t+1} = \frac{1}{\frac{1}{N_t} (1 + \frac{1}{\gamma_{i,j}}) h_{i,i,j}^H (\Sigma_i^t + I_{N_t})^{-1} h_{i,i,j}} \quad \forall i, j \quad (3.12) \\ \Sigma_i^t = \frac{1}{N_t} H_i \Lambda^t H_i^H \quad \text{and} \quad \Lambda^t = \lambda_1^t, \dots, \lambda_N^t.$$

- The optimal uplink receiver filter is given by

$$v_{i,j} = \frac{1}{\sqrt{N_t}} \left( \sum_{n,k} \frac{\lambda_{n,k} N_0}{N_t} h_{i,n,k} h_{i,n,k}^H + N_0 I \right)^{-1} h_{i,i,j}. \quad (3.13)$$

- The optimal transmit downlink beamforming vectors are given by  $w_{i,j} = \sqrt{\frac{\delta_{i,j}}{N_t}} v_{i,j}$ , with

$$\delta = F^{-1} 1 N_0.$$

Here,

$$\delta_i = [\delta_{i,1}, \dots, \delta_{i,K}] \in R^{1 \times K}, \quad \delta = [\delta_1, \dots, \delta_N]^T \in R^{NK \times 1}, \quad 1 \in [1, \dots, 1]^T \in R^{NK \times 1}$$

and the elements of the matrix  $F \in R^{NK \times NK}$  and of the submatrix  $F^{i,j} \in R^{K \times K}$  are given by,

$$F = \begin{pmatrix} F^{1,1} & \dots & F^{1,N} \\ \vdots & \ddots & \vdots \\ F^{N,1} & \dots & F^{N,N} \end{pmatrix} \quad (3.14)$$



$$F_{j,k}^{i,n} = \begin{cases} \frac{1}{\gamma_{i,j} N_t} |v_{i,j}^H h_{i,i,j}|^2, & n=i, k=j \\ \frac{-1}{N_t} |v_{n,k}^H h_{n,i,j}|^2, & (n,k) \neq (i,j). \end{cases} \quad (3.15)$$

This aforementioned solution cannot be implemented in a distributed manner. The computation of dual uplink power ( $\lambda_{i,j}$ ) and the scaling factors ( $\delta_{i,j}$ ) requires a central station which has the global CSI knowledge. In order to overcome this issue, we formulate our *reduced overhead* beamforming algorithm. The main idea is that under the massive MIMO regime (i.e. when  $N_t$  and  $K$  become large), some parameters can be approximated by their asymptotic equivalents using results from RMT. However, RMT results are not directly applicable to our scenario since the computation of  $\lambda_{i,j}$  explicitly depends on the channel vectors. Our approach in this work is to first propose an algorithm that depends only on the second order statistics of the channel vectors. Mathematically, it is not ensured that it achieves the optimal solution. We then prove that this algorithm is optimal in the large system domain (massive MIMO).

This latter algorithm is coined Reduced Overhead Beamforming algorithm-ROBF-[61] and is presented below:

- Starting from any initial  $\mu_{i,j}^0 > 0 \forall i,j$  the uplink power allocation is given by  $\mu_{i,j} = \lim_{t \rightarrow \infty} \mu_{i,j}^t$ , where

$$\mu_{i,j}^{t+1} = \frac{\gamma_{i,j}}{\sigma_{i,i,j} \bar{m}_i^t} \quad \forall i,j \quad (3.16)$$

and  $\bar{m}_i^t$  is evaluated as  $\bar{m}_i^t = \lim_{p \rightarrow \infty} \bar{m}_i^{t,p}$  (initializing with any  $\bar{m}_i^{t,0} > 0, \forall i$ )

$$\bar{m}_i^{t,p} = \left( \frac{1}{N_t} \sum_{n=1}^N \sum_{k=1}^K \frac{\sigma_{i,n,k} \mu_{n,k}^t}{1 + \sigma_{i,n,k} \mu_{n,k}^t \bar{m}_i^{t,p-1}} + 1 \right)^{-1}. \quad (3.17)$$

- The optimal receive uplink receive filter is given by

$$\hat{v}_{i,j} = \sqrt{\frac{1}{N_t}} \left( \sum_{n,k} \frac{\mu_{n,k} N_0}{N_t} h_{i,n,k} h_{i,n,k}^H + N_0 I \right)^{-1} h_{i,i,j}. \quad (3.18)$$

- The optimal transmit downlink beamforming vectors are given by  $\hat{w}_{i,j} = \sqrt{\frac{\bar{\delta}_{i,j}}{N_t}} \hat{v}_{i,j}$ .

The scaling factor  $\bar{\delta}_{i,j}$  is given as  $\bar{\delta} = (I - \Gamma \Delta^{-1} \rho)$  where

$$\bar{\delta}_i = [\bar{\delta}_{i,1}, \bar{\delta}_{i,2}, \dots, \bar{\delta}_{i,K}]^T \in \mathbb{R}^{1 \times K}, \quad \bar{\delta} = [\bar{\delta}_1, \bar{\delta}_2, \dots, \bar{\delta}_N]^T \in \mathbb{R}^{NK \times 1}$$

$$Y_i = \left[ \frac{\gamma_{i,1}}{\sigma_{i,i,1} \bar{G}_{i,i,1} \bar{m}_i^2}, \dots, \frac{\gamma_{i,K}}{\sigma_{i,i,K} \bar{G}_{i,i,K} \bar{m}_i^2} \right]$$

$$Y = [Y_1, \dots, Y_N]^T \text{ vector of size } N \times K$$

$$\Gamma = \text{diag} (Y) \text{ of size } NK \times NK$$

and the matrix  $\Delta \in \mathbb{C}^{NK \times NK}$  is defined as

$$\Delta = \begin{pmatrix} \Delta^{1,1} & \dots & \Delta^{1,N} \\ \vdots & \ddots & \vdots \\ \Delta^{N,1} & \dots & \Delta^{N,N} \end{pmatrix} \quad (3.19)$$

where each submatrix  $\Delta^{i,j} \in \mathbb{C}^{K \times K}$  is given by

$$\Delta_{j,k}^{i,n} = \begin{cases} 0, & n = i, k = j \\ \frac{1}{N_t} \bar{G}_{n,i,j} \bar{G}_{n,n,k} \bar{m}_n', & (n,k) \neq (i,j). \end{cases} \quad (3.20)$$

$\bar{m}_i'$  can be evaluated from  $\bar{m}_i$  as

$$\bar{m}_i' = \frac{\bar{m}_i^2}{1 - \frac{1}{N_t} \sum_{n=1}^N \sum_{k=1}^K \frac{(\sigma_{i,n,k} \mu_{n,k} \bar{m}_i)^2}{(1 + \sigma_{i,n,k} \mu_{n,k} \bar{m}_i)^2}} \quad (3.21)$$

and

$$\bar{G}_{i,n,k} = \frac{\sigma_{i,n,k}}{1 + \mu_{n,k} \sigma_{i,n,k} \bar{m}_i^2}. \quad (3.22)$$

The last quantity to be evaluated is  $\rho$ ,  $\rho = [\rho_1, \rho_2, \dots, \rho_N]^T \in \mathbb{R}^{NK \times 1}$  and

$$\rho_i = \left[ \frac{N_0}{\sigma_{i,i,1} \bar{G}_{i,i,1} \bar{m}_i^2}, \dots, \frac{N_0}{\sigma_{i,i,K} \bar{G}_{i,i,K} \bar{m}_i^2} \right]^T$$

### 3.1.2.3 Performance Analysis of the ROBF algorithm

We provide now the performance analysis of our algorithm.

**Theorem 1** *The ROBF iterative algorithm converges to a fixed point.*

*Proof.* The proof is provided in [61].

In [61], the solution provided by this fixed point is then characterized, and is shown to be asymptotically optimal in the sense that when the dimensions of the system grow large, the achieved downlink SINR converges to the target SINR, and the allocated uplink and downlink powers converge to the optimal solution.

Recall that the downlink SINR for the ROBF algorithm is given by

$$\Lambda_{i,j}^{\text{DL}}(\mu) = \frac{|\hat{w}_{i,j}^H h_{i,i,j}|^2}{\sum_{k \neq j} |\hat{w}_{i,k}^H h_{i,i,j}|^2 + \sum_{n \neq i,k} |\hat{w}_{n,k}^H h_{n,i,j}|^2 + N_0}. \quad (3.23)$$

**Theorem 2** *In the large system regime, the achieved downlink SINR for the ROBF algorithm converges almost surely to the target SINR  $\gamma_{i,j}$ . Mathematically stating*

$$\Lambda_{i,j}^{\text{DL}}(\mu) \xrightarrow[N_t, K \rightarrow \infty]{\text{a.s.}} \gamma_{i,j} \quad \forall i, j. \quad (3.24)$$

*Proof.* One can refer to [61] for a detailed proof.

**Theorem 3:** *The downlink power allocations yielded by the ROBF and CBF algorithms are equal in the asymptotic limit:*

$$\lim_{N_t, K \rightarrow \infty} \sum_{i,j} \hat{w}_{i,j}^H \hat{w}_{i,j} \xrightarrow[N_t, K \rightarrow \infty]{\text{a.s.}} \lim_{N_t, K \rightarrow \infty} \sum_{i,j} w_{i,j}^H w_{i,j} \quad (3.25)$$

*Proof.* The proof is provided in [61].

It is worth mentioning that the notation  $N_t, K \rightarrow \infty$  implicitly means that  $0 < \liminf_{K \rightarrow \infty} \frac{N_t}{K} \leq \limsup_{K \rightarrow \infty} \frac{N_t}{K} < \infty$ .

#### 3.1.2.4 Numerical Results

We present now some numerical results that corroborate the theoretical claims in the previous sections. We consider a hexagonal cellular system consisting of 2 cells. All numerical results are plotted in the following two figures by varying the positions of the UTs inside the cell over 500 iterations.

First, we examine the performance of the ROBF algorithm in satisfying the target SINR constraints. In the first figure, we plot the variation of the SINR (averaged across the UTs) with respect to the number of antennas per BS for 100 channel realizations. The number of users is  $K=25$  UTs per cell and the target SINR is 3 dB per UT. The bubbles represent the average achieved SINR values (averaged over the channel realizations), and the vertical lines around this bubble represent the variation of the achieved downlink SINR around the average value. It can be observed that for moderate number of antennas, the target SINR constraints are satisfied. In second figure, we plot the downlink power of the ROBF algorithm and compare it with the optimal centralized solution (CBF algorithm) and ZF beamforming. We consider  $K=25$  UTs per cell and target rate = 3 bits/s/Hz ( $\log(1+\gamma_{i,j})$ ) per UT. The downlink power allocated by our ROBF is very close to that allocated by CBF, which means that ROBF is nearly optimal in terms of minimizing the downlink power. In addition, it can be seen that for moderate number of antennas per BS, ROBF provides substantial power gains as compared to ZF beamforming.

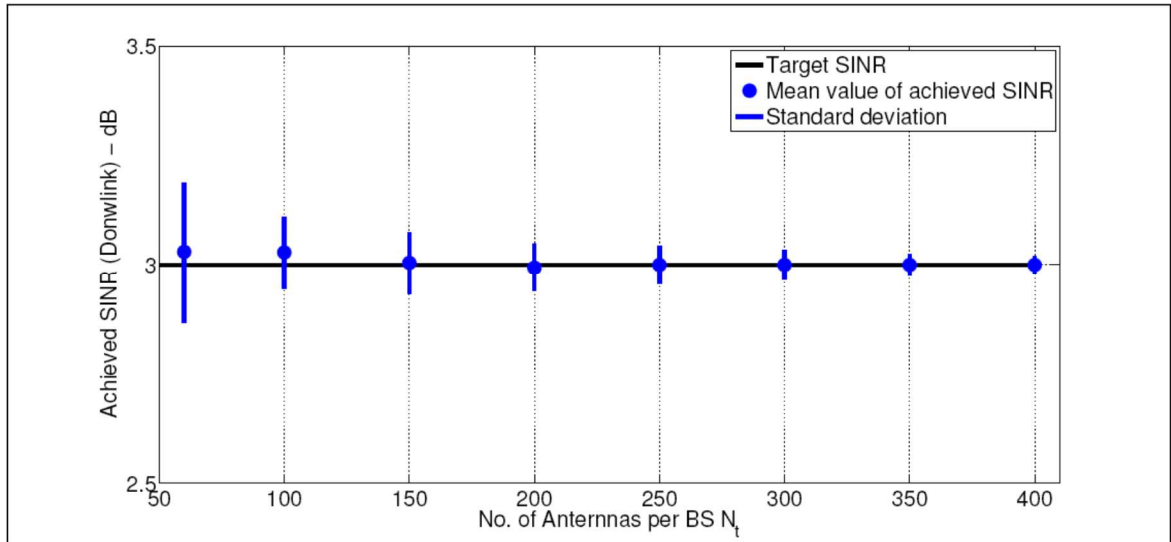


Figure -28: Fluctuations of the downlink SINR (ROBF algorithm) around the target value.  $K = 25$  UTs per cell and target SINR = 3 dB per UT.

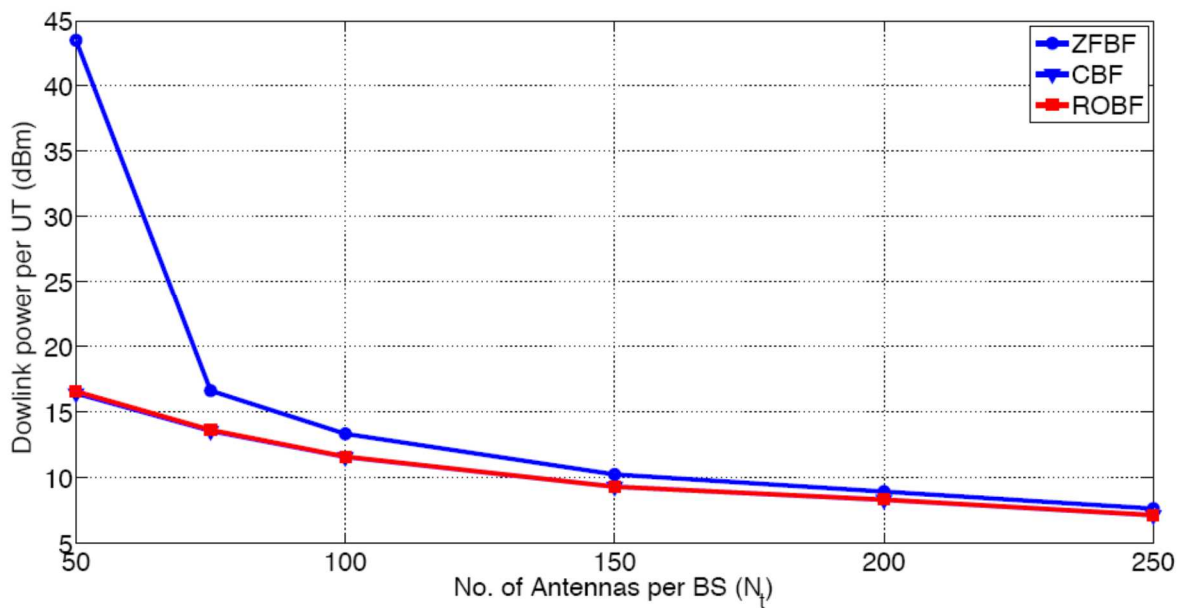


Figure -29: Comparison of downlink power per UT as a function of the number of antennas per BS.  $K = 25$  UTs per cell and target rate =  $3 \text{ bits/s/Hz} (\log(1 + \gamma_{i,j}))$  per UT.

### 3.1.3 Distributed CoMP schemes with limited Feedback and time average QoS

In this work, we consider the problem minimizing the time average energy expenditure subject to time average quality of service (QoS) constraints, in a MIMO multi-cell system. Our motivation to consider the time average QoS constraint comes from the fact that it provides the flexibility to dynamically allocate resources over the fading channel states as compared to instantaneous QoS constraints. In terms of energy savings, time average QoS constraint can lead to better performance, due to the fact that the transmissions can be delayed until favourable channel conditions are seen, thus minimizing the energy expenditure. We formulate our problem as a stochastic optimization problem and propose a solution based on the technique of Lyapunov

optimization, which provides simple online solutions based only on the current knowledge of the system state (as opposed to other approaches such as dynamic programming which suffer from very high complexity).

Our contributions in this work are as follows. We first formulate the *feasible QoS region*, i.e. the set of target QoS constraints that are achievable by some control policy. We model the time average constraint as a *virtual queue* and transform the problem into a queue stabilization problem while minimizing the average energy expenditure. We then use the technique of Lyapunov optimization to formulate a dynamic control strategy that satisfies the time average QoS targets. Our algorithm leads to a decentralized design in which the base stations (BSs) can formulate the beamforming vectors using only the local CSI. The BSs would only have to exchange virtual queue-length information among each other. We then provide a performance analysis of our algorithm in the case when the BSs exchange the virtual queue-length information with delays. Finally, we studied the impact of limited feedback when the BS can obtain the CSI of a limited number of users at a time and provide an algorithm to select the optimal set of users which must feedback their CSIs.

### 3.1.3.1 System Model

We consider a MIMO multi-cell scenario consisting  $N$  cells and  $K$  user terminals (UTs) per cell. The UTs in each cell are served by their respective BSs which are equipped with  $N_i$  antennas. Let UT  $i,j$  denote the user  $j$  in cell  $i$ . The BS of each cell serves only the UTs present in its cell. We consider a discrete-time block-fading channel model where the channel remains constant for a given coherence interval and then changes independently from one block to the other. We denote the channel vector from the BS  $i$  to the UT  $j,k$  during the time slot  $t$  by  $h_{i,j,k}[t] \in C^{N_i}$ . We define the channel matrix as  $h_{i,j}[t] = [h_{i,j,1}[t], \dots, h_{i,j,K}[t]] \in C^{N_i \times K}$ ;  $h_i[t] = [h_{i,1}[t], \dots, h_{i,N}[t]] \in C^{N_i \times KN}$  and  $H[t] = [h_1[t], \dots, h_N[t]] \in C^{N_i \times KN^2}$ . The channel process  $\{H[t], t = 0, 1, 2, \dots\}$  is assumed to be an independent and identically distributed (i.i.d) discrete time stationary ergodic random process with each column vector which takes values from the finite state space  $\{H_1, \dots, H_L\}$ . We denote the distribution  $\Pr(H[t] = H_l) = \pi_l$ ,  $l = 1, \dots, L$  where  $\sum_l \pi_l = 1$ .

Let us denote the beamforming (or precoding) vector corresponding to UT  $i,j$  during slot  $t$  by  $w_{i,j}[t] \in C^{N_i \times 1}$ . The signal received by UT  $i,j$  during time  $t$  is given by

$$y_{i,j}[t] = h_{i,i,j}^H[t]w_{i,j}[t]x_{i,j}[t] + \sum_{\substack{(n,k) \\ \neq (i,j)}} h_{n,i,j}^H[t]w_{n,k}[t]x_{n,k}[t] + z_{i,j}[t] \quad (3.26)$$

where  $x_{i,j}[t]$  represents the information signal for the UT  $i,j$  during the time slot  $t$  and  $z_{i,j}[t]$  is the noise with variance  $N_0$ . The QoS metric which we denote by  $\gamma_{i,j}[t]$  is

$$\gamma_{i,j}[t] = |w_{i,i,j}^H[t]h_{i,i,j}[t]|^2 - V_{i,j} \sum_{\substack{(n,k) \\ \neq (i,j)}} |w_{n,k}^H[t]h_{n,i,j}[t]|^2 \quad (3.27)$$

where  $V_{i,j}$  is a constant whose role will be specified later.

The transmission power by each BS  $P_i[t]$  depends on the beamforming vector during the time slot  $t$  which can be given as  $P_i[t] = \sum_{j=1}^K w_{i,j}^H[t] w_{i,j}[t]$ ,  $i = 1, \dots, N$ . The optimization problem to minimize the average energy expenditure subject to time average QoS constraint can be formulated as

$$\min \lim_{T \rightarrow \infty} \frac{1}{T} \sum_{t=0}^{T-1} \mathbb{E} \left( \sum_{i=1}^N P_i[t] \right) \quad (3.28)$$

$$s.t. \lim_{T \rightarrow \infty} \frac{1}{T} \sum_{t=0}^{T-1} \mathbb{E} (\gamma_{i,j}[t]) \geq \lambda_{i,j}, \quad \forall i, j \quad (3.29)$$

$$\sum_{j=1}^K w_{i,j}^H[t] w_{i,j}[t] \leq P_{peak} \quad \forall i, t \quad (3.30)$$

where  $P_{peak}$  is the peak power at which the BSs can transmit.

The above optimization problem is stochastic where the action during each time slot is the beamforming pre-coding vectors ( $w_{i,j}[t] \forall i, j$ ). In other words, the goal is to find the sequence of control actions that minimizes the time average power consumption while satisfying the time average QoS constraints. Let the optimal solution to the above optimization problem be denoted by  $P_{inf}$ . For more details on the system model and problem formulation, one can refer to [63].

### 3.1.3.2 Decentralized algorithm and performance analysis

The approach used to solve the problem is based on the concept of *virtual queue* [62][62]. The virtual queue associated with the time average constraint  $\bar{\gamma}_{i,j} \geq \lambda_{i,j}$  evolves in the following manner,

$$Q_{i,j}[t+1] = \max(Q_{i,j}[t] - \mu_{i,j}[t], 0) + A_{i,j}[t] \quad (3.31)$$

where  $A_{i,j}[t] = \nu_{i,j} \sum_{\substack{(n,k) \\ \neq (i,j)}} w_{n,k}^H[t] w_{n,i,j}[t]^2 + \lambda_{i,j}$  denotes the arrival process and  $\mu_{i,j}[t] = |w_{i,j}^H[t] h_{i,i,j}[t]|^2$  denotes the departure process. The notion of strong stability of the virtual queue is given as  $\sum_{i,j} \bar{Q}_{i,j}[t] < \infty$ . Ensuring the strong stability of the virtual queue implies that the time average of the arrival process is less than or equal to the service process [62], i.e.

$$\bar{A}_{i,j}[t] - \bar{\mu}_{i,j}[t] \leq 0 \quad \forall i, j. \quad (3.32)$$

In other words, the stochastic constraint is satisfied. Therefore, we reformulate the original problem into a queueing stability problem and use the technique of Lyapunov optimization [62] to solve it.

To this end, we define the quadratic Lyapunov function  $L: R^N \rightarrow R$  as:  $L([t]) = \frac{1}{2} \sum_{i,j} (Q_{i,j}[t])^2$ . We define the one-step conditional Lyapunov drift as

$$\Delta([t]) = \mathbb{E}\{L([t+1]) - L([t]) \mid L([t])\} \quad (3.33)$$

where  $\mathbb{E}\{\cdot\}$  is the mathematical expectation. According to the theory of Lyapunov optimization, a good method to choose the beamforming vector is to minimize an upper bound

of the Lyapunov drift-plus-penalty expression. This implies that the beamforming vector should be chosen in the following manner:

$$w_{i,j}[t] \in \underset{w}{\operatorname{argmax}} \sum_{i,j} \mathbb{E} [Q_{i,j}[t] |w_{i,j}^H h_{i,i,j}[t]|^2 - v_{i,j} Q_{i,j}[t] \sum_{\substack{(n,k) \\ \neq (i,j)}} |w_{n,k}^H h_{n,i,j}[t]|^2 - V w_{i,j}^H w_{i,j} | (t)]$$

where  $V$  is a constant. We assume that the BSs have the perfect knowledge of CSI of all its downlink channels ( $h_{i,n,k} \forall n, k$ ). Therefore, the above optimization problem reduces to greedily minimizing the term inside the expectation ( $\mathbb{E}[f(Y) | Y] = f(Y)$ ). The expectation can be removed and the problem reduces to the following optimization problem at each time,

$$\begin{aligned} \max_{\substack{\in \mathbb{N}^t \\ i,j}} \sum_{i,j} [Q_{i,j} |w_{i,j}^H h_{i,i,j}|^2 - v_{i,j} Q_{i,j} \sum_{\substack{(n,k) \\ \neq (i,j)}} |w_{n,k}^H h_{n,i,j}|^2 - V w_{i,j}^H w_{i,j}] & \quad (3.34) \\ \text{s.t.} \sum_j w_{i,j}^H w_{i,j} \leq P_{\text{peak}} & \quad \forall i. \end{aligned}$$

The objective function of the above optimization problem can be written as,

$$\begin{aligned} \max \sum_{i,j} w_{i,j}^H A_{i,j} w_{i,j} \\ \text{s.t.} \sum_j w_{i,j}^H w_{i,j} \leq P_{\text{peak}} & \quad \forall i \end{aligned}$$

where  $A_{i,j} = Q_{i,j} H_{i,i,j} - \sum_{\substack{(n,k) \\ \neq (i,j)}} v_{n,k} Q_{n,k} H_{i,n,k} - V$  and  $H_{i,n,k} = h_{i,n,k} h_{i,n,k}^H$ .

One can see that in order to formulate the matrix  $A_{i,j}$ , the BSs require the local CSI ( $h_{i,n,k} \forall n, k$ ). The BSs have then to exchange the queue-lengths among themselves. Therefore, our formulation naturally leads to a decentralized solution and reduces significantly the signaling overhead.

We now provide the decentralized solution to the above optimization problem. We denote this solution by the superscript "opt". The obtained result is shown in the following lemma.

**Lemma** *The optimal solution to the aforementioned optimization problem is that the BS serves, during each timeslot  $t$ , at most one UT per cell at its peak power. i.e.*

Let  $j^* = \underset{j}{\operatorname{argmax}} \lambda^{\max}(A_{i,j})$ . The power allocated to user  $j$  is,

$$P_{i,j}^{\text{opt}} = \begin{cases} P_{\text{peak}} & \text{if } j = j^* \text{ and } \lambda^{\max}(A_{i,j^*}) > 0 \\ 0 & \text{else.} \end{cases}$$

The beamforming vector allocated to the active user  $j$  is the eigen vector corresponding to the eigen value  $\lambda^{\max}(A_{i,j^*})$ .

The proof of this lemma can be found in [63].

**Theorem** Our algorithm yields the following performance bounds. The virtual queue is strongly stable and for any  $V \geq 0$ , the time average queue-length satisfies

$$\sum_{i,j} \bar{Q}_{i,j}^{\text{opt}} [t] \leq \frac{C_1 + VNKP_{\text{peak}}}{\varepsilon} \text{ and the time average power yields, } \sum_{i=1}^N \bar{P}_i^{\text{opt}} [t] \leq P_{\text{inf}} + \frac{C_1}{V}.$$

The proof can be found in [63]. The bound in the above theorem implies that the time average power allocated by our algorithm can be made arbitrarily close to the minimum average power by taking  $V$  arbitrarily very high. This comes at the expense of increasing the average queue-length of the virtual queue.

Our above algorithm is decentralized and reduces therefore the signaling overhead in the network. The BSs do not have to exchange the CSIs of the users since the beamforming is based on local CSI knowledge. On the other hand, the BSs must exchange the virtual queues between each other. This cannot be done on each timeslot. We therefore extend our work to the case where the BSs exchange the virtual queues once every  $D$  slots. In other words, each BS knows the outdated delayed queues of the other cells' users.

### Delayed Queue length exchange

Each BS  $i$  has perfect queue-length information of its local queues ( $Q_{i,j}[t] \forall j$ ) and the delayed queue-length information from the neighboring queues ( $Q_{n,k}[t-\tau], \forall n \neq i, k$ ). The BSs treat the delayed queue-length as the true value of the queue-length. The allocation is then done using our aforementioned algorithm by replacing ( $Q_{n,k}[t], \forall n \neq i, k$ ) by its delayed value ( $Q_{n,k}[t-\tau], \forall n \neq i, k$ ) as follows,

Let

$$A_{i,j}^{\tau} [t] = Q_{i,j}[t]_{i,i,j}(t) - \sum_{k \neq j} \nu_{i,k} Q_{i,k}[t]_{i,i,k} [t] - \sum_{n \neq i, k} \nu_{n,k} Q_{n,k}[t-\tau]_{i,n,k} [t] - V$$

The active user per cell and the power allocation policy are given by,

$$j_{\tau}^* = \underset{j}{\text{argmax}} \lambda^{\max}(A_{i,j}^{\tau}).$$

$$P_{i,j}^{\text{del}} = \begin{cases} P_{\text{peak}} & \text{if } j = j_{\tau}^* \text{ and } \lambda^{\max}(A_{i,j_{\tau}^*}^{\tau}) > 0 \\ 0 & \text{else} \end{cases}$$

where the superscript "del" denotes parameters corresponding to the solution with delayed queue-length information. The beamforming is the eigen vector corresponding to the maximum eigenvalue  $\lambda^{\max}(A_{i,j_{\tau}^*}^{\tau})$  of  $A_{i,j_{\tau}^*}^{\tau}$ .

The aforementioned algorithm has the following performance.

**Theorem** Our algorithm with delayed queue-length information exchange has the following performance. The time average queue-length satisfies,

$$\limsup_{T \rightarrow \infty} \frac{1}{T} \sum_{t=0}^{T-1} \sum_{i,j} \mathbb{E} Q_{i,j}^{\text{del}} [t] \leq \frac{C_1 + C_2 + VNKP_{\text{peak}}}{\varepsilon}$$

and the time average allocated power satisfies

$$\limsup_{T \rightarrow \infty} \frac{1}{T} \sum_{t=0}^{T-1} \sum_{i=1}^N \mathbb{E} P_i^{\text{del}} [t] \leq P_{\text{inf}} + \frac{C_1 + C_2}{V}.$$



where  $C_1$  and  $C_2$  are two finite constant. The proof of the above theorem can be found in [63]. For high values of  $V$ , the time average allocated power by our algorithm can be made arbitrarily close to the optimal solution.

### 3.1.3.3 Numerical Results

In order to assess the performance of our algorithms, we present in this section some numerical results. We consider a network consisting of 2 cells with 2 UTs per cell. Each BS has  $N$  antennas and  $P_{\text{peak}} = 10$  dB. In the first figure, we plot the time average power per BS versus the target QoS and compare our algorithm to the case where instantaneous QoS constraints is used instead of time average QoS. One can see that for the case with time average constraints, the average power is lower. For a target QoS of 10 dB, our algorithm provides up to 4dB reduction in terms of power consumption as compared to the case with instantaneous QoS constraints (for  $V = 800$ .) This is due to the fact that the time average QoS constraint provides greater flexibility in allocating resources over channel fading states. In order to assess the importance of  $V$ , we plot in the second figure the time average power consumption per BS versus the average queue-length for different values of  $V$ . The target time average QoS is 10 dB. When  $V$  increases, the time average power decreases and the average queue-length increases. This is in accordance with our theoretical results provided above. In the third figure, we examine the impact of the number of antennas on the power consumption. We plot the average power consumption with respect to the number of transmit antennas. It can be seen that the average power reduces with the increase in number of BS antennas.

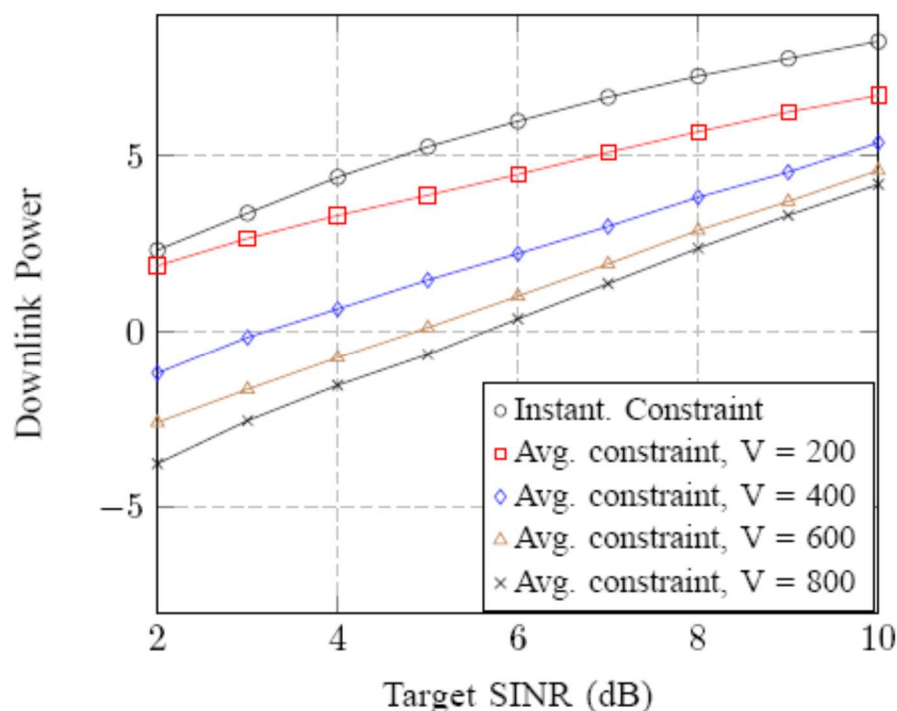


Figure -30: Average power Vs target QoS for a two cell scenario, each cell consisting of two UTs,  $N_t = 5$ ,  $P_{\text{peak}} = 10$  dB.

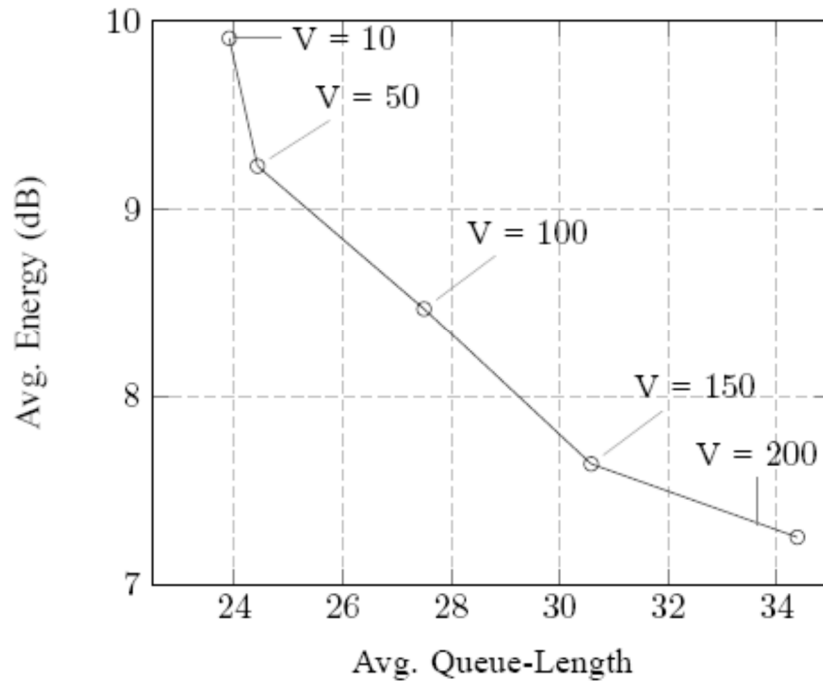


Figure -31: Time average power vs time average queue-length for a two cell scenario, each cell consisting of two UTs,  $N_t=5$ , peak power per BS = 10 dB Target QoS value= 10 dB.

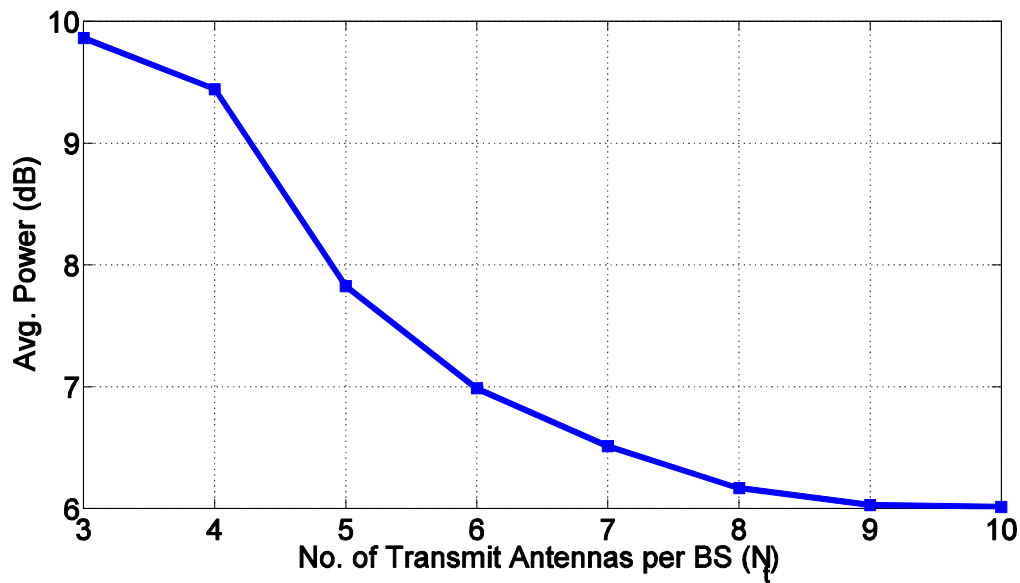


Figure-32: Average power vs number of transmit antennas, peak power = 10 dB, target QoS = 10 dB,  $V = 100$ .

## 3.2 Interference cancellation at the receiver and advanced transceivers

This section presents the work performed in T3.1 and T3.2 concerning transmitter and receiver schemes able to mitigate interference at the receiver, either uplink or downlink.

- Section 3.2.1 presents an interference mitigation scheme at the DL receiver when the transmitted signal is built with a linear dispersion code. The scheme is based on the concept of widely linear receivers. Indeed, provided that a user or its interferer uses a non-circular modulation, a widely linear minimum mean square receiver supersedes a simple MMSE receiver since it is able to reject an interferer using a single antenna (T3.1)
- Section 3.2.2 Interference aware receivers are introduced at the DL receiver at the UEs, in order to mitigate interference generated by non perfectly orthogonal precoders in DL MU-MIMO in one or several CoMP cells (T3.1).
- Section 3.2.3 focuses on UL LTE receivers in presence of interference caused by a Multi-user MIMO scheme. Taking into account that LTE UL uses SC-FDMA modulation, two receivers are compared, respectively the direct and indirect approach: based on the DMRS pilot symbols, either receiver filter coefficients are directly computed from the pilot symbols (direct), or the channel coefficients are first computed, and then the receiver coefficients are derived from them (indirect) (T3.2).
- Section 3.2.4 provides an SINR analysis focusing on the comparison between the conventional interference rejection combination (IRC) and the proposed interference rejection techniques taking into account the difference between the interfering pilots and the interfering data signal in terms of their covariance matrices. Moreover, the performance of the proposed schemes is evaluated under more practical considerations such as non-synchronized cases and triply selective channels due to time, frequency and spatial variations. (T3.2).
- Section 3.2.5. presents the improved version of the Enhanced Spatial Modulation (ESM) concept targeting higher spatial efficiency by employing multiple signal constellations, so that information bits are transmitted both by antenna *and* constellation combinations indices.. The impact on the number of receive antennas is also investigated showing that the performance gains increase as the number of receive antennas increases (T3.2).

### 3.2.1 Widely Linear receiver solutions to suppress or avoid interference with advanced MIMO schemes

According to Figure 4, this task, summarized in section 2.2.2, focusses on the advanced MIMO schemes for the LTE-A downlink in presence of interferences. The purpose is to give new alternatives to improve a BER gain for users (UE) thanks to the antenna diversity at eNodeB transmissions in the context of high density cellular-network.

In order to give more insight on the MIMO scheme, the new LTE UE receiver is defined at the output of one frequency bin where the propagation channels are assumed to be flat.

Let's note the definition of the first and second moment of the second order statistics

$$\begin{aligned} \text{First Moment : } \mathbf{R}_x &= E[\mathbf{y}\mathbf{y}^H] \\ \text{Second Moment : } \mathbf{C}_x &= E[\mathbf{y}\mathbf{y}^T] \end{aligned} \tag{3.35}$$

where  $\mathbf{y}$  is a stochastic vector and  $E[\ ]$  is the expectation. The WL adaptive equalizer exploits the second moment of the second order statistics of either the user symbols or interference symbols.

### 3.2.1.1 Signal modelling and LD MIMO Coding

The scenario of interest is the case of an LTE UE receiver with  $N_r$  antennas, at the output of a single frequency bin where the fading of the propagation channel is assumed to be flat. Symbols  $\{a_{ij}\}$  are transmitted from the eNodeB through  $N_e$  antennas with one LD MIMO scheme according to Figure 5. The signal at the input of the UE receiver is then

$$\mathbf{y}(i) = \mathbf{H} \mathbf{x}(i) + \mathbf{n}(i) \quad \text{where } \mathbf{x}(i) = \begin{bmatrix} x_1(i) \\ \vdots \\ x_{N_e}(i) \end{bmatrix} \quad (3.36).$$

where  $x_n(i)$  is the  $i$ -th transmitted signal at the  $n$ -th antenna after the LD MIMO coding of Figure 5 of Section 2.2.2,  $\mathbf{H}$  is the  $N_r \times N_e$  propagation channel matrix and  $\mathbf{n}(i)$  is the additive noise. In presence of interference this noise cannot be assumed to be spatially white. According to the LD MIMO code of Figure 5, the transmitted signal  $\mathbf{X}(i)$  verifies

$$\mathbf{x}(Ki+k-1) = \mathbf{Z}_k^{(\zeta_k)} \mathbf{a}(i)^{(\zeta_k)} \quad \text{for } 1 \leq k \leq K \quad (3.37)$$

where  $\zeta_n = +1/-1$  for any matrix  $\mathbf{M}$ ,  $\mathbf{M}^{(1)} = \mathbf{M}$  and  $\mathbf{M}^{(-1)} = \mathbf{M}^*$ . The parameters  $(\mathbf{Z}_k, \zeta_k)$  are associated to a given LD code and  $\mathbf{a}(i)$  is the  $L \times 1$  vector composed by the user symbols  $\{a_{ni}$  for  $1 \leq n \leq L\}$  according to Figure 5. For instance, the parameters of Alamouti LD code are

$$\text{Alamouti} : \mathbf{Z}_1 = \begin{bmatrix} 1 & 0 \\ 0 & 1 \end{bmatrix} \text{ and } \mathbf{Z}_2 = \begin{bmatrix} 0 & 1 \\ -1 & 0 \end{bmatrix} \text{ with } \begin{cases} \zeta_1 = 1 \\ \zeta_2 = -1 \end{cases} \quad (3.38)$$

The receiver considers the following space-time observation to take into account the LD Code structure of the transmitted data.

$$\mathbf{z}(i) = \begin{bmatrix} \mathbf{y}^{(\zeta_1)}(Ki) \\ \vdots \\ \mathbf{y}^{(\zeta_K)}(Ki+K-1) \end{bmatrix} = \mathbf{H}_{ST} \mathbf{a}(i) + \mathbf{n}_{ST}(i) \quad \text{where } \mathbf{H}_{ST} = \begin{bmatrix} \mathbf{H}^{(\zeta_1)} \mathbf{Z}_1^{(\zeta_1)} \\ \vdots \\ \mathbf{H}^{(\zeta_K)} \mathbf{Z}_K^{(\zeta_K)} \end{bmatrix} \text{ and } \mathbf{n}_{ST}(i) = \begin{bmatrix} \mathbf{n}^{(\zeta_1)}(Ki) \\ \vdots \\ \mathbf{n}^{(\zeta_K)}(Ki+K-1) \end{bmatrix} \quad (3.39)$$

where  $\mathbf{y}^{(1)}(i) = \mathbf{y}(i)$ ,  $\mathbf{y}^{(-1)}(i) = \mathbf{y}^*(i)$ ,  $\mathbf{H}^{(1)} = \mathbf{H}$  and  $\mathbf{H}^{(-1)} = \mathbf{H}^*$ . In this study, we focus on the following operational context:

- The LD MIMO Code are full rate with  $K = L$  according to Figure 5. Thus, the bit-rate of an equivalent SIMO transmission is equivalent to the MIMO transmission.
- According to (3.38), the matrices  $\mathbf{Z}_k$  of the LD MIMO are independent from the channel matrix (Open Loop).

The channel matrix  $\mathbf{H}$  and the second order statistics of the signals  $\mathbf{a}(i)$  and  $\mathbf{n}(i)$  are assumed to be perfectly known in this work

### 3.2.1.2 MMSE UE receiver with LD MIMO Coding

The purpose of the LD code MMSE receiver is the estimation of the symbols vector  $\mathbf{a}(i)$  with the following spatial filtering:  $\hat{\mathbf{a}}(i) = \mathbf{W}_{ST} \mathbf{z}(i)$ . As the noise vector  $\mathbf{n}_{ST}(i)$  cannot be

assumed to be spatially and temporally white due to interference, the matrix  $\mathbf{W}_{ST}$  is estimated from the minimization of the min square error  $\mathcal{E} = \|\mathbf{a}(i) - \mathbf{W}_{ST}\mathbf{z}(i)\|$ . The result is

$$\mathbf{W}_{ST} = \mathbf{R}_{az} \mathbf{R}_{zz}^{-1} \quad \text{where} \quad \begin{cases} \mathbf{R}_{az} = E[\mathbf{a}(i)\mathbf{z}^H(i)] = \mathbf{R}_{aa}\mathbf{H}_{ST}^H \\ \mathbf{R}_{zz} = E[\mathbf{z}(i)\mathbf{z}^H(i)] = \mathbf{H}_{ST}\mathbf{R}_{aa}\mathbf{H}_{ST}^H + \mathbf{R}_{n_{ST}n_{ST}} \\ \mathbf{R}_{aa} = E[\mathbf{a}(i)\mathbf{a}^H(i)] \\ \mathbf{R}_{n_{ST}n_{ST}} = E[\mathbf{n}_{ST}(i)\mathbf{n}_{ST}^H(i)] \end{cases} \quad (3.40)$$

where  $E[\cdot]$  is the stochastic mean and  $(^H)$  the matrix transpose and conjugate. Thus, the LD code MMSE receiver depends on the first moment  $\mathbf{R}_{aa}$  of the second order statistic of the symbols transmitted to the UE because  $\mathbf{R}_{az} = \mathbf{R}_{aa}\mathbf{H}_{ST}^H$ . Assuming that  $\mathbf{n}(i)$  and  $\mathbf{n}(j)$  are independent for  $j \neq i$ , the UE receiver depends as follows on the first moment of the additive noise according to (3.39) (3.40) :

$$\mathbf{R}_{n_{ST}} = \begin{bmatrix} \mathbf{R}_m^{(\zeta_1)} & \mathbf{0} & \mathbf{0} \\ \mathbf{0} & \ddots & \mathbf{0} \\ \mathbf{0} & \mathbf{0} & \mathbf{R}_m^{(\zeta_K)} \end{bmatrix} \quad \text{with} \quad \mathbf{R}_m = E[\mathbf{n}(i)\mathbf{n}^H(i)] \quad (3.41)$$

In presence of interference (or noise) such that  $\mathbf{n}(j)$  and  $\mathbf{n}(i)$  are statistically dependent, the covariance matrix  $\mathbf{R}_{n_{ST}}$  depends also on the second moments  $\mathbf{C}_{nn}(i-j) = E[\mathbf{n}(i)\mathbf{n}^T(j)]$  and first moment  $\mathbf{R}_{nn}(i-j) = E[\mathbf{n}(i)\mathbf{n}^H(j)]$ . The noise is said to be non-circular when the second moments  $\mathbf{C}_{nn}(i-j)$  are non-null. The noise can be non-circular in presence of non-circular interferences when the symbol rate is different from that of the user. Real constellations such as PAM or BPSK, or constant modulus modulations such as CPM are non-circular signals. For example the GMSK of the GSM radio-cellular networks is a particular case of non-circular signal.

The purpose is now to analyse the optimality of a given LD code as in [57]. According to (3.40) and some calculations, the matrix  $\mathbf{W}_{ST}$  of the MMSE UE receiver can be rewritten as

$$\mathbf{W}_{ST} = (\mathbf{I} + \mathbf{R}_{aa}\mathbf{H}_{ST}^H\mathbf{R}_{m_{ST}}^{-1}\mathbf{H}_{ST})^{-1} \mathbf{R}_{aa}\mathbf{H}_{ST}^H\mathbf{R}_{m_{ST}}^{-1} \quad (3.42)$$

Without interference, the covariance matrix  $\mathbf{R}_{n_{ST}}$  verifies  $\mathbf{R}_{n_{ST}} = \sigma^2\mathbf{I}$ . In this context with i.i.d symbols, the matrix  $\mathbf{W}_{ST}$  becomes

$$\mathbf{W}_{ST} = (\sigma^2\mathbf{I} + \mathbf{H}_{ST}^H\mathbf{H}_{ST})^{-1} \mathbf{H}_{ST}^H \quad (3.43)$$

because  $\mathbf{R}_{aa} = \mathbf{I}$ . According to (3.38), the Alamouti LD Code verifies

$$\mathbf{H}_{ST}^H\mathbf{H}_{ST} = \text{trace}(\mathbf{H}^H\mathbf{H})\mathbf{I} \quad (3.44)$$

And finally the matrix  $\mathbf{W}_{ST}$  of the MMSE UE receiver, is then

$$\mathbf{W}_{ST-opt} = \frac{1}{\sigma^2 + \text{trace}(\mathbf{H}^H\mathbf{H})} \mathbf{H}_{ST}^H \quad (3.45)$$

Without interference, the MMSE UE receiver with Alamouti LD code is equivalent to a SIMO transmission for the following channel vector

$$\mathbf{h}_{AL} = \sqrt{\frac{\text{trace}(\mathbf{H}^H \mathbf{H})}{\mathbf{h}^H \mathbf{h}}} \mathbf{h} \quad (3.46)$$

where  $\mathbf{h}$  is the channel vector of a conventional SIMO transmission where

$$\mathbf{y}_{SIMO}(i) = \mathbf{h} a_i + \mathbf{n}(i) \quad \text{where} \quad \begin{cases} E[|a_i|^2] = 1 \\ \mathbf{R}_{nn} = \sigma^2 \mathbf{I} \\ E[\mathbf{h}^H \mathbf{h}] = \gamma \times N_r \end{cases} \quad (3.47)$$

where  $\gamma$  is the power of the transmitted signal and  $a_i$  is the  $i$ -th transmitted symbol. According to (3.45)(3.47)-, the optimal MIMO scheme with the channel matrix  $\mathbf{H}$  is equivalent to the following SIMO scheme where

$$\mathbf{y}_{SIMO}^{Opt}(i) = \sqrt{\frac{\text{trace}(\mathbf{H}^H \mathbf{H})}{\mathbf{h}_i^H \mathbf{h}_i}} \mathbf{h}_i a_i + \mathbf{n}(i) \quad \text{where} \quad \begin{cases} E[|a_i|^2] = 1 \\ \mathbf{R}_{nn} = \sigma^2 \mathbf{I} \\ E[\text{trace}(\mathbf{H}^H \mathbf{H})] = \gamma \times N_r \end{cases} \quad (3.48)$$

where  $\mathbf{h}_i$  is the  $i$ -th column of the matrix  $\mathbf{H}$ . The comparison of the SIMO scheme of (3.46)-(3.47) and the MIMO scheme is shown in simulations in order to evaluate the optimality of a particular LD Code. According to (3.48), the optimal Rayleigh MIMO scheme is equivalent to a Gaussian SISO scheme when the channel matrix  $\mathbf{H}$  statistic is gaussian, and the number of transmit antennas  $N_e$  is large. Indeed

$$\frac{\text{trace}(\mathbf{H}^H \mathbf{H})}{E[\mathbf{h}_i^H \mathbf{h}_i]} \xrightarrow{N_e \rightarrow +\infty} \mathcal{N}(N_e, 1/\sqrt{N_e}) \quad (3.49)$$

where  $\mathcal{N}(x_{mean}, \sigma_x)$  is the Gaussian distribution where  $x_{mean}$  and  $\sigma_x$  are the mean and standard deviation respectively.

Let us note that in presence of Alamouti Code where  $\mathbf{H}_{ST}^H \mathbf{R}_{nn_{ST}}^{-1} \mathbf{H}_{ST} = \text{trace}(\mathbf{H}^H \mathbf{R}_{nn}^{-1} \mathbf{H}) \mathbf{I}$  and i.i.d user symbols with  $\mathbf{R}_{aa} = \mathbf{I}$ , the matrix  $\mathbf{W}_{ST}$  of the MMSE UE receiver becomes

$$\mathbf{W}_{ST-Al} = \frac{1}{1 + \text{trace}(\mathbf{H}^H \mathbf{R}_{nn}^{-1} \mathbf{H})} \mathbf{H}_{ST}^H \mathbf{R}_{nn_{ST}}^{-1} \quad (3.50)$$

According to (3.37), the symbols vector  $\mathbf{a}(i)$  can be estimated as following with the optimal Alamouti Code

$$\hat{\mathbf{a}}(i) = \frac{\sum_{k=1}^K \mathbf{Z}_k^T \mathbf{H}^{(\zeta_k)} \mathbf{R}_{nn}^{-1} \mathbf{y}^{(\zeta_k)} (Ki + k - 1)}{1 + \text{trace}(\mathbf{H}^H \mathbf{R}_{nn}^{-1} \mathbf{H})} \quad (3.51)$$

Thus, the MIMO receiver complexity can be reduced drastically and can take into account the presence of interferences. This receiver needs the estimation of the channel matrix  $\mathbf{H}$  and the covariance matrix  $\mathbf{R}_{nn}$  of the additive noise.

### 3.2.1.3 WL MMSE UE receiver with LD MIMO Coding

The MMSE UE receiver with LD MIMO code exploits in part the circular or non-circular properties of the additive noise and interference with the statistical moments  $\mathbf{R}_{nn}$  and  $\mathbf{C}_m(i-j)$  for  $i \neq j$

However, it neither exploits the non-circularity of the transmitted symbols with the second moment  $\mathbf{C}_{aa} = E[\mathbf{a}(i)\mathbf{a}^T(i)]$  nor exploits the powerful second moment  $\mathbf{C}_m = \mathbf{C}_m(0)$  of the noise.

The purpose of the WL MMSE receiver is to exploit an additional diversity due to the second moment of the second order statistics ( $\mathbf{C}_{aa}$  and  $\mathbf{C}_{nn}$ ) of the user and noise (or interference) respectively. The LD code WL MMSE receiver is then based on the following WL observation

$$\mathbf{z}_{WL}(i) = \begin{bmatrix} \mathbf{z}(i) \\ \mathbf{z}^*(i) \end{bmatrix} = \mathbf{H}_{WL} \mathbf{a}_{WL}(i) + \mathbf{n}_{WL}(i) \quad \text{where } \mathbf{a}_{WL}(i) = \begin{bmatrix} \Re(\mathbf{a}(i)) \\ \vdots \\ \Im(\mathbf{a}(i)) \end{bmatrix} \quad \text{and } \mathbf{n}_{WL}(i) = \begin{bmatrix} \mathbf{n}_{ST}(i) \\ \mathbf{n}_{ST}^*(i) \end{bmatrix} \quad (3.52)$$

where  $\Re(\cdot)$  and  $\Im(\cdot)$  are the real and imaginary part. According to (3.39), the algebraic structure of the WL Channel matrix is

$$\mathbf{H}_{WL} = \begin{bmatrix} \mathbf{H}_{ST} & j\mathbf{H}_{ST} \\ \mathbf{H}_{ST}^* & -j\mathbf{H}_{ST}^* \end{bmatrix} \quad (3.53)$$

The purpose of the LD code WL MMSE receiver is to jointly estimate the real and imaginary part of the symbols vector  $\mathbf{a}(i)$  with the following spatial filtering where

$$\hat{\mathbf{a}}_{WL}(i) = [\hat{\mathbf{a}}_I^T(i) \hat{\mathbf{a}}_Q^T(i)]^T = \mathbf{W}_{WL} \mathbf{z}_{WL}(i) \quad \text{and} \quad \hat{\mathbf{a}}(i) = \hat{\mathbf{a}}_I(i) + j\hat{\mathbf{a}}_Q(i) \quad (3.54)$$

In presence of interference the noise  $\mathbf{n}(i)$  cannot be assumed to be spatially and temporally white and circular. Thus, the covariance matrix of  $\mathbf{n}_{WL}(i)$  is not proportional to identity. In this context, the matrix  $\mathbf{W}_{WL}$  is estimated with respect to the minimization of the min square error  $\mathcal{E} = \|\mathbf{a}_{WL}(i) - \mathbf{W}_{WL} \mathbf{z}_{WL}(i)\|$ . The result is

$$\mathbf{W}_{WL} = \mathbf{R}_{az_{WL}} \mathbf{R}_{zz_{WL}}^{-1} \quad \text{where} \quad \begin{cases} \mathbf{R}_{az_{WL}} = E[\mathbf{a}_{WL}(i) \mathbf{z}_{WL}^H(i)] = \mathbf{R}_{aa_{WL}} \mathbf{H}_{WL}^H \\ \mathbf{R}_{zz_{WL}} = E[\mathbf{z}_{WL}(i) \mathbf{z}_{WL}^H(i)] = \mathbf{H}_{WL} \mathbf{R}_{aa_{WL}} \mathbf{H}_{WL}^H + \mathbf{R}_{nn_{WL}} \\ \mathbf{R}_{aa_{WL}} = E[\mathbf{a}_{WL}(i) \mathbf{a}_{WL}^H(i)] \\ \mathbf{R}_{nn_{WL}} = E[\mathbf{n}_{WL}(i) \mathbf{n}_{WL}^H(i)] \end{cases} \quad (3.55)$$

where the following WL covariance matrix of the UE symbols is depending on the both moments  $\mathbf{R}_{aa} = E[\mathbf{a}(i)\mathbf{a}^H(i)]$  and  $\mathbf{C}_{aa} = E[\mathbf{a}(i)\mathbf{a}^T(i)]$

$$\mathbf{R}_{aa_{WL}} = \frac{1}{2} \begin{bmatrix} \Re(\mathbf{R}_{aa}) + \Im(\mathbf{C}_{aa}) & \Im(\mathbf{C}_{aa}) \\ \Im(\mathbf{C}_{aa}) & \Re(\mathbf{R}_{aa}) - \Im(\mathbf{C}_{aa}) \end{bmatrix} \quad (3.56)$$

Assuming that  $\mathbf{n}(i)$  and  $\mathbf{n}(j)$  are independents for  $j \neq i$ , the noise WL covariance matrix is depending as following on the both moments  $\mathbf{R}_m = E[\mathbf{n}(i)\mathbf{n}^H(i)]$  and  $\mathbf{C}_m = E[\mathbf{n}(i)\mathbf{n}^T(i)]$

$$\mathbf{R}^{m_{WL}} = \begin{bmatrix} \mathbf{R}^{m_{ST}} & \mathbf{C}^{m_{ST}} \\ \mathbf{C}^{m_{ST}H} & \mathbf{R}^{m_{ST}*} \end{bmatrix} \text{ with } \begin{cases} \mathbf{C}^{m_{ST}} = \begin{bmatrix} \mathbf{C}^{m_{ST}(\zeta_1)} & \mathbf{0} & \mathbf{0} \\ \mathbf{0} & \ddots & \mathbf{0} \\ \mathbf{0} & \mathbf{0} & \mathbf{C}^{m_{ST}(\zeta_k)} \end{bmatrix} \\ \mathbf{C}^{m_{ST}} = E[\mathbf{n}(i)\mathbf{n}^T(i)] \end{cases} \quad (3.57)$$

According to (3.55), the matrix  $\mathbf{W}_{WL}$  of the WL MMSE UE receiver can be rewritten as

$$\mathbf{W}_{WL} = \left( \mathbf{I} + \mathbf{R}^{aa_{WL}} \mathbf{H}_{WL}^H \mathbf{R}^{m_{WL}}^{-1} \mathbf{H}_{WL} \right)^{-1} \mathbf{R}^{aa_{WL}} \mathbf{H}_{WL}^H \mathbf{R}^{m_{WL}}^{-1} \quad (3.58)$$

The expression of the WL filter  $\mathbf{W}_{WL}$  shows that the receiver take into account the presence of interference and also the possible non-circularity of both user, noise and interference. Thus, the WL receiver exploits the diversity associated to the potential non-circularity of signals. This potential new diversity is important for the performance improvements. The circularity properties of symbols depend on the constellations (ASK, QAM, O-QAM, etc ...). One of the aims of this task is to remove interference even in the case where the UE receiver is composed with a single antenna.

The purpose is now to establish the optimal WL MIMO LD Codes condition in presence of circular noise without interference. In this context, the covariance matrix  $\mathbf{R}^{m_{WL}}$  verifies  $\mathbf{R}^{m_{WL}} = \sigma^2 \mathbf{I}$  and  $\mathbf{W}_{WL}$  becomes

$$\mathbf{W}_{WL} = \left( \sigma^2 \times \mathbf{I} + \mathbf{R}^{aa_{WL}} \mathbf{H}_{WL}^H \mathbf{H}_{WL} \right)^{-1} \mathbf{H}_{WL}^H \text{ with } \begin{cases} \mathbf{H}_{WL}^H \mathbf{H}_{WL} = 2 \begin{bmatrix} \mathbf{H}_R & -j\mathbf{H}_I \\ j\mathbf{H}_I & \mathbf{H}_R \end{bmatrix} \\ \mathbf{H}_R = \Re(\mathbf{H}_{ST}^H \mathbf{H}_{ST}) \\ \mathbf{H}_I = \Im(\mathbf{H}_{ST}^H \mathbf{H}_{ST}) \end{cases} \quad (3.59)$$

according to (3.53). The optimality is given when  $\mathbf{R}^{aa_{WL}} \mathbf{H}_{WL}^H \mathbf{H}_{WL}$  is proportional to the identity matrix. It is thus depending on the statistical circularity of the UE symbols and the LD MIMO Codes parameters ( $\mathbf{z}_k, \zeta_k$ ) according to (3.38) (3.39). In addition according to (3.52)- (3.53)

$$\mathbf{H}_{WL}^H \mathbf{z}_{WL}(i) = \begin{bmatrix} \Re(\mathbf{H}_{ST}^H \mathbf{z}(i)) \\ \Im(\mathbf{H}_{ST}^H \mathbf{z}(i)) \end{bmatrix} \quad (3.60)$$

### Case of i.i.d and circular UE Symbols

In this context the complex symbols are such that  $\mathbf{R}^{aa} = \mathbf{I}$  and  $\mathbf{C}^{aa} = \mathbf{0}$ . According to (3.56), the WL-UE covariance matrix is  $\mathbf{R}^{aa_{WL}} = \mathbf{I}/2$  and the matrix  $\mathbf{W}_{ST}$  of the WL MMSE UE receiver becomes

$$\mathbf{W}_{WL} = \left( \sigma^2 \times \mathbf{I} + \mathbf{H}_{WL}^H \mathbf{H}_{WL} / 2 \right)^{-1} \mathbf{H}_{WL}^H \quad (3.61)$$

Thus, the WL MMSE receiver is optimal, if and only if the matrix  $\mathbf{H}_R = \Re(\mathbf{H}_{ST}^H \mathbf{H}_{ST})$  is proportional to the identity and  $\mathbf{H}_I = \Im(\mathbf{H}_{ST}^H \mathbf{H}_{ST})$  is null according to (3.63). This condition is equivalent to the one (see (3.44)) of MMSE receiver with LD Codes. Assuming that the optimality is verified, the filter becomes

$$\mathbf{W}_{WL-opt} = \frac{1}{\sigma^2 + \text{trace}(\mathbf{H}^H \mathbf{H})} \mathbf{H}_{WL}^H \quad (3.62)$$



because  $\mathbf{H}_{ST}^H \mathbf{H}_{ST} = \text{trace}(\mathbf{H}^H \mathbf{H}) \mathbf{I}$ . According to (3.54),(3.60)(3.62), the optimal receiver is given by

$$\hat{\mathbf{a}}_{WL}(i) = \begin{bmatrix} \Re(\hat{\mathbf{a}}(i)) \\ \Im(\hat{\mathbf{a}}(i)) \end{bmatrix} = \mathbf{W}_{WL-opt}^H \mathbf{z}_{WL}(i) = \begin{bmatrix} \Re(\mathbf{W}_{ST-opt}^H \mathbf{z}(i)) \\ \Im(\mathbf{W}_{ST-opt}^H \mathbf{z}(i)) \end{bmatrix} \quad \text{with } \mathbf{W}_{ST-opt} = \frac{\mathbf{H}_{ST}^H}{\sigma^2 + \text{trace}(\mathbf{H}^H \mathbf{H})} \quad (3.63)$$

where  $\mathbf{W}_{ST-opt}$  is according to (3.45) the matrix of the MMSE receiver with optimal LD Codes. Thus, the WL MMSE receiver is equivalent to the MMSE receiver for the optimal LD Code case with i.i.d circular UE symbols without interference. This is the case of the Alamouti Code where the performance of the MMSE receiver and the WL one are necessary identical without interference.

### Case of i.i.d and real UE Symbols

In this context the symbols are associated to ASK constellations such as BPSK where  $\mathbf{R}_{aa} = \mathbf{C}_{aa} = \mathbf{I}$ . According to (3.56), the WL-UE covariance matrix is

$$\mathbf{R}_{aa_{WL}} = \begin{bmatrix} \mathbf{I} & \mathbf{0} \\ \mathbf{0} & \mathbf{0} \end{bmatrix} \quad (3.64)$$

According to (3.45), the WL MMSE gives

$$\hat{\mathbf{a}}_{WL}(i) = \begin{bmatrix} \Re(\hat{\mathbf{a}}(i)) \\ \Im(\hat{\mathbf{a}}(i)) \end{bmatrix} = \mathbf{W}_{WL} \mathbf{z}_{WL}(i) = \begin{bmatrix} (\sigma^2 \times \mathbf{I} + 2\Re(\mathbf{H}_{ST}^H \mathbf{H}_{ST}))^{-1} \Re(\mathbf{H}_{ST}^H \mathbf{z}(i)) \\ \mathbf{0} \end{bmatrix} \quad (3.65)$$

such that only the real part of the symbol vector  $\mathbf{a}(i)$  can be estimated with

$$\Re(\hat{\mathbf{a}}(i)) = (\sigma^2 \times \mathbf{I} + 2\Re(\mathbf{H}_{ST}^H \mathbf{H}_{ST}))^{-1} \Re(\mathbf{H}_{ST}^H \mathbf{z}(i))$$

such that only the real part of the symbol vector  $\mathbf{a}(i)$  can be estimated with

$$\Re(\hat{\mathbf{a}}(i)) = (\sigma^2 \times \mathbf{I} + 2\Re(\mathbf{H}_{ST}^H \mathbf{H}_{ST}))^{-1} \Re(\mathbf{H}_{ST}^H \mathbf{z}(i)) \quad (3.66)$$

An LD Code is then optimal for WL MMSE receiver if  $\Re(\mathbf{H}_{ST}^H \mathbf{H}_{ST})$  is proportional to the identity in the case of real UE symbols. This condition is verified for Alamouti Code. In addition, the condition is also true for the double Alamouti of Figure 33 that is not optimal for the MMSE receiver.

MMSE receiver.

$$\mathbf{S}_{Double-Al}(\mathbf{a}) = \begin{pmatrix} \mathbf{S}_{Al}(\mathbf{a}_{12}) & -\mathbf{S}_{Al}(\mathbf{a}_{34})^* \\ \mathbf{S}_{Al}(\mathbf{a}_{34}) & \mathbf{S}_{Al}(\mathbf{a}_{12})^* \end{pmatrix} \quad \text{with } \mathbf{a} = \begin{bmatrix} \mathbf{a}_{12} \\ \mathbf{a}_{34} \end{bmatrix} \quad \text{and } \mathbf{a}_{ij} = \begin{bmatrix} a_i \\ a_j \end{bmatrix}$$

Figure 33 – Double Alamouti LD MIMO Code scheme with  $N_e=K=4$  according to Figure 6

### Synthesis

The optimality of the LD Codes for the WL MMSE receiver depends on the statistical properties of the UE symbols constellations. Indeed, the potential non-circularity of each constellation are associated to the moments  $\mathbf{R}_{aa} = E[\mathbf{a}(i)\mathbf{a}^H(i)]$  and  $\mathbf{C}_{aa} = E[\mathbf{a}(i)\mathbf{a}^T(i)]$ . The WL MMSE receiver gives better performance than the MMSE one for constellation where the second moments

$\mathbf{C}_{aa} = E[\mathbf{a}(i)\mathbf{a}^T(i)]$  for the user or  $\mathbf{C}_m = E[\mathbf{n}(i)\mathbf{n}^T(i)]$  for the noise are not null. The real constellations verifies this condition whereas the complex constellations such as QAM does not check  $\mathbf{C}_{aa} \neq \mathbf{0}$ .

This is the reason why, the O-QAM are considered in simulation for this task. For a given stream of symbols  $\{a_i\}$  of time duration T, the imaginary part is delayed of T/2 according to Figure 34. The LD code are apply on the following symbol vector

$$\mathbf{a}(i) = \begin{bmatrix} a_i \\ \Re(a_{i+1}) + j\Im(a_i) \\ a_{i+1} \\ \Re(a_{i+2}) + j\Im(a_{i+1}) \\ \vdots \end{bmatrix} \quad (3.67)$$

where the UE symbols can be the complex QAM of the LTE-A. For O-QAM the matrices  $\mathbf{R}_{aa}$  and  $\mathbf{C}_{aa}$  are as following for  $N_e = 4$

$$\mathbf{R}_{aa} = \begin{bmatrix} 1 & 0.5 & 0 & 0 \\ 0.5 & 1 & 0.5 & 0 \\ 0 & 0.5 & 1 & 0.5 \\ 0 & 0 & 0.5 & 1 \end{bmatrix} \quad \text{and} \quad \mathbf{C}_{aa} = \begin{bmatrix} 0 & 0.5 & 0 & 0 \\ 0.5 & 0 & -0.5 & 0 \\ 0 & -0.5 & 0 & 0.5 \\ 0 & 0 & 0.5 & 0 \end{bmatrix} \quad (3.68)$$

and for  $N_e = 2$

$$\mathbf{R}_{aa} = \begin{bmatrix} 1 & 0.5 \\ 0.5 & 1 \end{bmatrix} \quad \text{and} \quad \mathbf{C}_{aa} = \begin{bmatrix} 0 & 0.5 \\ 0.5 & 0 \end{bmatrix} \quad (3.69)$$

where  $\mathbf{C}_{aa}$  is not null for complex symbols  $a_i$  in presence of a temporal shift of the imaginary part.

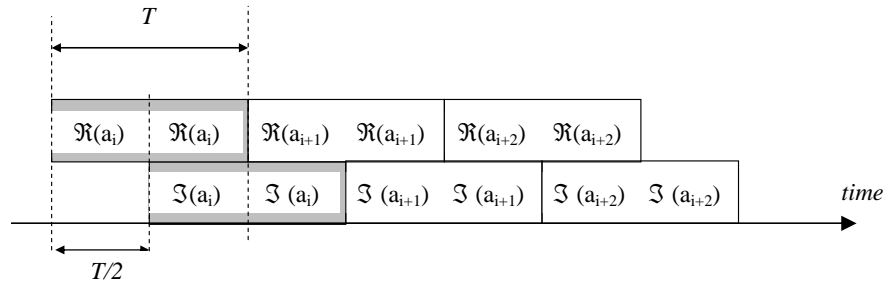


Figure 34 – Offset of the imaginary part of a symbol constellation such as O-QAM

### 3.2.1.4 Simulations

The simulations are given with BSPK, QPSK and O-QPSK. The channels distribution is Rayleigh with  $E[\mathbf{H}^H \mathbf{H}] = N_r \rho \sigma^2$ ,  $N_r$  is the number of user antenna,  $\rho$  is the linear signal noise ratio and  $\sigma^2 = \text{trace}(E[\mathbf{n}_0(t)\mathbf{n}_0^H(t)]) / N_r$  is the noise level without interference with  $\mathbf{n}(t) = \mathbf{n}_0(t)$ . In presence of interference the noise verifies

$$\mathbf{n}(i) = \mathbf{h}_n b_i + \mathbf{n}_0(i) \quad (3.70)$$

where  $\{b_i\}$  is a stream of i.i.d symbols,  $\mathbf{h}_n$  is the interference channel vector with Rayleigh distribution,  $E[\mathbf{h}_n^H \mathbf{h}_n] = N_r \rho_n \sigma^2$  and  $\rho_n$  is the interference signal noise ratio.

In addition, the transmission interfaces call

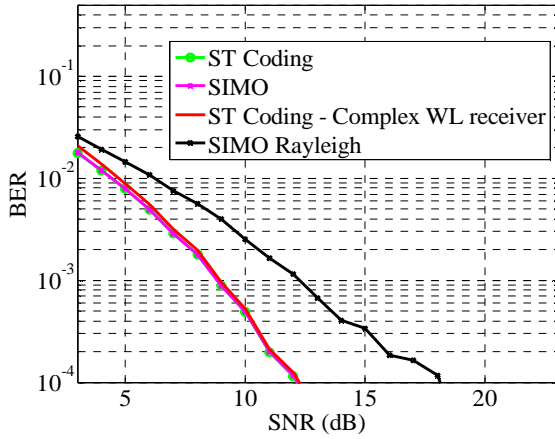
- **SIMO** corresponds to a SIMO transmission of channel vector  $\mathbf{h}_{SIMO} = \sqrt{\frac{\text{trace}(\mathbf{H}^H \mathbf{H})}{N_r}} \mathbf{h}_i$  where  $\mathbf{H}$  is the previous Rayleigh distribution and  $\mathbf{h}_i$  is the  $i$ -th column of  $\mathbf{H}$ . It corresponds to the optimal MIMO LD Codes scheme without interference and i.i.d symbols. When the number of transmission antennas in  $\mathbf{H}$  is infinite, the norm of the SIMO channel is a constant such that  $\mathbf{h}_{SIMO}^H \mathbf{h}_{SIMO} = N_r \Rightarrow$  This is the AWGN case.
- **SIMO Rayleigh**. The distribution of channels  $\mathbf{h}$  is Rayleigh with  $E[\mathbf{h}^H \mathbf{h}] = N_r \rho \sigma^2$
- **ST Coding**. The MMSE receiver  $\hat{\mathbf{a}}(i) = \mathbf{W}_{ST} \mathbf{z}(i)$  is simulated according to (3.40).
- **ST Coding – Complex WL** : The WL-MMSE receiver is simulated according to (3.52)(3.54). The LD Codes of interest are either Alamouti (see Figure 6 of Section 2.2.2) or double-Alamouti (see Figure 33) for which performance with different cases of transmission antennas number are analysed. Simulations are conducted with 1000 realizations of channel matrices. For each scenario the Binary Error Rate (BER) is represented with respect to the UE Signal Noise Ratio (SNR) in decibel with  $SNR = 10 \log_{10}(\rho)$ .

The results of Figure 35 to Figure 37 correspond to the scenarios without interference and UE receiver with  $N_r=2$  antennas for multiple constellations (BPSK, QPSK and O-QPSK). The MIMO Alamouti and double-Alamouti scheme performance are represented on the left and right sub-figures respectively. According to section 3.2.1.2, an LD Code is optimal when the BER curves of 'SIMO' (Magenta) and 'ST Coding' are close. Thus, the results show that the Alamouti Code is optimal for 'ST Coding' independently from the constellation. However, the Double Alamouti is not optimal more particularly for BPSK constellation.

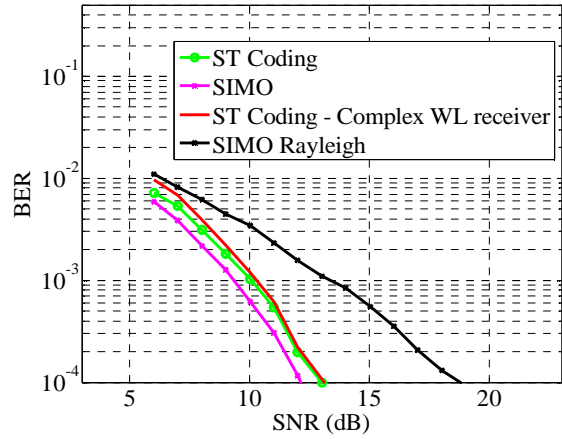
The difference between the black curves of 'SIMO Rayleigh' shows the gap of performance of the LD Codes MIMO scheme in front of the SIMO scheme transmission. Indeed, the transmission with multiple antennas has the advantage to improve the interface in term of loss of SNR due to the fading of the propagation channel.

The green curves of 'ST Coding' and red curves of 'ST Coding – Complex WL' compare the conventional LD Codes MIMO receiver to the WL receiver. The performance of the two receivers are identical for Alamouti Code with BPSK and QPSK constellation. In the case of O-QPSK, the WL receiver gives the best performance. The WL receiver with Double Alamouti Codes improves the performances only for O-QPSK. More generally, the WL receiver gives better performance than 'ST-Coding' receiver in presence of O-QPSK and in presence of QPSK there is no difference. Thus, the downlink LTE interface can be improved by transforming on the one hand the QAM into O-QAM and on the other hand adopt a WL receiver with a LD Code MIMO scheme.

Figure 38 compares Alamouti to Double Alamouti for O-QPSK. Performance with Alamouti and Double Alamouti are equivalent for the 'ST-Coding' receiver and the Double-Alamouti gives better performance for the WL receiver.

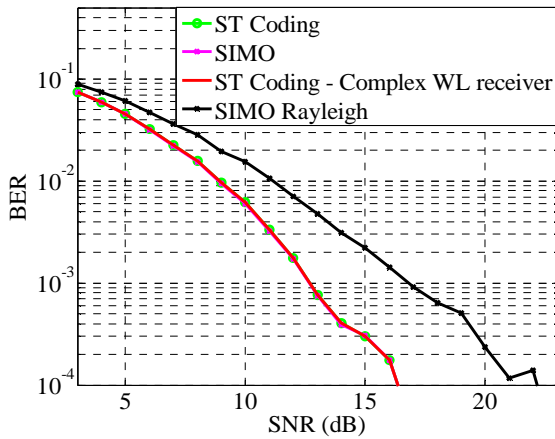


**(Alamouti)**

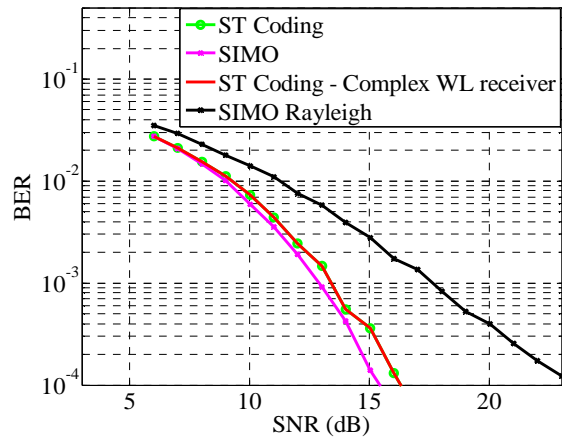


**(Double-Alamouti)**

**Figure 35 – BPSK without interference Nr=2**

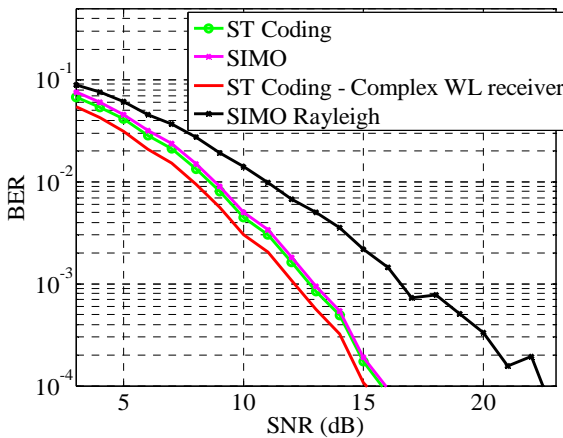


**(Alamouti)**

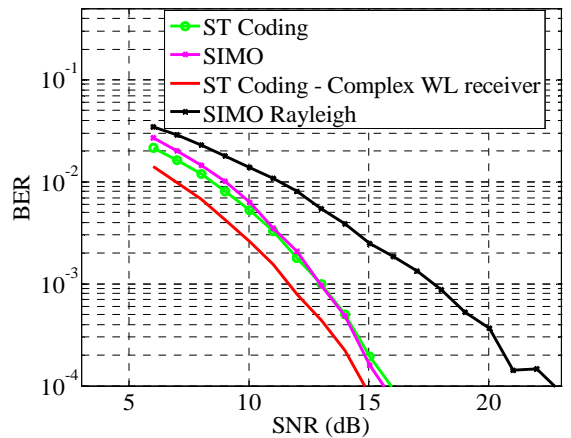


**(Double-Alamouti)**

**Figure 36 – QPSK without interference Nr=2**

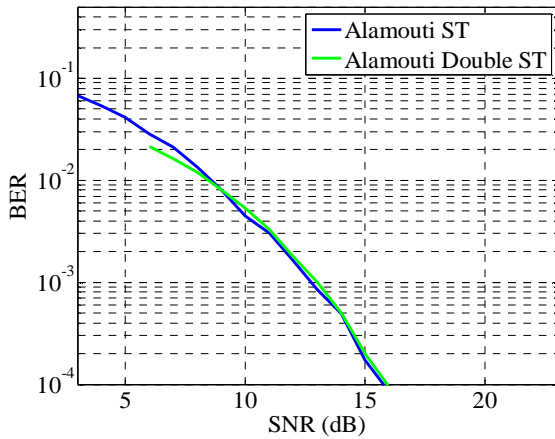


**(Alamouti)**

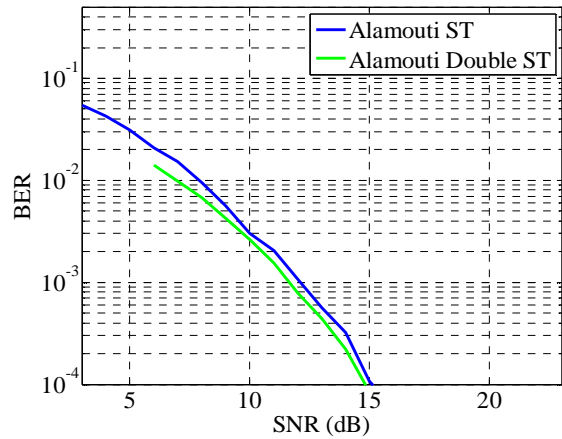


**(Double-Alamouti)**

**Figure 37 – O-QPSK without interference Nr=2**



(ST Coding)



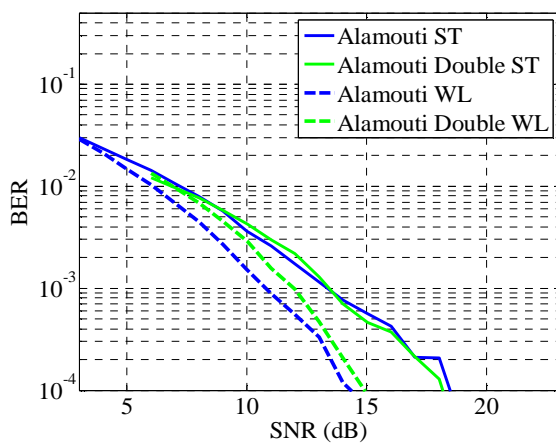
(ST Coding - Complex WL receiver)

Figure 38 – O-QPSK without interference  $N_r=2$

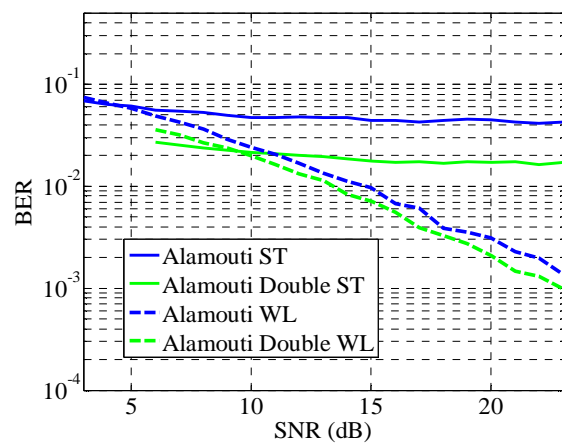
In the second part of simulations, performance are analysed in presence of interferences. In the following figures, the solid line corresponds to the 'ST Coding receiver' and dash-lines to the WL linear receiver. The results of MIMO scheme with Alamouti and Double-Alamouti are in blue green respectively.

Figure 39 to Figure 42 give the performance of different constellations in presence of BPSK interference. Results are given for  $N_r=2$  antennas and single antenna in the left and right sub-figures respectively. A receiver gives acceptable performance in presence of interferences when the BER performance improves when the SNR increases. Thus, the performance gives acceptable performance with single antenna for UE ( $N_r=1$ ) only for BPSK or O-QPSK constellations with the WL receiver. More generally, the performance with Double-Alamouti Code is better than for the Alamouti case.

With  $N_r=2$  the receivers do not fail in presence of interference. However, performance of the Double-Alamouti Codes is better than Alamouti in presence of QPSK and O-QPSK constellations for UE. More generally in presence of BPSK interference, the WL receiver gives the smaller BER. The best improvement of the WL receiver in presence of BPSK interference is for the O-QPSK constellation for UE.

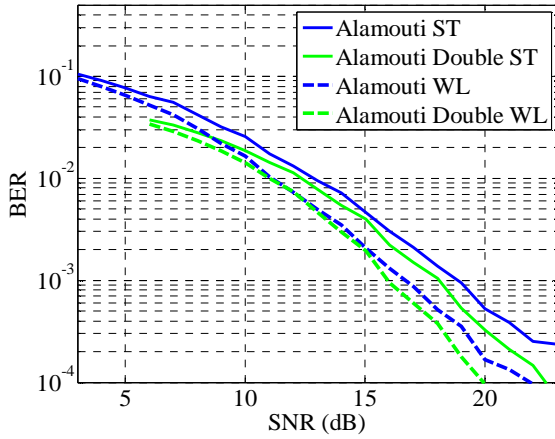


( $N_r=2$ )

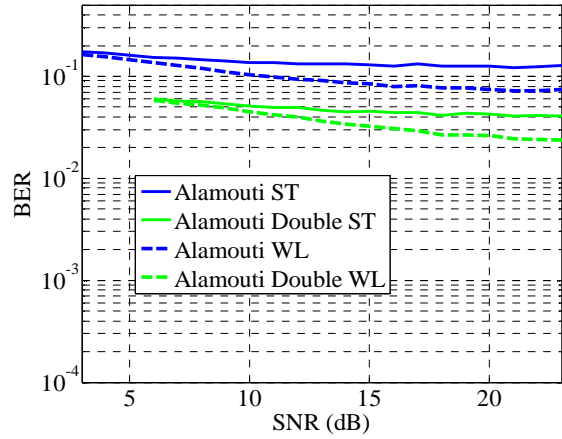


( $N_r=1$ )

Figure 39 – BPSK with BPSK interference of same power to UE

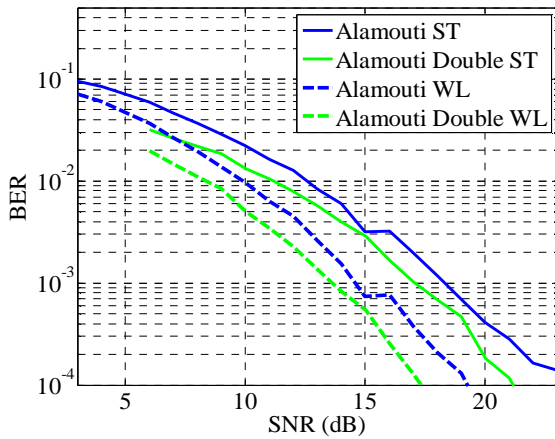


$(N_r=2)$

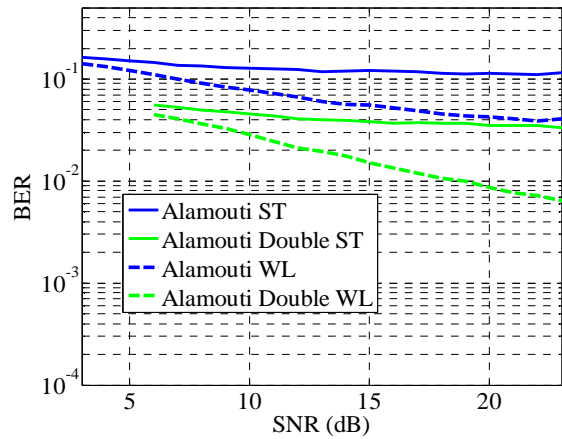


$(N_r=1)$

Figure 40 – QPSK with BPSK interference of same power to UE

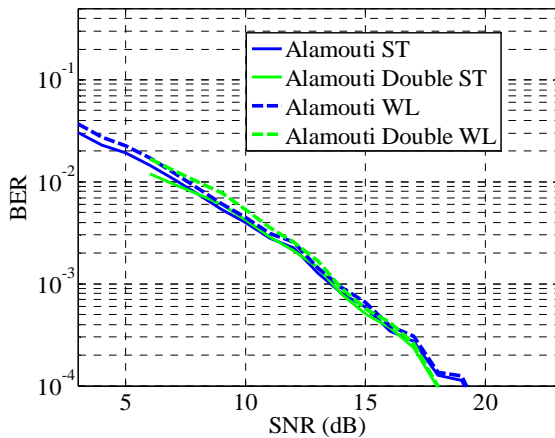


$(N_r=2)$

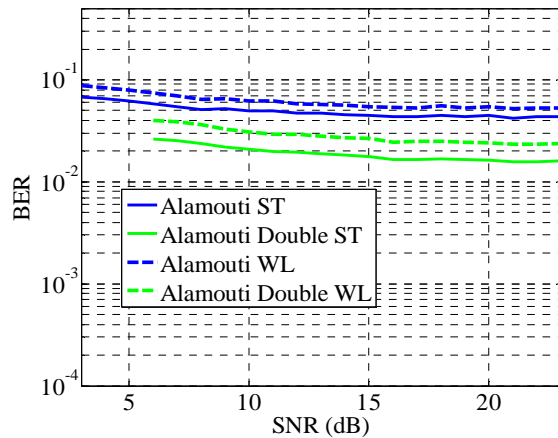


$(N_r=1)$

Figure 41 – O-QPSK with BPSK interference of same power to UE



$(N_r=2)$



$(N_r=1)$

Figure 42 – BPSK with O-QPSK interference of same power to UE

In Figure 43, the results with O-QPSK constellation for UE and interference are given for  $N_r=1$  and  $N_r=2$ . The receivers do not give acceptable performance with  $N_r=1$ . However it is not the case with  $N_r=2$  where the WL receivers and the Double-Alamouti Codes gives the best performance.

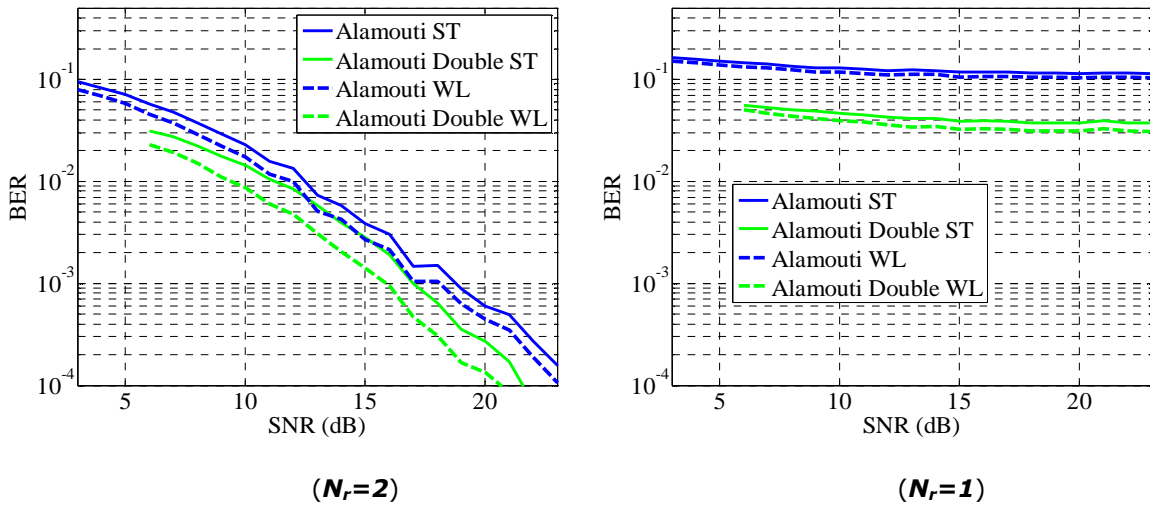


Figure 43 – O-QPSK with O-QPSK interference of same power to UE

In Figure 44, the results with QPSK constellation for interference constellation are given for  $N_r=2$  where the receivers give acceptable performance. In presence of a BPSK constellation for UE there is no difference between Alamouti and Double Alamouti LD Codes. In addition the WL receiver does not gives the best performance. However for O-QPSK constellation for UE, the WL receivers and the Double-Alamouti Codes give the best performance.

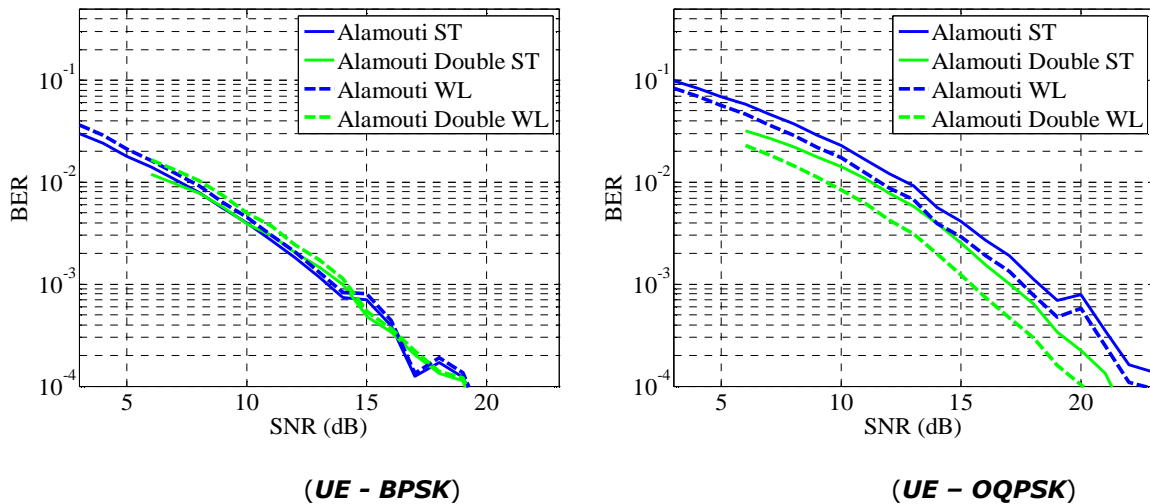


Figure 44 – UE with QPSK interference of same power and  $N_r=2$

### 3.2.1.5 Conclusions

Without interference, an LD MIMO Code scheme is optimal when it is equivalent to a SIMO scheme where the gain of the SIMO channel vector is equal to the average of the  $N_e$  MIMO transmitted channel vectors gains. An optimal MIMO scheme with an infinite number of transmitted antennas is equivalent to an AWGN SIMO transmission where the performance (BER) depends on the noise power. In addition, an optimal LD MIMO Code for the MMSE receiver is also optimal for the WL MMSE receiver. Also a non-optimal MIMO Code for MMSE receiver can be optimal for WL MMSE receiver.

In this context, the Alamouti MIMO code with  $N_e=2$  transmission antenna is optimal for MMSE receiver and WL MMSE receiver. The Alamouti-MMSE receiver is then equivalent to the WL Alamouti-MMSE one either without interference or with circular interference (QAM, ...). The WL Alamouti-MMSE improves the BER only in presence of non-circular symbols (BSPK, O-QAM (see Figure 35, etc...)) for user or interference.

When the number of transmission antennas  $N_e$  is larger than 2, the performance of LD Code (MMSE and WL MMSE) receivers improves. Without interference, the Alamouti-MMSE receiver is a little bit more performant to the MMSE receiver in presence of real or circular constellations such as QAM. Indeed, the optimal LD Code MMSE receiver does not exist in full rate and open loop context. In presence of non-circular constellation such as O-QAM, the WL MMSE receiver is more performant than the (WL or not) Alamouti MMSE receivers. In presence of interference, the (WL or not) MMSE receiver is better to the (WL or not) Alamouti-MMSE.

Whatever the interference context, the WL MMSE receiver gives better performance than the MMSE when the user or interference constellations are non-circular (BPSK, O-QAM) with a non-null second moment. In presence of one interference, the receivers needs at least  $N_r=2$  antennas. With a single antenna either the user or the interference must be non-circular.

Thus, the downlink LTE interface can be improved by on the one hand modifying the standard by replacing QAM by O-QAM modulation and in computing on the other hand a WL receiver with an LD Code MIMO scheme such as the double-Alamouti of Figure 33 with  $N_e=4$

### 3.2.2 Downlink multi-user CoMP with interference aware receivers

As explained in section 2.2.3, the work of D3.2 was extended to a DL LTE UE in CoMP between two cells, each of them serving another user on the same time-frequency resource in MU-MIMO (Figure 8). In this case, the UE receiver is impaired by two interferers (instead of just one in the study in D3.2). The three IA receivers studied in the first part of the project have been improved and adapted to this new scenario.

We recall the notations of [3]

- $N_R \in \mathbb{N}^+$  is the number of receive antennas (at the UE side),
- $N_T \in \mathbb{N}^+$  is the number of transmit antennas (at the eNB side),
- $\mathbf{H}_{i,0} \in \mathbb{C}^{N_R \times N_T}$ ,  $i \in \{1,2\}$  is the channel from eNB $i$  to UE0,
- $\mathbf{w}_{i,j} \in \mathbb{C}^{N_T \times 1}$ ,  $i \in \{1,2\}$ ,  $j \in \{0,1,2\}$  is the precoder applied at eNB $i$  for UE $j$ ,
- $x_i \in \mathbb{C}$ ,  $i \in \{0,1,2\}$  are the data intended to UE $i$ ,
- $\mathbf{y} \in \mathbb{C}^{N_R \times 1}$  is the signal received at UE0,
- $\mathbf{z} \in \mathbb{C}^{N_R \times 1}$  is AWGN with variance  $N_0$ .

The signal received at UE0 can then be written as in (3.71). Here, the interference is represented by the second sum.

$$\mathbf{y} = x_0 \sum_{i=1}^2 \mathbf{H}_{i,0} \mathbf{w}_{i,0} + \sum_{i=1}^2 \mathbf{H}_{i,0} \mathbf{w}_{i,i} x_i + \mathbf{z} \quad (3.71)$$

#### SL-MMSE

As explained in [3] section 3.2.2, SL-MMSE equalization aims at finding  $\mathbf{b} \in \mathbb{C}^{1 \times N_R}$  such as  $e = E\{\|\mathbf{b}^H \mathbf{y} - x\|^2\}$  is minimal. It has been shown in the first part of the project that the solution is given by:

$$\mathbf{b}^H = E_x \mathbf{g}_e^H \mathbf{R}_y^{-1} \quad (3.72)$$



with  $E_x$  the transmit signal energy,  $\mathbf{R}_y \in \mathbb{C}^{N_R \times N_R}$  the covariance matrix of the receive signal vector and  $\mathbf{g}_e$  the effective channel:

- $\mathbf{g}_e = \sum_{i=1}^2 \mathbf{H}_{i,0} \mathbf{w}_{i,0} \in \mathbb{C}^{N_R \times 1}$ ,
- $\mathbf{R}_y = E_x \mathbf{g}_e \mathbf{g}_e^H + \mathbf{R}_\eta$ ,
- $\mathbf{R}_\eta = E_x (\mathbf{g}_1 \mathbf{g}_1^H + \mathbf{g}_2 \mathbf{g}_2^H) + N_0 \mathbf{I}_{N_R}$ ,
- $\mathbf{g}_i = \mathbf{H}_{i,0} \mathbf{w}_{i,i} \quad i \in \{1,2\}, \in \mathbb{C}^{N_R \times 1}$ ,
- $N_0$  the noise variance,

The filtering operation of SL-MMSE implies to compute corresponding LLRs. The LLR of a bit  $c$  is the ratio of the probability that  $c = 0$  over the probability that  $c = 1$ , knowing the received filtered symbol  $\hat{x}$  and the channel. This LLR can be written:

$$LLR(b) = \log \left( \frac{P(\hat{x}|c = 0, \mathbf{H}_{1,0}, \mathbf{H}_{2,0})}{P(\hat{x}|c = 1, \mathbf{H}_{1,0}, \mathbf{H}_{2,0})} \right) \quad (3.73)$$

The probability at the numerator and at the denominator is given by:

$$P(\hat{x}|c = a, \mathbf{H}_{1,0}, \mathbf{H}_{2,0}) = \frac{\sum_{x \in \chi_a} e^{-\frac{|\hat{x} - E[\hat{x}]|^2}{2\sigma^2}}}{\sqrt{2\pi\sigma^2}}, \quad a \in \{0,1\} \quad (3.74)$$

where  $\chi_a$  is the subset of the transmit alphabet giving the value of bit  $a$  and  $\sigma^2 = E[|\hat{x} - E[\hat{x}]|^2]$ .

With SL-MMSE receiver, the filtered received signal can be written:

$$\hat{x} = \mathbf{b}^H \mathbf{g}_e x_0 + \mathbf{b}^H (\mathbf{g}_1 x_1 + \mathbf{g}_2 x_2) + \mathbf{m}^H \mathbf{z} \quad (3.75)$$

From (3.72)  $\mathbf{b}^H \mathbf{g}_e = E_x \mathbf{g}_e^H \mathbf{R}_y^{-1} \mathbf{g}_e$ . As  $\mathbf{R}_y$  is a hermitian matrix.  $\mathbf{b}^H \mathbf{g}_e$  is therefore a real scalar (but note that  $\mathbf{b}^H \mathbf{g}_1$  and  $\mathbf{b}^H \mathbf{g}_2$  are complex scalar). The first and second order moments of  $\hat{x}$  are respectively  $E[\hat{x}] = \mathbf{b}^H \mathbf{g}_e x_0 + \mathbf{b}^H (\mathbf{g}_1 x_1 + \mathbf{g}_2 x_2) = \alpha x_0 + \varphi$  and  $\sigma^2 = \mathbf{b}^H \mathbf{b} N_0$ . For the QPSK modulation shown on Figure 45, with  $r_i$  the real part of a complex  $r$ , the LLR of the least significant bit  $c_0$  is finally:

$$LLR(bc_0) = \alpha / \sigma^2 (\hat{x}_I - \varphi_I) \quad (3.76)$$

The same formula applies for the most significant bit replacing imaginary parts by real parts. When assessing the performance of the receivers, the term  $\varphi$  is ignored. This assumption is justified by the fact that the interfering symbols  $x_1$  and  $x_2$  are unknown at the receiver of interest UE0.

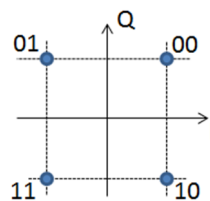


Figure 45. Considered QPSK modulation

### IA-ML

In the first part of the project, simulations showed that the reduced complexity implementation of the IA-ML (Interference Aware Max Log MAP) receiver could not reject all interference at cell edge in the presence of two interferers. In the following, the performance of this receiver with full complexity, i.e.  $O(M^3)$  with  $M$  the size of the desired and interfering constellations, is assessed.

### Serial interference cancellation receiver

Successive interference cancellation (SIC) receiver first decodes the interferers, then reconstructs the interfering received signal and finally subtracts it from the received signal. This process is shown in Figure 46 where:

- $y$  is the received signal, sum of the interfering received signals  $y_1$  and  $y_2$  and of the desired signal.
- $x_1$  and  $x_2$  are the data intended to interfering users.
- $x_0$  is the desired data.
- $\hat{x}$  stands for the estimation of  $x$ .

Note that an estimation of the channel is required for all the blocks on Figure 46.

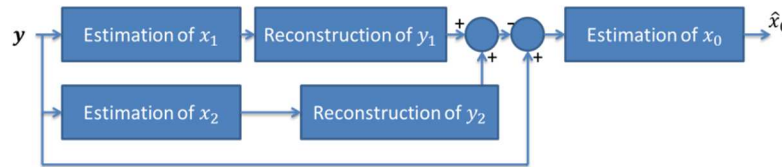


Figure 46. Serial interference cancellation receiver

In the first part of the project the estimation of the interfering signal ('Estimation' module on Figure 46) has been realized thanks to SL-MMSE receiver. In this study, the estimation of the interfering signals is realized thanks to IA-ML algorithm. The new receiver is therefore named SIC IA-ML.

The SIC IA-ML receiver is by far the most complex of the receivers studied; the reconstruction of the interfering signal indeed requires the implementation of a complete transmitter.

Simulations

The scenario for assessing the performance of these receivers is shown on Figure 8. The distance  $d$  is fixed at  $ISD/2$  (500m). By varying  $\theta$ , the robustness of the IA receivers with respect to a non perfect location of UE0 is assessed. BER of UE0 (Figure 8) is chosen as the performance indicator for the algorithms studied. UE0 is equipped with 2 receive antennas.

**enBs with two transmit antennas**

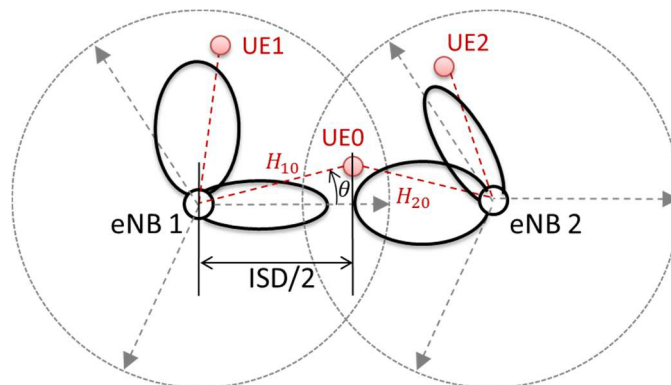


Figure 47. Scenario for D3.6.B

A precoder that maximizes the antenna gain in the direction of UE0 together with its orthogonal precoder are selected in the standard for the scheme of Figure 8 with  $\theta = 0^\circ$ , see Figure 48:  $w_{1,0}$  (resp.  $w_{1,1}$ ,  $w_{2,0}$  and  $w_{2,2}$ ) is the precoder with index 0 (resp. 1, 1 and 0).

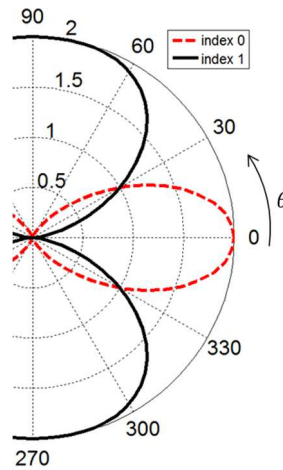


Figure 48. Diagrams of the precoders used in the scenario for  $N_T = 2$

### Results

In Figure 49 are shown the performance of the algorithms described above with only one interferer.  $N_T = 2$ . QPSK is used for all the UEs, as in all the simulations below. It is first worth noticing that if no interference rejection algorithm is implemented at the receiver a high BER floor is observed. The three algorithms are nevertheless able to reject all the interference from the interfering user, even with an imperfect location of UE0 (up to  $\theta = 15^\circ$ ). As expected, when  $\theta$  is growing the performance are getting worse. It must be noted that SIC IA-ML algorithm performs better than IA-ML algorithm for  $\theta > 30^\circ$ . This result can be intuitively deduced from Figure 48: indeed, for  $\theta > 30^\circ$  the level of the interference becomes higher than the level of the desired signal; it is therefore beneficial to decode first the interference.

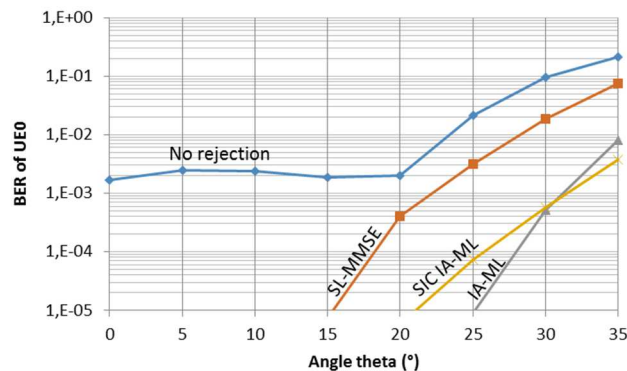


Figure 49. Performance of the receivers in the presence of one interferer.

In the following the SIC IA-ML receiver will not be studied, as its complexity is prohibitive.

Figure 50 shows the performance of the receivers in the presence of two interferers. Continuous lines are the performance of the receivers considering the second interferer (UE2) like noise. They show that the contribution of UE2 on the interference is not negligible: even with a perfect location of UE0 ( $\theta = 0^\circ$ ) the BER is not lower than  $10^{-5}$ . However, when the receivers are aware of both interferers they succeed in rejecting the interference ( $\text{BER} < 10^{-5}$ ) for UE0 location up to  $\theta = 3^\circ$  for SL-MMSE and  $\theta = 4.5^\circ$  for IA-ML.

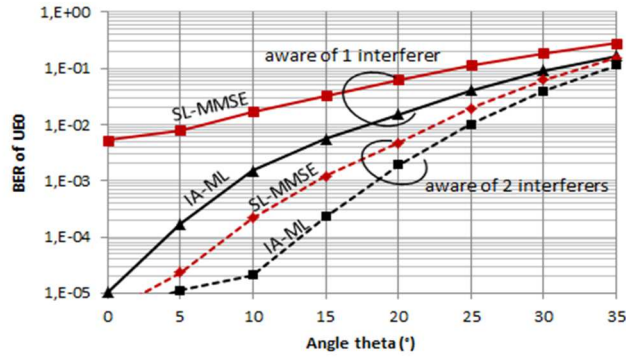


Figure 50. Performance of the receivers in the presence of two interferers.  $N_T = 2$ .

**enBs with four transmit antennas**

Figure 52 presents the performance of the receivers in the presence of two interferers, with four transmit antennas at the transmitters. The curves with two transmit antennas have been added for easier comparison. The precoders diagram are shown in Figure 51:  $w_{1,0}$  (resp.  $w_{1,1}$ ,  $w_{2,0}$  and  $w_{2,2}$ ) is the precoder with index 0 (resp. 5, 5 and 0) taken from [7]. These precoders maximize the antenna gain in the direction of targeted UE.

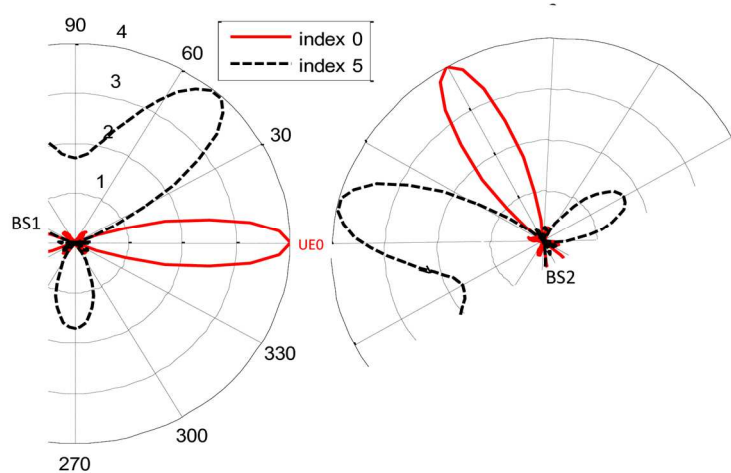


Figure 51. Diagrams of the precoders used in the scenario for  $N_T = 4$

Still taking  $BER=10^{-5}$  for interference rejection threshold, it must be noticed that performance of algorithms are better when the size of the precoder is higher (four instead of two): both algorithms are able to reject interference for  $\theta$  up to  $10^\circ$ . This result can be explained by the narrower beams when precoding with four antennas than with two antennas.

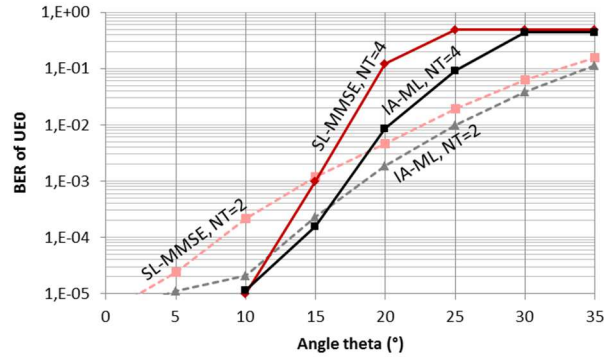


Figure 52. Performance of the receivers in the presence of two interferers.  $N_T = 4$ .

#### Hardware implementation issues

The computational complexity of SL-MMSE, including the complexity of the LLRs, and IA-ML algorithms was assessed in WP7. Both algorithms were shown to be implementable.

#### Conclusion

It was shown in this study that cooperation between cells together with MU-MIMO using precoders defined by 3GPP, is possible. The use of the precoders defined in the standard allows a low rate feedback from UEs to eNBs but their poor spatial resolution causes interferences at the receivers. Efficient interference rejection algorithms can be implemented at the receiver. Those receivers are able to reject interference from two co-scheduled UEs, even when their location in the cell is not optimal with respect to the precoders used at the eNBs.

### 3.2.3 Advanced interference mitigation in the uplink

This section focuses on the receiver optimization of users (UEs) signals in presence of interferences in LTE-A uplink. The purpose is to give new receiver alternatives solutions for high density user context and frequency selective propagation channel with processing in frequency domain.

The uplink interface LTE is represented in Figure 9 where the  $k$ -th user  $UE_k$  transmits a set of  $M$  symbols to the Base Station (or enodeB) through  $M$  adjacent frequency bins of bandwidth 15kHz. The bandwidth of one transmitted UE signal is then  $M \times 15$ kHz. The enodeB receives multiple users that share the same time-frequency Resource Block (RB) of Figure 11.

According to Figure 9, the purpose is to determine the transmitted symbols  $a^k(m, i)$  of each user ( $1 \leq k \leq K$ ) from the observation signals  $\mathbf{y}(i)$  at the output of the antennas of the Base Station (or EnodeB). The DFT (resp. iDFT) is the Digital Fourier Transform (resp. its inverse) and the FFT (resp. IFFT) is the Fourier Transform (resp. its inverse). The general scheme of the FDE MMSE Equalization is given in Figure 53. The space-time multi-users symbol vector is defined as  $\mathbf{a}_m^T(i) = [a^1(m, i) \ \dots \ a^K(m, i)]$  and  $(^T)$  denotes the transpose. The vector  $\tilde{\mathbf{a}}_m(i)$  at the output the FDE MMSE Equalizer must be close to the space-time multi-users symbol  $\mathbf{a}_m(i)$ .

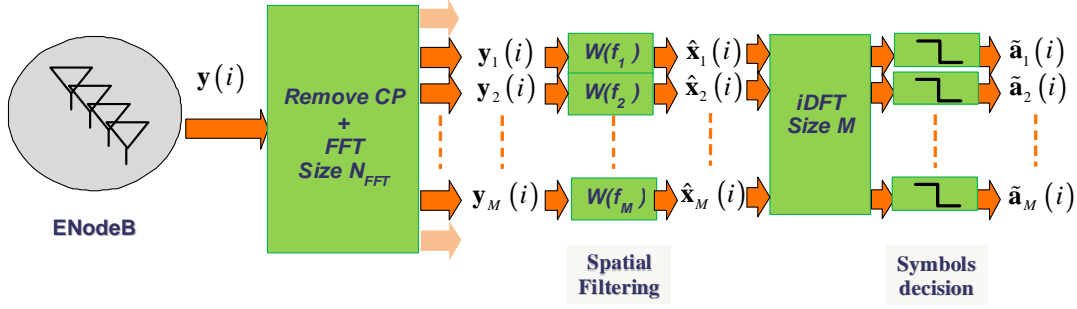


**Figure 53 - General scheme for FDE MMSE Equalization in the context of SC-FDMA users transmission**

The eNodeB receives the user transmitted symbol through a propagation channel in presence of multiple interferences. According to Figure 9 and Figure 53, the signals at the output of eNodeB antennas and  $m$ -th frequency bin are such that

$$\mathbf{y}_m(i) = \mathbf{H}(f_m)\mathbf{x}_m(i) + \mathbf{n}_m(i) \quad \text{where } \mathbf{x}_m(i) = \begin{bmatrix} x^1(m,i) \\ \vdots \\ x^K(m,i) \end{bmatrix} \quad (3.77)$$

where  $x^k(m,i)$  is the transmitted signal for the  $m$ -th frequency bin and  $k$ -th user,  $\mathbf{n}_m(i)$  is the additive noise composed by the interferences and internal receiver noise. The signal  $x^k(m,i)$  depends on the set of symbols  $\{a^k(m,i) \text{ with } 1 \leq m \leq M\}$  according to a DFT. In the context of a frequency selective propagation channel, the amplitude of the  $N_r \times K$  matrix channel  $\mathbf{H}(f_m)$  depends on the frequency bin  $f_m$ . In presence of a multi-paths channel of delay spread  $\Delta\tau = (2L+1)/B_{LTE}$  the expression of  $\mathbf{H}(f_m)$  is

$$\mathbf{H}(f_m) = \sum_{k=0}^{2L-1} \mathbf{H}_k \exp(j2\pi(f_m + \Delta f)t_k) \quad \text{where } t_k = \frac{k}{B_{LTE}} \text{ and } \Delta\tau B_{LTE} = 2L+1 \quad (3.78)$$

where  $B_{LTE}$  is the LTE transmitted bandwidth and  $\mathbf{H}_k$  is the temporal channel response for the delay  $t_k$ .

According to Figure 53 and equation (3.77) the FDE MMSE Equalization needs a spatial filter  $\mathbf{W}(f_m)$  such that

$$\mathbf{x}_m(i) = \mathbf{W}(f_m)\mathbf{y}_m(i) \quad (3.79)$$

Assuming that the noise  $\mathbf{n}_m(i)$  is spatially white, the first well known spatial filter is the conventional MMSE

$$\begin{aligned} \mathbf{W}_{MMSE-W}(f_m) &= \mathbf{H}^H(f_m) \left( \sigma(f_m)^2 \mathbf{I}_N + \mathbf{H}(f_m)\mathbf{H}^H(f_m) \right)^{-1} \\ &= \left( \sigma(f_m)^2 \mathbf{I}_K + \mathbf{H}^H(f_m)\mathbf{H}(f_m) \right)^{-1} \mathbf{H}^H(f_m) \end{aligned} \quad (3.80)$$

where  $N$  is the number of eNodeB antennas,  $K$  the number of users and  $\sigma(f_m)^2$  is the noise power. The channel matrix  $\mathbf{H}(f_m)$  and the noise power  $\sigma(f_m)^2$  must be estimated. However, in presence of interference the additive noise is not spatially white and the conventional MMSE with  $\mathbf{W}_{MMSE-W}(f_m)$  cannot cancel this interference

This is the reason why the purpose of this work is to design the spatial filter  $\mathbf{W}(f_m)$  in order to both cancel interference and equalize in the frequency domain. The approach takes into account the frequency selectivity of the channel matrices.

These adaptive filters  $\mathbf{W}(f_m)$  or the matrix  $\mathbf{H}(f_m)$  are estimated from the Demodulation Reference Signal (DMRS) represented in Figure 11. The DMRS sequences of each user sharing the same resource blocks, are orthogonal in the frequency domain. According to Figure 11, the signals  $\mathbf{y}_m(i)$  are synchronized to DMRS sequence for the time index  $i = i_{DMRS}$ .

$$\mathbf{y}_m(i_{DMRS}) = \mathbf{H}(f_m) \mathbf{d}_m + \mathbf{n}_m(i_{DMRS}) \quad (3.81)$$

where  $\mathbf{x}_m(i_{DMRS}) = \mathbf{d}_m$ . The vector  $\mathbf{d}_m$  is composed by the DMRS sequences of each user at frequency bin  $f_m$ .

Two different approaches are considered to determine the adaptive filter  $\mathbf{W}(f_m)$ :

- **The indirect approach**: The filter is built from the channel matrix  $\mathbf{H}(f_m)$  and the signal  $\mathbf{y}_m(i)$  observed at the output of antennas. The approach needs the estimation of the matrix  $\mathbf{H}(f_m)$  of equation (3.78), where  $L_0$  is the channel order depending on the delay spread.

- **The direct approach**: The filter is directly built from the signals  $\mathbf{y}_m(i_{DMRS})$  and the DMRS sequences  $\mathbf{x}_q(i_{DMRS}) = \mathbf{d}_q$  for  $1 \leq q \leq M$ . The estimation needs the following space-time modelling of  $\mathbf{W}(f_m)$

$$\mathbf{W}(f_m) = \sum_{k=0}^{2L_{w_0}-1} \mathbf{W}_k \exp(j2\pi(f_m + \Delta f)t_k) \quad (3.82)$$

where  $L_{w_0}$  is the order of the adaptive filter.

### 3.2.3.1 The indirect approach

The determination of the matrix  $\mathbf{H}(f)$  needs the estimation of the temporal matrices  $\mathbf{H}_k$  for  $0 \leq k \leq 2L-1$  jointly to the channel order  $L_0$ . According to (3.81) and for a given value of  $L$

$$\{\hat{\mathbf{H}}_k \text{ for } 0 \leq k \leq 2L-1\} = \arg \min_{\{\mathbf{H}_k\}} \varepsilon^{indirect}(L) \quad \text{where} \quad \varepsilon^{indirect}(L) = \sum_{m=1}^M \left\| \mathbf{y}_m(i_{DMRS}) - \sum_{k=0}^{2L-1} \mathbf{H}_k \mathbf{d}_m \exp(j2\pi(f_m + \Delta f)k) \right\|^2 \quad (3.83)$$

The results are

$$\hat{\mathbf{H}}_{ST}^L = [\hat{\mathbf{H}}_0 \quad \dots \quad \hat{\mathbf{H}}_{2L-1}] = \hat{\mathbf{R}}_{yd}^L (\hat{\mathbf{R}}_{dd}^L)^{-1}$$

$$\text{with} \quad \begin{cases} \hat{\mathbf{R}}_{yd}^L = \frac{1}{M} \sum_{m=1}^M \mathbf{y}_m(i_{DMRS}) \mathbf{d}_{m,ST}^H(L) \\ \hat{\mathbf{R}}_{dd}^L = \frac{1}{M} \sum_{m=1}^M \mathbf{d}_{m,ST}(L) \mathbf{d}_{m,ST}^H(L) \end{cases} \quad \text{and} \quad \begin{cases} \mathbf{d}_{m,ST}(L) = \begin{bmatrix} \mathbf{d}_m \\ \mathbf{d}_m z_m \\ \vdots \\ \mathbf{d}_m z_m^{(2L-1)} \end{bmatrix} \\ z_m = \exp(j2\pi(f_m + \Delta f)) \end{cases} \quad (3.84)$$

The channel matrices  $\mathbf{H}(f_m)$  can then be built according to (3.78) with the matrices  $\hat{\mathbf{H}}_k$ . The order is estimated with the minimization of the estimation error, where

$$\hat{L}_0 = \arg \min_L \varepsilon^{\text{indirect}}(L) \quad \text{with} \quad \varepsilon^{\text{indirect}}(L) = \frac{\text{trace}(\hat{\mathbf{R}}_{yy}^L - \hat{\mathbf{R}}_{yd}^L \hat{\mathbf{R}}_{dd}^{L-1} \hat{\mathbf{R}}_{dy}^L)}{N} \quad (3.85)$$

and  $N$  is the number of antennas of the receiver.

According to (3.79), the adaptive MMSE estimation of  $\mathbf{W}(f_m)$  gives

$$\mathbf{W}(f_m) = \mathbf{R}_{xy}(f_m) \mathbf{R}_{yy}^{-1}(f_m) \quad \text{with} \quad \begin{cases} \mathbf{R}_{xy}(f_m) = E[\mathbf{x}_m(i) \mathbf{y}_m^H(i)] \\ \mathbf{R}_{yy}(f_m) = E[\mathbf{y}_m(i) \mathbf{y}_m^H(i)] \end{cases} \quad (3.86)$$

Assuming that  $\mathbf{R}_{xx}(f_m) = E[\mathbf{x}_m(i) \mathbf{x}_m^H(i)]$  is proportional to the identity, an estimator of the matrix  $\mathbf{W}(f_m)$  is

$$\hat{\mathbf{W}}_{\text{indirect}}(f_m) = \hat{\mathbf{H}}^H(f_m) \hat{\mathbf{R}}_{yy}^{-1}(f_m) \quad \text{with} \quad \begin{cases} \hat{\mathbf{H}}(f_m) = \sum_{k=0}^{2\hat{L}_0-1} \hat{\mathbf{H}}_k \exp(j2\pi(f_m + \Delta f)t_k) \\ \hat{\mathbf{R}}_{yy}(f_m) = \frac{1}{I} \sum_{i=1}^I \mathbf{y}_m(i) \mathbf{y}_m^H(i) \end{cases} \quad (3.87)$$

where  $I$  can be the duration of one RB with  $I=14$  according to Figure 11. The computation of the filter  $\mathbf{W}(f_m)$  according to (3.87) is a particular solution for the adaptive indirect approach.

All the solutions depend on the estimation of the channel matrices with a temporal interpolation in the frequency domain. This approach avoids the issue of the direct estimation of the channel matrix with the single observation  $\mathbf{y}_m(i_{\text{DMRS}}) = \mathbf{H}(f_m) \mathbf{d}_m + \mathbf{n}_m(i_{\text{DMRS}})$ . Indeed and according to (3.86), the most direct possibility requires to inverse the estimate  $\hat{\mathbf{R}}_{yy}(f_m) = \mathbf{y}_m(i_{\text{DMRS}}) \mathbf{y}_m^H(i_{\text{DMRS}})$  of  $\mathbf{R}_{yy}(f_m)$ . This solution does not work because the matrix  $\hat{\mathbf{R}}_{yy}(f_m)$  is not full rank. This is why we have introduced a time-domain estimation approach.

### 3.2.3.2 The direct approach

In this approach, the matrix  $\mathbf{W}(f_m)$  is directly estimated with the modelling of (3.82) in order to avoid the direct estimation with a single DMRS vector  $\mathbf{d}_m$ . The linear modelling of the matrix allows to estimate  $\mathbf{W}(f_m)$  with the set of vectors  $\{\mathbf{d}_q \text{ for } 1 \leq q \leq M\}$ . According to (3.79), (3.82) and for a given value of  $L_w$

$$\begin{aligned} \{\hat{\mathbf{W}}_k \text{ for } 0 \leq k \leq 2L_w - 1\} &= \arg \min_{\{\mathbf{w}_k\}} \varepsilon^{\text{direct}}(L_w) \\ \varepsilon^{\text{direct}}(L_w) &= \sum_{m=1}^M \left\| \mathbf{d}_m - \sum_{k=0}^{2L_w-1} \mathbf{w}_k \mathbf{y}_m(i_{\text{DMRS}}) \exp(j2\pi(f_m + \Delta f)k) \right\|^2 \end{aligned} \quad (3.88)$$

The results are

$$\begin{aligned} \hat{\mathbf{W}}_{ST, L_w} &= [\hat{\mathbf{W}}_0 \quad \dots \quad \hat{\mathbf{W}}_{2L_w-1}] = \hat{\mathbf{R}}_{dy}^{L_w} \left( \hat{\mathbf{R}}_{yy}^{L_w} \right)^{-1} \\ \text{with} \quad \begin{cases} \hat{\mathbf{R}}_{dy}^{L_w} &= \frac{1}{M} \sum_{m=1}^M \mathbf{d}_m \mathbf{y}_{m,ST}^{L_w}(i_{\text{DMRS}})^H \\ \hat{\mathbf{R}}_{yy}^{L_w} &= \frac{1}{M} \sum_{m=1}^M \mathbf{y}_{m,ST}^{L_w}(i_{\text{DMRS}}) \mathbf{y}_{m,ST}^{L_w}(i_{\text{DMRS}})^H \end{cases} \quad \text{and} \quad \begin{cases} \mathbf{y}_{m,ST}^L(i) &= \begin{bmatrix} \mathbf{y}_m(i) \\ \mathbf{y}_m(i) z_m \\ \vdots \\ \mathbf{y}_m(i) z_m^{(2L_w-1)} \end{bmatrix} \\ z_m &= \exp(j2\pi(f_m + \Delta f)) \end{cases} \end{aligned} \quad (3.89)$$



The channel matrices  $\hat{\mathbf{W}}_{direct}(f_m)$  can then be built according to (3.82) with the matrices  $\hat{\mathbf{W}}_k$  as

$$\hat{\mathbf{W}}_{direct}(f_m) = \sum_{k=0}^{2L_{w_0}-1} \hat{\mathbf{W}}_k \exp(j2\pi(f_m + \Delta f)t_k) \quad (3.90)$$

The order can be estimated with the following minimization of the estimation error

$$\hat{L}_{w_0} = \arg \min_{L_w} \mathcal{E}^{direct}(L_w) \quad \text{where} \quad \mathcal{E}^{direct}(L) = \frac{\text{trace}(\hat{\mathbf{R}}_{dd}^L - \hat{\mathbf{R}}_{dy}^L \hat{\mathbf{R}}_{yy}^{L-1} \hat{\mathbf{R}}_{yd}^L)}{K} \quad (3.91)$$

where  $\hat{\mathbf{R}}_{dd}^L = (\sum_{m=1}^M \mathbf{d}_m \mathbf{d}_m^H) / M$  and  $K$  is the number of users.

### 3.2.3.3 Simulations

The simulations are given with QPSK for users and interference. According to (3.78) and Figure 9 of Section 2.2.2, the received signals in the temporal domain is

$$\mathbf{y}(t_{ki}) = \sum_{q=0}^{2L_0-1} \mathbf{H}_q \mathbf{x}(t_{ki} - q/B_{LTE}) + \mathbf{n}(t_{ki})$$

$$\text{where} \quad \begin{cases} \mathbf{H}(f) = \sum_{q=0}^{2L_0-1} \mathbf{H}_q \exp(j2\pi(f + \Delta f)t_q) \\ \mathbf{y}(t_{ki}) = \sum_{m=1}^M \mathbf{y}_m(i) \exp(-j2\pi(f_m + \Delta f)t_{ki}) \\ \mathbf{x}(t_{ki}) = \sum_{m=1}^M \mathbf{x}_m(i) \exp(-j2\pi(f_m + \Delta f)t_{ki}) \end{cases} \quad \text{and} \quad \begin{cases} t_{ki} = \frac{k + M(i-1)}{B_{LTE}} \\ t_q = q/B_{LTE} \end{cases} \quad (3.92)$$

The distributions of the channels  $\mathbf{H}_q$  are Rayleigh with  $E[\mathbf{x}(t)\mathbf{x}^H(t)] = \mathbf{I}$ ,  $E[\mathbf{H}_q^H \mathbf{H}_q] \times (2L_0 + 1) = N_r K \rho \sigma^2$ ,  $K=2$  is the number of users,  $N_r$  is the number of user antenna,  $\rho$  is the linear signal noise ratio and  $\sigma^2 = \text{trace}(E[\mathbf{n}_0(t)\mathbf{n}_0^H(t)]) / N_r$  is the noise level without interference where  $\mathbf{n}(t) = \mathbf{n}_0(t)$ . In presence of interference the noise verifies

$$\mathbf{n}(t) = \mathbf{i}(t) + \mathbf{n}_0(t) \quad \text{with} \quad \mathbf{i}(t) = \mathbf{u}_q b(t) \quad (3.93)$$

where  $E[|b(t)|^2] = 1$ ,  $\mathbf{u}_q$  is the interference channel vector with Rayleigh distribution such that  $E[\mathbf{u}_q^H \mathbf{u}_q] = N_r \rho_{br} \sigma^2$  and  $\rho_{br}$  is the interference noise ratio.

The results of the different algorithms are compared

- **MMSE-ref** : This is the reference MMSE algorithm of (3.80) where the channel matrix  $\mathbf{H}(f)$  is the true one. The curve is a red solid line.
- **MMSE-ref-data** : It is the indirect approach of equation (3.87) where the channel matrix  $\mathbf{H}(f)$  is the true one. Without interference, this approach is equivalent to 'MMSE-ref' when the covariance matrix  $\mathbf{R}_{yy}(f_m)$  is estimated with an infinite duration. For a finite duration  $I$  and without interference, the degradation 'MMSE-ref-data' depends on the estimation error  $\hat{\mathbf{R}}_{yy}(f_m) - \mathbf{R}_{yy}(f_m)$ . The associated BER curves are red solid line with a round marker.

- **Indirect ( $L$ )** : It is the indirect approach of equation (3.87). The curves are solid lines with different colours. The black line corresponds to the case where the order  $L$  is estimated.
- **Direct ( $L_w$ )**: It is the indirect approach of equation (3.90). The curves are solid lines with different colours. The black line corresponds to the case where the order  $L_w$  is estimated.

In simulations, there are  $K=2$  users with the same  $SNR=10\log_{10}(\rho)$ . The number of antennas of the receiver is  $N_r=3$ . The Binary Error Rate of each approach is represented with respect to the SNR. In the general case the channel order of direct and indirect approaches are different with  $L_0 \leq L_{w0}$ . The channel order is  $L_0=1$ .

Figure 54, Figure 55 and Figure 56 display the performance of the Direct and Indirect approaches without interference for  $M=96$  and  $M=192$  respectively. The red curves are associated to the reference algorithms. In the black one, the equalizers estimate the order and in the others curves the orders ( $L$  or  $L_w$ ) are fixed to given values.

Simulations confirm that the MMSE-ref gives the best performance without interference. The MMSE-ref-data is slightly less performant than the MMSE-ref because of the estimation errors of the covariance matrix  $\mathbf{R}_{yy}(f_m)$ . The results show that the equalizer order is correctly estimated for  $M=96$  because the black curves correspond to the curves with the smaller BER with  $L=L_w=1$ . This is also the case for the indirect equalizer whatever the value of  $M$ . For  $M=192$ , the optimal order is  $L_{w0}=2$  for the direct approach and  $L_0=1$  for the indirect one. According to Figure 56, performance is better for  $M=192$  than  $M=96$ . However, the direct approach is the best for the smaller UEs bandwidth with  $M=96$  and the indirect equalizer is the best for the larger UEs bandwidth with  $M=192$ . In addition, the influence of the estimation errors of the adaptive equalizer is more important for larger SNR because the difference with the optimal performance, in red, is more important.

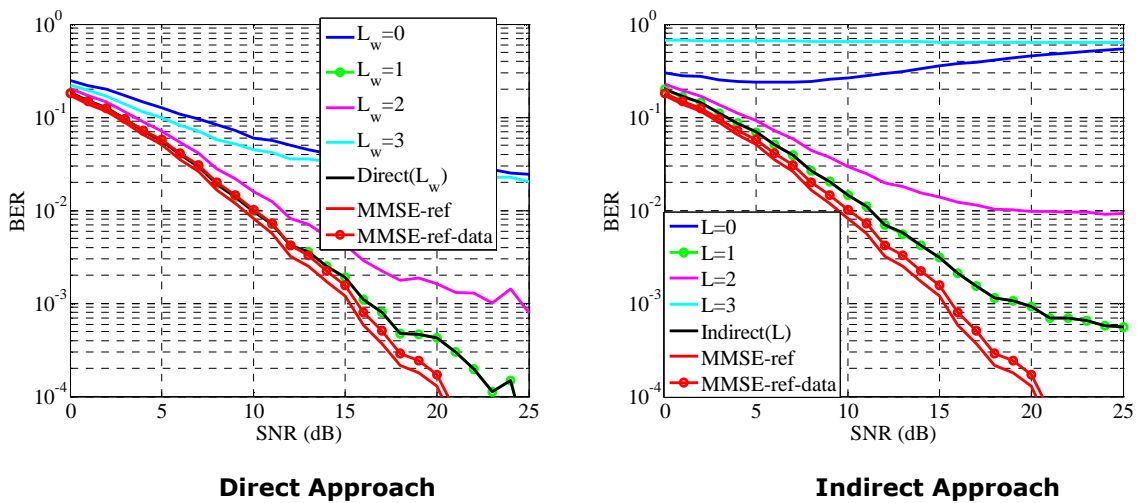


Figure 54 – BER without interference  $N_r=3, L_0=1$  and  $M=96$

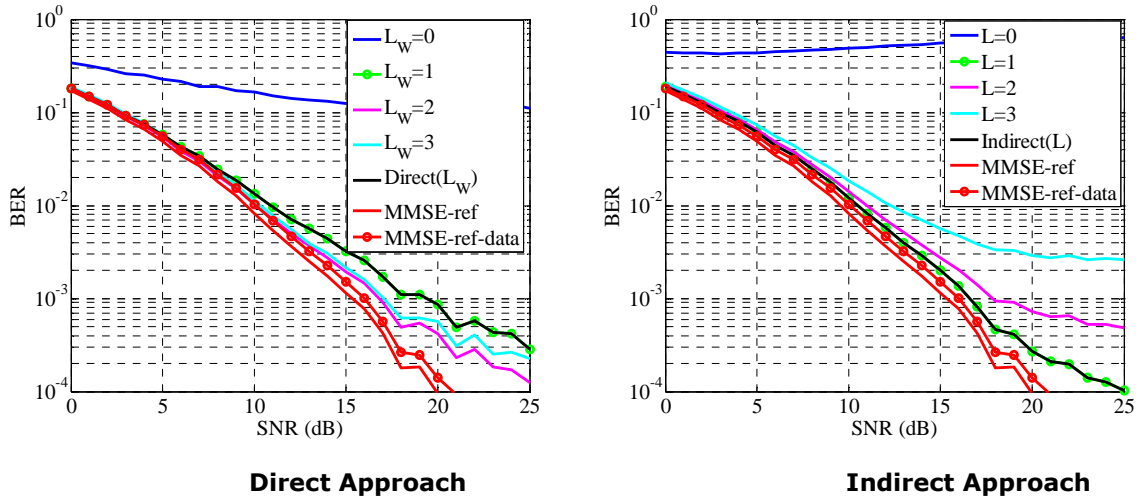


Figure 55 – BER without interference  $N_r=3$ ,  $L_0=1$  and  $M=192$

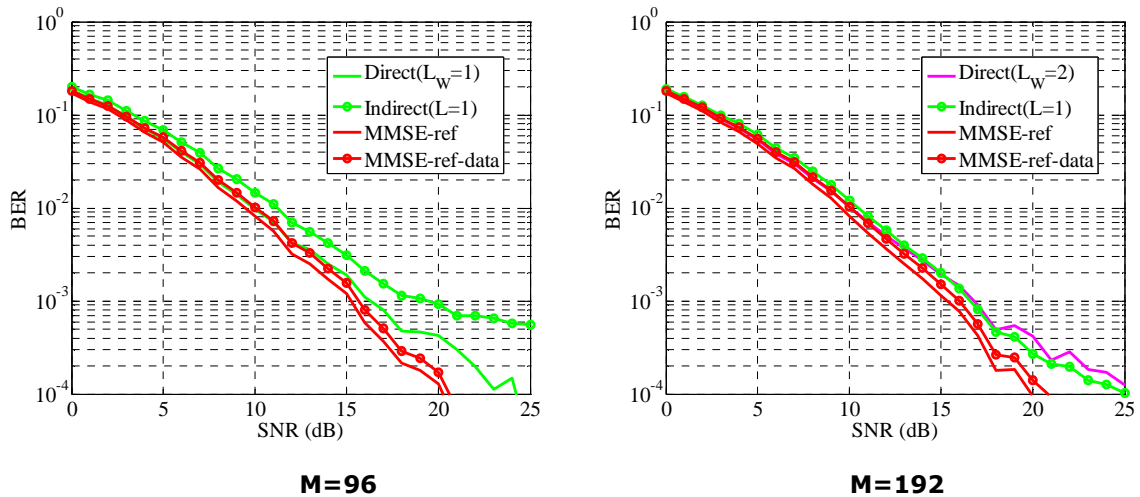
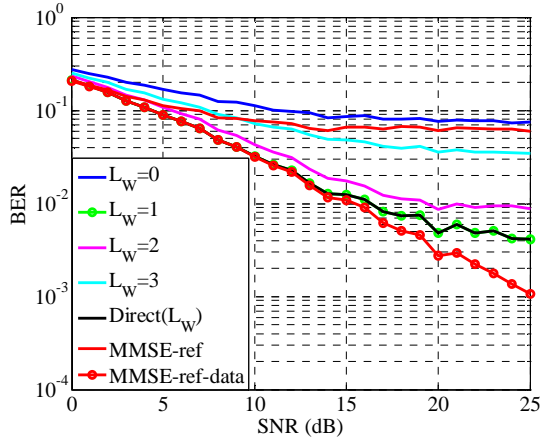


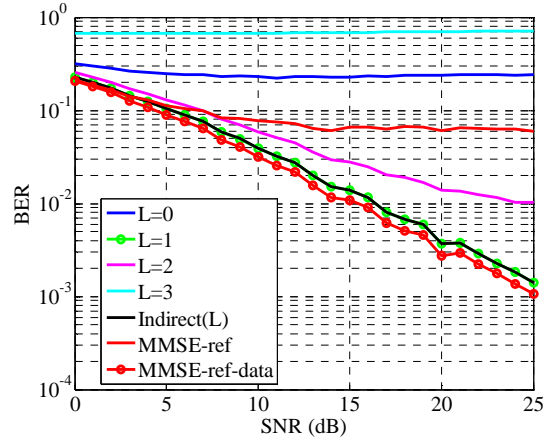
Figure 56 – Direct Approach without interference  $N_r=3$ ,  $L_0=1$

Figure 57, Figure 58 and Figure 59 display the performance of the Direct and Indirect approaches with interference for  $M=96$  and  $M=192$  respectively. The interference level is such that  $dJ=10\log_{10}(\rho/\rho_{br})=5\text{dB}$ . In this context, the MMSE-ref-data can be considered as the reference because MMSE-ref assumed that the additive noise is spatially white.

Simulations confirm that the MMSE-ref receiver does not give acceptable performance and that MMSE-ref-data gives the best performance in presence of interference. In addition, the performance of MMSE-ref-data is slightly better for  $M=192$  than  $M=96$ . The results show that the equalizer order is correctly estimated for  $M=96$  because the black curves give the smallest BER with  $L=L_w=1$ . For  $M=192$ , the optimal order is  $L_{w0}=3$  for the direct approach and is  $L_0=1$  for the indirect one. According to Figure 59, the performance of the optimal direct equalizer is similar for  $M=96$  and  $M=192$ . However, the performance of the indirect approach does not give acceptable results for  $M=192$  when SNR is larger than 15dB. Indeed, the difference of performance between the green curves of 'Indirect ( $L=1$ )' and red curve 'MMSE-ref-data' depends mainly on the estimation error of the propagation channel matrix  $\mathbf{H}(f_m)$ . In presence of interference the more robust algorithm is then the direct approach of section 3.2.3.2.

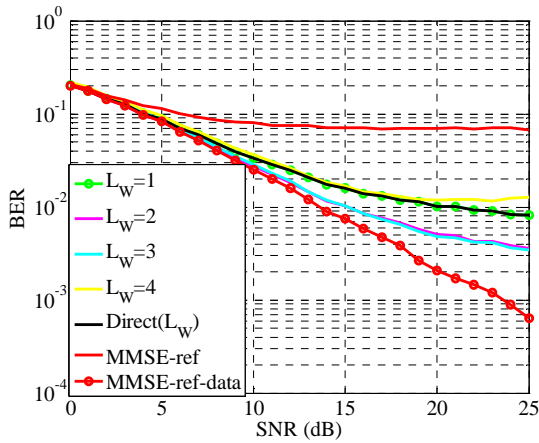


**Direct Approach**

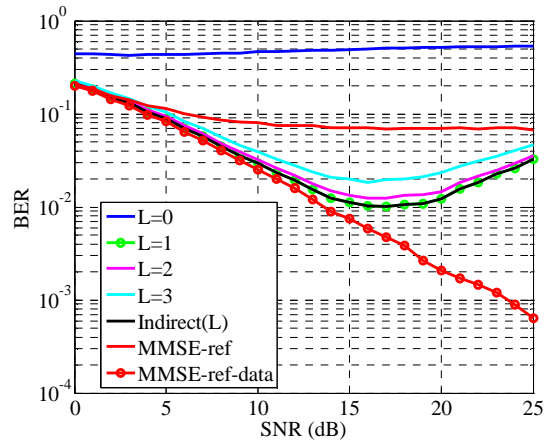


**Indirect Approach**

**Figure 57 – BER with interference (dJ=5dB) Nr=3, L<sub>0</sub> =1 and M=96**

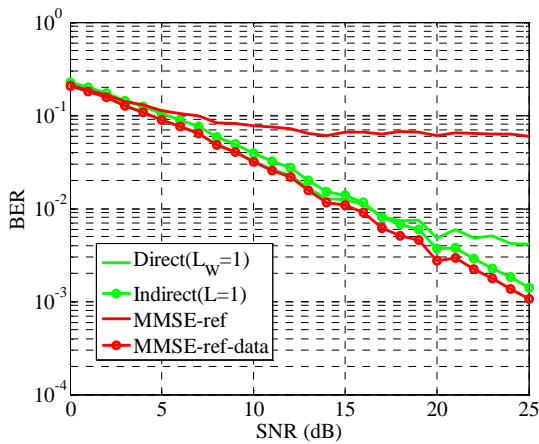


**Direct Approach**

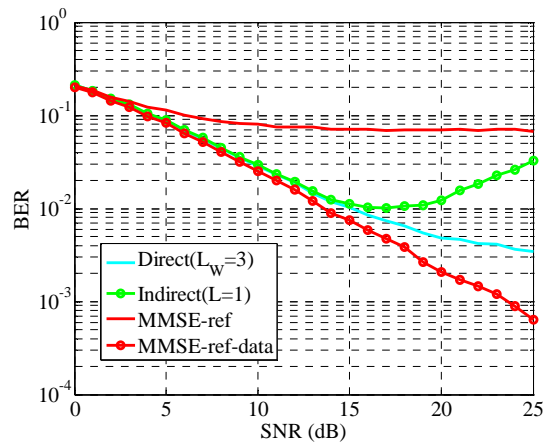


**Indirect Approach**

**Figure 58 – BER with interference (dJ=5dB) Nr=3, L<sub>0</sub>=1 and M=192**



**M=96**



**M=192**

**Figure 59 – Direct Approach with interference (dJ=5dB) Nr=3, L<sub>0</sub>=1**

### 3.2.3.1 Conclusions

The estimation of the spatial filtering matrix for frequency equalization needs the estimation of either the channel order  $L_0$  for the indirect method or the estimation of  $L_{W0}$  for the direct one. This is the main result of this work. Most of the time the channel order is fixed to the value of the Cyclic prefix (CP) in LTE-A transmission. In fact, the values of  $L_0$  and  $L_{W0}$  are much smaller than the LTE-A CP. This kind of estimation can also be of interest to reduce computation cost.

In addition, the Binary Error Rate (BER) of users symbols  $\{a^k(m,i)\}$  depends on the accurate estimation of the adaptive filter estimation  $\mathbf{W}(f_m)$  and thus on the errors  $\varepsilon^{indirect}(L)$  and  $\varepsilon^{direct}(L_W)$ . This is the reason why the orders  $L$  and  $L_W$  are estimated with the minimization of errors  $\varepsilon^{indirect}(L)$  and  $\varepsilon^{direct}(L_W)$  respectively. The simulations show the necessity to estimate these orders.

In presence of frequency selective propagation channels, the more robust algorithm is the direct approach of section 3.2.3.2. This result is particularly true in presence of interference

## 3.2.4 Interference Cancellation within Imperfect Channel Information in LTE DL Transmission

### 3.2.4.1 Introduction

In this contribution, we provide the signal-to-interference-plus-noise ratio (SINR) analysis focusing on the comparison between the conventional interference rejection combination (IRC) and the proposed schemes given in our previous report [4]. Moreover, the performance of our proposed schemes is evaluated under more practical considerations. These scenarios include non-synchronized cases and triply selective channels where both the serving and the interfering channels are time variant, frequency selective and spatially correlated.

In the following report, we try to answer two basic questions:

- what is the performance loss of a conventional IRC receiver?
- what is the impact of propagation delays of serving and interfering Evolved Node B (eNBs)?

We first show the analysis results, and then the corresponding numerical results can be found in the following chapter.

### 3.2.4.2 System model

Recall the system model in [4] where the received signal is subject to different kinds of interference caused by the interfering pilot and data signals. In order to model this, we have to consider four different types of intervals depending on the pilot/data structure:

$$\begin{aligned} Y_p &= \mathbf{H}\mathbf{X}_p + \alpha\bar{\mathbf{H}}\bar{\mathbf{p}}\bar{\mathbf{X}}_{d1} + \mathbf{Z}_p \\ Y_{d1} &= \mathbf{H}\mathbf{p}\mathbf{X}_1 + \alpha\bar{\mathbf{H}}\bar{\mathbf{p}}\bar{\mathbf{X}}_{d2} + \mathbf{Z}_{d1} \\ Y_{d2} &= \mathbf{H}\mathbf{p}\mathbf{X}_2 + \alpha\bar{\mathbf{H}}\bar{\mathbf{X}}_{p1} + \mathbf{Z}_{d2} \\ Y_{d3} &= \mathbf{H}\mathbf{p}\mathbf{X}_3 + \alpha\bar{\mathbf{H}}\bar{\mathbf{X}}_{p2} + \mathbf{Z}_{d3} \end{aligned}$$

where  $\mathbf{Y}_p, \mathbf{Y}_{d1}, \mathbf{Y}_{d2}, \mathbf{Y}_{d3}$  are the received signal matrices,  $\mathbf{X}_p$  is the serving pilot matrix,  $\mathbf{X}_1, \mathbf{X}_2, \mathbf{X}_3$  are the serving data matrices,  $\bar{\mathbf{X}}_{d1}, \bar{\mathbf{X}}_{d2}$  are the interfering data matrices,  $\bar{\mathbf{X}}_{p1}, \bar{\mathbf{X}}_{p2}$  are the interfering pilot matrices and  $\mathbf{Z}_p, \mathbf{Z}_{d1}, \mathbf{Z}_{d2}, \mathbf{Z}_{d3}$  are AWGN matrices,  $\alpha$  is a positive real number related to the signal-to-interference ratio (SIR),  $\mathbf{p}, \bar{\mathbf{p}}$  are the  $N_T = 2$  dimensional precoding vectors with  $N_T$  denoting the number of transmit antennas,  $\mathbf{H}$  denotes the desired channel state information (CSI), and  $\bar{\mathbf{H}}$  denotes the interfering CSI. An illustration is shown in Figure 60.

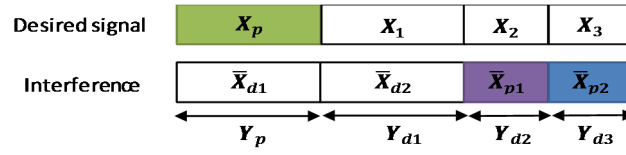


Figure 60 One-dimensional model arranging pilot and data symbols

### 3.2.4.3 SINR analysis of IRC

We first consider the conventional IRC scheme shown in [1], which treats interference as a stationary Gaussian process. The IRC detector can be written as:

$$\hat{\mathbf{X}}_{irc} = \hat{\mathbf{h}}^H \left( \hat{\mathbf{h}}\hat{\mathbf{h}}^H + \frac{1}{N_p} \hat{\mathbf{V}}\hat{\mathbf{V}}^H \right)^{-1} \mathbf{Y}_d$$

where  $\hat{\mathbf{X}}_{irc}$  is the estimate of the transmitted data matrices ( $\mathbf{X}_1, \mathbf{X}_2, \mathbf{X}_3$ ),  $\hat{\mathbf{h}} = \hat{\mathbf{H}}\mathbf{p}$  is the estimated CSI  $\hat{\mathbf{H}}$  combining with the precoding vector  $\mathbf{p}$ ,  $N_p$  denotes the signal length of the pilot signal  $X_p$ , the estimated interfering signal  $\hat{\mathbf{V}} = \mathbf{Y}_p - \hat{\mathbf{H}}\mathbf{X}_p$  and  $\mathbf{Y}_d$  is the received matrix that  $\mathbf{Y}_d = (\mathbf{Y}_{d1}, \mathbf{Y}_{d2}, \mathbf{Y}_{d3})$ . Unlike the proposed detectors, this scheme decodes  $\mathbf{X}_2$  and  $\mathbf{X}_3$  with incorrect covariance matrices. The covariance mismatch leads to different SINR results as follows:

$$\begin{aligned} \text{SINR}_{x_1} &= \frac{\beta^2}{\beta(1-\beta)} \\ \text{SINR}_{x_2} &= \frac{\beta^2}{\beta(1-\beta) + \psi_1} \\ \text{SINR}_{x_3} &= \frac{\beta^2}{\beta(1-\beta) + \psi_2} \end{aligned}$$

where  $\beta^2$  is the desired signal power and  $\psi_1, \psi_2$  are the residual interference terms due to the covariance mismatch. If the data energy is much larger than the noise  $E_s \gg N_0$ . We can show that  $\psi_1 > 0, \psi_2 > 0$ , and

$$\psi_1, \psi_2 \propto (\text{SNR})^2 \cdot \alpha^2 \cdot \frac{E_p}{E_d}$$

where  $E_p$  is the average pilot power,  $E_d$  denotes the average data power, and  $\alpha^2$  is the average power of interference. Hence, the IRC scheme suffers from mismatch-induced performance degradation when 1) SNR is high, 2) a strong interference is present, and 3) the pilot-to-data power ration is high, i.e.,  $\frac{E_p}{E_d} \gg 1$ . It is worth mentioning a special case when the interfering eNB transmits no data, but sends pilot symbols only. In this case, we have  $E_d = 0$  such that  $\frac{E_p}{E_d} = \infty$ . This happens in several inter-cell interference coordination (ICIC) approaches and results in significant performance degradation of an IRC receiver.

### 3.2.4.4 The asynchronous case

Suppose the length of the DFT window is  $N_F$ , the length of the CP is denoted by  $N_{CP}$ , the maximum channel delay spread is  $N_t$ , and the timing difference between two received signals is denoted by  $\tau$  as shown in Figure 61. All of these parameters are given in terms of the number of OFDM samples. We should consider two ranges for the propagation delay  $\tau$ : 1) those causing no inter-symbol interference (ISI) and 2) those which lead to ISI.

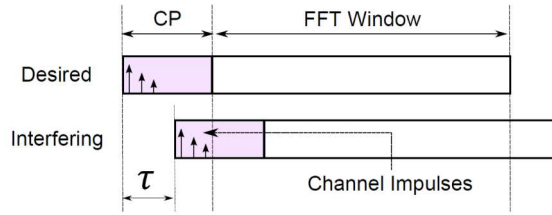


Figure 61 An example of an asynchronous interference

**Case without ISI:** The first subset of delays  $\tau \in [0, \dots, N_{cp} - N_L]$  does not destroy orthogonality of OFDM systems and only introduces a phase rotation in each subcarrier. Assuming the channels are non-selective, the received signal at the  $(t, k)$ th slot is

$$\mathbf{y} = \mathbf{h}\mathbf{x} + e^{\frac{-2\pi k\tau}{N_F}} \bar{\mathbf{h}}\bar{\mathbf{x}} + \mathbf{z},$$

where the delay is within a range of  $0 < \tau < N_{cp} - N_L$ . Note that the phase rotation term  $\exp(-2\pi k\tau/N_F)$  is unknown and degrades the channel estimate of the interfering channels. Also, since the phase rotation is a function of subcarrier index  $k$  instead of an index of time or space, there is no impact on the spatial covariance estimation, i.e., the covariance matrix of  $\mathbf{y}$  has no extra distortion due to the timing delay  $\tau$ , given as follows

$$\Sigma_{\mathbf{y}} = \mathbf{h}\mathbf{h}^H + \bar{\mathbf{h}}\bar{\mathbf{h}}^H + N_0\mathbf{I},$$

Recall that IRC-DL only needs to estimate the covariance matrix without the channel estimate of interference, but both LS-C and LMMSE-C schemes need the channel estimate of interference. Therefore, we can expect that IRC-DL will perform better than LS-C and LMMSE-C under this scenario.

**Case with ISI:** If the delay  $\tau$  is outside the above range, orthogonality among the subcarriers is destroyed. Mathematically, we have

$$\mathbf{y} = \mathbf{h}\mathbf{x} + \kappa e^{\frac{-j2\pi k\tau}{N_F}} \bar{\mathbf{h}}\bar{\mathbf{x}} + \alpha\varphi_{\tau}^{tk} + \mathbf{z},$$

for  $\tau < 0$  or  $\tau > N_{cp} - N_L$ ,  $\kappa \approx (N_f - \Delta(\tau))/N_F$ ,  $\Delta(\tau)$  is a positive value related to delay  $\tau$ , and  $\varphi_{\tau}^{tk}$  is the ISI term. The impact on the covariance matrices is shown as:

$$\Sigma_{\mathbf{y}} = \mathbf{h}\mathbf{h}^H + \kappa^2 \bar{\mathbf{h}}\bar{\mathbf{h}}^H + \alpha^2 \text{var}(\varphi_{\tau}^{tk}) + N_0\mathbf{I} \approx \mathbf{h}\mathbf{h}^H + \left(1 - \frac{\Delta(\tau)}{N_F}\right)^2 \bar{\mathbf{h}}\bar{\mathbf{h}}^H + \alpha^2 \left(2\frac{\Delta(\tau)}{N_F} - \left(\frac{\Delta(\tau)}{N_F}\right)^2\right) \mathbf{I} + N_0\mathbf{I}$$

The ISI term  $\varphi_{\tau}^{tk}$  is approximated by Gaussian noise. In this case, the delay  $\tau$  degrades the interfering channel estimation by introducing the phase rotation and the distortion term of  $\alpha\varphi_{\tau}^{tk}$ . For the covariance estimation, the delay  $\tau$  has no impact on the estimate because the covariance matrix  $\Sigma_{\mathbf{y}}$  is not a function of time or frequency, i.e., without the time index  $t$ , and the frequency index  $k$  after the approximation. Therefore, a similar conclusion can be made that IRC-DL will perform better than LS-C and LMMSE-C, and more gains will be obtained compared to the result in the ISI-free case.

Finally, the performance of the proposed schemes will be evaluated in the numerical section.

### 3.2.4.5 Numerical Results

To evaluate the proposed schemes under a time varying and frequency selective channel, we assume the serving channel distribution information (CDI) is perfectly known but the interfering CDI is unknown. The system parameters are given as follows: normal CP  $N_{cp} = 72$ , DFT-size  $N_F = 1024$ , and 2 GHz carrier frequency. All of them are in terms of OFDM samples. The discrete-time MIMO fading channel is generated using the triply selective channel. In what follows, we denote CDI on both channels by (serving CDI/ interfering CDI) and the UE receiver performs the data detection

by the proposed scheme but replacing the serving channel estimator by the 2D-MMSE channel estimator instead of the LS channel estimator.

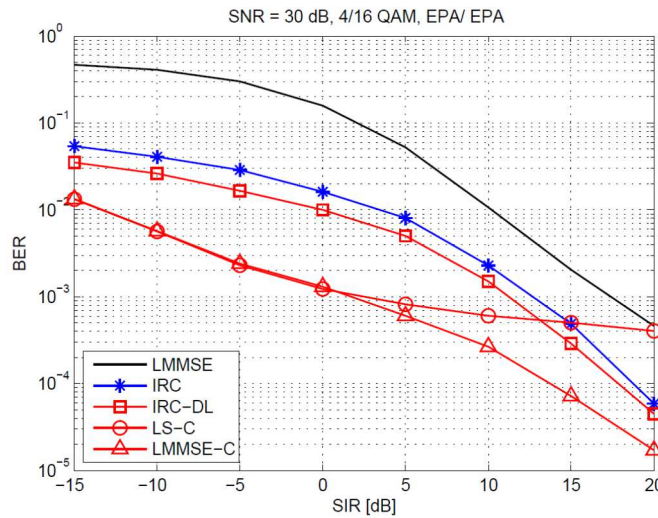


Figure 62 BER vs. SIR under SNR= 30 dB with triply selective channels

Figure 62 shows the BER performance for SNR = 30 dB on triply selective channels. CDI of both channels is given by: the maximum Doppler frequency equal to  $f_d = 10$  Hz, the power delay profiles is given by Extended Pedestrian A model (EPA) of LTE specification, and no spatial correlation for the transmit (TX) antennas and the receive (RX) antennas. Under these slow fading and slightly selective assumptions, the results are similar the one corresponding to the constant channels.

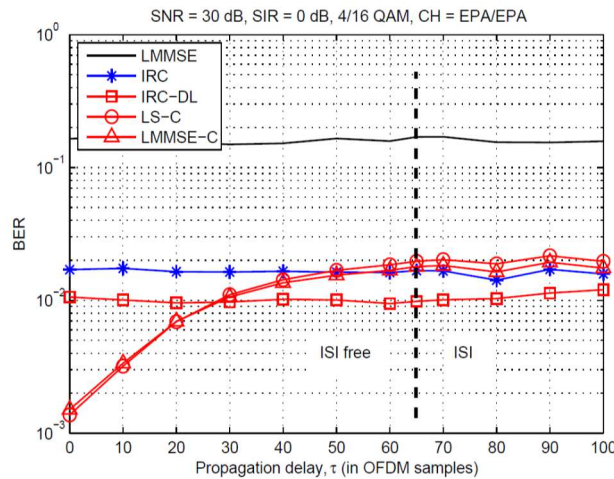


Figure 63 BER vs. different propagation delay,  $\tau$

Figure 63 illustrates the asynchronous case on triply selective channels. CDI of both channels is given as: 10 Hz of the Doppler frequency, the Extended Pedestrian A model (EPA) of the power delay profile, and no spatial correlation between antennas. According to EPA, the maximal channel delay spread is given by  $N_L = 7$  OFDM samples. Therefore, the maximal delay of ISI-free region will be  $\tau = 65$  OFDM samples shown by the dashed line in Fig. 4. Moreover, we show that our schemes provide substantial improvements on the triply selective channels without propagation delay  $\tau = 0$ . When the timing delay increases, we show how robust the IRC-DL is, i.e., there is no performance degradation even in the ISI region.



### 3.2.4.6 Conclusions

This study considers interference suppression schemes for MIMO-OFDM systems. In such systems, the statistical property of interference impacts its suppression schemes. Therefore, given the pilot-data structure of interference, we derived novel schemes without the high cost of computation.

The numerical results have demonstrated that separately handling the interfering pilots and data signals allows substantial improvements, which also clearly reveal the importance of judicious exploitation of the structure and statistics of interfering signal (such as those from neighboring cells).

More specifically, our results are evaluated by the simulations including flat and triply selective channels with or without timing delays of arrival signals. In the synchronous case, we find that the proposed LMMSE-C provides better performance than the other schemes. This scheme is based on the SIC criterion that decodes interfering pilots with the estimate of the interfering channel. In the asynchronous case, since it is difficult to estimate the interfering channel, the proposed IRC-DL scheme based on the LMMSE criterion provides reliable performance. This scheme only estimate the distinct statistical properties based on the pilot-data structure, treating interference as noise without decoding it.

## 3.2.5 Enhanced Spatial Modulation Schemes

### 3.2.5.1 Introduction

In this contribution, we extend the contribution of enhanced spatial modulation (ESM) in [4] that allows multiple signal constellations to be used by different active antenna combinations. In order to achieve high spatial efficiency, the new technique, referred to as ESM-64QAM, can provide one more bit compared to the previous work in [4]. Compared to conventional MIMO schemes, e.g., spatial multiplexing (SMX) and spatial modulation (SM), at the same spectral efficiency, ESM offers significantly better pairwise error probability (PEP) performance. Moreover, the impact on the number of receive antennas is also investigated, which shows that the performance gains increases as the number of receive antennas increases, and these curves eventually converge to the theoretical performance bounds.

### 3.2.5.2 System model

Following the same system model in [4], at the receiver the received signal can be written as:

$$\mathbf{y} = \mathbf{H}\mathbf{x} + \mathbf{n} \in \mathcal{C}^{N_R}.$$

This model is the same as the conventional MIMO system model, however the main difference in SM systems is that only part of transmit (TX) antennas are activated. This property can be mathematically modeled by using zero elements in the transmitted vector, for example,  $\mathbf{x} = [+1, 0, 0, 0]$  denotes the symbol +1 is transmitted by using the first TX antenna, and  $\mathbf{x} = [+1, -1, 0, 0]$  denotes two symbols transmitted simultaneously by using the first and the second TX antennas. When the channel state information is perfectly known at the receive side, the SM-type signal can be decoded by the ML decoder that estimates the transmitted symbol vector according to:

$$\hat{\mathbf{x}} = \arg \min_{\mathbf{x} \in \mathcal{X}} \|\mathbf{y} - \mathbf{H}\mathbf{x}\|^2,$$

where  $\|\cdot\|$  denotes the vector norm,  $\mathcal{X}$  denotes the constellation of the transmitted symbols, and the minimization is performed over all possible transmitted symbol vectors.

### 3.2.5.3 Proposed schemes: ESM with 64-QAM

To achieve higher throughputs, we now describe ESM schemes using higher-level signal constellations. The design process is similar to that with the previous constellations in [4], but here we have more throughputs. The proposed ESM scheme based on two TX antennas and 64QAM as primary modulation is denoted by the 2TX9b scheme in which the transmitted signal vector  $\mathbf{x}$  takes its values from the signal space given below:

$$x \in \left\{ \begin{bmatrix} C_{64} \\ 0 \end{bmatrix}, \begin{bmatrix} 0 \\ C_{64} \end{bmatrix}, \begin{bmatrix} \mathcal{A}_8^0 \\ \mathcal{A}_8^0 \end{bmatrix}, \begin{bmatrix} \mathcal{A}_8^1 \\ \mathcal{A}_8^1 \end{bmatrix}, \begin{bmatrix} \mathcal{A}_8^2 \\ \mathcal{A}_8^2 \end{bmatrix}, \begin{bmatrix} \mathcal{A}_8^3 \\ \mathcal{A}_8^3 \end{bmatrix}, \begin{bmatrix} \mathcal{A}_8^4 \\ \mathcal{A}_8^4 \end{bmatrix}, \begin{bmatrix} \mathcal{A}_8^5 \\ \mathcal{A}_8^5 \end{bmatrix} \right\},$$

In addition to the signal space of 2TX8b shown in [4], this one includes 4 other combinations. They correspond to the transmission in parallel of two symbols taking their values from one of 4 other secondary constellations. So, in summary, compared to 2TX8B this design doubles the number of combinations and involves 6 secondary constellations instead of 2. We denote the 4 secondary signal constellations used in this design as 8-APK2, 8-APK3, 8-APK4, and 8-APK5, respectively. These signal constellations are shown in Figure 64. A simple inspection indicates that the average transmit signal power in this scheme is  $E_s = 59.5$ . The 8 combinations of TX antenna and the constellations transmitted from them are explicitly shown in Table 5.

Extension of 2TX9b to 4 TX antennas is not straightforward. In 4TX11b, there are 32 combinations of the antennas and constellations requiring 5 bits for combination selection, and each combination transmits 6 bits, leading to a throughput of 11 bpcu. Note that we have 40 combinations if we follow the same extension as in 4TX10b, which is more than what is required. From those, we choose 32 combinations as follows: C1 - C4 with 64QAM transmitted from a single antenna, C5 - C10 with 8APK0 transmitted from two antennas, C11 - C16 with 8APK1, C17 - C22 with 8APK2, C23 - C28 with 8APK3, C29 - C30 with 8APK4, and C31 - C32 with 8APK5. Note that the 8APK4 and 8APK5 signal constellations whose average power is higher than the other signal constellations are only used in two combinations each, whereas the 8APK0 - 8APK3 constellations are used in 6 combinations each. The purpose of this is to limit the average transmit power. The resulting average signal power is 51.75.

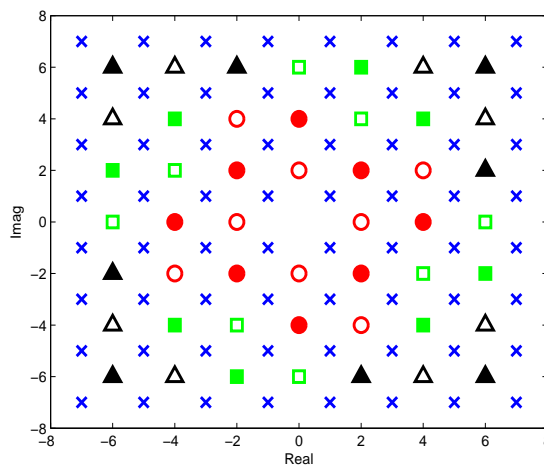


Figure 64 An illustration of ESM-2TX9b: crosses are 64QAM, the heavy/empty circles are the 8APK0/8APK1, the heavy/empty squares are the 8APK2/8APK3, and the heavy/empty triangles are 8APK4/8APK5 signal constellations

Table 5. Enhanced SM, 2 TX, 9 BPCU

	TX1	TX2
C1	64QAM	0
C2	0	64QAM
C3	8APK0	8APK0
C4	8APK1	8APK1
C5	8APK2	8APK2
C6	8APK3	8APK3
C7	8APK4	8APK4
C8	8APK5	8APK5

### 3.2.5.4 Receiver Complexity Analysis

In this section, we show that in addition to improving performance over conventional SM, the proposed ESM also reduces the complexity of the ML decoder. Reduction of the receiver complexity will be demonstrated by explicitly evaluating the respective complexities of SM and ESM in the 4TX8b case before summarizing the complexity figures of the two transmission schemes for different spectral efficiencies. In this analysis, we define complexity as the number of complex multiplications required per ML decoder decision.

For 4TX8b SM, the ML decoder needs to compute  $w_{ij} = y - h_i s_j$ , where  $h_i$  with  $i = 1, 2, 3, 4$  denotes the  $i$ -th column of the channel matrix  $H$ , and  $s_j$  with  $j = 1, 2, \dots, 64$  denotes a 64QAM symbol. This step involves 256 complex multiplications. Next, it needs to compute the squared modulus of each one of the  $w_{ij}$  terms, and this step involves another 256 complex multiplications. In other words, the total number of complex multiplications in this scheme is 512 per channel use.

**Table 6 Receiver Complexity ( $N_R = 1$ )**

	<b>2TX4b</b>	<b>2TX6b</b>	<b>2TX8b</b>	<b>2TX9b</b>
SM	32	128	512	1024
ESM	32	112	416	836
	<b>4TX6b</b>	<b>4TX8b</b>	<b>4TX10b</b>	<b>4TX11b</b>
SM	128	512	2048	4096
ESM	96	352	1344	2912

In the case of 4TX8b ESM, we need to consider separately 3 groups of antenna/constellation combinations. First, in combinations C1 - C4, a 16QAM symbol is transmitted from one of the 4 TX antennas. For those combinations, the ML decoder needs to compute  $w_{ij} = y - h_i s_j$ , with  $i = 1, 2, 3, 4$  and  $j = 1, 2, \dots, 16$ , and this involves 64 complex multiplications. Next, in combinations C5 - C10, two QPSK0 symbols are transmitted from two active antennas. For those combinations, the ML decoder needs to compute  $w_{ijkl} = y - h_i s_j^0 - h_k s_l^0$ , with  $i, k = 1, 2, 3, 4$  and where  $s_j^0$  and  $s_l^0$  ( $j, l = 1, 2, 3, 4$ ) denote two symbols taken from the  $Q_4^0$  signal constellation. The number of complex multiplications involved in this step is only 16. Finally, in combinations C11 - C16, two QPSK1 symbols are transmitted from two active antennas. For those combinations, the ML decoder needs to compute  $w_{ijkl} = y - h_i s_j^1 - h_k s_l^1$ , with  $i, k = 1, 2, 3, 4$  and where  $s_j^1$  and  $s_l^1$  ( $j, l = 1, 2, 3, 4$ ) denote two symbols taken from the  $Q_4^1$  signal constellation. Here, the number of complex multiplications is also 16. So, the total number of complex multiplications involved in the steps above is 96, although the number of  $w_{ij}$  and  $w_{ijkl}$  values computed is 256 (64 values corresponding to combinations C1 - C4, 96 values corresponding to combinations C5 - C10, and 96 values corresponding to combinations C11 - C16). Next, the decoder needs to compute the squared modulus of all  $w_{ij}$  and  $w_{ijkl}$  values to determine the 256 metrics involved. So, the total number of complex multiplications per decoding step in the ML decoder is 352, which is significantly smaller than the corresponding number in SM. In this particular case, the decoder complexity reduction with respect to conventional SM is 31.2%.

The complexity analysis reported above for the 4TX8b case was also made for all SM and ESM schemes and the results are reported in Table 6. The results indicate that ESM significantly reduces the ML decoder complexity compared to conventional SM, particularly in the case of 4 TX antennas. Note that in the 4TX10b case, the ML decoder complexity of ESM is 34.4% smaller than that of conventional SM.

### 3.2.5.5 Numerical Results

We report here the results of Monte Carlo simulations, which were obtained using Rayleigh fading MIMO channels with 4 receive antennas ( $N_R = 4$ ) and assuming perfect CSI at the receiver. We

also assume perfect synchronization and rectangular pulse shaping. That is, we neglect the problems of antenna switching with Nyquist pulse shaping, which may be challenging in practice. This problem was addressed in some recent papers, which proposed solutions such as employing a multiple-RF antenna switching architecture or simply using a large roll-off factor in the pulse shaping filters to ensure that the power is concentrated in a short period of time.

In the simulations, symbol vectors were randomly generated and transmitted over the channel, ML detection was performed using the received noisy signal samples, and symbol vector error events were counted. The obtained symbol vector error rate (SVER) was used to compare the respective performances of conventional SM and ESM. Unlike bit error rate (BER) performance evaluation, the SVER does not need to define the bit mapping, and the simulations are much quicker.

In Figure 65, the SVER curves of 2TX9b show that ESM gains around 4 dB over QSM and 6 dB over SM and has about 0.8 dB loss compared to SMX at  $SVER = 10^{-3}$ . Again, the average SNR loss of ESM with respect to SMX can be attributed to the use of 64QAM in combinations C1 - C2, while SMX uses one 16QAM stream and one 32QAM stream in parallel to achieve a spectral efficiency of 9 bpcu.

**Figure 66**, which shows that ESM gains around 3 dB over SMX, 5 dB over QSM, and as much as 9 dB over SM at  $SVER = 10^{-2}$ . The substantial gain of ESM over SM in the 4TX11b case can be explained by the fact that SM requires 512QAM for transmitting 11 bpcu, while ESM only needs 64QAM as primary modulation to achieve the same spectral efficiency.

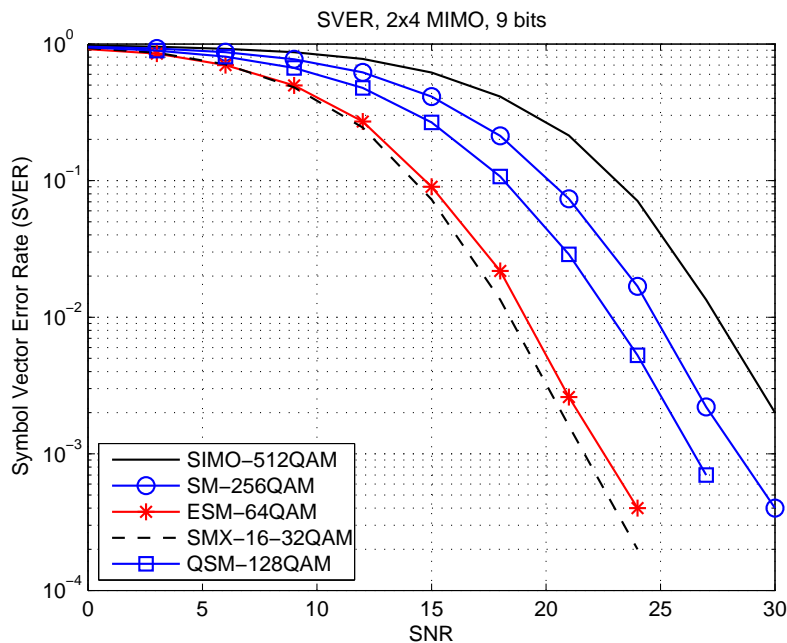
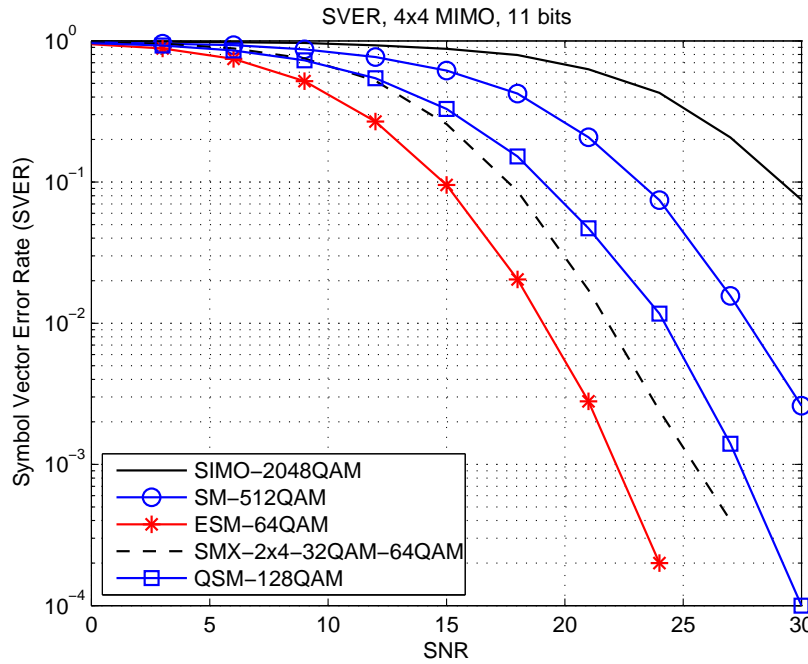
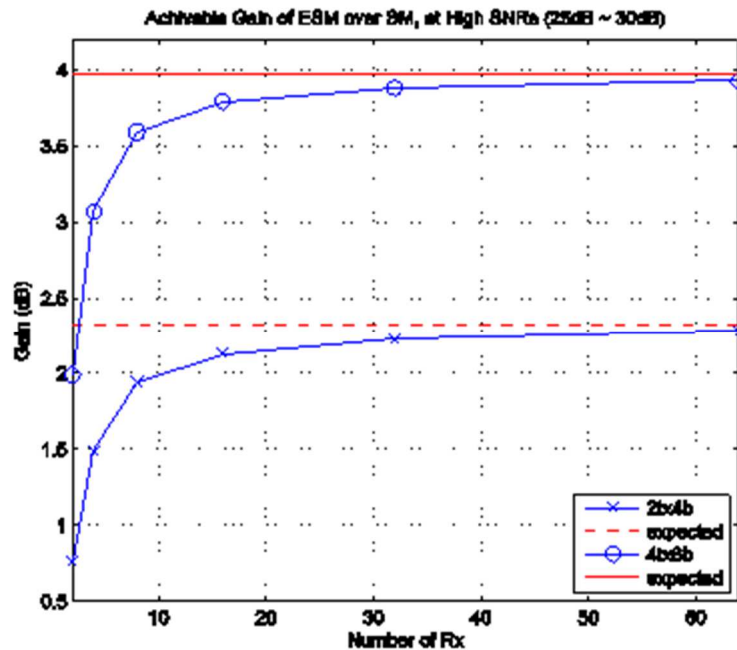


Figure 65 The SVER performance of 2TX9b.



**Figure 66** The SVER performance of 4TX11b

A final investigation in this work concerned the relation between the expected gains from the minimum distance analysis and the gains achieved with a finite number of receive (RX) antennas. The results are reported in Figure 67. The specific numbers of RX antennas used here are 2, 4, 8, 16, 32, and 64. The average SNR gains which appear in this figure are those of ESM over SM. The expected gains corresponding to the 2TX4b and 4TX6b cases are indicated by the dotted line and the solid line, respectively. The curve with crosses gives the gain as a function of the number of RX antennas for the 2TX4b case. It shows that the expected gain of 2.32 dB can be approached when the number of RX antennas increases. Specifically, the gain is virtually to 2 dB with 8 RX antennas and 2.3 dB with 16 RX antennas. A similar observation can be made for the 4TX6b case. Here, the expected gain (the solid-line curve) is 4 dB, and the curve with circles, which gives the gain as a function of the number of RX antennas indicate that the gain achieved with 8 RX antennas is 3.6 dB and the gain with 16 RX antennas is 3.8 dB.



**Figure 67** Impact of the number of Rx antennas

### 3.2.5.6 Conclusions

A new type of Spatial Modulation, referred to as ESM-64QAM, has been presented by enabling one or two active Tx antennas and using multiple signal constellations. On Rayleigh fading channels, we showed that the proposed technique outperforms conventional SM and SMX for the same bpcu.

In our numerical results, it was found that with 2 TX antennas ESM potentially gains up to 6 dB over conventional SM, up to 4 dB over QSM, and up to 2 dB over SMX. With 4 TX antennas, ESM leads to higher gains: it gains up to 9 dB over SM, up to 5 dB over QSM, and some 3 dB over SMX with 2 RF chains. Moreover, the receiver complexity analysis of ML detection revealed that while ESM achieves a substantial performance gain over conventional SM, it also significantly reduces the complexity of the optimum decoder.

## 3.3 Flexible interference management concept

This section contains the work done in T3.3 and T3.1, dealing mainly with cross-layer issues on how to mitigate interference

- Section 3.3.1 deals with the construction of an interference map. Such a map can be used to predict interference, which can be useful eg. in a handover procedure. This map is built in two steps: a first map is obtained via a statistical model, based on PPP (Poisson Point Process) that needs as inputs the network's nodes density, the path loss parameters and the distance between the considered UE and its first interfering node ([5]). Section 3.3.1 shows how this map is refined by using the interference measurements reported by active UEs to the central base station. The final map is obtained by a Kriging interpolation on the errors between measurements and initial map. This method was evaluated by using an emulation of a real interference map, given by the ray tracing tool described in 2.3.5 (T3.3)
- Section 3.3.2 is the follow-up of Section 2.3.3, where it was shown that the performance improvement of JT Comp UEs was obtained to the detriment of the legacy UEs. To address the weakness of the conventional scheduler, a centralized opportunistic approach was proposed, introducing more fairness between the non-CoMP UEs and CoMP UEs. The objective of Section 3.3.2 is to evaluate the effectiveness of this algorithm for other categories of CoMP. It is shown that network load is a key factor in choosing the best CoMP categories (JT, DPS). Indeed when the load is low, a lot of spectral resource is available, coherent JT outperforms the other categories. In contrast, at high loads, available resources are scarce, only CoMP categories that do not need additional spectral resource are efficient. The contribution suggests that the combined use of both Coherent JT and DPS W/o allows obtaining a very wide range of use from low to high network load with just one scheme (T3.1).
- In Section 3.3.3, it is first shown that a scheduler prioritizing non-CoMP users in the presence of mobility outperforms many other strategies in contrast to the scenario without mobility. Taking this fact into account, a mobility-aware scheduler is proposed, which deprioritizes mobile CoMP users. This scheduler improves the performance by giving the chance to mobile cell-edge users to be served in better radio conditions where cell coordination is not required. (T3.1)
- Section 3.3.4 : The impact of beamforming in a large-scale real environment is assessed considering a dense outdoor small-cell deployment. A Monte-Carlo process is performed, making it possible to estimate both the interference decrease and the traffic load decrease achievable thanks to the beamforming. The study shows significant improvement of the DL and UL users' performance thanks to the interference rejection provided by the beamforming (T3.3)

### 3.3.1 Joint location and interference prediction for ICIC

In deliverable D3.4 [5], we proposed a new Location-dependent ICI estimation model that estimates the ICI level as a function of the UE location. The analytical model is based on stochastic geometry, exploiting the mathematical tools of Poisson Point Process (PPP). Compared to the location-dependent ICI estimation models existing in the literature, the major feature of the

proposed model is that in addition to the fading and path loss parameters, it takes into account the shadowing effects and its impact on the ICI level estimation. Thus, the analytical model needs as inputs:

1. the density  $\lambda_k$  of the network's nodes and their transmission power  $P_k$ ,
2. the radio channel propagation parameters: the constant path loss  $Pl_0$ , the path loss exponent  $\gamma$ , the fast fading and the shadowing standard deviations designed respectively as:  $\sigma_f$  and  $\sigma_s$ ,
3. the radius of the observation zone  $R_{ob}$ , as defined in Figure 11 in [5] Sec. 4.2,
4. the distance between the UE and the first interfering eNB  $r$ .

The interference estimation model was developed for both co-tier and cross-tier scenarios. In co-tier case, each tier operates at a dedicated frequency bandwidth (i.e., small cells and macro cells operate on distinct frequency bandwidths and interference is generated only by the eNBs of the concerned tier). In cross-tier case, there is a single frequency bandwidth used by all tiers (i.e., macro cells and small cells use the same frequency bandwidth and interference is generated by all eNBs in the concerned area). The analytical estimation of the ICI in both cases is illustrated in

Figure 68, where  $\eta_k = \frac{1}{Pl_0 P_k}$  is defined for each tier as a function of its eNB transmission power  $P_k$ .

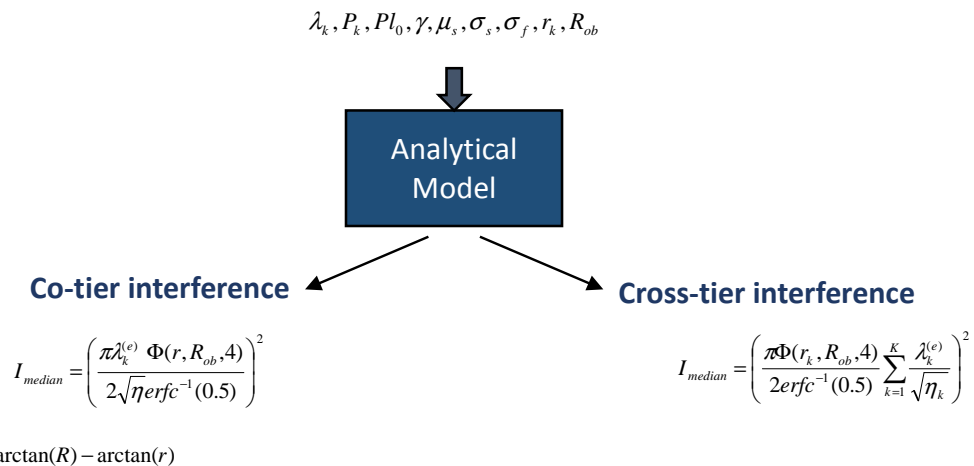


**Figure 68: Location-dependent ICI estimation model**

Most of the inputs are constants and provided to the network controller (i.e., the network controller is considered as the entity responsible for the IM construction) as a function of the studied area except the distance  $r$  between the UE and its first interfering eNB, which varies as a function of the UE location.

In fact, the statistical interference map is obviously biased in comparison with the ICI level that would be physically experienced by the UEs, for various reasons (e.g., strong a priori spatial distribution assumptions). Besides, it may be also practically challenging to get reliable a priori information in real systems, due to the possible inaccuracy and/or low representativeness of the assumed statistical model parameters in practical operating environments. On the other hand, the location-dependent ICI estimation model allows an interference map initialization when starting from scratch. To construct a more reliable interference map, an update on the IM is performed with a self-learning procedure.

As defined in the standard, the active UEs report their measurements to the eNB. Accordingly, based on this information, the observed "gap" between the measured ICI level and the estimated

level can be evaluated at all the sensing points. Since the active UEs can be sparsely (i.e., under low deployment density) and/or non-uniformly distributed in the geographic area of interest, the whole IM has to be updated with regards to the finite number of observed gaps, using spatial interpolation of the perceived prediction errors. Two spatial interpolation techniques are thus investigated: (i) the Inverse Distance Weighting (IDW), and (ii) the Kriging.

### 3.3.1.1 Interference map update:

To deal with the reliability of the Interference map in real systems, a self-learning procedure is performed in order to update the IMs according to the sensed information. The update can be performed using a statistical shape analysis such as Procrustes analysis that defines the required transformations to be applied to the initial map based on the observed shape deviations (i.e., scaling, rotation...) [64], or interpolation techniques as detailed in [65] (Section 4.4.3). In this work, the IM is updated according to the gap observed between the estimated ICI level and the deterministic ICI values based on the information collected at spatially distributed "sensing" positions i.e. ICI levels obtained by active UE measurements.

These measurements will be emulated here by the deterministic interference map provided by Siradel. Figure 69 shows the Interference map in dBm obtained by Siradel ray-tracing tool in a macro scenario, where the macro eNBs are generated by a PPP of intensity  $\lambda_k = 7 \cdot 10^{-6}$ . The central BS is represented by a black star and the interfering eNBs by blue triangles. The UEs are connected to the nearest eNB (i.e., the cells are generated with a Voronoi decomposition).

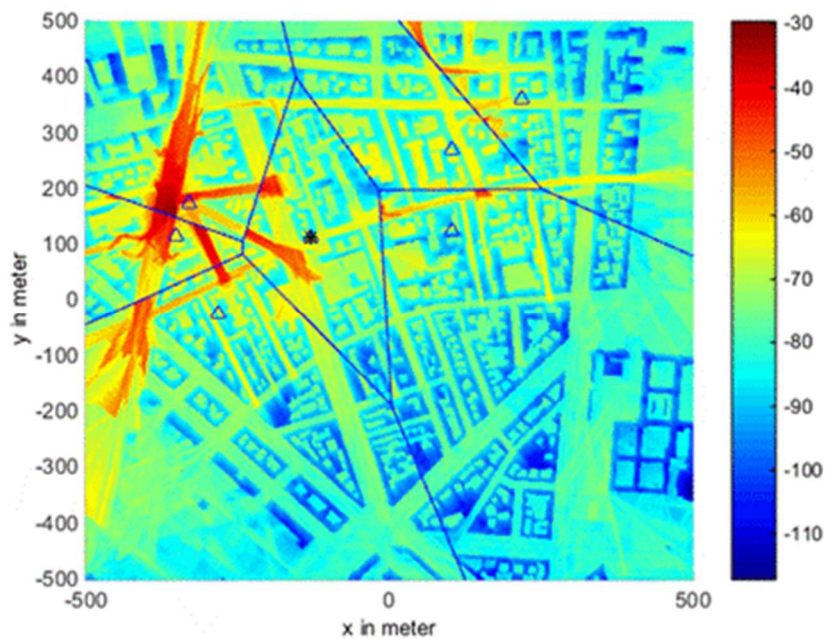


Figure 69: Deterministic interference map (Siradel)

The gap to be interpolated is noted by:

$$\mathcal{E}(x_i) = \hat{I}(x_i) - I(x_i) \quad (3.94)$$

where,  $\hat{I}(x_i)$  and  $I(x_i)$  are respectively the estimated and the observed ICI level at the sensing position  $x_i$ .

Thus, the updated IM noted  $I_u$  is built as

$$I_u(x) = \hat{I}(x) + \hat{\mathcal{E}}(x) \quad (3.95)$$



where,  $\hat{I}(x)$  and  $\hat{\varepsilon}(x)$  are respectively, the theoretical ICI level obtained by the stochastic based location dependent ICI estimation model and the estimated gap at any position  $x$  of the concerned area (i.e., including the non-sensing positions).

To estimate the gap  $\hat{\varepsilon}(x)$  at any location of the area of interest, spatial interpolation techniques that are widely used in the context of radio environment cartography [25][66][67], are investigated. We focus on two well-known techniques: (i) the Inverse Distance Weighting (IDW), and (ii) the Kriging.

These two spatial interpolation techniques allow the estimation of unobserved gap values according to a set of neighbourhood observed gap values, through a weighted linear combination. Thus, with the IDW interpolation, the unobserved ICI gap values estimation are expressed as:

$$\hat{\varepsilon}(x) = \sum_{i=1}^N \lambda(x_i) \varepsilon(x_i) \quad (3.96)$$

where,

$$\lambda(x_i) = \frac{d(x, x_i)^{-p}}{\sum_{i=1}^N d(x, x_i)^{-p}} \quad (3.97)$$

is the Shepard's weighting function, calculated from the distances between the location of the unobserved gap value  $x$  and the locations of the observed gap values  $x_i$ ,  $N$  is the number of considered observed gap values, and  $p$  is a real positive power (usually  $p$  is set to 4 or 6).

Unlike the IDW technique, the Kriging weights are based on spatial correlation between the considered observations such that,

$$C \lambda = C_0 \quad (3.98)$$

where  $C$  is the covariance matrix of the observations at the sensing positions  $x_i$ , and  $C_0$  is the covariance vector of the observations at the interpolation position  $x$  and at the sensing positions  $x_i$ .

An alternative way to describe the spatial relationship of the observed values is the variogram (or semi-variogram). Contrary to the covariance matrix, the variogram can be calculated even if the mean of the observation values is unknown. Thus, the variogram is more convenient to describe the spatial relationship inside a data set and is described as,

$$\gamma(\tau) = \frac{1}{2} \text{Var}[\varepsilon(x_i) - \varepsilon(x_i + \tau)] \quad (3.99)$$

with  $\tau$  representing a distance, eg.  $\tau = d(x_i, x_j)$  with  $1 < i < N$  and  $1 < j < N$ .

Under the hypothesis of first and second order stationarity, the semi-variogram is given as:

$$\gamma(\tau) = C(0) - C(\tau) \quad (3.100)$$

with  $C$  the scalar covariance.

The experimental semi-variogram has to be calculated from the given data that are discrete and often irregularly sampled. It can then be approximated through a continuous parameter model. The most frequently used in the radio environment cartography are:

1. the exponential model defined as:

$$\gamma(\tau) = \eta + c(1 - \exp(\frac{-3\tau}{r})) \quad (3.101)$$

with,  $\eta$  is the nugget,  $c$  is the sill and  $r$  is the range of the variogram (i.e. the correlation length).

- the Von Kàrmàn model defined as:

$$\gamma(\tau) = \frac{c}{2^{\nu-1}\Gamma(\nu)} (\tau/r)^\nu K_\nu(\tau/r) \tag{3.102}$$

where  $\Gamma$  is the gamma function,  $K_\nu$  is the modified Bessel function of the second kind of order  $0 \leq \nu \leq 1$  [68].

In the following, both the IDW and the Kriging (using the exponential and the Von Kàrmàn variogram models) interpolations are investigated. We consider that the sensing (i.e., the measured ICI values) is performed by the active UEs. Thus, the number of sensing positions is proportional to the population density and the rate of active UEs in this area. Regular and irregular sensing positions are considered. We assume that the studied area is in Paris with a population density of 21 564 pop. per km<sup>2</sup> which are equipped with mobile phone that can collaborate to the sensing procedure during their active mode, with an active UE rate of 45%.

First, an IM coined “low resolution fingerprinting” will be studied, where the deterministic ICI values at the sensing positions will be spatially interpolated, based on the IDW and the Kriging (with the exponential and the Von Kàrmàn variogram) methods. This map will be compared to the deterministic IM (i.e., provided by Siradel). The CDFs of ICI level estimation error were obtained, as illustrated in Figure 70. From this comparison, it appears that the ICI error obtained with regular sensing positions is close to the ICI error obtained with irregular sensing positions, whatever the spatial interpolation technique used. At 50 percentile the IDW generates an ICI error of 6 dB, where the Kriging interpolation generates about 2dB independently of the variogram model used. The performance of the Kriging method is due to the used weights based on the data correlation. Notice that using the exponential variogram model generate less ICI error, however the performance gap obtained with the two variogram models is very small (of the order of 0.01 dB). Based on this numerical results, in the following only the Kriging method with the exponential variogram will be used.

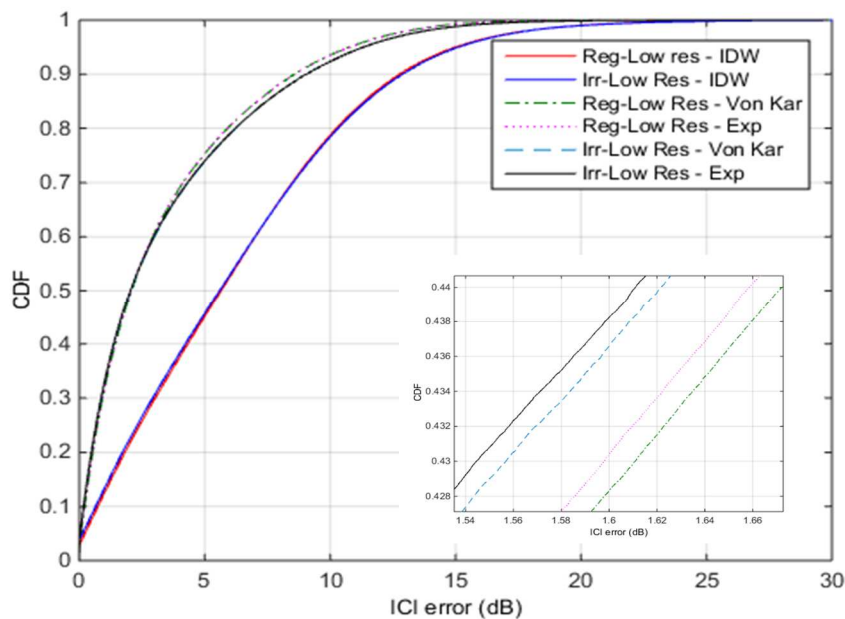


Figure 70 CDF of ICI error in regular sensing positions

Next, the performance of the updated IM as in (3.95) is presented, by comparison with that of the above low resolution fingerprinting (i.e., IM obtained by interpolating the deterministic ICI values). The comparison is based on the CDF of ICI error with respect to the deterministic IM (i.e., IM provided by Siradel) (see Figure 71). As said before, the type of sensing positioning has a low impact on the performance. The ICI error obtained with the regular and the irregular sensing positioning is very small. However, the performance of the updated IM is higher. At 90 percentile, the ICI error obtained with the updated IM (i.e., using the theoretical IM at the initialization step) is about 5 dB, where it is about 9 dB in case of a low resolution fingerprinting. This is due to the IM initialization step. Since the prior information provided by the theoretical IM and the map used in the initialization step allows smoothed gap values with a high correlation compared to the deterministic ICI values.

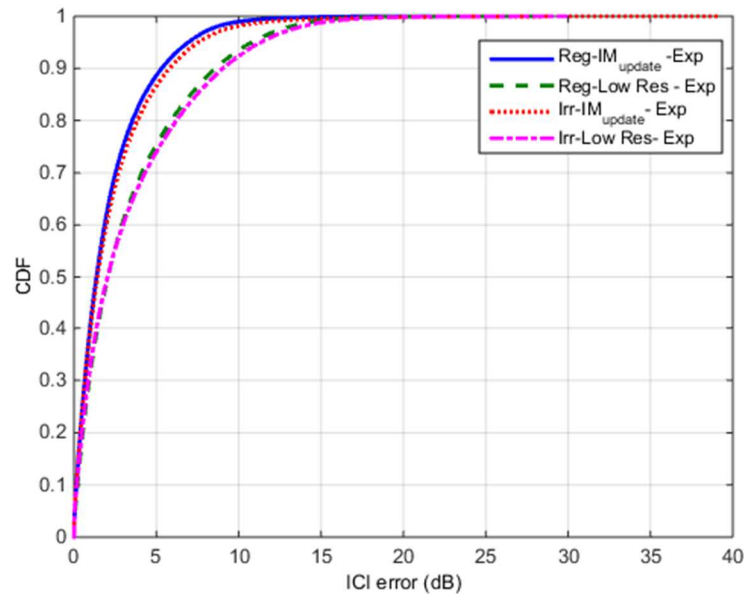


Figure 71 CDF of ICI error: low resolution fingerprinting and updated IM

An active UE rate of 45% is not realistic. Thus, the performance of the proposed updated IM is studied with respect to different values of active UE rate. It is expected that with less sensing positions the performance of the updated IM and the low resolution fingerprinting will decrease. Our goal is to show the performances of the proposed algorithm in such scenarios. We assume an irregular sensing positioning, where the updated IM and the low resolution fingerprinting IM are generated with the Kriging method based on the exponential variogram. Figure 72 shows the CDF of ICI error obtained in such scenario. The red and black curves represent the CDFs of ICI error obtained with the updated IM (i.e., the proposed algorithm) and the low resolution IM, respectively. The Active UE rates are shown with different line types. Notice that when the active UE rate decrease, the ICI error increase independently of the used technique for the IM construction. However, the updated IM generates a low ICI error compared to the low resolution fingerprinting. In addition, the gap introduced when the active UE rate decreases, increases in case of low resolution fingerprinting compared to the IM update technique. At 90 percentile, when the active rate decrease from 40% to 15%, the ICI error of the updated IM increases from 5.92 dB to 6.63 dB, while the ICI error of the low resolution fingerprinting increases from 9.17 dB to 11.65 dB. In fact, even in low active UE rate (i.e., active UE rate of 15%), we obtain a better performance with the proposed algorithm than with the low resolution technique. This is due to the initialization step and to the update of the IM map according to the gap between the deterministic ICI level observed at the sensing positions and the theoretical IM. Notice that this improvement is achieved with low computational complexity, since the theoretical IM can be constructed offline and the additional complexity considered in the update stage is the gap computation with a computational complexity of  $O(N)$ . Figure 73

shows the IM obtained with the proposed algorithm using the Kriging interpolation with the exponential variogram.

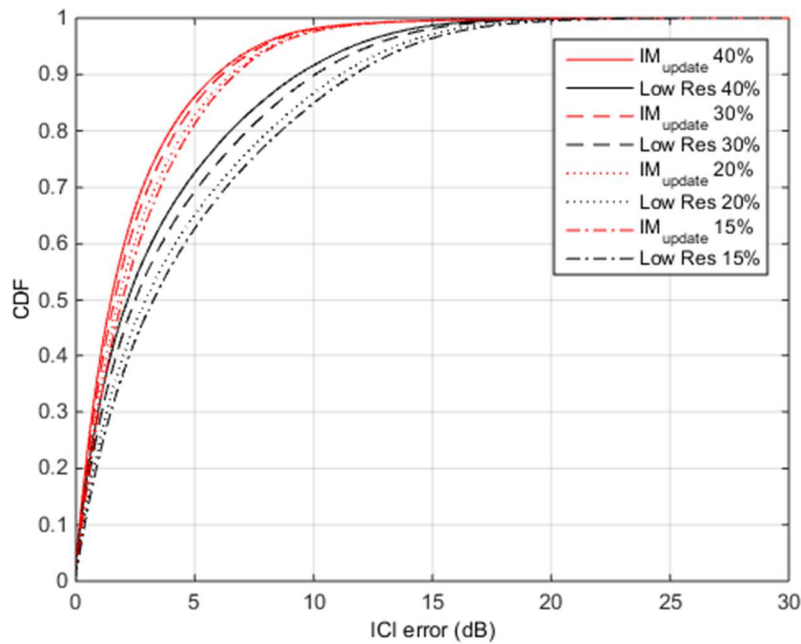


Figure 72: CDF of ICI error: updated IM and low resolution IM vs active UE rates

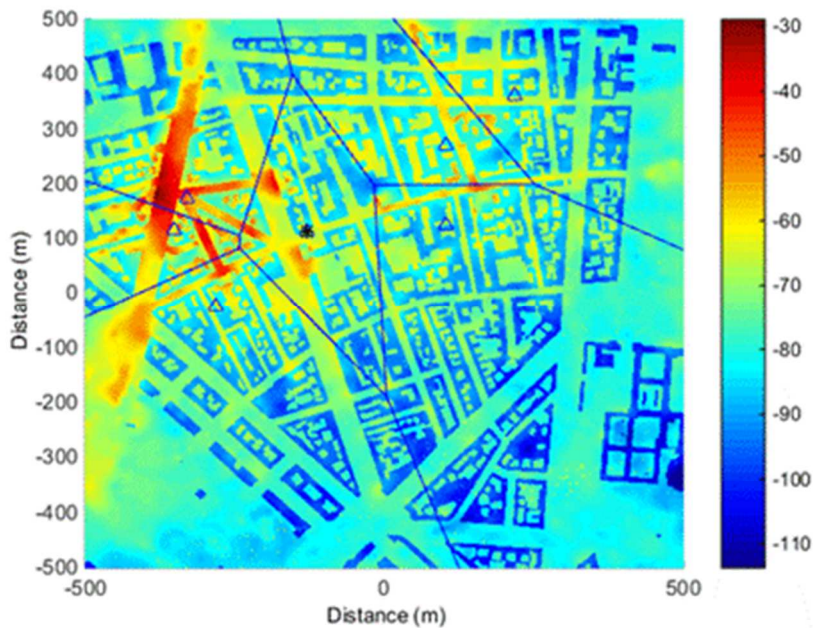


Figure 73: Semi-deterministic IM based on exponential variogram: irregular sensing positions with active UE rate of 15%

3.3.1.2 Conclusion:

Our objective in the framework of this work package is the construction of an Interference Map in order to assist a subsequent ICIC mechanism. First, we developed a stochastic based location

dependent ICI estimation model that considers the shadowing, the fast fading and the path loss. This analytical model copes with the HetNet complexity, since such a method is able to take into account different network configurations, especially the small cells configuration. However, for this analytical IM, it may be practically challenging to get reliable a priori information in real systems, due to the possible low representativeness of the statistical model parameters in practical operating environments. To build a more reliable IM, it is proposed here to update the initialization IM in a self-learning procedure. The update is performed by a spatial interpolation technique based on the ICI gaps observed by collaborative UEs at sensing positions either regular or irregular. Two spatial interpolation techniques are studied: (i) Inverse Distance Weighting (IDW), and (ii) Kriging. In the Kriging technique, exponential and Von Karman variogram models are investigated. The performance analysis shows that, unlike the sensing positioning type, where regular and irregular positioning sensing give a similar ICI estimation error, the choice of the spatial interpolation technique has a larger impact on the ICI estimation performance. Numerical results show that IDW is less reliable than Kriging spatial interpolation technique, since the latter weights are based on the inputs correlation. The best ICI estimation is given with Kriging based on the exponential variogram. In addition, the performance of the proposed algorithm is studied as a function of the active UE rate. The performance of the updated IM is shown to degrade more slowly than the low resolution fingerprinting.

### 3.3.2 Advanced scheduling for intra and inter-site CoMP

All CoMP categories (JP, JT, DPS) are expected to improve the system performance but the way of achieving this depends on the category: a best reception quality is obtained by choosing dynamically (for example at the beginning of each packet transmission) the best serving cell for DPS or by transmitting simultaneously the same data flow on the same spectral resource from different transmission points for coherent JT. The reception of a larger information amount is obtained by taking advantage of a better SNR for non-coherent JT. The muting mode of "DPS With muting" (DPS W/) and of "DPS with Dynamic Blanking" (DPS DB) makes further improvements by avoiding the first interfering cell compared to "DPS without muting" (DPS W/o). From a point of view of resource blocks (RB) requirement, DPS W/o does not need additional RBs in contrast to DPS W/ (muted RBs cannot be allocated to other users) and of JT (additional RB are necessary to JT). The proposed advanced scheduling algorithm can address all these JT categories.

One of the great DL CoMP challenges is the joint management of non-CoMP UEs and CoMP UEs. In practice, all UEs will not take advantage of the improvement brought by CoMP because either some of them are not CoMP compatible (legacy UEs) or the requirements permitting the CoMP support (when RSRP difference between serving cell and another cell does not satisfy the threshold requirement for example) are not met. In some cases the decision of whether a UE is qualified as a CoMP UE or not has significant consequences on system performance: the transmission performance improvement for one UE brought by CoMP should at least compensate the reduction of the available spectral resources for other UEs. Thus in case of high load the resource allocation to a CoMP UE could reduce the probability of a non-CoMP UE to access spectral resources and hence reduce its throughput. From the point of view of user experience it is not appropriate that UEs which cannot take benefit from CoMP or legacy UEs be penalized (by undergoing less throughput) when the CoMP-feature is enabled.

A large amount of research work has focused on the scheduling algorithm so far. [33] proposed a two-stage centralized MAC scheduling approach for JT CoMP which adds only low complexity to the 3GPP LTE Release 8 system. [34] deals with the problem of the relevancy that exists in the scheduling for users under different cells in the same coordination cluster. The resources firstly allocated to a JT UE at coordinated cells are unavailable to any other UEs. [34] proposed an optimization method that combines fairness level and estimated throughput. [35] proposed an orthogonality based (among the channel matrices of users within a group) proportional fair scheduling scheme for virtual MIMO and CoMP in TD-LTE uplink. Here the originality of the approach consists in using the transfer functions (that are commonly used in the analysis of systems such as SISO filters) to analyze the impact of scheduling on the throughput of each UE.

The description of the proposed algorithm in order to achieve this goal can be found in [69]. The main results from the paper are summarized below.

The principle of the proposed scheduling scheme is based on an opportunistic approach to effectively solve the problem of scheduling fairness between legacy UEs and CoMP UEs.

The problem addressed here is the following: CoMP transmission aims at improving the quality of service of users at cell-edge. To achieve this, some JP CoMP categories use more spectral resources, thus reduce the resources access probability of non-CoMP UEs (legacy UEs). From the point of view of user experience it is inappropriate that UEs which cannot take benefit from CoMP or legacy UEs are penalized (by undergoing less throughput) when CoMP feature is enabled. To address this issue, an effective scheduling scheme based on an opportunistic approach is proposed. The goal of the proposed scheduling is to maintain for all the UES the system performance as if the CoMP feature were disabled and after adopt an opportunistic approach only for the CoMP candidates

Considering different CoMP categories and different load assumptions (see Table 7) the effectiveness of the proposed algorithm is shown in the table.

**Table 7 Percentage of throughput gain (or loss) brought by CoMP vs.the case where CoMP feature is disactivated, respectively for a Conventional Scheme [67] (Reference) and for the proposed algorithm (Proposed) in terms of Cell-Edge ( $\Delta_{05}$ ) and Cell Average ( $\Delta_{50}$ ) Throughput.**

CoMP Cat.:		DPS W/o		JT coherent		DPS W/	
	Load	$\Delta_{05}$	$\Delta_{50}$	$\Delta_{05}$	$\Delta_{50}$	$\Delta_{05}$	$\Delta_{50}$
Reference	20%	11.0	0.0	29.6	0.4	11.2	-0.2
	60%	13.2	6.3	13.3	12.6	-9.5	-5.0
	100%	16.6	4.8	10.7	-10.3	-12.6	-22.4
Proposed	20%	12.0	0.0	29.4	0.4	12.2	-0.2
	60%	15.3	8.1	22.7	17.7	8.7	4.8
	100%	16.1	4.5	3.6	2.8	-0.9	-1.0

As shown in the following figure, network load is a key factor in choosing the best CoMP categories. Indeed when the load is low, a lot of spectral resources are available, coherent JT may be applicable and outperforms the other categories. In contrast, at high loads, available resources are scarce, only CoMP categories that do not need additional spectral resource are efficient. This is the case of the DPS W/o muting and DPS with dynamic blanking (since it includes DPS W/o). As shown in Figure 74, Coherent JT and DPS W/o should play complementary roles in facing the challenges of the network load: the combined use of both Coherent JT and DPS W/o allows obtaining a very wide range of use from low to high network load with just one scheme. The proposed algorithm is also compatible with Frequency Selective Scheduling (FFS). Performance evaluation shows significantly greater gains for the DPS W/o due to the fact that UE could benefit from more bandwidth in certain cases (a kind of load balancing).

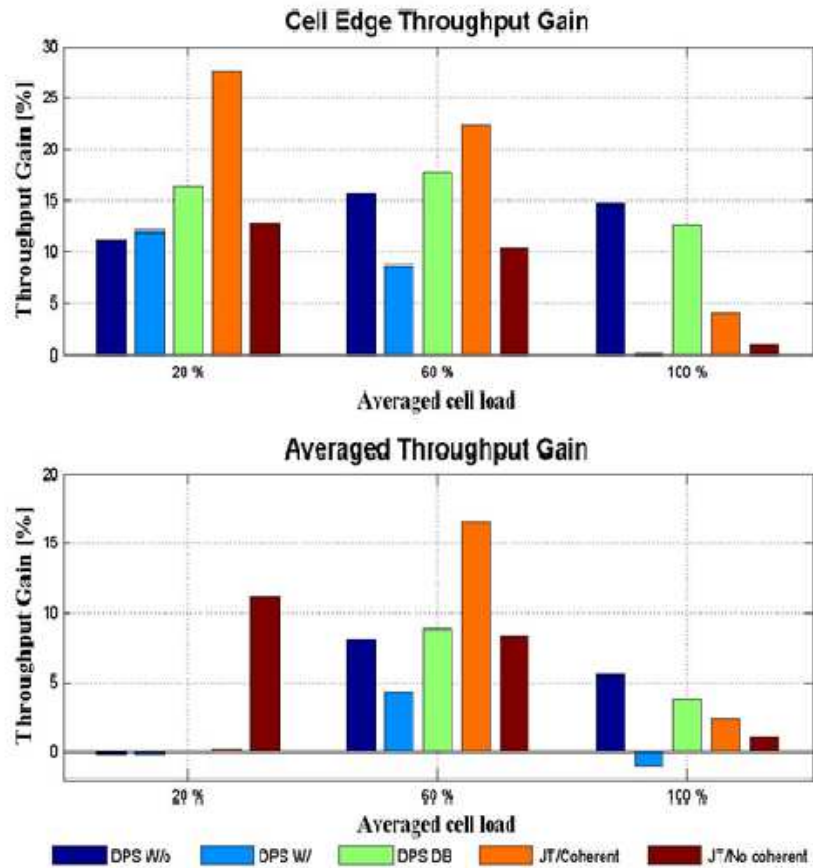
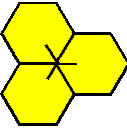
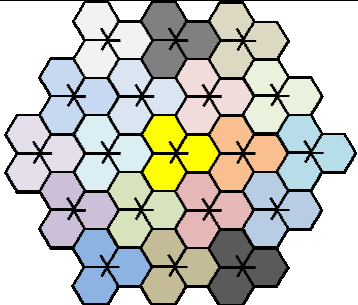
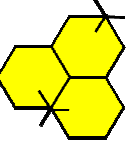
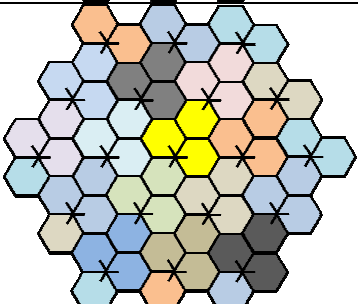
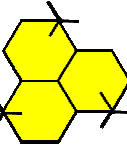
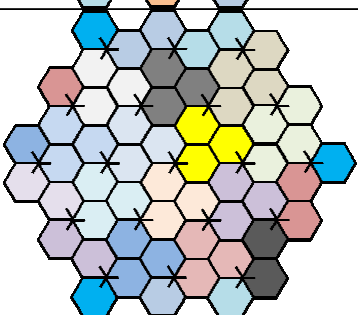
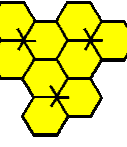
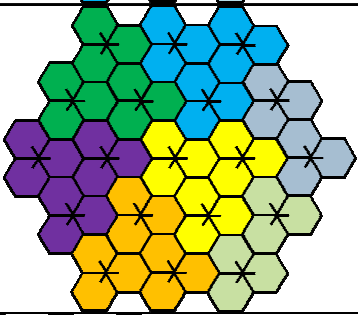
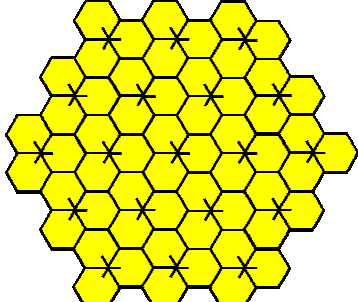
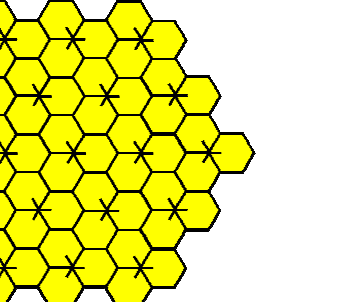


Figure 74 Impact of system load on JP CoMP Categories performance

To address the dimensioning cluster size problem, 5 following scenarios are considered:

- Intra-site cooperation (i.e. 3 cells of a same site),
- inter-site cooperation (i.e. 3 cells of 3 different sites),
- intra + inter-site cooperation (i.e. 2 cells of a same site and one of another site)
- 3 GPP Scenario 2 cooperation,
- Full cooperation (All the network is a CoMP cluster).

The following figure shows the cluster and the network for each of the considered scenario.

Scenario	Cluster	Network
<p><b>Intra-site cooperation</b></p>		
<p><b>Inter and intra cooperation</b></p>		
<p><b>Inter-site cooperation</b></p>		
<p><b>3 GPP Scenario 2 cooperation</b></p>		
<p><b>Full cooperation</b></p>		

**Figure 75 Deployment scenarios for DPS performance assessment**

Notice that no black fiber is needed in the case of Intra-site Cooperation and that the need to deploy a Backhaul Network Fiber increases with the other scenario. Full cooperation is an unrealistic case but performances obtained with this case correspond to upper bound performance for the dimensioning cluster size problem. The following figure gives the DPS performance for different cluster sizes.



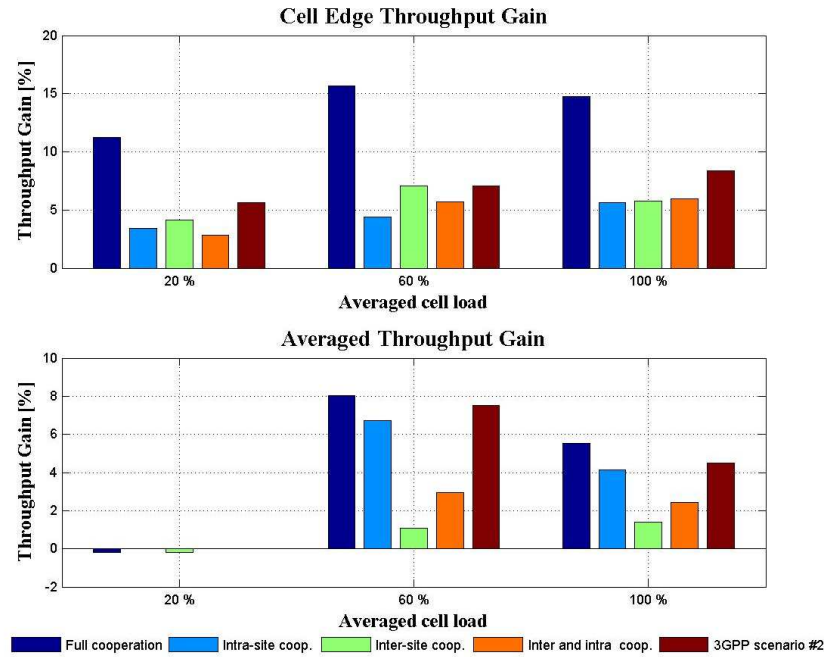


Figure 76 Impact of cluster size on DPS performance

Obviously the smaller the coordinating cluster size, the smaller the throughput gains. For instance, 56% of CoMP Candidates (CC) UEs in the case of full cooperation will no longer be CC UES in 3GPP scenario #2. However, it seems that most of the expected gain can be obtained using intra-site deployment, which has the smallest cluster size. In other deployment cases, with respect to intra-site deployment, the low cell-edge throughput gain improvement is counterbalanced by a substantial increase of the cost of rolling-out the network (black fiber is needed).

### 3.3.3 Cross-layer performance evaluation of CoMP

Inter-cell interference is one of the key challenges faced in mobile communication systems. It restricts the re-usability of the radio resource and limits spectral efficiency. Since the days of GSM, various techniques are used to cope with interference

CoMP, a main feature on the LTE-A roadmap, is mentioned as a promising approach to mitigate its effects through the coordination of multiple cells. We focus in this work on joint processing (JP) schemes, where all cells of the coordination cluster are involved in the transmission. Thus cooperating cells resources are not available for other users. JP schemes have been demonstrated as an efficient approach to improve cell-edge user's throughput but this is at the cost of higher resource consumption. Thus there is a tradeoff between the performance of cell-edge users and the ability of the network to process all traffic.

However, it was common in the previous studies to assume *static* or *semi static* users in the performance evaluation of CoMP schemes. We study in this work the impact of mobility on the performance of intra-site coordination under several scheduling strategies

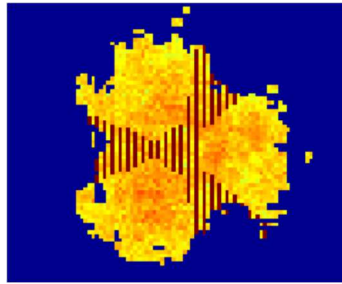


Figure 77: A tri sector site with coordination areas

### 3.3.3.1 Reference Model

#### **Cellular Network**

A UE in the cell-edge region may be able to receive signals from multiple cells and the UE's transmission may be received at multiple cells, so if the signaling transmitted from the multiple cells is coordinated, the downlink performance can be increased significantly. That is the main idea of the Joint processing coordination.

In order to study the intra-site joint processing coordination, we consider a tri-sector site constituted of  $K=3$  sectors, where each sector  $k=1,2,3$  is modeled by two main zones: a non-coordination zone and a coordination zone. We refer by zone  $k, k+1$  (with modulo  $K$  notation) to the coordination zone between sectors  $k$  and  $k+1$ . The coordination zones  $k, k+1$  (hatched area), as illustrated by Figure 77, are those where the difference between the signals received from sectors  $k$  and  $k+1$  doesn't exceed a given threshold  $\delta P$ , involving both sectors in the transmission. Figure 77 illustrates the case of  $\delta P = 12$  dB. We refer by zone  $k$  to the non-coordination zone (area without hatching) where only sector  $k$  is involved in the transmission.

We model each zone  $k$  and zone  $k, k+1$  by a set of  $N_k$  and  $N_{k,k+1}$  regions respectively. In each region, radio conditions are supposed to be homogeneous and thus users are served at the same physical data rate on the downlink. We model each region by a queue with a specific service rate corresponding to the physical data rate in this region. The considered site can be viewed as a set of  $\sum_{k=1}^K N_k + N_{k,k+1}$  queues with  $K$  coupled processors.

#### **Traffic model**

We consider elastic traffic only and we assume that new data flows are generated in each region of each zone at the random times of a Poisson process. We assume that service rates are exponential.

The resources of each sector  $k$  are shared between CoMP users in coordination zones  $k, k+1$  and  $k-1, k$  and non-CoMP users in the non-coordination.

For the sake of simplicity, we assume that users in each zone share the allocated radio resources equally, independently of their radio conditions. However, when the network operates under an opportunistic scheduler which exploits the fast fading, a rate gain should be taken into account.

#### **Static Allocation SA**

A simple strategy consists in allocating a fixed fraction of resources to CoMP and non-CoMP users' data flows: a CoMP frequency sub-band is introduced to perform CoMP operation, so that all users selected to be served in CoMP mode use this pre-configured frequency sub-band. CoMP users' data flows are allocated some fixed fraction of the resources of each coordinated sector.

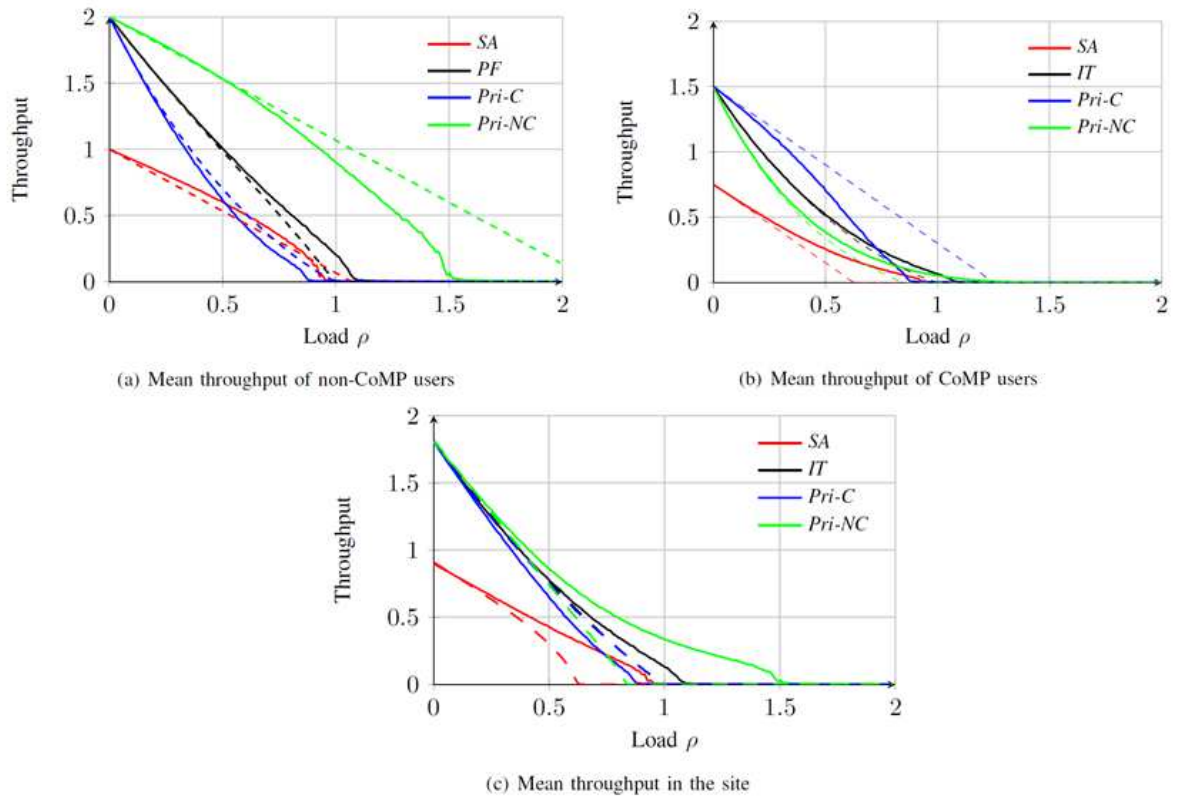


**Figure 78: Throughput performance with mobility (solid lines) and without mobility (dashed line)**

#### Iterative scheduler *IT*

Indeed, a centralized scheduler should be implemented in each site. For instance, if a user in zone 1 is selected to be served by the scheduling algorithm, the scheduler can either select a user in zone 2 and a user in zone 3 or select a user in zone 23 to be served simultaneously. Similarly, if a user in zone 12 is selected for instance, another user in zone 3 is served simultaneously.

#### Priority to non-CoMP users *Pri-NC*

Under this policy, non-CoMP users in each sector are scheduled first and are allocated all the radio resources whenever active. CoMP users in any zone wait until resources become available, these users equally share resources with other CoMP users in the other coordination zones.

#### Priority to CoMP users *Pri-C*

Under this policy, CoMP users are scheduled first and are allocated all radio resources whenever active. Non-CoMP users in each cell are served only when there are no active CoMP users in the given cell.

#### Numerical results

We consider a low interference scenario (beamforming system) where the mean coordination gain only 50% and  $\delta P = 12\text{dB}$ . We assume that the mean service rate of non-CoMP users is  $\mu = 2$  while the mean service rate of CoMP users is  $\mu = 1.5$ . For the static allocation scheme we suppose that the band is equally partitioned between CoMP and non-CoMP users.

Figure 78 compares the throughput performance of the four policies. Observe that the iterative scheduler (*IT*) outperforms the three other strategies. The priority to non-CoMP (*Pri-NC*) strategy leads to degraded performance. These results show that in the absence of mobility a fair strategy is the best strategy to be applied. However, the priority to CoMP (*Pri-C*) strategy has almost similar mean performance as the iterative scheduler.

### 3.3.3.2 Impact of mobility

We add mobility to the previous model. We consider only intra-site mobility as inter-site mobility will have only limited impact on the performance. We suppose that users can move from one zone to another zone. We assume exponential movement.

#### Numerical results

Consider the same scenario as in the previous case with a movement rate  $\nu = 1$ . The results are obtained by the numerical evaluation of the stationary distribution of the Markov process and shown in Figure ref (solid lines). Inter-zone mobility improves the mean throughput in the site for all strategies except for the *Pri-C* strategy. Under this strategy, mobility leads to throughput degradation both for non-CoMP users and for CoMP users. However, prioritizing non-CoMP users in the presence of mobility outperforms all other strategies in sharp contrast to the scenario without mobility. This is due to the fact that cell edge users are more likely served in good radio conditions without performing CoMP operations, minimizing the waste of resources. Based on this observation, the following conclusion may be drawn: it is not worth losing a resource to serve a CoMP user if that user is moving and can benefit from better channel conditions. So if predicted accurately, mobility can be an interesting property which can include the scheduling strategy. Following this conclusion, we will introduce a more advanced mobility-aware scheduler in the next section.

Motivated by the above conclusions, we consider now a mobility-aware scheduler which uses the mobility as additional information in order to schedule users. For instance, we assign to each CoMP user a score which is inversely proportional to its speed. This score is used by the scheduler. The more the CoMP user is static the more it is prioritized.

We have assumed so far that all users have the same mobility behavior. In particular, they are all static or all mobile. In order to evaluate the mobility-aware scheduler, we extend the results to multiple classes of mobility,

The numerical evaluation of the stationary distribution of the Markov process is shown in Figure 79 for the same previous scenario but with two equiprobable classes of users: a static class and a mobile. Results show that the mobility aware scheduler improves the performance as well as the stability condition.

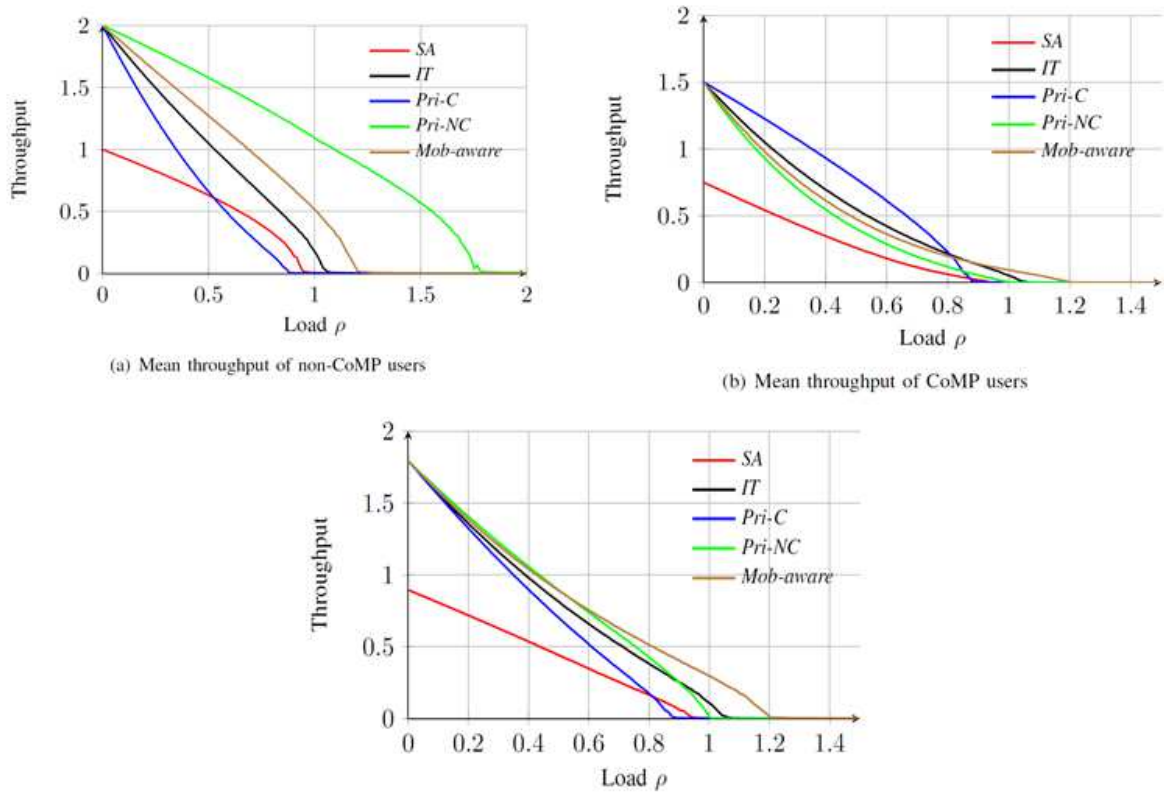


Figure 79: Throughput performance with two classes of mobility.

### 3.3.3.3 System level simulation

In order to validate the previous model we do system-level simulations based on the LTE technology. We consider the 21 hexagonal cells formed by 7 tri-sector sites. The main parameters are summarized in Table 8. Traffic consists of file transfers only. Flows arrive according to a Poisson process with uniform spatial distribution. File sizes are generated from an exponential distribution with mean  $\sigma = 1.25$  Mb. Scheduling decisions are taken in each eNodeB at each TTI (1ms). We consider intra-site coordination with a threshold  $\delta P = 12$  dB and a centralized scheduler in each site.

Table 8 Simulation Setting

Network topology	Macro cells only
Environment	Urban
Context	Outdoor
Inter-site distance	500 m
PathLoss	ITU Model
Radio access technology	LTE
Number of tx/rx antennas	MIMO 2x2
number of streams	1
Receiver	MRC
Codebook	3GPP
Carrier frequency	2 GHz
Bandwidth	10 MHz
$\delta P$ for intra-site CoMP	12 dB
Mean file size	1.25 Mb

We implement the two priority schedulers. We simulate 20 minutes and estimate for each scheduling strategy the cell-average throughput as the ratio of mean flow size to mean flow duration.

Figure 80 shows the mean user performance in terms of mean user throughput and mean number of users as a function of the arrival rate per eNodeB/s for each scheduler.

Results show that in sharp contrast to the scenario without mobility prioritizing non-CoMP users in the presence of mobility outperforms the strategy that prioritizes CoMP users. This confirms the previous results obtained by the analysis of flow level traffic model.

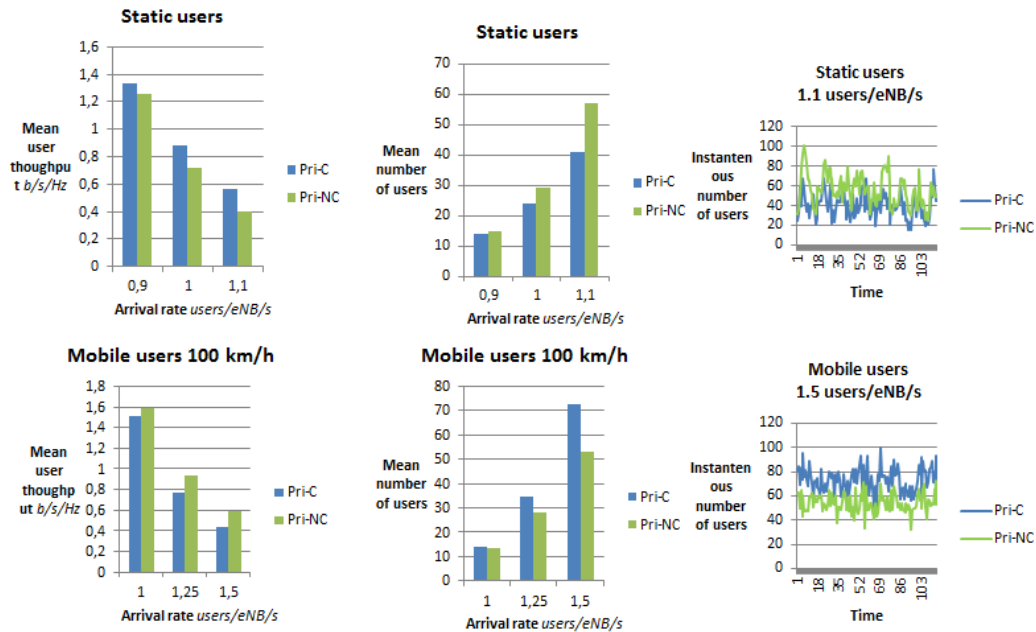


Figure 80: Performance obtained by system level simulation.

#### 3.3.3.4 Conclusion

In this work we study the impact of mobility on the performance of intra-site coordination under several scheduling strategies. We show that in low interference scenario, it is not worth to perform coordination for a mobile user which is able to move and get better radio conditions. Following this observation, we propose in part B a mobility-aware scheduler which deprioritizes mobile CoMP users. We show that this scheduler improves the performance by giving the chance to mobile cell-edge users to be served in better radio conditions where cell coordination is not required. This scheduler is suitable for elastic traffic where the delay is tolerable. However, it can no longer work when considering traffic with real-time constraints such as video streaming (Netflix, YouTube, ...).

#### 3.3.4 Impact of beamforming in a large-scale real environment

A first study of the impact of beamforming was performed in [3], showing the decrease of the interference level in a dense urban environment, but assuming a constant traffic load of the cells. A new simulation approach has been developed, so-called Monte-Carlo, where discrete users are randomly dropped in the prediction area, and KPI statistics are built from a succession of runs. At each run, the simulator determines the user's attachment (considering an omni-directional radiation), selects the per-user antenna beam that maximizes the SNR, and calculates the DL/UL interferences depending on the selected antenna beams and user activities. The users' throughputs are then obtained from a mapping with their estimated SINR, making it possible to evaluate the traffic load of the cells to which they are attached. The simulation process is then able to estimate both the interference decrease and the traffic load decrease achievable thanks to the beamforming.

The simulation approach is evaluated with a dense LTE outdoor small-cell network deployed in the urban environment shown in Figure 81 using the ray-based channel modelling of Section 2.3.5. There is no co-channel macro-cell here. The impact of the beamforming on the user throughput is assessed in both DL and UL directions in a scenario with medium traffic load (i.e. the average small-cell traffic load is around 15%). More specifically, the evaluation consists in the comparison between three different antenna systems installed at the small-cell: 1) a single omni-directional antenna with 2.15 dBi, i.e. the reference scenario; 2) LTE TM6 (Transmission Mode) with two omni-directional antennas; and 3) LTE TM6 with four omni-directional antennas. The maximum emitted power is kept constant in all test scenarios. The other simulation parameters are reported in

Table 9.



Figure 81. Small-cell network deployed in a dense urban environment (dots are small cell locations)

Table 9. Simulation parameters

<b>System</b>	OFDMA FDD 2x10 MHz Central frequency: 2600MHz
<b>Small-cell layout</b>	Deployment: 14 small-cells in 0.2 km <sup>2</sup> (69 cells per km <sup>2</sup> ) Height: 6 m above ground Maximum transmit power: 5 W UL noise figure: 2.5 dB
<b>User equipment</b>	UL transmit power: 23 dBm Antenna: omni-directional, 0 dBi, 1.5m above ground DL noise figure: 9 dB 2 antennas
<b>User traffic</b>	Data traffic 60% indoor 200 Mbps/km <sup>2</sup> DL 20 Mbps/km <sup>2</sup> UL

At each Monte-Carlo iteration, a random set of users are dropped in the blue area of Figure 81. As the Monte-Carlo simulation proved to rapidly converge, 30 independent drops were sufficient to reach constant performance statistics. The performance has been estimated from only the users attached to the five central small-cells represented by red dots in Figure 81. Indeed the interference calculated at the users located close to the external boundary of the simulation area is underestimated and thus the resulting user performance is not fair.

Table 10 summarizes the simulation results for both DL and UL directions, including: the DL cell load (ratio of allocated cell resources); the median peak user throughput; and the peak throughput at the cell-edge (10% worst percentile). The small-cells obviously take great advantage from the

beamforming effect, with a mean DL traffic load reduced by up to 37%. Compared to the single omni-directional antenna, the LTE TM6 leads to a significant increase of the median DL peak throughput (up to +24%), and even more at the cell edge (up to +121%). The gain on the UL performance is highly significant as well. The median and cell-edge peak throughputs are respectively improved by up to +24% and up to +700%.

**Table 10. Results from the small-cell network simulation**

		Single omni antenna	LTE TM6 – 2 antennas	LTE TM6 – 4 antennas
<b>Downlink</b>	<b>Mean traffic load</b>	16 %	12 %	10 %
	<b>Median SINR</b>	16.1 dB	19.4 dB	22.5 dB
	<b>Cell-edge SINR</b>	3.3 dB	6.6 dB	10.2 dB
	<b>Median peak throughput</b>	42 Mbps	48 Mbps	52 Mbps
	<b>Cell-edge peak throughput</b>	14 Mbps	23 Mbps	31 Mbps
<b>Uplink</b>	<b>Median SINR</b>	14.1 dB	18.1 dB	21.9 dB
	<b>Cell-edge SINR</b>	-5.1 dB	-1.3 dB	2.9 dB
	<b>Median peak throughput</b>	42 Mbps	52 Mbps	52 Mbps
	<b>Cell-edge peak throughput</b>	1 Mbps	3.5 Mbps	8 Mbps

In conclusion of this contribution, the impact of beamforming has been characterized considering LTE TM6 with 2 and 4 antennas. Both interference level decrease and resulting traffic load decrease have been evaluated in a dense small-cell network. Users' performance is significantly improved in DL and UL thanks to the interference rejection provided by the beamforming.

### 3.4 RF design

This section presents the work done in Task T3.4 during the second period of SHARING.

The scope of this study is to evaluate the requirements of an RF front-end to support different Carrier Aggregation (CA) configurations and provide energy savings. The power amplifier (PA) is one of the most power consuming components at RF front-end. Depending on the CA configuration (intra-band contiguous or intra-band non-contiguous) and the number of component carriers (CCs), different output back-off (OBO) level is required at PA. Therefore a reconfigurable RF front-end was proposed capable to adapt its performance using different operating points at PA and improve energy efficiency. The solution was compared to a conventional PA with single operating point to evaluate energy efficiency enhancements.

In the context of WP7, a demonstrator combining RF front end and antenna system has been tested. It shows the compatibility between both subsystems and demonstrate the possibility of increasing the energy efficiency as well as the level of integration of a small cell base station despite the use of a new technology enabler such as carrier aggregation.

#### 3.4.1 Reconfigurable RF front-end to support carrier aggregation

This section presents the detailed work done not previously reported in D3.5. The PA OBO requirements to support intra-band contiguous CA were analyzed combining the results from the



CCDF evaluation and the ACLR evaluation. The requirements were defined taking into account only the 1dB compression point output power at PA. In this document, it presents the performed simulations adding the TOI parameter. The TOI relates nonlinear products caused by the third-order nonlinear term to the linearly amplified signal. There is a rule-of-thumb that holds for many amplifiers that the 1dB compression point output power fall approximately 10dB below TOI. All previous simulations were done following this assumption. Nevertheless, this study has evaluated the TOI impact performing different simulations defining TOI value 8dB, 10dB and 12dB above the 1dB compression point output power.

Figure 82 presents the simulated results for different TOI values from 1CC to 5CCs supporting intra-band contiguous CA. The analysis was done without evaluating TOI parameter, with TOI value of 8dB, 10dB and 12dB above the 1dB compression point output power. The simulated results without evaluating TOI parameter and with TOI value 10dB above the 1dB compression point output power are equivalent. Therefore it works out that the PA model applies the mentioned rule-of-thumb.

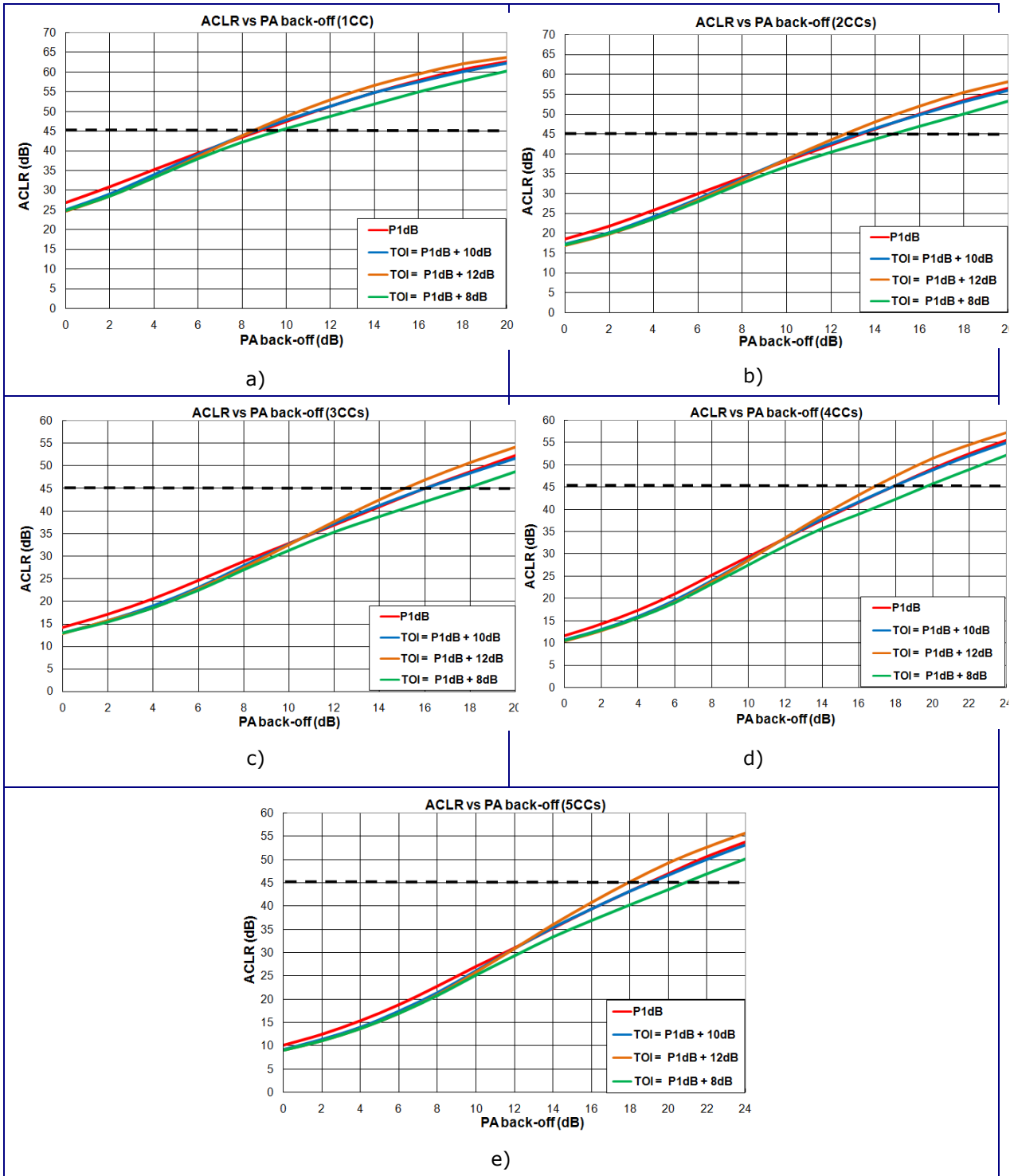


Figure 82 ACLR results vs PA OBO requirement modifying TOI parameter for a) 1CC, b) 2CCs, c) 3CCs, d) 4CCs and e) 5CCs in intra-band contiguous CA configuration.

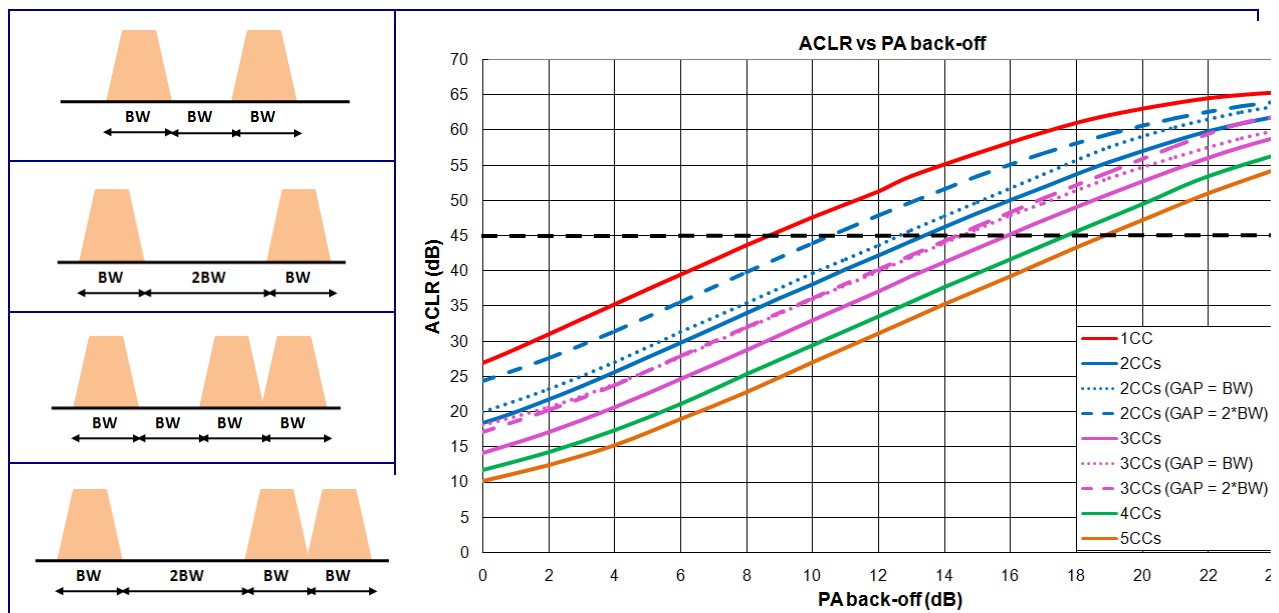
Table 11 summarizes PA OBO requirements considering ACLR specification in relation to TOI value for different number of CCs in intra-band contiguous CA configuration.

**Table 11 PA OBO requirements considering ACLR specification for different TOI values in intra-band contiguous CA configuration.**

Number of CCs	TOI = P1dB + 10dB	TOI = P1dB + 8dB	TOI = P1dB + 12dB
1	8.7 dB	9.6 dB	8.5 dB
2	13.4 dB	14.8 dB	12.6 dB
3	15.9 dB	17.7 dB	15.2 dB
4	17.7 dB	19.5 dB	16.8 dB
5	18.9 dB	20.8 dB	17.9 dB

The higher is the number of CCs, the higher is the TOI impact over PA OBO requirements. To sum up, the rule-of-thumb of 1dB compression point output power 10dB below TOI can be assumed. Nevertheless, some variations can be expected depending on the specific PA.

Furthermore, the analysis was extended to intra-band non-contiguous CA configuration. Different simulations were performed and the simulated results are presented below. Figure 83 presents ACLR simulated results from 2CCs to 3CCs supporting intra-band non-contiguous CA. The simulated results for intra-band contiguous CA are also included to be compared. For the simulations, the gap among CCs was defined equal to the bandwidth and twice over the bandwidth.



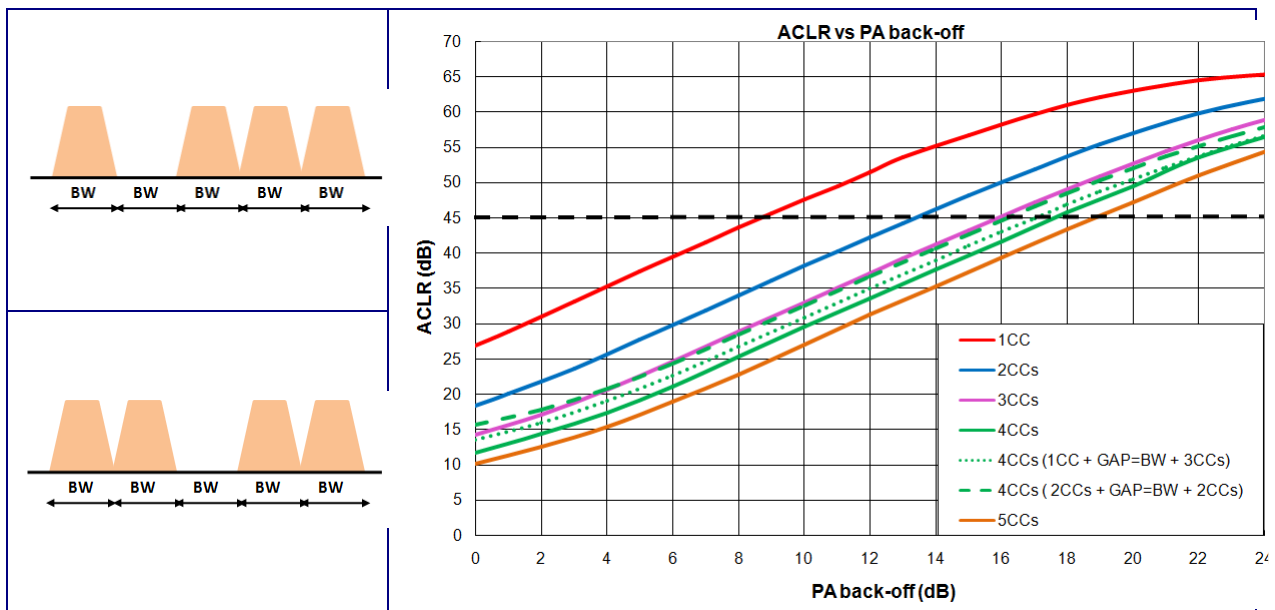
**Figure 83 ACLR simulated results from 2CCs to 3CCs supporting intra-band non-contiguous CA.**

Table 12 shows the simulated results for intra-band contiguous CA and intra-band non-contiguous CA up to 3 CCs. To support intra-band non-contiguous CA, PA OBO requirements are less restrictive than for intra-band contiguous CA because the impact on adjacent channels is not so significant. Furthermore the higher is the gap among CCs, the lower is the PA OBO value.

**Table 12 PA OBO requirements up to 3CCs in different CA configurations.**

Number of CCs	Intra-band contiguous	Intra-band non-contiguous	
		GAP = BW	GAP = 2*BW
1	9.6 dB	-	-
2	13.4 dB	12.6 dB	10.5 dB
3	15.9 dB	14.5 dB	14.3 dB

The evaluation was also done for 4CCs in intra-band non-contiguous CA configuration. In this configuration, the CCs were positioned grouping 2CCs or 3CCs with a gap equal to the bandwidth. Figure 84 shows the simulated results and Table 13 presents PA OBO requirements depending on the configuration.



**Figure 84 ACLR simulated results for 4CCs supporting intra-band non-contiguous CA.**

**Table 13 PA OBO requirements for 4CCs in different CA configurations.**

Number of CCs	Intra-band contiguous	Intra-band non-contiguous	
		1CC + GAP = BW + 3CCs	2CCs + GAP = BW + 2CCs
4	17.7 dB	17 dB	16.2 dB

Finally, intra-band non-contiguous CA for 5CCs is depicted in Figure 85. The CCs were positioned grouping 3CCs or 4CCs with a gap equal to the bandwidth. Table 140 summarizes the simulated results for 5CCs in intra-band non-contiguous CA configuration.

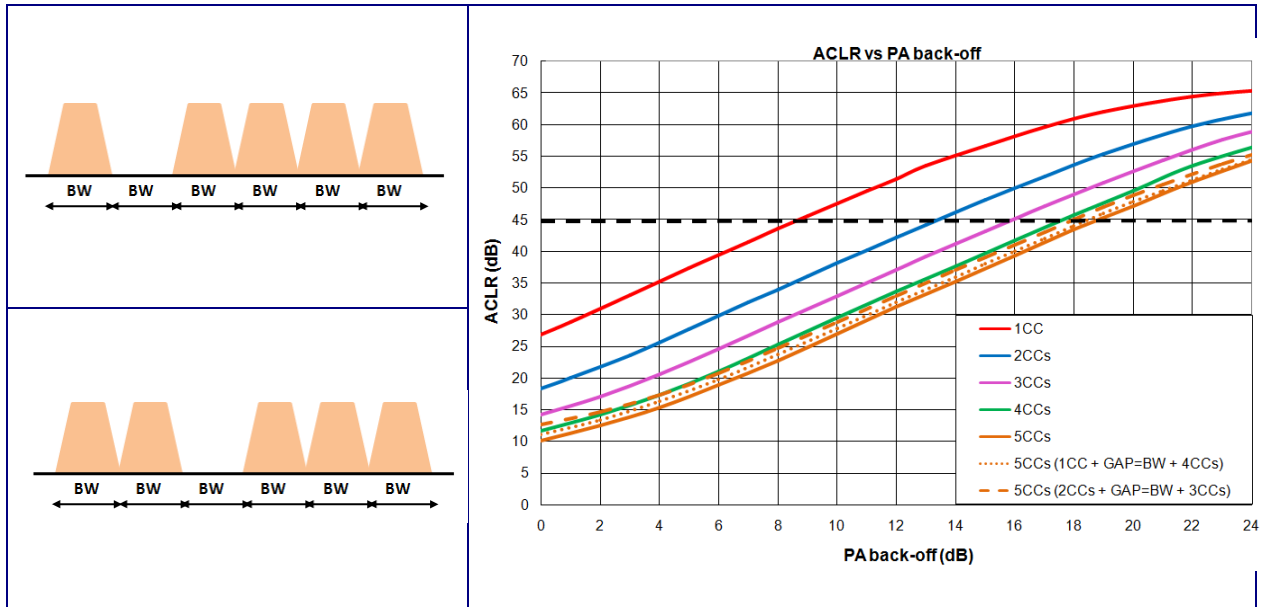


Figure 85 ACLR simulated results for 5CCs supporting intra-band non-contiguous CA.

Table 14 PA OBO requirements for 5CCs in different CA configurations.

Number of CCs	Intra-band contiguous	Intra-band non-contiguous	
		1CC + GAP = BW + 4CCs	2CCs + GAP = BW + 3CCs
5	18.9 dB	18.5 dB	18 dB

The analysis was completed for intra-band contiguous CA and intra-band non-contiguous CA from 1CC to 5CCs defining the PA OBO requirements. The solution was evaluated in the hardware prototype developed in WP7 (Figure 86).

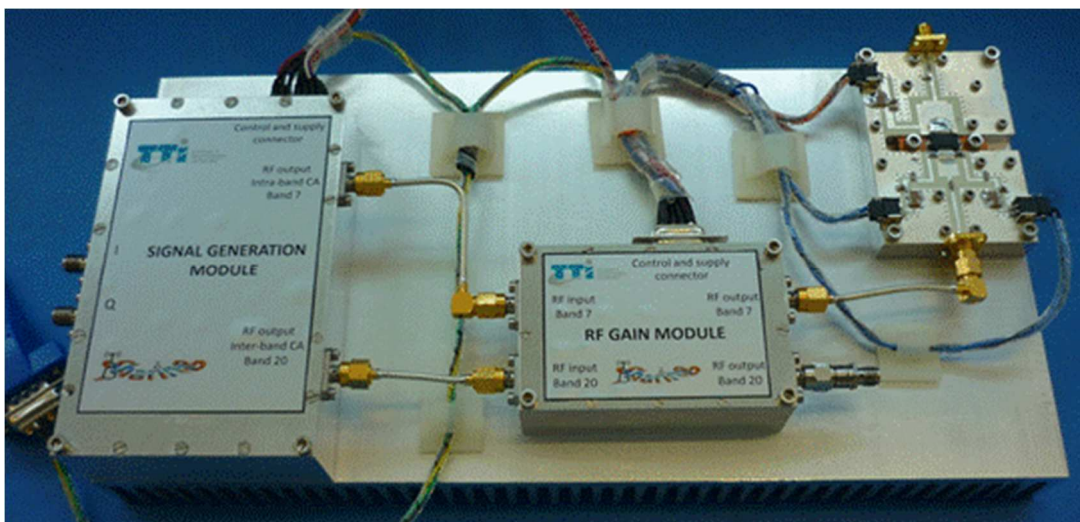


Figure 86 Picture of the hardware prototype developed in WP7.

Figure 87 shows the measured results related to power gain and PAE in the AFT20S015N prototype which are used to evaluate energy efficiency improvements provided by the proposed solution. The 1dB compression point output power in AFT20S015N prototype is around 38.6 dBm.

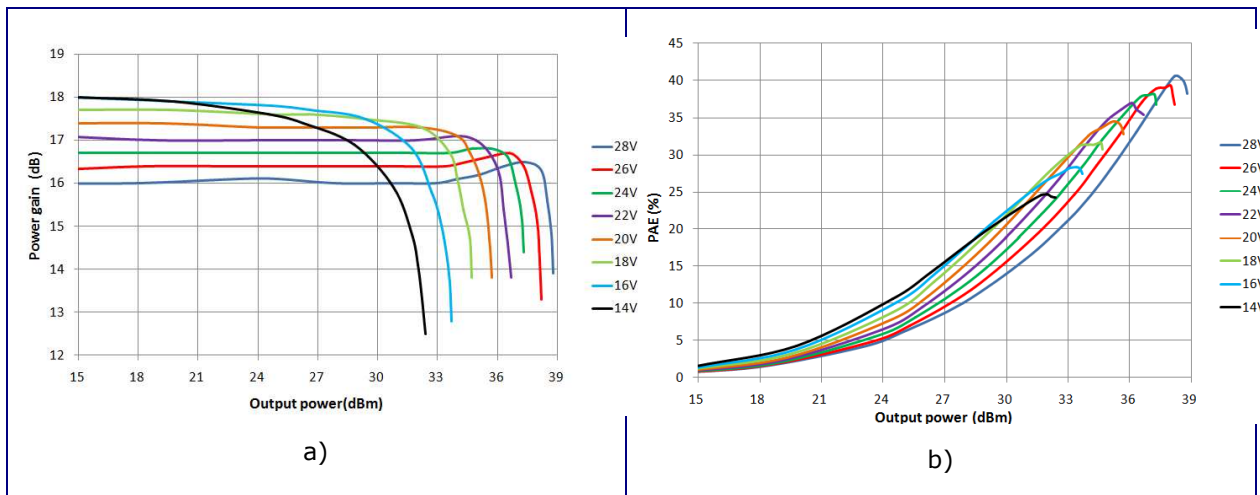


Figure 87 a) Power gain and b) PAE results for different operating points in AFT20S015N prototype.

#### 3.4.1.1 Conclusions on RF and antenna design

A complete evaluation about PA OBO requirements for different intra-band CA configurations (intra-band contiguous and intra-band non-contiguous) was done. The evaluation has analyzed LTE-A waveform and ACLR specification using E-UTRA test models. The impact of TOI value at PA was also analyzed performing different simulations. It concluded that some variations in PA OBO requirements are expected depending on each particular PA, because not all PA parameters are included in the simulations. The defined PA OBO requirements should be used as reference values for typical PAs.

Using the commercial PA, AFT20S015N, the proposed solution was analyzed in terms of PAE enhancement, showing PAE improvement up to 45% between the most restrictive CA configuration and the least restrictive one. Therefore the proposed solution using the reconfigurable RF front-end to support CA provides clearly energy savings compared to conventional PA with single operating point.

## 4 CONCLUSIONS

This document reflects all research work conducted by SHARING project WP3. Part A is a summary of the entire work, while Part B contains the work that has not yet been reported. WP3 was dedicated to advanced techniques needed to cope with traffic increase, and to fulfil the objective of “services for everyone everywhere”. Several new features have been introduced in 3GPP LTE to address these issues, such as CoMP (Coordinated Multi-Points), Carrier Aggregation (CA), and advanced receivers. Features such as MIMO and Multi-User-MIMO also contribute to the same objectives.

However, the project did not limit itself to investigate existing solutions in 3GPP, but also considered new schemes, potential candidates for 5G.

CoMP issues were investigated, both from the physical (PHY) layer point of view (comparison between distributed and centralized implementations) and from a cross-layer (PHY and MAC) perspective, including system level aspects. Also, a ray tracing tool was used to produce realistic channel measurements that were used as inputs by a new method, based on a semi-deterministic approach, for building an interference map,

Advanced receivers with interference mitigation features have been proposed, both UL and DL. Some of these Interference mitigating schemes involve both uplink and downlink, such as intergerence alignment schemes, or linear dispersion codes.

A new RF front-end has also been proposed in order to accommodate Carrier Aggregation. On the one hand, a wide band reconfigurable and energy-savvy RF was developed, covering all bands at stake, and on another hand, a frequency agile antenna was developed, to accommodate the lower frequency band while keeping the antenna size small. Both were prototyped, and further integrated in a single Proof-of-concept in the context of WP7.

## 5 REFERENCES

- [1] 3GPP TR 36.814 Release 9, "Technical Specification Group Radio Access Network; Evolved Universal Terrestrial Radio Access (E-UTRA); Further advancements for E-UTRA physical layer aspects"
- [2] 3GPP TR 36.819 Release 11, "Technical Specification Group Radio Access Network; Coordinated multi-point operation for LTE physical layer aspects"
- [3] SHARING D3.2 "Multi-point cooperation schemes at the transmitter: innovative concepts and performance evaluation" Jan 2015
- [4] SHARING D3.3 "Advanced Transceivers and interference cancellation schemes at the receiver: Innovative Concepts and Performance Evaluation" Jan 2015
- [5] SHARING D3.4 "Flexible Interference Management Concept: Innovative Concepts and Performance Evaluation" Jan 2015
- [6] SHARING D3.5 "Progress in RF Front-End, Antenna Design" Jan 2015
- [7] 3GPP TR 36.211 "Technical Specification Group Radio Access Network; Evolved Universal Terrestrial Radio Access (E-UTRA) Physical Channels and Modulation" release 9 Mars 2010
- [8] 3GPP TR 36.866 Release 12 "Technical Specification Group Radio Access Network; Network Assisted Interference Cancellation and Suppression for LTE
- [9] M. Ali Maddah-Ali and D. Tse, "Completely stale transmitter channel state information is still very useful," *Information Theory, IEEE Transactions on*, vol. 58, no. 7, pp. 4418–4431, 2012.
- [10] S. Yang, M. Kobayashi, P. Piantanida, and S. Shamai, "Secrecy degrees of freedom of MIMO broadcast channels with delayed CSIT," *IEEE Trans. Inf. Theory*, vol. 59, no. 9, pp. 5244–5256, Sept. 2013.
- [11] S. Kottath, D. Gesbert, E. Hardouin, "Opportunistic Feedback Mechanisms in Multicell MIMO Networks," *IEEE-ICC 2015*, London, UK, Jun. 2015
- [12] S. Kottath, D. Gesbert, H. Khanfir, E. Hardouin, "Broadcast channel feedback in multiple-antenna transmitter cooperation networks: Accuracy or consistency?," *EW2014*, 20th European Wireless Conference, Barcelona, Spain, May 14-16, 2014.
- [13] Bai, Z.; Badic, B.; Iwelski, S.; Scholand, T.; Balraj, R.; Bruck, G.; Jung, P., "On the Equivalence of MMSE and IRC Receiver in MU-MIMO Systems," *Communications Letters, IEEE*, vol.15, no.12, pp.1288,1290, December 2011
- [14] Ghaffar R.; Knopp R., "Interference-aware receiver structure for multi-user MIMO and LTE," *EURASIP Journal on Wireless Communications and Networking* 2011
- [15] Ghaffar, R.; Knopp, R., "Spatial Interference Cancellation Algorithm," *Wireless Communications and Networking Conference*, 2009. *WCNC 2009. IEEE*, vol., no., pp.1,5, 5-8 April 2009
- [16] J. Salo, G. Del Galdo, J. Salmi, P. Kyösti, M. Milojevic, D. Laselva, and C. Schneider. (2005, Jan.) MATLAB implementation of the 3GPP Spatial Channel Model (3GPP TR 25.996) [Online]. Available: <http://www.tkk.fi/Units/Radio/scm/>
- [17] A. Aghaei, K. Plataniotis, S. Pasupathy, « Widely Linear MMSE Receivers for Linear Dispersion Space-Time Block-Codes », *IEEE Transactions on Wireless Communications*. Vol. 9, N° 1, Jan. 2010.
- [18] S. Alamouti, "A Simple Transmit diversity technique for wireless communications", *IEEE Journal on Select Areas in Communications* Vol. 16, N°. 8, October 1998
- [19] P. Chevalier, F. Dupuy, "Widely Linear Alamouti Receiver for the reception of real-valued constellations corrupted by interferences – The Alamouti-SAIC-MAIC Concept", *IEEE Transactions on Signal Processing*, vol. 59(7), pp. 3339-3354, 2011.
- [20] A. Naguib, N. Seshadri, A. Calderbank, « Applications of space-time Block Codes and Interference Suppression for High Capacity and High Data Rate Wireless Systems », *Proceedings of the 32<sup>nd</sup> Asilomar conference* Nov. 1998



- [21] P. Chevalier and F. Picon "New Insights Into Optimal Widely Linear Array Receivers for the Demodulation of BPSK, MSK, and MSK Signals Corrupted by Noncircular Interferences—Application to SAIC" *IEEE Transactions on Signal Processing*, Vol 54, N°3, March 2006.
- [22] P. Pinto, A. Giorgetti, M. Z. Win, and M. Chiani, "A Stochastic Geometry Approach to coexistence in Heterogeneous Wireless Networks," in *IEEE Journal on Selected Areas in Communications*, vol. 27, no. 7, pp. 1268 - 1282, September, 2009.
- [23] A. Papoulis and S. U. Pillai, *Probability, Random Variables and Stochastic Processes*, Mc-Graw-Hill, 2002.
- [24] M. L. Rodrigues, L. Vieira, and M. Campos, "Fingerprinting-based radio localization in indoor environments using multiple wireless technologies", in proceedings of IEEE Personal Indoor Mobile Radio Communications (PIMRC'11), Toronto, Canada, 2011.
- [25] R. C. Darakanath, J. d. Naranjo, and A. Ravanshid, "Modeling of Interference Map for Licensed Shared Access in LTE-Advanced Networks Supporting Carrier Aggregation", in *Wireless Day - International Federation for Information processing (IFIP)*, Niagara falls, Canada, 2013.
- [26] S-J. Kim, E. Dall'Anese, and G. B. Giannakis, "Cooperative Spectrum Sensing for Cognitive Radios Using Krige Kalman Filtering", in *IEEE Journal of selected topics in signal processing*, vol. 5, No. 1, 2011.
- [27] A. Babaei, M. Haenggi, P. Agrawal, and B. Jabbari, "Interference statistics of a Poisson field of interferers with random puncturing", in proceedings of Military Communications Conference (MILCOM), Baltimore, MD, USA, 2011.
- [28] S. Wang, and W. Guo, "Downlink Interference estimation without feedback for Heterogeneous Network Interference Avoidance," in proceedings of International Conference on Telecommunications (ICT'14), Lisbon, Portugal, 2014.
- [29] T.L. Jensen, S.Kant, J.Weinger, and B.H. Fleury, "Fast link adaptation for mimo ofdm," *IEEE Trans. Veh. Technol.*, vol.VT-59, pp. 3766–3778, Oct. 2010.
- [30] R.Visoz, A.O. Berthet, and M. Lalam, "Semi-analytical performance prediction methods for iterative mmse-ic multiuser mimo joint decoding," *IEEE Trans. Commun.*, vol.58, no.9, pp. 2576–2589, Sept. 2010.
- [31] B. Ning, R. Visoz, and A. O. Berthet, "Physical layer abstraction for turbo coded mimo systems with Immse-ic based turbo equalization," *Proc. IEEE GLOBECOM'13 workshop*, Atlanta, USA, Dec. 2013.
- [32] Y. Fadlallah, R. Visoz, A.O. Berthet, "A novel calibration framework for the physical layer abstraction of (turbo) codeword IC receivers," *Proc. IEEE VTC'15 Spring*, Glasgow, Scotland, May 2015.
- [33] S. Brueck, L. Zhao, J. Giese, M. A. Amin, "Centralized scheduling for joint transmission Coordinated Multi-Point in LTE-Advanced," *International ITG Workshop Smart Antennas*, Bremen, Feb. 2010.
- [34] Xiaona Li and Qimei Cui and Yinjun Liu and Xiaofeng Tao, "An effective scheduling scheme for CoMP in heterogeneous scenario" *PIMRC, 2012 IEEE* 23<sup>rd</sup>
- [35] S. Wang, F. Wang, Y. Wang, D. Yang, "A novel scheduling scheme based on MU-MIMO in TD-LTE uplink," *Proc. of IEEE WCNC*, Cancun, Mar. 2011.
- [36] B. Sah & all, "A Frequency Domain Joint MMSE-SIC Equalizer for MIMO SC-FDMA LTE-A Uplink", *IEEE* 2014
- [37] M. Jiang & all, "Design of High Performance MIMO Receivers for LTE/LTE-A Uplink", *IEEE* 2010
- [38] S. Ali Cheema & all, "Link Adaptation for LTE-A Systems Employing MMSE Turbo Equalization", *WSA* 2014
- [39] G. Berardinelli & all, "Turbo Receivers for Single User MIMO LTE-A Uplink", *IEEE* 2009
- [40] G. Berardinelli & all, "SVD-based vs. Release 8 codebooks for Single User MIMO LTE-A Uplink", *IEEE*

2010

- [41] B. Yin & all, "Reconfigurable multi-standard uplink MIMO receiver with partial interference cancellation", IEEE ICC 2012
- [42] Z. Lin & all, "Analysis of Receiver Algorithms for LTE SC-FDMA Based Uplink MIMO Systems", IEEE trans. On Wireless Com., January 2010
- [43] SHARING D7.3 "Integration of selected implementations into platforms & interfaces finalization" December 2015
- [44] 3GPP TR36.104 Release 12, "Base station (BS) radio transmission and reception"
- [45] S. Best, "Optimization of the bandwidth of electrically small planar antennas," presented at the Antenna Applications Symp., Monticello, IL, 2009.
- [46] D. F. Sievenpiper, D. C. Dawson, M. M. Jacob, T. Kanar, S. Kim, J. Long and R. G. Quarfoth, "Experimental Validation of Performance Limits and Design Guidelines for Small Antennas," Antennas and Propagation, IEEE Transactions on , vol.60, no.1, pp.8-19, Jan. 2012.
- [47] P. de Kerret and D. Gesbert, "CSI sharing strategies for transmitter cooperation in wireless networks," IEEE Wireless Commun. Mag., vol. 20, no. 1, pp. 43-49, Feb. 2013.
- [48] Y. Corre and Y. Lostanlen, "Three-dimensional urban EM wave propagation model for radio network planning and optimization over large areas", IEEE Transactions on Vehicular Technology, vol. 58, no. 7, pp. 3112-3123, Sept. 2009.
- [49] N. Jindal, "MIMO broadcast channels with finite-rate feedback," *IEEE Trans. Inf. Theory*, vol. 52, no. 11, pp. 5045-5060, Nov. 2006.
- [50] P. de Kerret and D. Gesbert, "Degrees of freedom of the network MIMO channel with distributed CSI," *IEEE Trans. Inf. Theory*, vol. 58, no. 11, pp. 6806-6824, Nov. 2012.
- [51] P. de Kerret and D. Gesbert, "Regularized ZF in cooperative broadcast channels under distributed CSIT: A large system analysis," in *Proc. IEEE Int. Symp. on Inf. Theory*, 2015.
- [52] M. Maddah-Ali and D. Tse, "Completely stale transmitter channel state information is still very useful," *IEEE Trans. Inf. Theory*, vol. 58, no. 7, pp. 4418-4431, Jul. 2012.
- [53] C. B. Peel, B. M. Hochwald, and A. L. Swindlehurst, "A vector-perturbation technique for near-capacity multi-antenna multiuser communication-part I: channel inversion and regularization," *IEEE Trans. on Commun.*, vol. 53, no. 1, pp. 195-202, 2005.
- [54] Q. H. Spencer, A. L. Swindlehurst, and M. Haardt, "Zero-forcing methods for downlink spatial multiplexing in multiuser MIMO Channels," *IEEE Trans. Signal Process.*, vol. 52, no. 2, pp. 461-471, Feb. 2004.
- [55] R. Radner, "Team decision problems," *The Annals of Mathematical Statistics*, 1962.
- [56] S. Wagner, R. Couillet, M. Debbah, and D. Slock, "Large system analysis of linear precoding in correlated MISO broadcast channels under limited feedback," *IEEE Trans. Inf. Theory*, vol. 58, no. 7, pp. 4509-4537, July 2012.
- [57] A. Aghaei, K. Plataniotis, S. Pasupathy, « Widely Linear MMSE Receivers for Linear Dispersion Space-Time Block-Codes », IEEE Transactions on Wireless Communications Vol. 9, N°1, January 2010.
- [58] S. Lakshminarayana, J. Hoydis, M. Debbah, and M. Assaad, "Asymptotic Analysis of Distributed Multi-cell Beamforming," in International Symposium on Personal Indoor and Mobile Radio Communications (PIMRC'10), Sep. 2010, pp. 2105-2110.
- [59] A. Wiesel, Y. Eldar, and S. Shamai, "Linear Precoding via Conic Optimization for Fixed MIMO Receivers," *IEEE Trans. Signal Process.*, vol. 54, no. 1, pp. 161-176, Jan. 2006.
- [60] H. Dahrouj and W. Yu, "Coordinated Beamforming for the Multicell Multi-antenna Wireless System," *IEEE Trans. Wireless Commun.*, vol. 9, no. 5, pp. 1748-1759, May 2010.
- [61] S. Lakshminarayana, M. Assaad, M. Debbah, "Coordinated Multicell Beamforming for Massive MIMO: A Random Matrix Approach," *IEEE Transactions on Information Theory*, May 2015.
- [62] M. Neely, Stochastic Network Optimization with Application to Communication and Queueing

Systems. Morgan & Claypool, 2010.

- [63] S. Lakshminaryana, M. Assaad, M. Debbah, "Energy-Efficient Design in MIMO Multicell Systems with Time average QoS Constraints," IEEE JSAC, October 2015.
- [64] "[A Survey of the Statistical Theory of Shape](#)", by David G. Kendall, Statistical Science, Vol. 4, No. 2 (May, 1989), pp. 87–99
- [65] SHARING Deliverable D3.1, "New Opportunities, challenges and innovative concepts candidates for multi-point transmission and reception", July, 2014
- [66] Alaya-Feki, A.; Ben Jemaa, S.; Sayrac, B.; Houze, P.; Moulines, E., "Informed spectrum usage in cognitive radio networks: Interference cartography," in Personal, Indoor and Mobile Radio Communications, 2008. PIMRC 2008. IEEE 19th International Symposium, pp.1-5, 15-18 Sept. 2008.
- [67] Seung-Jun Kim; Dall'Anese, E.; Giannakis, G.B., "Cooperative Spectrum Sensing for Cognitive Radios Using Kriged Kalman Filtering," in Selected Topics in Signal Processing, IEEE Journal of , vol.5, no.1, pp.24-36, Feb. 2011.
- [68] R. Sidler, ""Kriging and Conditional Geostatistical Simulation Based on Scale-Invariant Covariance Models," Diploma thesis, Institute of geophysics Department of Earth Science, October 20,2003
- [69] T.Clessienne "Opportunistic Scheduling Algorithm for Joint-Processing DL CoMP" - submitted to VTC 2016

## **6 GLOSSARY**

<b>ACRONYM</b>	<b>DEFINITION</b>
3GPP	Third Generation Partnership Project
ACLR	Adjacent Channel Leakage Ratio
AP	Access Point
AWGN	Additive White Gaussian Noise
BC	Broadcast Channel
BER	Bit Error Rate
BF	Beamformer
BPSK	Binary Phase Shift Keying
BS	Base Station
CA	Carrier Aggregation
CB	Coordinated Beamforming
CC	Component Carrier
CCDF	Complementary Cumulative Distribution Function
CDF	Cumulative Distribution Function
CN	Condition Number
CoMP	Coordinated Multi-Point
CS	Coordinated Scheduling
CSI	Channel State Information
CSIT	Channel State Information at Transmitter
DL	Downlink
DMRS	Demodulation Reference Signal
DoF	Degree of Freedom
DPS	Dynamic Point Selection
eICIC	enhanced Inter-Cell Interference Coordination
DMRS	Demodulation Reference Signal
DoF	Degree of Freedom
DPS	Dynamic Point Selection
ESM	Effective SINR Metrics

E-UTRA	Evolved Universal Terrestrial Radio Access
FDD	Frequency Division Duplex
FDE	Frequency Domain Equalization
HetNET	HEterogeneous NETwork
IA	Interference Alignment
IA	Interference Aware
IC	Interference Cancellation
IC	Interference Channel
ICI	Inter-Cell Interference
ICIC	Inter-Cell Interference Coordination/Cancellation
IM	Interference Map
IRC	Interference Rejection Combining
IRC-DL	IRC Diagonal Loading
IS	Interference Suppression
ISD	Inter-Site Distance
JP	Joint Processing
JT	Joint Transmission
KPI	Key Performance Indicator
L-CWIC	Linear CodeWord Interference Cancellation
LD	Linear Dispersion
LMMSE	Linear Minimum Mean Square Error
LMMSE-C	LMMSE with compensation
LS-C	Least squares estimation with compensation
LTE	Long Term Evolution
LTE-A	Long Term Evolution – Advanced
LUT	Look-Up Table
MAC	Media Access Control
MCS	Modulation and Coding Scheme
MIESM	Mutual Information ESM

MIMO	Multiple Input Multiple Output
MISO	Multiple Input Single Output
ML	Maximum Likelihood
MMSE	Minimum Mean Square Error
MU-MIMO	Multiple User MIMO
OBO	Output back-off
OFDM	Orthogonal Frequency Division Multiplexing
OFDMA	Orthogonal Frequency Division Multiplexing Access
O-QAM	Orthogonally Multiplexed Quadrature Amplitude Modulation
PA	Power Amplifier
PAE	Power Added Efficiency
PAPR	Peak to Average Power Ratio
PCB	Printed Circuit Board
PEP	Pairwise Error Probability
PHY	Physical Layer
PIC	Parallel Interference Cancellation
PER	Packet Error Rate
PPP	Poisson Point Process
QAM	Quadrature Amplitude Modulation
QoS	Quality of Service
QPSK	Quadrature Phase Shift Keying
RB	Resource Block
RMT	Random Matrix Theory
RRM	Radio Resource Management
RSRP	Reference signal Receive Power
RSS	Received Signal Strength
RX	Receiver
SAIC	Single Antenna Interference Cancellation
SC-FDMA	Single Carrier- Frequency Division Multiple Access

SdoF	Secrecy Degree of Freedom
SIC	Successive/Sequential Interference Cancellation
SIR	Signal to Interference Ratio
SINR	Signal to Interference plus Noise Ratio
SL-MMSE	Single Layer MMSE
SM	Spatial Modulation
SMX	Spatial Multiplexing
SNR	Signal to Noise Ratio
SOCP	Second Order Cone Programming
TDD	Time Division Duplex
TOI	Third Order Intercept Point
TX	Transmitter
UE	User Equipment
UL	Uplink
WL	Widely Linear
ZF	Zero Forcing